11-7-2015

Hydrodynamics of Accumulators of Compressed Air for an UWCAES Plant

Ahmadreza Vaselbehagh
University of Windsor

Hydrodynamics of Accumulators of Compressed Air for an UWCAES Plant

by

Ahmadreza Vasel-Be-Hagh

A Dissertation
Submitted to the Faculty of Graduate Studies
through the Department of Mechanical, Automotive & Materials Engineering
in Partial Fulfillment of the Requirements for
the Degree of Doctor of Philosophy
at the University of Windsor

Windsor, Ontario, Canada

Hydrodynamics of Accumulators of Compressed Air for an UWCAES Plant

by

Ahmadreza Vasel-Be-Hagh

APPROVED BY:

R. E. Khayat, External Examiner
Western University

S. Cheng
Department of Civil and Environmental Engineering

B. Zhou
Department of Mechanical, Automotive & Materials Engineering

V. Stoilov
Department of Mechanical, Automotive & Materials Engineering

D. S.-K. Ting, Co-Advisor
Department of Mechanical, Automotive & Materials Engineering

R. Carriveau, Co-Advisor
Department of Civil and Environmental Engineering

2 June, 2015

DECLARATION OF CO-AUTHORSHIP AND PREVIOUS PUBLICATIONS

I hereby declare that this dissertation incorporates material that is result of joint research, as follows:

Chapter	Details
Chapter 6	This chapter incorporates the outcome of a joint research project undertaken in collaboration with Professor John Stewart Turner. The author initiated the work under supervision of Dr. David S.-K. Ting and Dr. Rupp Carriveau, and performed the key ideas, primary contributions and data analysis and interpretation. Later, Professor John Stewart Turner kindly accepted to join the team as an advisor on the draft manuscript.

I am aware of the University of Windsor Senate Policy on Authorship and I certify that I have properly acknowledged the contribution of other researchers to my dissertation, and have obtained written permission from each of the co-author(s) to include the above material(s) in my dissertation.

I certify that, with the above qualification, this dissertation, and the research to which it refers, is the product of my own work.

This dissertation includes 8 original papers that have been previously published/under review for publication in peer reviewed journals, as indicated in the following table (see page iv).

I certify that I have obtained a written permission from the copyright owner(s) to include the above published material(s) in my dissertation. I certify that the above material describes work completed during my registration as graduate student at the University of Windsor.

I declare that, to the best of my knowledge, my dissertation does not infringe upon anyone's copyright nor violate any proprietary rights and that any ideas, techniques, quotations, or any other material from the work of other people included in my dissertation, published or otherwise, are fully acknowledged in accordance with the standard referencing practices. Furthermore, to the extent that I have included copyrighted material that surpasses the bounds of fair dealing within the meaning of the Canada Copyright Act, I certify that I have obtained a written permission from the copyright owner(s) to include such material(s) in my thesis.

I declare that this is a true copy of my dissertation, including any final revisions, as approved by my dissertation committee and the Graduate Studies office, and that this

Chapter	Publication	Status
Chapter 2	Vasel-Be-Hagh, A. R., Carriveau, R. and Ting, D. S.-K. 2013 Numerical Simulation of Flow Past an Underwater Energy Storage Balloon. Computers and Fluids, 88, 272 -286.	*Published*
Chapter 3	Vasel-Be-Hagh, A. R., Carriveau, R. and Ting, D. S.-K. 2014 Flow past an Accumulator Unit of an Underwater Energy Storage System: Three Touching Balloons in Floral Configuration. Journal of Marine Science and Application 13(4), 467-476.	*Published*
Chapter 4	Vasel-Be-Hagh, A. R., Carriveau, R. and Ting, D. S.-K. 2015 Flow over Submerged Energy Storage Balloons in Closely and Widely Spaced Floral Configurations. Ocean Engineering, 95, 59-77.	*Published*
Chapter 5	Vasel-Be-Hagh, A. R., Carriveau, R. and Ting, D. S.-K. 2015 A Balloon Bursting Underwater. Journal of Fluid Mechanics, 769, 522-540.	*Published*
Chapter 6	Vasel-Be-Hagh, A. R., Carriveau, R., Ting, D. S.-K. and Turner, J. S. 2015 On the Drag of Buoyant Vortex Rings. under review.	*Under Review*
Appendix A	Vasel-Be-Hagh, A. R., Ting, D. S.-K. and Carriveau, R. 2013 Correlating Flow Pattern with Force Coefficients in Air Flow past a Tandem Unit of Three Circular Cylinders. International Journal of Fluid Mechanics Research, 40(3), 235-253.	*Published*
Appendix B	Vasel-Be-Hagh, A. R., Carriveau, R. and Ting, D. S.-K. 2013 Energy Storage using Weights Hydraulically Lifted above Ground. International Journal of Environmental Studies, 70(5), 792-799.	*Published*
Appendix C	Vasel-Be-Hagh, A. R., Carriveau, R. and Ting, D. S.-K. 2014 Underwater Compressed Air Energy Storage Improved through Vortex Hydro Energy. Sustainable Energy Technologies and Assessments, 7, 1-5.	*Published*

dissertation has not been submitted for a higher degree to any other University or Institution.

ABSTRACT

The present document is a manuscript-based dissertation covering Ahmadreza Vasel-Be-Hagh's PhD research from September, 2011 to May, 2015. The research was particularly focused on studying hydrodynamics of underwater accumulators of compressed air for an underwater compressed air energy storage (UWCAES) plant. The accumulator units were floral configurations of droplet-shaped balloons installed close to the bed of deep water. The research was carried out in two major parts: water flow over the balloons and flow produced by the bursting of the balloons. In the first part, three-dimensional simulations were conducted to investigate water flow over accumulators. The simulation was carried out at a free stream Reynolds number of 2.3×10^5 using URANS k–ω and LES Dyna–SM turbulence models. The structure of the flow was investigated using iso-surfaces of the second invariant of the velocity gradient and three-dimensional path lines. Several shedding vortex tubes were identified downstream of the balloons. The dynamics of these vortex tubes was further illustrated through time series snapshots containing vorticity lines on two-dimensional planes perpendicular to the flow direction. The frequency of the shedding and the turbulent movements of the vortex tubes were studied through power spectrum analysis of the force coefficients. In the second part, the flow produced by the bursting of balloons was studied experimentally using photographs taken by three cameras with speed of 60 frames per second at a resolution of 1080P. It was observed that if a sufficiently large air-filled balloon quickly burst underwater, a vortex ring bubble was generated. The effect of dimensionless surface tension on general characteristics of the vortex ring bubble including rise velocity, rate of expansion, circulation and trajectory was investigated. It was observed that as the dimensionless surface tension increased, the rise velocity, the circulation and consequently the stability of the vortex ring bubble increased; however, the rate of expansion tends toward constant values. A semi-analytical model was also developed suggesting that the vortex ring expansion is essentially due to the buoyancy force. An expression was also obtained for the circulation in terms of the initial volume of the balloon and the depth at which balloon bursts. Extending from the mentioned semi-analytical model, a perturbation analysis was performed to find an expression for the radius of the buoyant vortex rings. The radius equation includes two terms; the zeroth-order solution representing the effect of buoyancy, and the first-order perturbation correction describing the influence of viscosity. The zeroth-order solution is an explicit function of time; the first-order perturbation modification, however, includes the drag coefficient which is unknown and of interest. Fitting the photographically measured radius into the modified equation yields the time history of the drag coefficient of the corresponding buoyant vortex ring.

To my late parents

ACKNOWLEDGEMENTS

I would like to express my sincere gratitude to Dr. David Ting and Dr. Rupp Carriveau for their excellent guidance and support during my PhD program. The invaluable comments and assistance from the committee members Dr. Shaohong Cheng, Dr. Vesselin Stoilov, Dr. Biao Zhou and Dr. Roger Khayat are gratefully acknowledged. Technical assistance from Mr. Andy Jenner is appreciated.

This work is made possible by the Ontario Trillium Foundation for an Ontario Trillium Scholarship. The financial support from the Department of Mechanical, Automotive and Materials Engineering in the form of Graduate Assistantships is also acknowledged.

Contents

List of Figures

List of Tables

Chapter 1

Introduction

1.1 Overview

Over the last decade the electricity market has changed drastically and renewable energy sources have been introduced as alternatives for fossil-fuel based electricity generation. However, renewable energy sources suffer from a number of challenges including their highly intermittent nature, low energy density, grid congestion, and stability issues. Storage facilities have the potential to offer a solution to these challenges. One of the most efficient and environmentally safe storage technologies is compressed air energy storage (CAES), which is a modification of the basic gas turbine technology [1-2]. However, the application of this underground energy storage is limited to the land based power stations [3]; while much of renewable resources are offshore [4]. Hence, a new energy storage system based on CAES for application in the seas has been developed [5-6]. In this storage plant, namely under water CAES or UWCAES, the surplus electrical energy generated in the off-peak hours is utilized to compress air into submerged distensible accumulators. The accumulators are moored to the sea floor; hence, the stored air is under hydrostatic pressure, ready to be released back to the surface to drive turbines to supply the electrical grid when needed (see figure 1.1). A successful Pilot Experiment in Lake Ontario has led to design and construction of two planned demonstration facilities to be deployed at fresh and salt water sites [5]. The present research aims at providing a good estimate of hydrodynamic loading and structure of the flow as one of the most demanding tasks to develop an optimal design for foundation, support structures and valve connections. Gaining knowledge of hydrodynamic loading is also a primary step for performing any shape and cost analysis. In a recent study conducted at the European Marine Energy Centre in Orkney, Pimm et al. [7] discussed challenges associated with underwater accumulators focusing on tears occurring during the installation and

operation. They also tested two different accumulators in a water tank and found a small leak causing the air hose and the accumulator to fill with water. The dynamic nature of the hydrodynamic loads produced by the crossing current can severely affect the observed tears and leakages; hence, having insights into force characteristics of the crossing flow can be very useful in choosing a more durable material for manufacturing future balloons. It was the above-mentioned considerations that prompted us to study flow over droplet shaped underwater balloons. Hence, at the first step, the fundamental case of flow over a single isolated balloon was studied and then the practical case of flow over floral units of balloons was examined.

Another serious issue associated with UWCAES plant is the balloon rupture which is quite conceivable owing to internal over pressure or collision with a sharp object or debris. A review of bubble dynamics indicated a paucity of published works that explore the flow produced by an underwater bursting balloon. Addressing this gap is thus another objective of this dissertation. To this end, an experimental study was conducted first in a 2-m^3, and then, in a 25-m^3 tank and a theoretical model was developed by modifying the drag-based model proposed by Sullivan et al. [8]. More details on the specific phases of the present research are given in the next section.

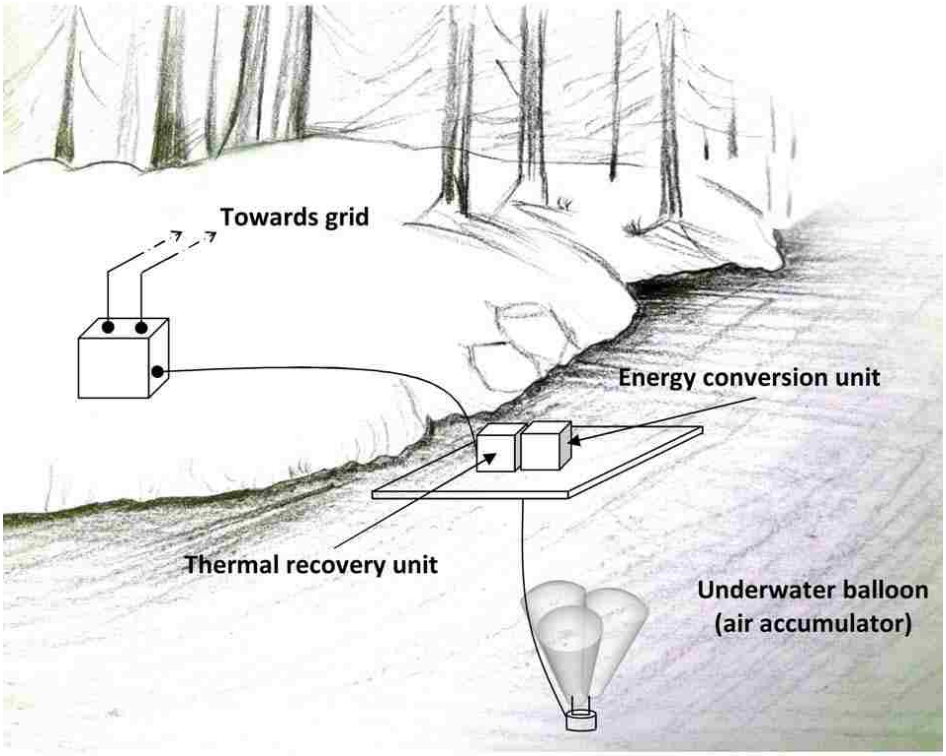

FIGURE 1.1: Typical underwater compressed air energy storage plant; the accumulator unit consists of three distensible balloons arranged in floral configuration.

1.2 Research Phases

The major phases of the present research along with the time duration of each phase are presented in figure 1.2. More details on each phase are given below.

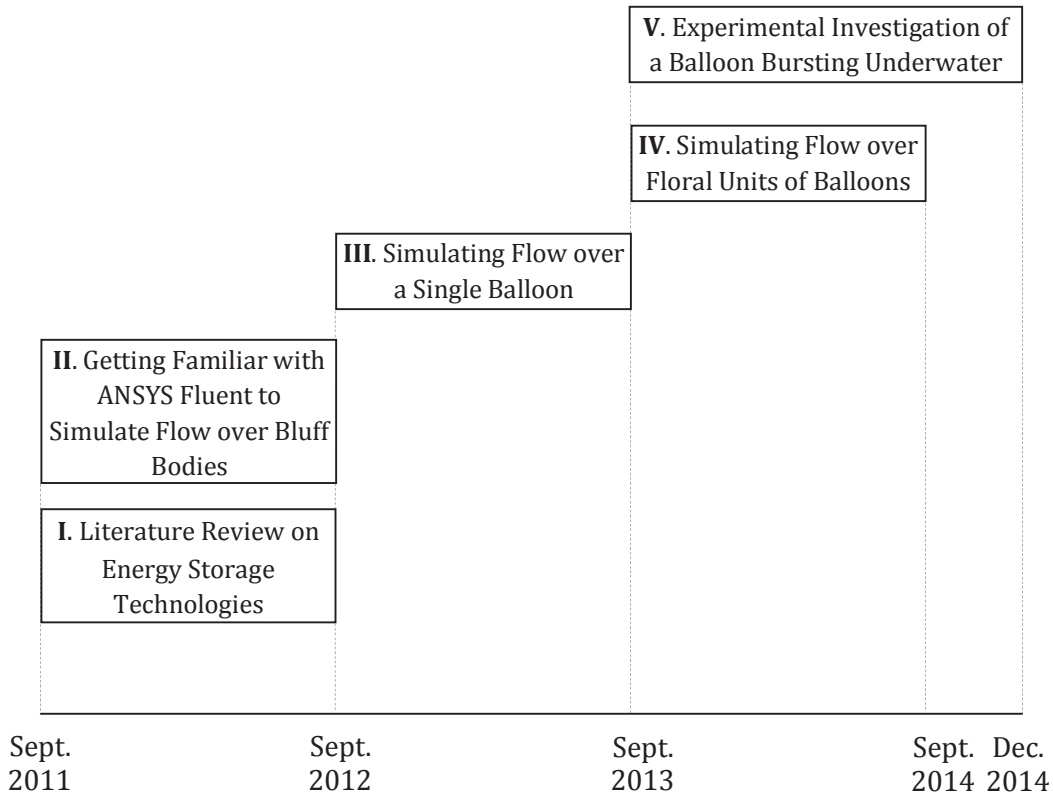

FIGURE 1.2: Main research phases.

1.2.1 Phase I: Literature Review on Energy Storage Technologies

As a preliminary step, a literature survey was conducted to review existing energy storage technologies to become more familiar to the application of this research. It was at this step that two new ideas emerged.

The first one was a new design to address the major challenges associated with the conventional pumped hydro energy storage. In contrast to the conventional pumped hydro energy storage where surplus power is stored as elevated water, the proposed energy storage applies pumped water to elevate weights several times heavier than water. This provides a considerable operational flexibility since weights and consequently gear pumps can be balanced in accordance with the instantaneous excess electrical power. The discharge rate can also be controlled by the external weight; discharge can occur very

rapidly via activation of the external weights. This allows the storage to adjust quickly to the fluctuating demand. Beyond this, the suggested solution has inherent installation and maintenance advantages. For instance, it does not need to be constructed at high altitudes, and so, no tall water tank tower and long piping are needed. Consequently, capital and maintenance costs can be significantly reduced. See Appendix A for more information.

The second one was a self-powered energy storage technology (UWCAES-VHE) as a hybrid of Underwater Compressed Air Energy Storage (UWCAES) and the Vortex Induced Vibration Aquatic Clean Energy (VIVACE) converter invented by Bernitsas et al. [9] to harness Vortex Hydro Energy (VHE). The power generated by the oscillating accumulators effectively compensates for UWCAES energy losses such that the roundtrip efficiency of the energy storage is significantly increased. See Appendix B for more information.

1.2.2 Phase II: Getting Familiar with CFD Tools

The primary purpose of the second phase was getting familiar with ANSYS Fluent software by simulating flow over regular bluff bodies. Gaining a thorough knowledge of postprocessing softwares including Techplot and MATLAB was also a key objective of this phase. To put the candidate's knowledge into practice, he simulated flow past three circular cylinders in a tandem arrangement. Complete details of this simulation can be found in Appendix C.

1.2.3 Phase III: Flow over a Single Balloon

In the third phase, a three-dimensional simulation was conducted to investigate water flow over a single droplet shaped balloon installed close to the bed of deep water. The simulation was carried out at a free stream Reynolds number of 2.3×10^5 using URANS k-ω and LES Dyna-SM turbulence models. See Chapter 2 for details of the geomerty, the boundary conditions, the mesh, the numerical methodology, simulation reults and discussions.

1.2.4 Phase IV: Simulating Flow over Floral Units of Balloons

After studying the fundamental case of flow over a single isolated balloon, the practical case of flow over floral units of balloons was examined. Solution and numerical strategy

were similar to those of a single balloon described in Chapter 2. This phase was conducted in two different parts; in the first part, balloons were assumed to be arranged in widely and closely spaced configurations (see Chapter 3), in the second part, the accumulator unit was assumed to consist of three touching balloons (see Chapter 4).

1.2.5 Phase V: A Balloon Bursting Underwater

One of the latest studies on the vortex ring bubbles was the lattice Boltzmann simulation conducted by Cheng et al. [10]. The main motivation of their study was to assess whether the ring bubble continues to expand while the rise velocity decreases, as was predicted by Turner [11], Walters and Davidson [12], Pedley [13] and Lundgren and Mansour [14], or, ultimately a steady state is achieved at which the ring radius and rise velocity become constant, as was predicted by Joseph et al. [15]. They found that, in contrast to Joseph et al.'s prediction, the ring radius increases and the rising velocity decreases with time until the vortex ring becomes unstable and breaks down into small spherical cap bubbles. For further investigation, we extended the model proposed by Sullivan et al. [8] to include buoyant vortex rings, and unexpectedly, achieved a steady state solution suggesting that similar to the spherical bubbles, the vortex ring bubbles eventually attain a constant velocity, as was predicted by Joseph et al. [15]. This implication prompted us to experimentally assess whether the modified model matches with reality or not. Another major motivation for the present work was the conspicuous lack of an investigation concerning the flow produced by the bursting of balloons. According to the literature, the common technique for the generation of a vortex ring bubble is the rapid ejection of fluid into a water tank through an orifice exit [8, 16-18]. In other words, the initial source of energy is kinetic, whereas the vortex ring bubbles studied herein are powered by the potential energy initially stored in the underwater balloons. Beyond this, an investigation exploring high-Bond-number vortex rings was not evident in the literature. A secondary motivation for the present work was to close this gap by studying vortex rings up to Bo=1000 produced by large balloons bursting in a 25-m^3 water tank. See Chapter 5 for more details. Extending from the model proposed in Chapter 5, a perturbation analysis was performed to modify Turner's radius by taking into account the viscous effect. The modified radius includes two terms; the zeroth-order solution representing the effect of buoyancy, and the first-order perturbation correction describing the influence of viscosity. The zeroth-order solution is explicit Turner's radius; the first-order perturbation modification, however, includes the drag coefficient which is unknown and of interest. Fitting the photographically measured radius into the modified equation yields the time history of the drag coefficient of the corresponding buoyant

vortex ring. To give further clarification, the proposed model was applied to calculate the drag coefficient of a buoyant vortex ring at a Bond number of approximately 85.

References

[1] Denholm, P., Kulcinski, G.L., 2004, Life cycle energy requirements and greenhouse gas emissions from large scale energy storage systems, Energy Conversion and Management, 45, 2153-2172.

[2] Rahman, F., Rehman, S, Abdul-Majeed, M.A., 2012, Overview of energy storage systems for storing electricity from renewable energy sources in Saudi Arabia. Renewable and Sustainable Energy Reviews, 16(1), 274-283.

[3] Ibrahim, H., Ilinca, A., Perron, J., 2008, Energy storage systems-Characteristics and comparisons, Renewable and Sustainable Energy Reviews, 12(5), 1221-1250.

[4] MacKay, D.J.C., 2008, Sustainable energy-without the hot air. Cambridge UIT Cambridge Ltd, Cambridge, England, 60-67.

[5] Cheung, B., Cao, N., Carriveau, R., Ting, D.S.-K , 2012a, Distensible air accumulators as a means of adiabatic underwater compressed air energy storage. International Journal of Environmental Studies, 69(4), 566-577.

[6] Cheung, B., Carriveau, R., Ting, D.S.-K., 2012b, Storing energy underwater. ASME Mechanical Engineering Magazine, 134(12), 38-41.

[7] Pimm, A.J., Garvey, S.D., Jong, M., 2014, Design and testing of energy bags for underwater compressed air energy storage, Energy, 66, 496-508.

[8] Sullivan, I. S., Niemela, J. J., Hershberger, R. E., Bolster, D., Donnelly, R. J., 2008, Dynamics of thin vortex rings. Journal of Fluid Mechanics, 609, 319-347.

[9] Bernitsas, M.M., Raghavan, K., Ben-Simon, Y., Garcia, E.M.H., 2008. VIVACE vortex induced vibration aquatic clean energy: a new concept in generation of clean and renewable energy from Fluid Flow. Journal of Offshore Mechanics and Arctic Engineering, 130, 1–15.

[10] Cheng, M., Lou, J., Lim, T. T., 2013, Motion of a bubble ring in a viscous fluid. Physics of Fluids, 25, 1-19.

[11] Turner, J. S., 1957, Buoyant vortex rings. Proceedings of the Royal Society of London A, 239, 61-75.

[12] Walters, J. K., Davidson, J. F., 1963, The initial motion of a gas bubble formed in an inviscid liquid. Journal of Fluid Mechanics, 17, 321-336.

[13] Pedley, T. J., 1968, The toroidal bubble. Journal of Fluid Mechanics, 32, 97-112.

[14] Lundgren, T. S., Mansour, N. N., 1991, Vortex ring bubbles. Journal of Fluid Mechanics, 224, 177-196.

[15] Joseph, D., Funada, T., Wang, J., 2007, Potential Flows of Viscous and Viscoelastic Liquids. Cambridge University Press.

[16] Walker, J. D. A., Smith, C. R., Cerra, A. W., Doligalski, T. L., 1987, The impact of a vortex ring on a wall. Journal of Fluid Mechanics, 181, 99-140.

[17] Hershberger, R. E., Bolster, D., Donnelly, R. J., 2010, Slowing of vortex rings by development of Kelvin waves. Physical Review E, 82, 036309.

[18] Gan, L., Dawson, J. R., Nickels, T. B., 2012, On the drag of turbulent vortex rings. Journal of Fluid Mechanics, 709, 85-105.

Chapter 2

Numerical Simulation of Flow past an Underwater Energy Storage Balloon

A. R. Vasel-Be-Hagh, D. S.-K. Ting, R. Carriveau

Turbulence and Energy Laboratory, Lumley Centre for Engineering Innovation, University of Windsor, Ontario, Canada N9B 3P4

Vasel-Be-Hagh, A.R., Carriveau, R., Ting, D.S.-K., 2013. Numerical Simulation of Flow Past an Underwater Energy Storage Balloon. Computers and Fluids, 88, 272-286.

2.1 Introduction

The energy industry continues to advance with clean electricity generation through the development of renewable energy technologies. However, it is still dealing with the challenge of non-constant supply from these characteristically intermittent generators. Great variation in the power generated by wind turbines from windy to calm days and variation in output from photovoltaics between sunny and cloudy days limits the potential for base load penetration of these generators. Energy storage promises great potential as a way of managing timely distribution of these resources in the most efficient way. Viable energy storage solutions could enable these resources to become dispatchable and suitable for base load service.

Such a potential solution is currently being studied by the authors, namely underwater compressed air energy storage (UWCAES) [1]. In this system, flexible accumulators are installed close to the bed of a deep water source, i.e. a lake or ocean. Surplus electrical energy is used to compress air into underwater accumulators. Hence the stored air is under the hydrostatic

pressure applied by the water, ready to be released to drive turbo expander generators to deliver power to the grid when desired. The Professional (PF) series of underwater lift balloon produced by SUBSALVE USA CORPORATION [2] have served as a suitable choice to perform as the accumulator unit of the UWCAES system. The generally droplet-shaped series of different sized PF lift balloons are presented in figure 2.1.

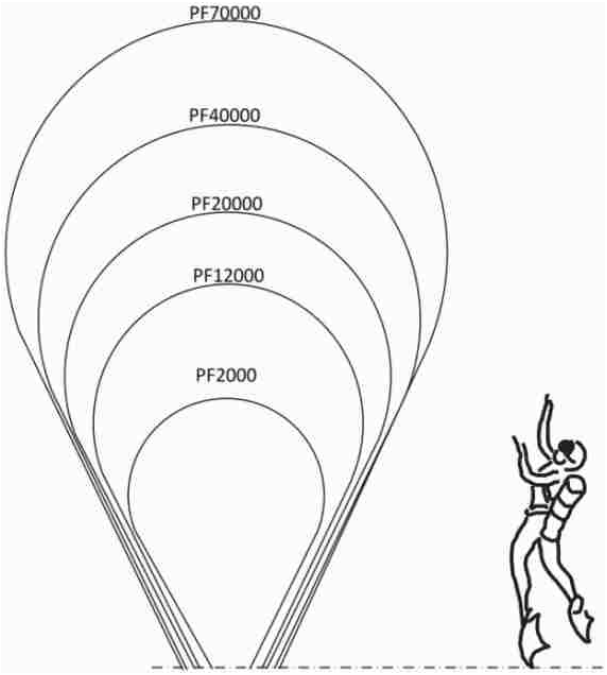

FIGURE 2.1: General shape of various professional (PF) series of lift bags produced by SUBSALVE USA CORP. The PF20000 model was considered in the current study.

There has been significant progress in the understanding of fluid structure interactions over the last couple of decades. The focus, however, has been limited to flow over circular cylinders (Lam and Cheung [3], Ting et al. [4], Sumner et al. [5], Zhang and Zhou [6], Sumner and Richards [7], Shao and Zhang [8], Lee and Yang [9], Bao et al. [10], Yang and Zheng [11], Sarkar [12], Griffith et al. [13], Vakil and Green [14-15], Gazzola et al. [16], Harimi and Saghafian [17]), square cylinders (Shyam Kumar and Vengadesan [18], Huang et al. [19], Alam et al. [20], Mahbub et al. [21], Bao et al. [22]), rectangular cylinders (Lin and Huang [23], Mannini et al. [24], Lam et al. [25], Shimada and Ishihara [26]) and elliptical cylinders (Peng et al. [27]); these are primarily two-dimensional studies. There are also several three-dimensional studies but they are mostly concerned with the flow over regular shapes such as spheres (Taneda [28], Constantinescu and Squires [29], Yoon and Yang [30], Khoury et al. [31], Dixona et al. [32], Hassanzadeh et al. [33]), circular cylinders (Narasimhamurthy et al. [34], Cao et al. [35], Zhou et al. [36], Kanaris et al. [37], Uzun and Hussaini [38]) and square cylinders (Sheard et al. [39]).

Our review of flow over bluff bodies indicated a dearth of published research that explored the cross-flow around a droplet-shaped bluff body like underwater balloons. Hence, the current numerical study was carried out to examine flow over an underwater balloon, specifically the

PF20000 model. This research was driven by a need to provide insight into the potential hydrodynamic behaviour of the submerged UWCAES accumulators. Subsequently, the authors were asked to investigate the force characteristics and the structure of the flow. Due to the absence of any experimental evidence, the simulation was carried out using both URANS and LES turbulence models for the sake of results comparison. In addition, mesh and domain independence analyses were done for both of the turbulence models separately.

2.2 Computational Details and Boundary Conditions

In the present paper, the characteristic diameter used to calculate the Reynolds number was defined as

$$D = \frac{6 \times V}{A} \tag{2.1}$$

where V and A are volume and surface area respectively. According to equation 2.1, the characteristic diameter of the PF20000 balloon used as the accumulator unit of the UWCAES is 2.31m [40]. The Pilot Study of the UWCAES was carried out in the Lake Ontario [1]. According to Centre for Operational Oceanographic Products and Services [41] the mean offshore current velocity of this lake is approximately $V_{mean} \approx 0.2 \sim 0.25$Knot that is 0.1∼0.13 m/s. By choosing V=0.115 m/s, Reynolds number of the flow crossing the full scale balloon, D=2.31m, is $Re = \rho VD/\mu = (998 \times 0.115 \times 2.31)/1.15 \times 10^{-3} = 2.3 \times 10^5$ where $\mu = 1.15 \times 10^{-3}$ is the dynamic viscosity of water at mean temperature of the lake water which, according to National Weather Service Forecast Office [42], was approximately $15°C$ during 2011.

In order to decrease computational expenses, dimensions of the balloon were scaled down by a factor of 100. As the bluff body force coefficients are functions of the Reynolds number, the free stream velocity was scaled up 100 times to retain the same Reynolds number. Therefore, the free stream velocity was set to be V=100×0.115m/s=11.5m/s. Dimensions of the scaled balloon are presented in figure 2.2 Original dimensions of the PF20000 balloon are reported in inches on the SUBSALVE USA CORPORATION web site [40]; therefore, in figure 2.2 the scaled dimensions are presented in both meters and inches (inches in brackets) to ensure the decimal accuracy.

The dimensions of the computational domain are given in figure 2.3 in terms of the characteristic diameter. Blockage ratio BR of the balloon is the most determinative parameter in choosing the height and the width of the computational domain. Prasanth et al. [43-44] demonstrated that the effects of the blockage ratio on the interactions between flow and bluff bodies are more significant at low Reynolds numbers so that the blockage ratio should be 1% or less, whereas at large Reynolds numbers it does not affect significantly. For instance, they showed that at Reynolds numbers larger than 100 the characterisitcs of the flow crossing a circular cylinder are very close for blockage ratios of 1 and 5%. At a Reynolds number in the order of what is studied in the present paper, i.e. 10^{-5} , the blockage ratio is mostly chosen to be in the range of 3∼25% (see Table 1). However, in the present paper, to ensure the negligibility of the walls effect the height and the width of the computational domain were chosen to be 11D and 13.2D

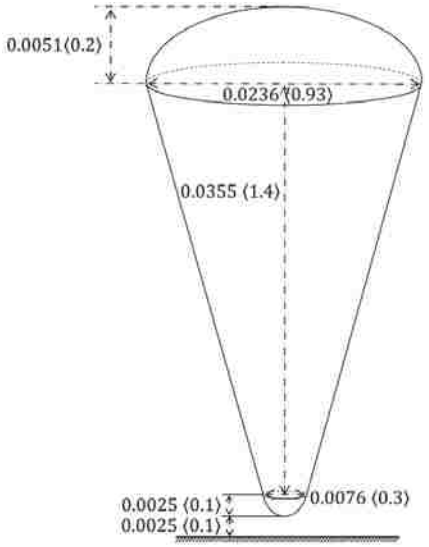

FIGURE 2.2: Scaled PF20000 balloon. Values are in meters, and brackets are in inch.

respectively to end in a blockage ratio of 0.88% which is too much smaller than what is normally chosen for the similar cases (table 2.1). The blockage ratio was calculated as $BR = a_c/A_c$, where $a_c \approx 1.06in^2$ and $A_c \approx 120.24in^2$ are cross sectional areas of the balloon and the computaional domain respectively.

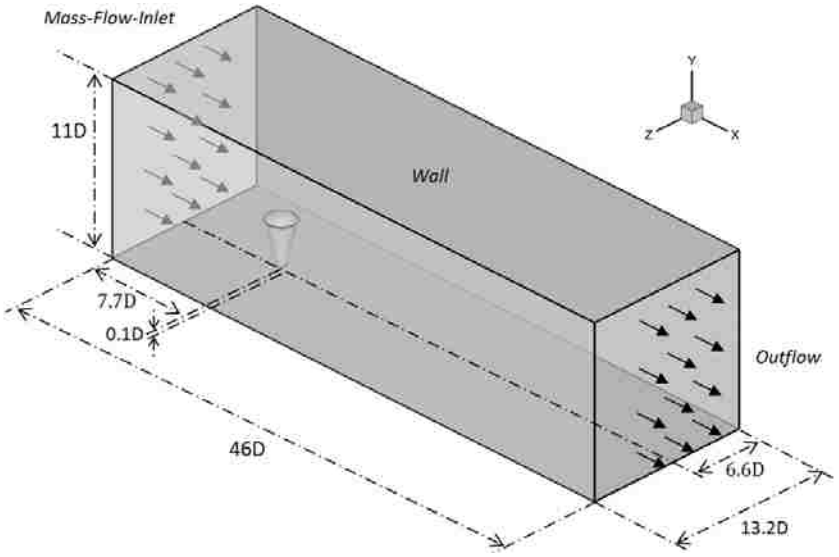

FIGURE 2.3: Computational area and employed boundary conditions (not to scale).

Although the dependency of the results on the upstream distance L_u (the distance between the inlet boundary and the middle of the balloon) and downstream distance L_d (the distance between the middle of the balloon and the outlet boundary) is more significant at low Reynolds numbers [32, 52-53], the present simulation was repeated for three different domain sizes to ascertain the

TABLE 2.1: Blockage ratios set for bluff bodies in high-Reynolds-cross flows.

	Reynolds number $\times 10^5$	Blockage ratio (%)
Drescher [45]	1.1	24
McGregor and Etkin [46]	1.2	2.6
Fung [47]	1.9-13.6	10.5
Schewe [48]	71	10
Blackman [49]	1.2-6	10
Bearman [50]	1.4-2.4	3
Sun et al. [51]	3.2	6.5

independency of the results from upstream and downstream distances. Effects of the upstream and downstream distances on the mean force coefficients are shown in table 2.2.

TABLE 2.2: Domain size independence study.

	(L_u, L_d)	C_d	C_l
URANS	(7.7D, 46D)	0.980	0.131
	(12D, 56D)	0.984	0.131
	(16D, 66D)	0.986	0.131
LES	(7.7D, 46D)	0.692	0.061
	(12D, 56D)	0.694	0.061
	(16D, 66D)	0.695	0.061

It is observed that the drag coefficient is more sensitive to the domain size compared to the lift coefficient. According to table 2.2, upstream and downstream distances larger than 12D and 56D do not significantly affect the simulation results, so, the present paper was conducted for L_u =12D and L_d =56D. There is a distance of 0.1D between its lowest point and the solid bed. It should be mentioned that the origin of the coordinate system used in this study is fixed right underneath the balloon on the bed surface; accordingly the bottom of the balloon is at (0, 0.254×10^{-2}m $\langle 0.1 \rangle$, 0).

The boundary conditions that are employed in the current simulation are also depicted in figure 2.3. A mass-flow-inlet condition with a mass flow rate of 888.5 kg/s is set at the inlet boundary, resulting in an inlet velocity of 11.5 m/s to retain the Reynolds number at 2.3×10^5. An outflow condition with flow rate weighting of 1 is used at the outlet boundary, as it is the only outlet of the computational domain. In the real application the accumulator unit is installed in deep water, therefore, to be in accordance with the real case a free surface condition should be applied on the top boundary of the computational domain. To define the free surface boundary condition a two-phase model must be added to the simulation which brings the advection equations of VOF or Level Set LS functions and also the algorithms of phase interface reconstruction. Due to the extremely low blockage ratio (BR $\approx$ 0.88%) of the balloon in the computational domain, this condition is not expected to significantly affect the physical behaviour of the flow over the balloon; therefore, to avoid the extra calculations of a two phase model a non slip boundary condition was simply applied on the top boundary. The no slip boundary condition is also applied at all

solid-liquid interferences including side and bottom walls of the computational domain and the surface of the balloon, which is here assumed rigid (non-distensible).

2.3 Numerical Methodology

Since, to our knowledge, flow over the present bluff body has not been investigated yet the authors preferred to apply the well known numerical models which have been validated by others via simulating flow over spheres and cylinders to make the solution as reliable as possible.

2.3.1 LES Model

LES governs dynamics of large eddies by removing eddies with scales smaller than the grid spacing (or any other filter width) from unsteady Navier-Stokes equations. The filtered Navier–Stokes equations are as follows

$$\frac{\partial \overline{u}_i}{\partial \overline{x}_i} = 0 \tag{2.2}$$

$$\frac{\partial \overline{u}_i}{\partial t} + \overline{u}_j \frac{\partial \overline{u}_i}{\partial x_i} = -\frac{1}{\rho}\frac{\partial \overline{P}}{\partial x_i} + \frac{\partial}{\partial x_i}(2\nu S_{ij} - \tau_{ij}) \tag{2.3}$$

As it is seen, the filtering brings some additional unknown terms τ_{ij} namely subgrid scale (SGS) stresses which need to be determined through an SGS model. In the current paper, the SM model proposed by Smagorinsky [54] was applied to compute the SGS stresses. The main assumption of the SM model is the equality of the SGS with the product of an eddy-viscosity μ_t and the resolved rate of strain tensor S_{ij}:

$$\tau_{ij} - \frac{1}{3}\tau_{kk}\delta_{ij} = -2\mu_t \overline{S}_{ij} \tag{2.4}$$

where the rate of strain tensor S_{ij} and the eddy-viscosity μ_t are defined as

$$\overline{S}_{ij} = 1/2((\frac{\partial \overline{u}_i}{\partial x_j}) + (\frac{\partial \overline{u}_j}{\partial x_i})) \tag{2.5}$$

$$\mu_t = \rho L_s^2 \mid \overline{S} \mid \tag{2.6}$$

in which $\mid \overline{S} \mid$ is computed via $\mid \overline{S} \mid = \sqrt{2\overline{S}_{ij}\overline{S}_{ij}}$. The mixing length L_s is defined by

$$L_s = min(\kappa d C_s V^{\frac{1}{3}}) \tag{2.7}$$

where κ, d and C_s are von Kármán constant, distance to the closest wall and Smagorinsky parameter respectively. The Smagorinsky parameter C_s can be kept constant (0.1 is recommended) or dynamically computed during the simulation using the information provided by the smaller scales of the resolved fields (Lilly [55] and Germano et al. [56]). Mylonas and Sayer [57] found that the dynamic model gives a better prediction for the drag coefficient of a yacht keel when compared to their experiments. Thus, the dynamic model was adopted in this study.

2.3.2 URANS Model

The URANS equations are formulated by time-averaging the standard Navier-Stokes equations. By doing this, time-dependent turbulent fluctuations are eliminated from the resulting set of equations, and so the only variables left to be resolved are those of the mean flow. The turbulent effects such as Reynolds stresses are determined using one of RANS turbulence models; the standard K-ω turbulence model was applied in the current paper. Although in such high Re flows URANS models may not capture particular flow unsteadiness, nevertheless, they are expected to be able to predict the mean values with satisfactory accuracy. Transport equations of the K-ω turbulence model applied in the present paper are as follows

$$\frac{\partial \rho k}{\partial t} + \frac{\partial \rho k u_i}{\partial x_i} = \frac{\partial}{\partial x_i}[(\mu + \frac{\mu_t}{\sigma_k})\frac{\partial k}{\partial x_i}] + G_k - Y_k + S_k \tag{2.8}$$

$$\frac{\partial \rho \omega}{\partial t} + \frac{\partial \rho \omega u_i}{\partial x_i} = \frac{\partial}{\partial x_i}[(\mu + \frac{\mu_t}{\sigma_\omega})\frac{\partial \omega}{\partial x_i}] + G_\omega - Y_\omega + S_\omega \tag{2.9}$$

in which subscripts k and ω stand for turbulent kinetic energy and specific dissipation rate respectively. G_k and G_ω represent the generation of k and ω respectively, Y_k and Y_ω represent their dissipation due to turbulence, S_k and S_ω are source terms, μ_t is turbulence viscosity and σ is a constant which was defined by Shih et al. [58].

2.3.3 Numerical Solution

First, all nonlinear governing equations are linearized to a scalar system of equations through an implicit method. The Gauss-Siedel solver along with a segregated algebraic multi-grid (AMG) method is applied to solve this system of equations. The Pressure implicit with split operator (PISO) algorithm is used for the pressure-velocity coupling. Compared to the other algorithms i.e. simple, simplec and coupled, the PISO algorithm requires more cpu to process, on the other hand, it significantly decreases number of iterations before convergence occurs. In addition, this algorithm is more appropriate for skewed cells. In the LES turbulence model, physical diffusion is significantly affected by numerical diffusion; consequently, the central differencing schemes should be a suitable approach to conduct the spatial discretization. However, in the central differencing schemes there is no numerical damping, thus, the numerical fluctuations affect the physical ones. The commercial code, Fluent obviates this issue through the application of a strategic condition. It changes the spatial discretization scheme from central differencing to

an upwind scheme for any oscillation with a wavelength less than twice the local grid spacing. This feature was a primary motivator to conduct the current simulation with the Fluent code. Furthermore, several researchers have already verified the accuracy of the Fluent LES model in simulating flow over bluff bodies (Shao and Zhang [8], Vakil and Green [14-15], Dixona et al. [32], Mylonas and Sayer [58], Catalano et al. [59], Huang et al. [60], Liu et al. [61]).

2.4 Mesh

Due to the non-regular shape of the balloon, an unstructured mesh was generated close to its boundary. In the current simulation, to reach a mesh-independent solution with a thoroughly unstructured mesh an unsuitably large number of cells were required. Therefore, the computational domain was divided into 27 blocks; and an unstructured mesh was applied only in the block that contains the balloon. The T-Grid type of Tet-hybrid cells was chosen to generate this unstructured mesh. In all other subregions the Cooper type of hex-wedge cells was used to establish a structured mesh. Isometric, +X, +Y and +Z views of the mesh are illustrated in figure 2.4. This mesh was created using GAMBIT 2.3.16.

In the LES model of the Fluent code, the wall boundary condition is implemented using the law-of-the-wall approach. Accordingly, there is a logarithmic relation between $u^+ = u/u_\tau$ and $y^+ = y \times u_\tau/\nu$ where $u_\tau = \sqrt{\tau_w/\rho}$ is the friction velocity in which τ_w and ρ are wall shear stress and density of the fluid respectively. Therefore, there are no computational restrictions on the near wall mesh density, however, it is strongly recommended to use mesh spacing on the order of $y^+ = 1$ [62]. Subsequently, for the current simulation, a mesh with a y^+ of approximately 1.0 was adopted. Figure 2.5 shows a close up view of the present mesh on a two dimensional plane perpendicular to the Y axis at Y=0.3D. In this figure, the unstructured mesh in the near vicinity of the balloon is illustrated. The non-uniformity of the mesh density in the two structured neighbouring regions is necessitated by their connection to the unstructured cells.

To investigate the quality of the problem discretization, mesh-independence analyses were carried out for both URANS and LES models separately. The mesh study was conducted by examining effects of the mesh density on the value of time averaged force coefficients that represent primary parameters of this study. Force coefficients of the balloon are depicted versus total number of cells in figure 2.6. Panels (a) and (b) illustrate variation of the force coefficients with mesh refinement calculated by the URANS k-ω turbulence model. Panels (c) and (d) present LES predictions of the force coefficients in different mesh densities. Grids which are coarser than a critical resolution are not able to capture spatial variations of the model at scales smaller than the element size, therefore, the simulation may not reproduce correctly element average values and this leads a wrong drag coefficient value. Although no meaningful inference can be drawn for the variation trend of these wrong values, the inconsistency observed in the variations can be generally attributed to force distribution on the balloon surface and numerical diffusion generated by the discretization schemes. With variation of the mesh resolution the distribution of the force components on the balloon surface may be significantly affected and consequently the force coefficients may change without a consistent trend. In addition, at specifics resolutions a mix

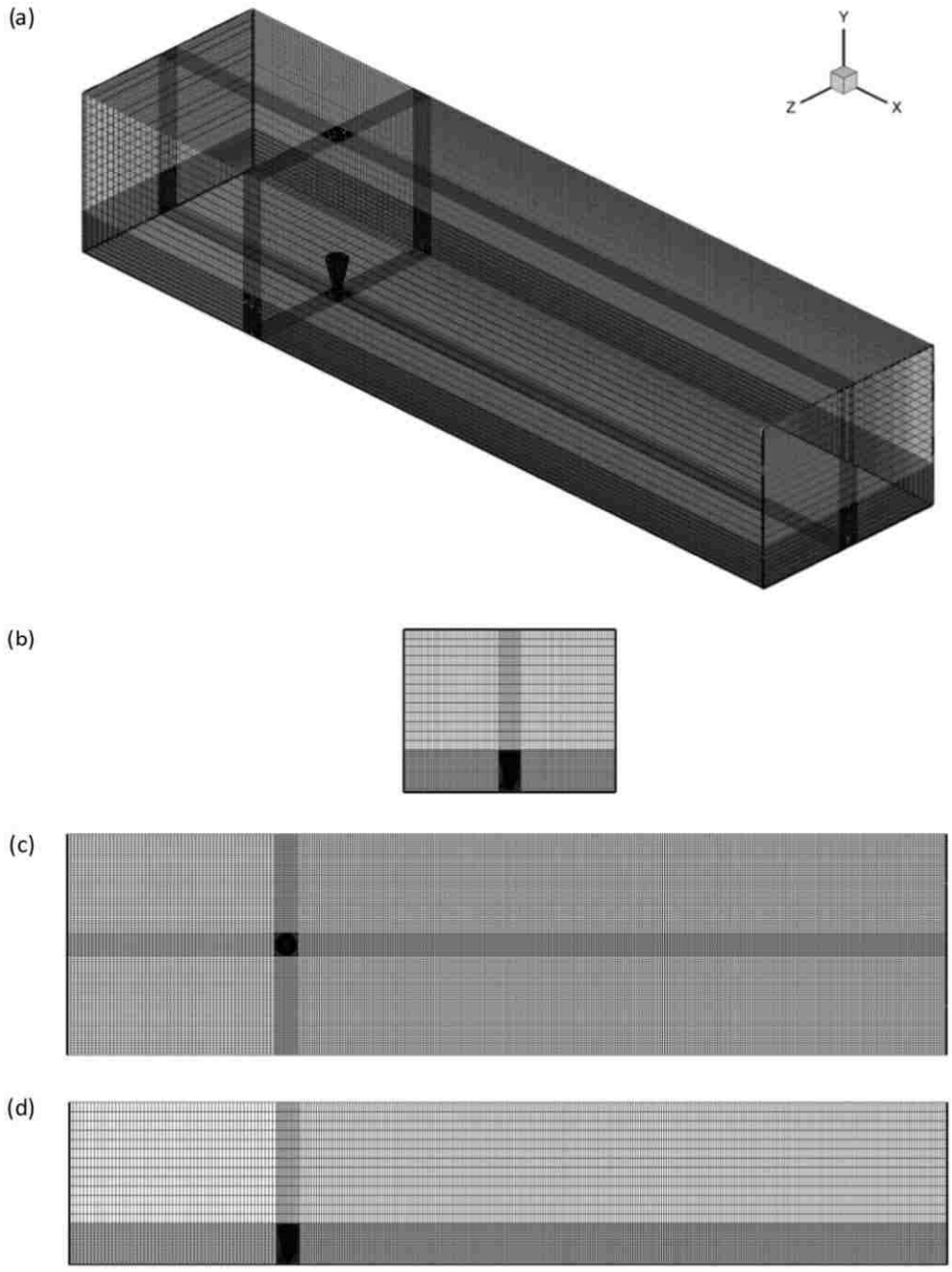

FIGURE 2.4: Panels (a), (b), (c) and (d) illustrate Isometric, +X, +Y and +Z views of the mesh respectively.

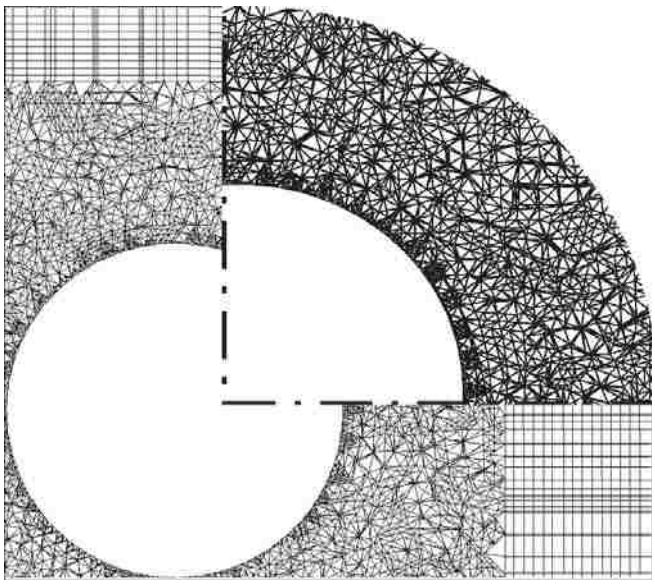

FIGURE 2.5: Two dimensional view of the cross stream mesh just close to the balloon surface.

between grid size and discretization schemes of the nonlinear terms of the governing equations may happen which causes an excessive value of numerical diffusion and changes the calculated force coefficients. Eventually, however, it is expected to reach a mesh resolution beyond which the final results are independent of the grid size. For the URANS model, the mesh independency is obtained once the number of cells is larger than 1.75×10^6. Also it is observed that beyond 4.1×10^6 cells, the force coefficients of the balloons predicted by the LES model do not vary with mesh size. Accordingly, grids with 1.97×10^6 and 4.85×10^6 cells were used to conduct the URANS and LES simulations respectively.

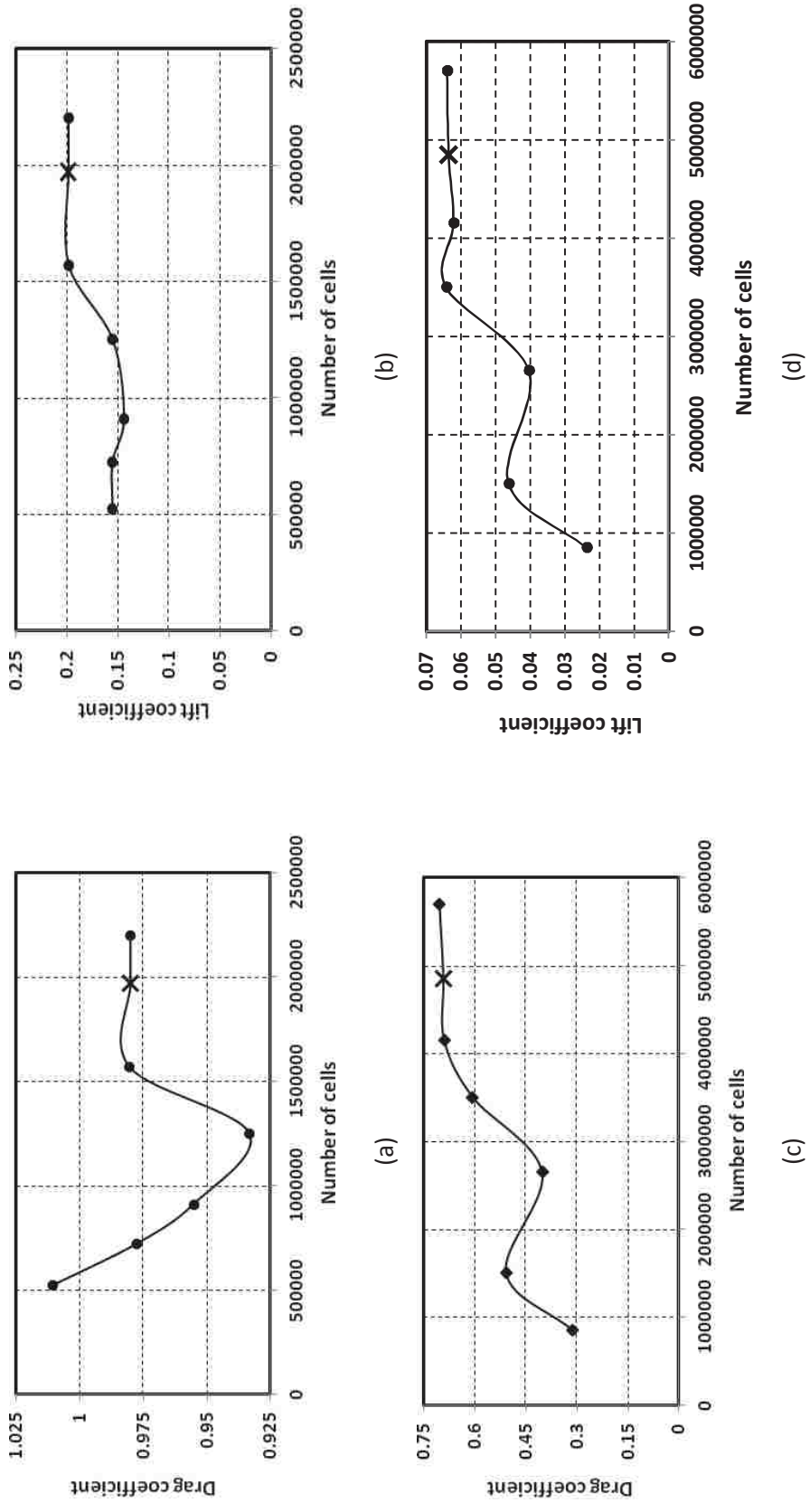

FIGURE 2.6: Mesh independence study for the balloon; (a and b) force coefficients predicted by URANS k-ω versus number of cells, (c and d) force coefficients predicted by LES Dyna-SM versus number of cells.

2.5 Results and Discussion

In this section, the structure of the flow is taken into consideration through the LES simulation first, and then force characteristics predicted by LES Dyna-SM and URANS k-ω turbulence models are compared and discussed.

2.5.1 Structure of the Flow

Schematic motion of two typical particles a and b around a cylindrical surface element is illustrated in figure 2.7(a). Since these particles are moving at the same linear and angular velocities $\omega = V/r$, the $\overline{ab}$ line leaves the leeward surface with no spin on the X axis. It just coherently moves side to side in the wake of the cylindrical body.

Figure 2.7(b) shows the motion of particles a and b around a surface element of a droplet-shaped body. In this case the particles are moving around unequal curves, consequently, the angular velocity of particle b is larger than the angular velocity of particle a. So particle b turns around the surface ahead of particle a, and gradually rotates the $\overline{ab}$ line. Therefore, the $\overline{ab}$ line leaving the leeward surface has a swirling motion, in addition to its sideward motions, in the wake of the droplet-shaped body. These rotations on the surface elements could generate vortical cores on the leeward surface. These vortical cores swirl the flow and form shedding vortex tubes downstream of the bluff body.

In the case of spherical surface, the $\overline{ab}$ line tends to rotate about both X and Z axes; this leads formation of vortex rings downstream of the sphere. These vortex rings are well described by Howe et al. [63].

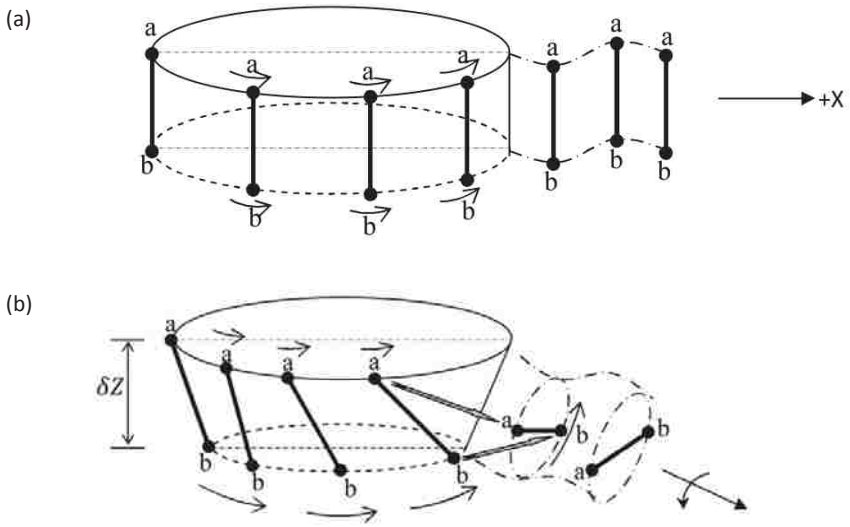

FIGURE 2.7: The schematic motion of two typical particles; (a) around a cylindrical surface element, (b) around a surface element of a droplet-shaped body.

Isosurfaces of the second invariant of the velocity gradient, namely the Q criterion proposed by Hunt et al. [64] are used to investigate the proposed vortical cores along the leeward surface of the balloon. The Q criterion is defined as

$$Q \equiv \frac{1}{2}({u_{i,i}}^2 - u_{i,j}u_{j,i}) = \frac{1}{2}(\parallel \Omega \parallel^2 - \parallel S \parallel^2) \tag{2.10}$$

where tensors Ω and S are the anti-symmetric and symmetric parts of the velocity gradient tensor ∇u respectively. Physically, Ω denotes vorticity rate and S represents the strain rate tensors. Therefore, in a pure irrotational straining motion $\nabla u = S$, and in the solid body rotation flow $\nabla u = \Omega$. The $\parallel \Omega \parallel$ term is the absolute value of the vorticity rate tensor Ω which is defined as $[Tr(\Omega\Omega^T]^{0.5}$, where Ω^T is transpose of Ω, and Tr, or the trace, is sum of the elements lying along the main diagonal. The term $\parallel S \parallel$ is defined similarly. Accordingly, if the strain rate is much higher than the vorticity rate ($\parallel S \parallel \gg \parallel \Omega \parallel$) shear flow is dominant. In contrast, if the rotation strength is much greater than the shear strength ($\parallel \Omega \parallel \gg \parallel S \parallel$), the flow will be highly rotational. Truesdell [65] defined a kinematic vorticity number in the non-dimensional form of $N_k = \parallel \Omega \parallel / \parallel S \parallel$ to evaluate the degree of rotation. Accordingly, for a kinematic vorticity number of zero $N_k = 0$, the flow is irrotational, and if it approaches infinity $N_k \to \infty$ a solid body rotational flow occurs.

The instantaneous isosurfaces of the Q criterion are illustrated in figure 2.8 in the range of $4 \times 10^3 \leq Q \leq 3 \times 10^6$. Panel (a) shows the isosurface associated with Q=3×10^6 indicating an extremely rotational region on the approximate middle of the leeward surface of the balloon (the circled region). In this region the kinematic vorticity number N_k is roughly 3200 indicating that the flow tends toward rigid body rotation. This small region is the most rotational core in the fluid domain which sources a very strong swirling tube flow downstream of the balloon. As it is depicted in panel (b), when Q decreased to 2×10^6 another highly rotational core with the kinematic vorticity number N_k of 2500 was revealed on the top of the leeward surface of the balloon. The next strongly rotational flow was observed on the lower part of leeward surface of the balloon with Q= 1×10^6, see panel (c). The kinematic vorticity number N_k is approximately 1300 in this region. With a greater decrease in the Q, other vortical sources emerge on the leeward surface of the balloon. These sources are depicted in panels (d) to (f). It is observed that they are mostly concentrated on the lower half of the balloon.

To put the strength of the above-described vortical cores into perspective, their Q criterion values should be considered in comparison with those of well known classical flows. Hence, to the best of our knowledge, a literature review on Q criterion was conducted. Many researchers who used Q criterion isosurfaces to identify vortical flows did not report the value corresponding to those isosurfaces (Farana et al. [66], Ozcan et al. [67], Severac et al. [68], Tanahashi et al. [69], Vernet [70], Kunnen et al. [71], Stoesser et al. [72], Garrick [73], Kamkar et al. [74], Chang et al. [75], Lee et al. [76], Yang and Knudsen [77]). They simply used the Q criterion isosurfaces to qualitatively show the structure of the flow. However, there were several studies in which the Q value was given. For instance, Krajnovic and Basara [78] studied flow around a finite circular cylinder at Reynolds number of 2×10^4 and reported a value of Q=1.3×10^5 for the most rotational regions, i. e. at edges of the free end. Zhou et al. [79] studied the flat-plate boundary layer

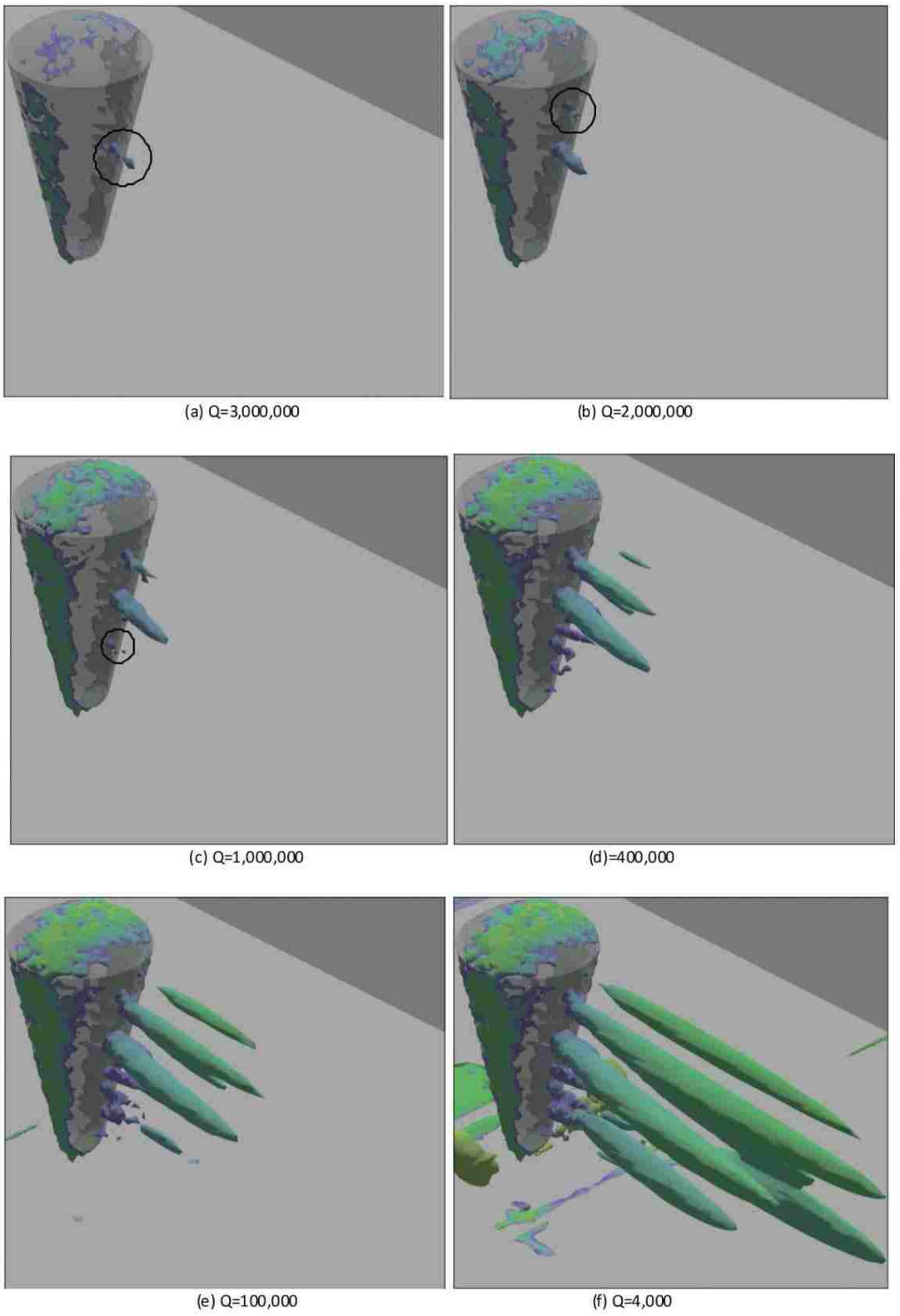

FIGURE 2.8: Q criterion isosurfaces downstream of the widely spaced configuration of the balloons.

transition process at Reynolds number of 5×10^4 through representing isosurfaces of Q=10. Paik and Sotiropoulos [80] used Q criterion isosurfaces with value of 50 to depict vortices in turbulent swirling flow through an abrupt axisymmetric expansion at Re=3×10^4. Omori et al. [81] illustrated the vortex structure in low shear and stronger sheared flow past a circular cylinder at Re of 3800 by means of isosurfaces of Q=10. Morton and Yarusevych [82] and KotouC et al. [83] calculated a Q criterion on the order of 10^3 for flow over a step circular cylinder and a sphere at Reynolds numbers of 300 and 400 respectively. For more reviews, see (Dubief and Delcayre [84], Howard and Pourquie [85], Sohankar [86], Paik et al. [87], David et al. [88], Dupont and Brunet [89], Zhou and Zhong [90-91]). According to the available literature, the Q criterion in the close vicinity of the leeward surface of the balloon is at least an order of magnitude larger than what has been reported for the classical cases. This indicates the flow downstream of the balloon could be significantly rotational.

Vortical cores detected on the leeward surface of the balloon generate shedding vortex tubes. These vortex tubes swirl the flow downstream of the balloon. The turbulent swirling flows are visualized through instantaneous three dimensional pathlines in figure 2.9. These pathlines are coloured by vorticity magnitude. The three strongest swirling tube flows generated by the extremely vortical cores depicted in figures 2.8(a-c) are clearly observed here.

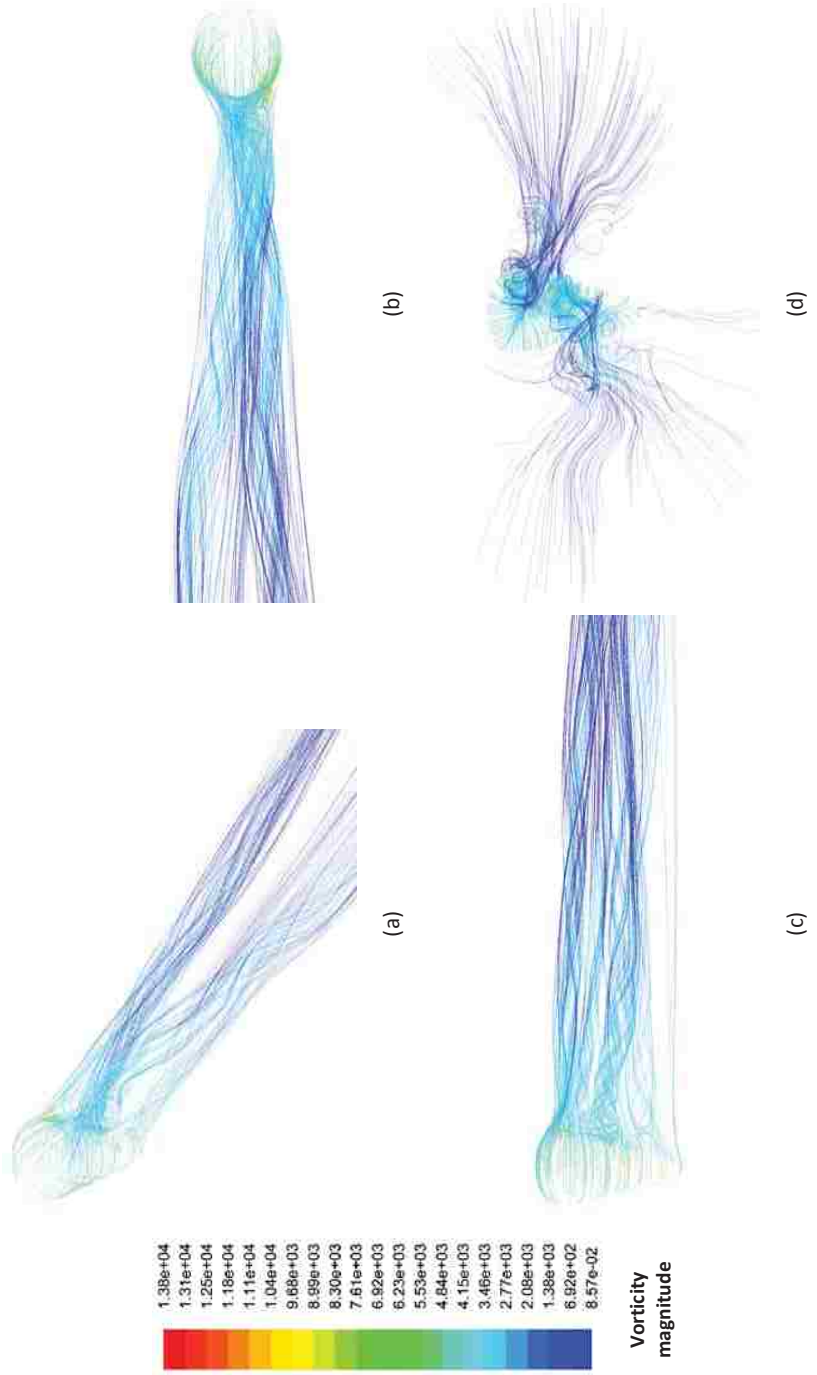

FIGURE 2.9: Three-dimensional pathlines down stream of the balloon. Pathlines are colored by vorticity magnitude.

Accompanying the full rotations of fluid particles around these swirling flows, there are some partial revolving motions due to the turbulent change of the tube flow directions. The tube flows are found to be randomly moving in different directions, sometimes interfering with and breaking up from each other. The directions of these flows are always changing chaotically, however, their sources appear fixed on the leeward surface of the balloon. To visualize dynamics of the tube flows swinging, it would be more revealing to examine the time evolution of the tube flows cross sections. Hence, in figure 2.10 vorticity lines are illustrated on six vertical planes ($P_1, ..., P_6$) perpendicular to the flow direction, that is at X=D, 2D, 3D, 4D, 5D and 6D. The solid lines and dashed lines, respectively, represent the positive (counter clockwise) and negative (clockwise) values of vorticity. At each row of this figure five time-series snapshots are presented to illustrate the time history of the vortex tubes cross sections at a specific distance downstream of the balloon. The non-circular shape of the cross sections of the vortex tubes is attributed to the highly turbulent nature of the flow. It is important to point out that the vorticity contours and the picture of the balloon in the background are drawn to the same scale to enable comparison of the vortices size with the balloon dimensions. As it is shown in figure 2.10(a), black lines with vorticity level in the range of $\pm 1000 \sim \pm 3500$ 1/s are utilized to portray flow pattern on the plane located at X=D. Farther downstream, the vorticity of the flow gradually dissipates. Consequently, blue lines with a lower vorticity level in the range of $\pm 600 \sim \pm 1000$ 1/s are used to illustrate the flow pattern more vividly. As can be seen in panel (e), blue lines are still observed at X=5D, however, red lines with vorticity level of $\pm 300 \sim \pm 600$ are added to the vorticity contour to better illustrate the flow pattern evolution. The chaotic fluctuations of the swirling tube flows in random directions can be observed in these snapshots. It is noted that in distances beyond X=3D, there are different layers in some of the tube flows; inner layers are swirling clockwise and outer layers are swirling counter clock wise, and vice versa. As it is seen, the vorticity level decreases by moving downstream, therefore, the radius of the vortex tubes and their movement amplitude increases. This causes the interference of tube flows. The visualized flow pattern is very similar to what has been observed downstream of a tappered cylinder in cross folw. Sujudi and Haimes [92] developed a mathematical algorithm based on critical point theory to identify the center of three-dimensional swirling flows. The critical points are defined as points where the stream line slope is indeterminate and the velocity is zero relative to appropriate observer [93]. They tested their algorithm for flow past an infinite tapering surface and found several vortical cores on or very close to the surface. They also showed the corresponding swirling flows in the same direction of the main crossing flow. They mathematically proved that the structure of the vortical cores and the correspond swirling flows are very coherent for strong swirls. Valles et al. [94] also visualized the vortical cores producing swirling tube flows downstream of a slender tapered circular cylinder. The swirling flows, however, were generated in an oblique direction, particularly close to the leeward surface (see figure figure 2.11). This is probably due to the low Reynolds number ($Re \approx 130 \sim 180$) and very small tapered ratio of the studied cylinder which was approximately 45 times less than that of the droplet-shaped bluff body of the current paper. Gaster [95] visualized stronger and straighter swirling tube flows behind a cylinder with a tapered ratio of approximately 16 times less than that of the current droplet-shaped bluff body.

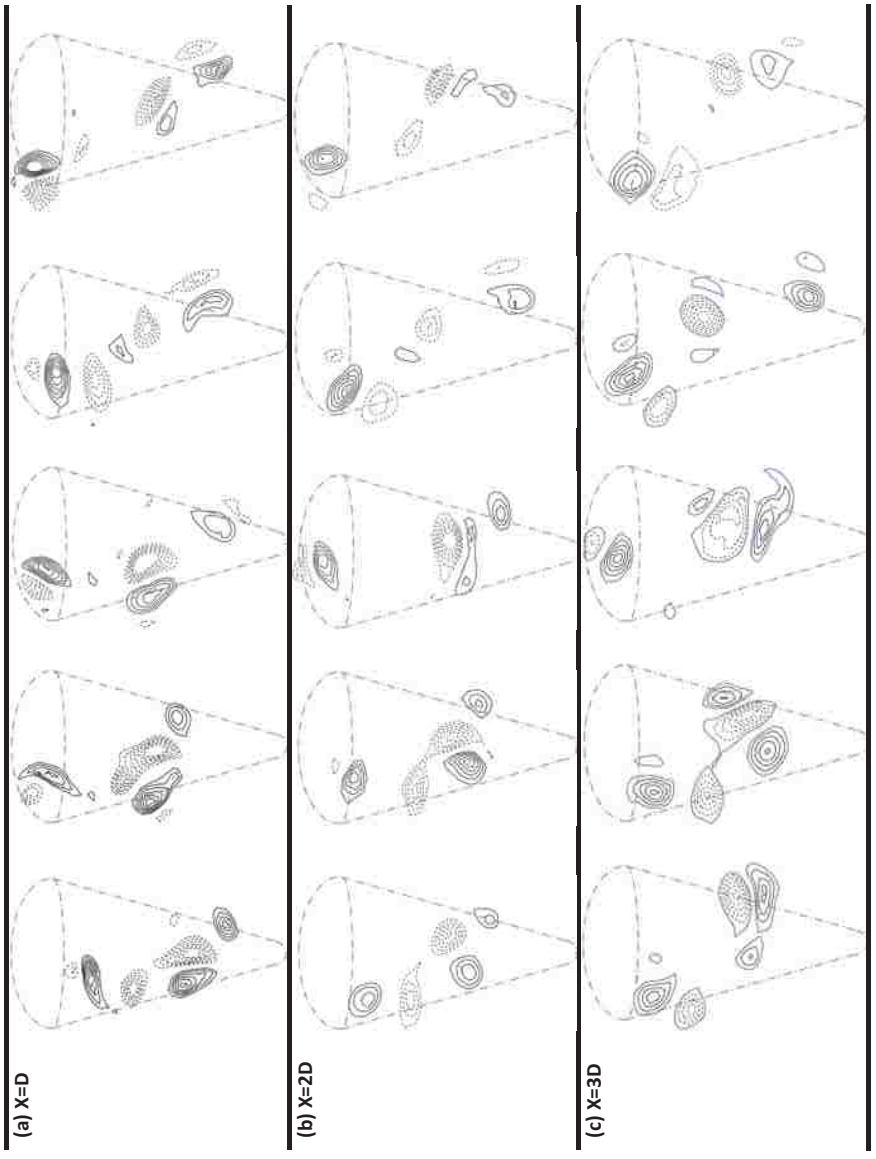

FIGURE 2.10: Cross section of swirling tube flow on planes perpendicular to the flow direction. Each row displays time evolution of flow pattern at a specific distance downstream of the balloon.

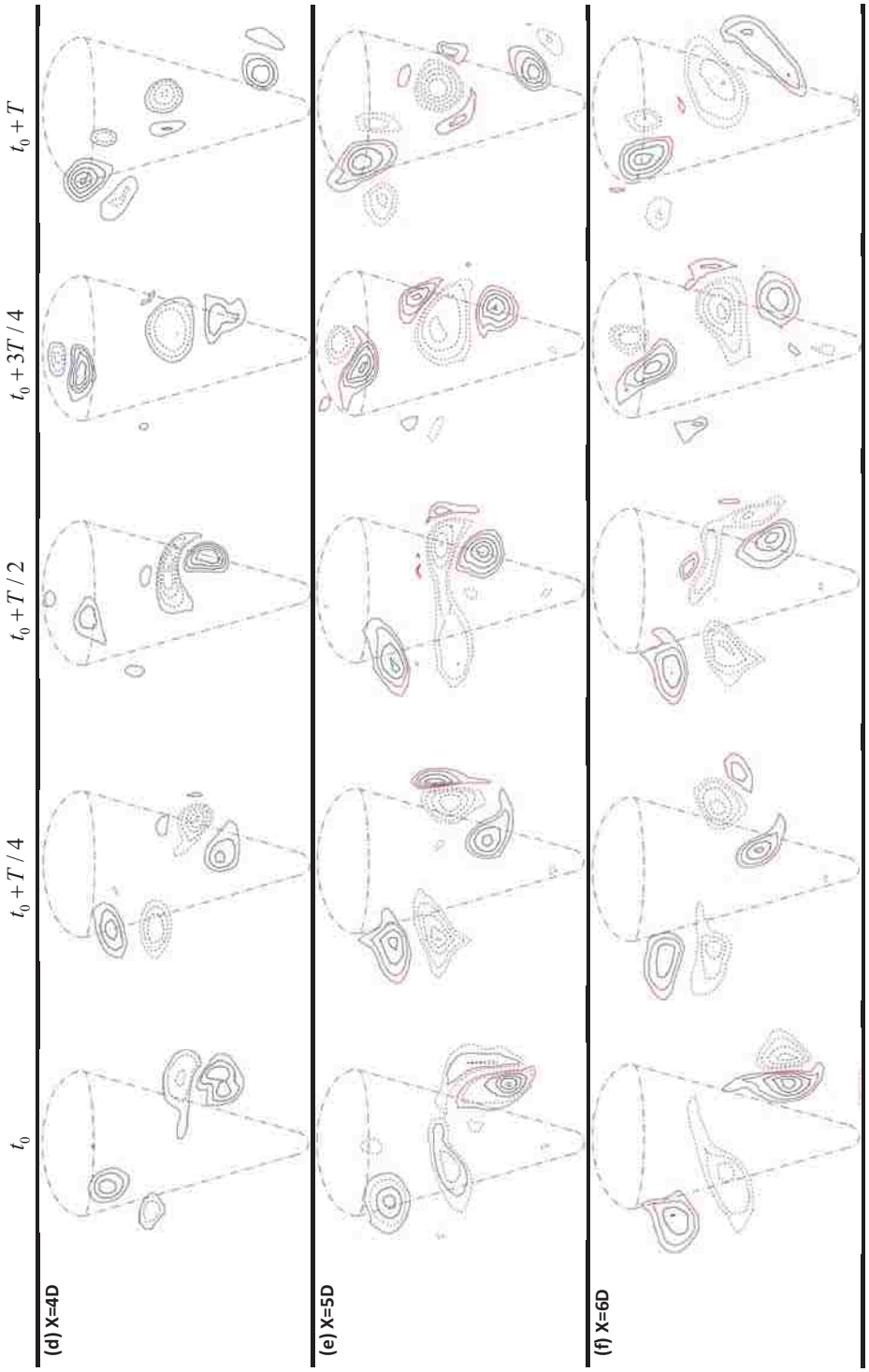

FIGURE 2.10: (continued)

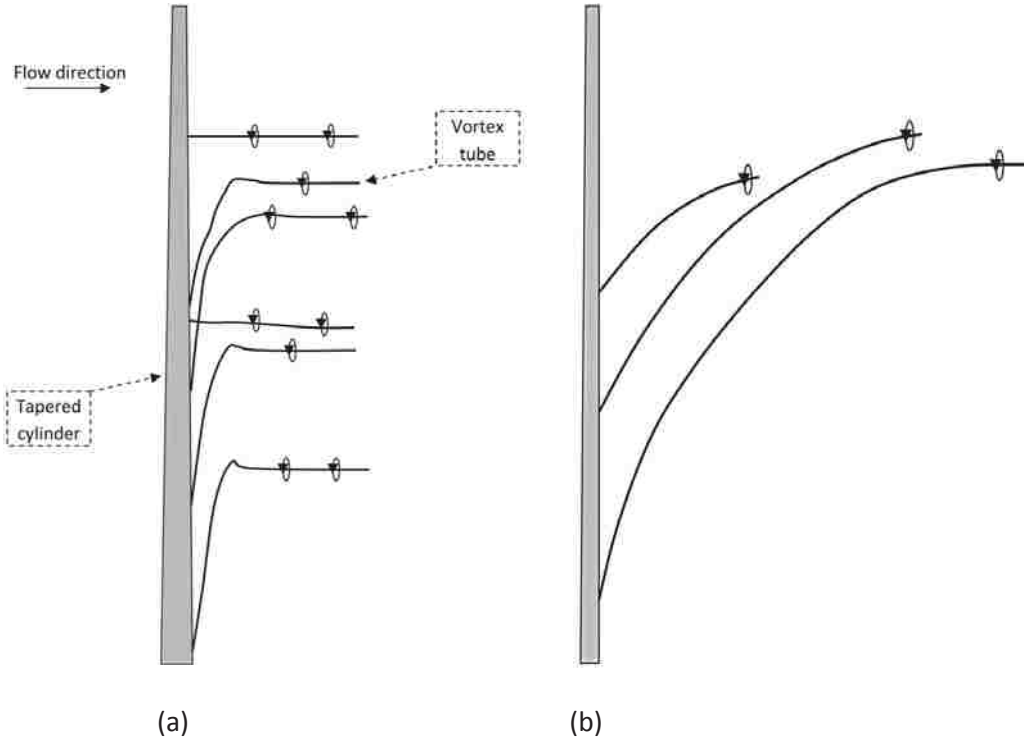

FIGURE 2.11: Swirling tube flows downstream of slender tapered cylinders; (a) visualized by Sujudi and Haimes [91] using critical point method, (b) visualized by Valles et al. [93] by numerically solving full navier stokes equations.

2.5.2 Force characteristics

Force characteristics are calculated using two turbulence models; URANS that uses the sub model of $k-\omega$, and LES with sub-grid model of Dyna-SM. Force coefficients $F/0.5(\rho A_c U^a)$ are calculated using the maximum vertical cross sectional area of a single balloon, i.e. $A_c = 7.81 \times 10^{-4} m^2 \langle 1.1 \rangle$.

Figure 2.12 illustrates URANS prediction for the time history of the force coefficients of the balloon. This figure indicates that URANS gives an almost steady prediction for the force coefficients. That is to say, after some initial instability, all cases go into weak steady oscillations with small amplitudes in the order of 10^{-2} and low frequencies in the range of St$\approx 10^{-2} \sim 10^{-2}$. To enable a closer observation, all force coefficients have been magnified between 18s and 20s. This model appears to have missed capturing the turbulent nature of such a high-Reynolds number flow. This failure may be due to the model's consideration of all turbulence length scales and the corresponding resolution of the governing equations for just the mean values. Thus, while the force coefficient fluctuation is not captured, URANS does seem to appropriately predict the mean values for this high Reynolds number flow. Catalano et al. [59] examined this by studying flow over a single circular cylinder at Reynolds numbers of 5×10^5 and 10^6. They showed that the mean values of the force coefficients obtained by URANS $k-\omega$ and also LES

are in good accordance with the experimental results. Corson et al. [96] used both URANS and LES models to simulate flow over a circular cylinder at Reynolds number of 1.4×10^5. They also confirmed that the time-averaged results of URANS and LES were relatively close, though, URANS tended to overestimate them.

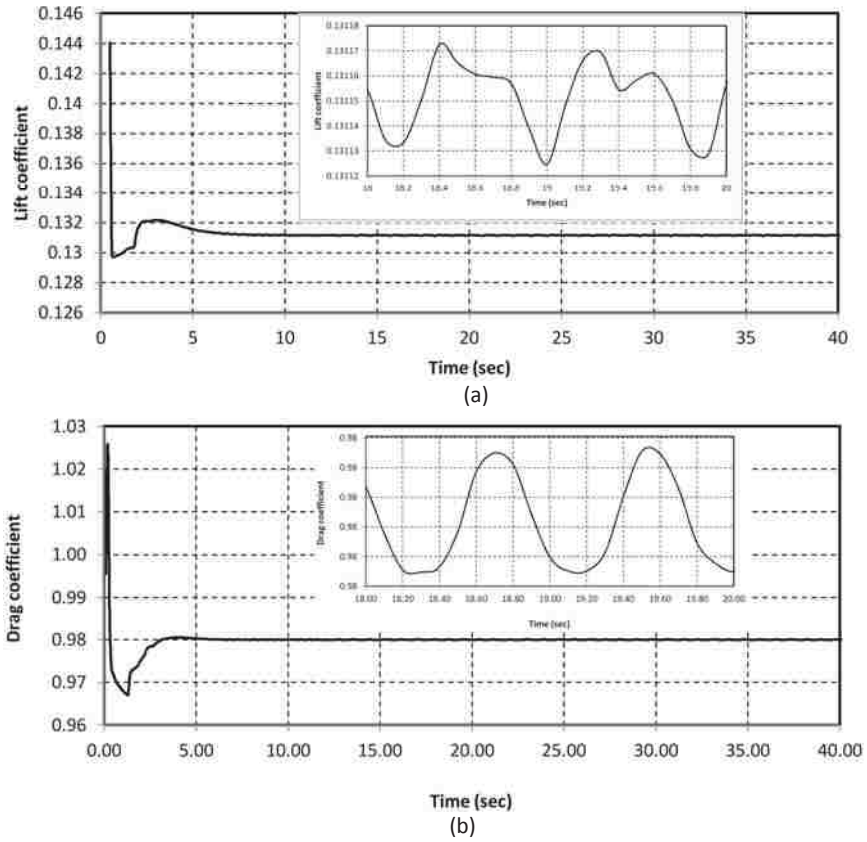

FIGURE 2.12: Time history of the force coefficients of the balloon predicted by URANS; (a) Lift coefficient, (b) drag coefficient.

In contrast to URANS, LES directly resolves the large eddies, and only the small scale eddies which are more related to fluid properties and not geometry-dependent are modelled. Consequently, as is seen in figure 2.13, the fluctuations in the flow over the balloon and the resulting oscillations in the force coefficients were quantified in better detail by the LES simulation. It is observed that against the URANS results which were well organized and periodic (see figure 2.12), the LES results display broadband turbulence characteristics; with amplitude of approximately 10 times what was captured by the URANS. It is important to point out that both lift and drag coefficients in figure 2.13 show statistically stationary behaviour; confirming that the transient results have converged. The mean values of the drag and lift coefficients predicted by the LES simulation are compared with those obtained by the URANS in table 2.3. From this table one can see that the mean values predicted by LES are smaller compared to those of URANS. The discrepancy between mean values predicted by URSANS and LES can be attributed to three main reasons. Firstly, the mesh generated for LES model is different from the URANS mesh. Secondly, URANS model is originally based on the time averaged Navier-Stokes

equations, whereas the LES model solves the spatially filtered Navier-Stokes equations and provides mean values only by averaging the unsteady flow field computed with very small time step, 10^{-5} for the present paper, over a long sampling time. Accordingly, it seems that URANS can better predict the mean values but it is not able to capture fluctuations and flow pattern changes correctly. The third reason is the different between stress tensors of URANS and LES models which is due to the different filtering of Navier-Stokes equations in each of these models. The stress tensor in URANS model is $(-\overline{u'_j u'_i})$, however, the LES stress tensor is $\overline{u_i u_j} - \overline{u_i}\,\overline{u_j}$ where $\overline{u}$ and u' are the mean and the fluctuating components of velocity respectively.

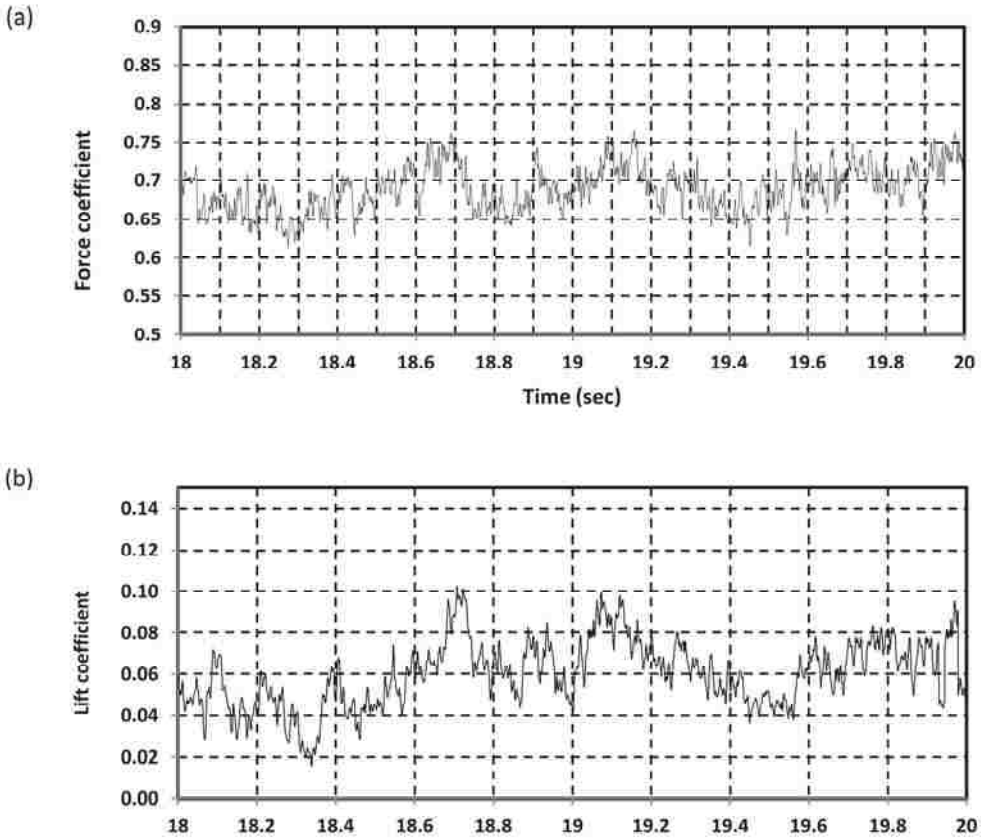

FIGURE 2.13: Time history of the force coefficients of the balloon predicted by LES; (a) Lift coefficient, (b) drag coefficient.

TABLE 2.3: Mean values of the force coefficients predicted by URANS and LES.

	Drag coefficient	Lift coefficient
URANS k-ω	0.98	0.13
LES Dyna SM	0.69	0.06

To the best of our knowledge no research has been done yet on cross-flow over a droplet-shaped bluff body, however, to put these values into perspective they are compared with the values associated with the cylindrical and spherical bodies. It should be mentioned that studies on these basic shapes are not under the same boundary conditions considered in this study, subsequently, the most comparable cases are chosen. The lift coefficient of single sphere and single cylinder

is zero, the values were non-zero for the balloon. This is owing to the asymmetric shape of the balloon about the X-Z plane (see figure 2.14). Concerning the drag coefficient, Achenbach [97] and Clift et al. [98] measured a value of $C_D = 0.51$ for a single sphere and Cantwell and Coles [99] reported a range of $0.78 \leq C_D \leq 1.43$ for a single circular cylinder with different end conditions at a Reynolds number of 2.3×10^5. Heseltine [100] reported a drag coefficient of 1.2 for a circular cylinder at Reynolds number of 2.3×10^5. It is observed that the drag coefficient of the balloon (table 2.3) is between the drag coefficient of a sphere and that of a cylinder at the studied Reynolds number. The reason that the drag coefficient of the balloon is smaller than the drag coefficient of a cylinder can be attributed to the ellipsoidal shape of the balloon at the tips which decreases the pressure in the near wake region. It is expected that the drag coefficient of the balloon approaches to the drag coefficient of a sphere at the lower limit. Therefore, to decrease the drag coefficient of the balloon it should be tried to make it closer to the spherical shape.

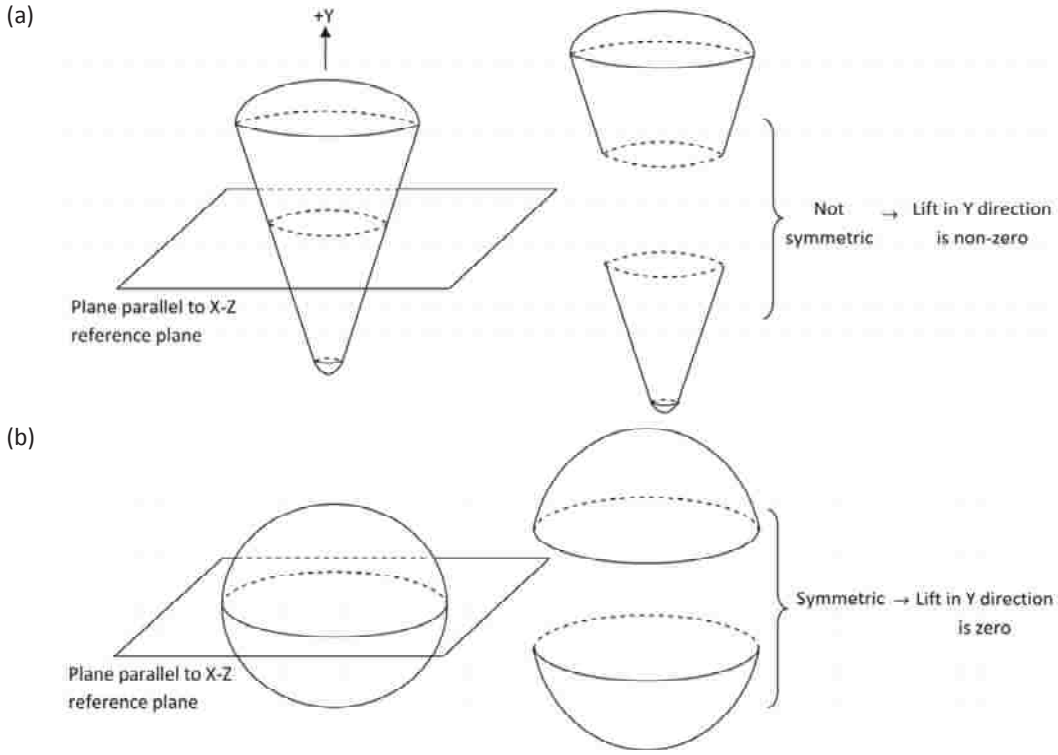

FIGURE 2.14: (a) asymmetrical shape of the balloon about X-Z plane, (b) symmetrical shape of sphere about X-Z plane.

Power spectra of non-sinusodial oscillations of the force coefficients captured by LES are presented in figure 2.15. These diagrams are plotted in log-log axes. In this figure panels (a) and (b) display the power spectrum of the lift and drag coefficients respectively. These power spectra were estimated using Periodogram algorithm (Stoica and Moses [101]). The Strouhal number ($St = f.D/U$) falls in the range of $0.06 \sim 1.2$. Some high and low peaks are observed in this range indicating the dominant frequencies in which the vortex tubes are shed randomly from the balloons.

Panel (a) shows two relatively intense peaks at Strouhal numbers of approximately 0.46 and 0.65 in the power spectrum of the lift coefficient. The peak at St≈0.65 is observed more prominently in power spectra correspond to the drag coefficients (see panel (b)). Another peak corresponding to St≈0.24 is also observed in the drag power spectrum. These Strouhal numbers likely represent the frequency in which fluctuating vortex tubes are shed from the balloon surface. Norman and McKeon [102] observed a similar scenario in the wake of a single sphere for $5\times10^4 \leq Re \leq 5\times10^5$. They found that as Reynolds number increases, the energy in the vortex shedding forcing begins to decay so that at Reynolds number of 2.3×10^5 a very weak peak is located in the power spectrum. No Strouhal peak was observed with further increase in Reynolds number, i.e. no vortex sheds from the sphere surface.

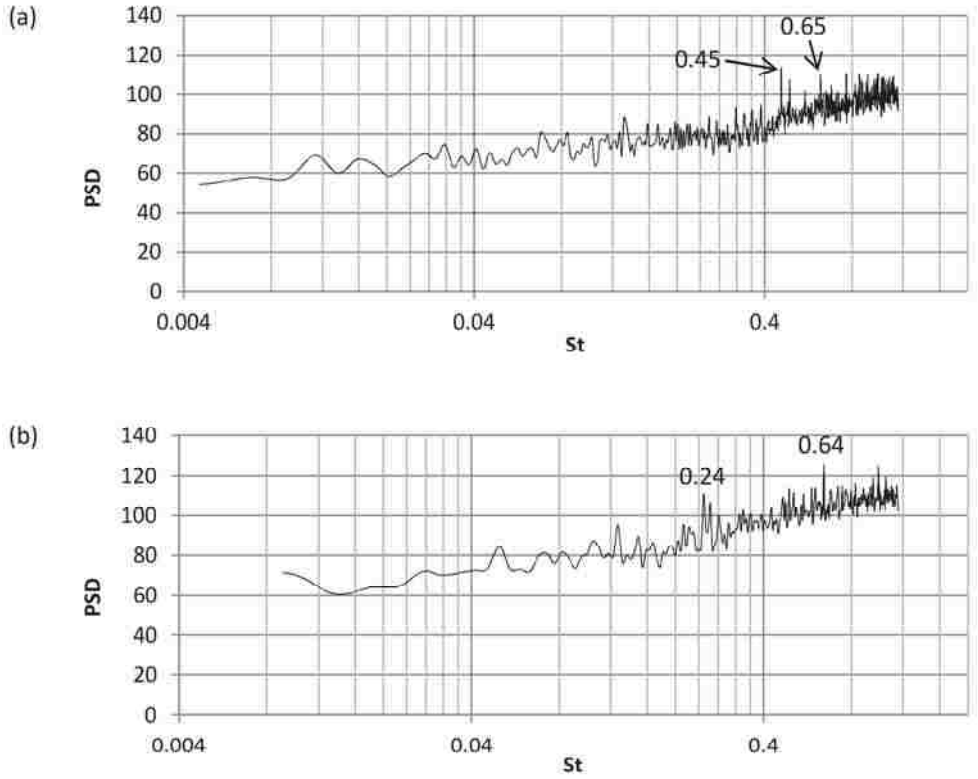

FIGURE 2.15: Power spectrum diagrams associated with the force coefficients of the balloon; (a) Power spectrum of the lift coefficient of the balloon, (b) Power spectrum of the drag coefficient of the balloon.

2.6 Conclusion

Flow past an underwater balloon was numerically investigated using URANS and LES turbulence models. The force characteristics and the structure of the flow around such droplet-shaped bluff body are disclosed. The major findings of the study are summarized:

- When flow crosses a droplet-shaped bluff body, fluid particles move around non-equal radius circles. This causes a rotation about the flow direction, leading to the generation of vortex tubes.
- Among several vortical cores identified by Q criterion, three were prominent; first one in the middle, second one on the lower part and the third one on the top of the leeward surface of the balloon, ordered by the strength.
- The swirling tube flows were found to be fluctuating around in a highly turbulent manner, so that beyond X=3D they were directly contacting and interacting with each other.
- The turbulent movements and the shedding of the vortex tubes mostly occurred in different Strouhal numbers of approximately 0.24, 0.45 and 0.65.
- The URANS model predicted larger force coefficients than the LES.
- Unlike cylindrical and spherical bluff bodies, the lift coefficient of the balloon is not zero, which is due to its non-symmetric shape about X-Z plane.
- At the studied Reynolds number, the mean drag coefficient of the balloon was smaller than the drag coefficient of a cylinder and larger than the drag coefficient of a sphere.

Acknowledgements

This work is made possible by Natural Sciences and Engineering Research Council of Canada. The lead author is most grateful to the Ontario Trillium Foundation for an Ontario Trillium Scholarship.

References

[1] Cheung, B., Cao, N., Carriveau, R., Ting, D.S-K., 2012. Distensible air accumulators as a means of adiabatic underwater compressed air energy storage. International Journal of Environmental Studies, 69, 566-577.

[2] SUBSALVE USA CORPORATION, http://www.subsalve.com/, Accessed on Jan, 2012.

[3] Lam, K., Cheung, W.C., 1988. Phenomena of vortex shedding and flow interference of three cylinders in different equilateral arrangements. Journal of Fluid Mechanics, 196, 1-26.

[4] Ting, D.S-K., Wang, D.J., Price, S.J., Paidoussis, M.P., 1998. An experimental study on the fluidelastic forces for two staggered circular cylinders in cross-flow. Journal of Fluids and Structures, 12: 259-294.

[5] Sumner, D., Price, S.J., Paidoussis, M.P., 1999. Tandem cylinders in impulsively started flow. Journal of Fluids and Structures, 13, 955-965.

[6] Zhang, H., Zhou, Y., 2001. Effect of unequal cylinder spacing on vortex streets behind three side by side cylinders. Physics of Fluids, 13, 3675-12.

[7] Sumner, D., Richards, M.D., 2003. Some vortex-shedding characteristics of the staggered configuration of circular cylinders. Journal of Fluids and Structures, 17, 345-350.

[8] Shao, J., Zhang, C., 2008. Large eddy simulations of the flow past two side-by-side circular cylinders. International Journal of Computational Fluid Dynamics, 22, 393–404.

[9] Lee, K., Yang, K., 2009. Flow patterns past two circular cylinders in proximity. Computers and Fluids, 38, 778–788.

[10] Bao, Y., Zhou, D., Huang, C., 2010. Numerical simulation of flow over three circular cylinders in equilateral arrangements at low Reynolds number by a second-order characteristic-based split finite element method. Computers and Fluids, 39, 882–899.

[11] Yang, X., Zheng, Z.C., 2010. Nonlinear spacing and frequency effects of an oscillating cylinder in the wake of a stationary cylinder. Physics of Fluids, 22, 043601-15.

[12] Sarkar, S., 2010. Vortex dynamics of a cylinder wake in proximity to a wall. Journal of Fluids and Structures, 26, 19-40.

[13] Griffith, M.D., Leontini, J., Thompson, M.C., Hourigan, K., 2011. Vortex shedding and three dimensional behaviour of flow past a cylinder confined in a channel. Journal of Fluids and Structures, 2011, 27,: 855-860.

[14] Vakil, A., Green, S.I., 2011. Two-dimensional side-by-side circular cylinders at moderate Reynolds numbers. Computers and Fluids, 51: 136-44.

[15] Vakil, A., Green, S.I., 2009. Drag and lift coefficients of inclined finite circular cylinders at moderate Reynolds numbers. Computers and Fluids, 38, 1771–1781.

[16] Gazzola, M., Mimeau, C., Tchieu, A.A., Koumoutsakos, P., 2012. Flow mediated interactions between two cylinders at finite Re numbers. Physics of Fluids, 24, 043103-17.

[17] Harimi, I., Saghafian, M., 2012. Numerical simulation of fluid flow and forced convection heat transfer from tandem circular cylinders using overset grid method. Journal of Fluids and Structures, 28, 309-327.

[18] Shyam Kumar, M.B., Vengadesan, S., 2009. Large eddy simulations of flow interference between two unequal sized square cylinders. International Journal of Computational Fluid Dynamics, 23(10), 671–686.

[19] Huang, R.F., Lin, B.H., Yen, S.C., 2010. Time-averaged topological flow patterns and their influence on vortex shedding of a square cylinder in cross flow at incidence. Journal of Fluids and Structures, 26, 406-429.

[20] Alam, M.M., Zhou, Y., Wang, X.W., 2011. The wake of two side-by-side square cylinders. Journal of Fluid Mechanics, 669: 432-471.

[21] Mahbub Alami, M., Zhou, Y., Wang, XW., 2011. The wake of two side-by-side square cylinders. Journal of Fluid Mechanics, 669, 432-471.

[22] Bao, Y., Wu, Q., Zhou, D., 2012. Numerical investigation of flow around an inline square cylinder array with different spacing ratios. Computers and Fluids, 55, 118-131.

[23] Lin M.Y., Huang L.H., 2010. Vortex shedding from a submerged rectangular obstacle attacked by a solitary wave. Journal of Fluid Mechanics, 651, 503-18.

[24] Mannini, C., Soda, A., Schewe, G., 2010. Unsteady RANS modelling of flow past a rectangular cylinder: Investigation of Reynolds number effects. Computers and Fluids, 39, 1609-24.

[25] Lam, K., Lin, Y.F., Zou, L., Liu, Y., 2012. Numerical study of flow patterns and force characteristics for square and rectangular cylinders with wavy surfaces. Journal of Fluids and Structures, 28, 359-377.

[26] Shimada, K., Ishihara, T., 2012. Predictability of unsteady two-dimensional k- model on the aerodynamic instabilities of some rectangular prisms. Journal of Fluids and Structures, 28, 20-39.

[27] Peng, Y.F., Sau, A., Hwang, R.R., Yang, W.C., Chih-Min Hsieh., 2012. Criticality of flow transition behind two side-by-side elliptic cylinders. Physics of Fluids, 24, 034102 (36 pp.).

[28] Taneda, S., 1978. Visual observations of the flow past a sphere at Reynolds numbers between 10^4 and 10^5. Journal of Fluid Mechanics, 85, 187–192.

[29] Constantinescu, G.S., Squires, K.D., 2000. LES and DES investigation of turbulent flow over a sphere. American Institute of Aeronautics and Astronautics AIAA, 0540, 1-11.

[30] Yoon, D.H., Yang, K.S., 2009. Characterization of flow pattern past two spheres in proximity. Physics of Fluids, 21, 073603 (8 pp.).

[31] El Khoury, G.K., Andersson, H.I., Pettersen, B., 2010. Crossflow past a prolate spheroid at Reynolds number of 10000. Journal of Fluid Mechanics, 659, 365-374.

[32] Dixona, A.G., Taskina, M.E., Nijemeisland, M., Stitt, E.H., 2011. Systematic mesh development for 3D CFD simulation of fixed beds: Single sphere study. Computers and Chemical Engineering, 35, 1171–1185.

[33] Hassanzadeh, R., Sahin, B., Ozgoren, M., 2011. Numerical investigation of flow structures around a sphere. International Journal of Computational Fluid Dynamics 25, 535–545.

[34] Narasimhamurthy, V.D., Andersson, H.I., 2009. Pettersen, B. Cellular vortex shedding behind a tapered circular cylinder. Physics of Fluids, 21, 044106 (8 pp.).

[35] Cao, S., Ozono, S., Tamura, Y., Ge, Y., Kikugawa, H., 2010. Numerical simulation of Reynolds number effects on velocity shear flow around a circular cylinder. Journal of Fluids and Structures, 26, 685-702.

[36] Zhou, T., Wang, H., Razali, S.F.M., Zhou, Y., Cheng, L., 2010. Three-dimensional vorticity measurements in the wake of a yawed circular cylinder. Physics of Fluids, 22, 015108 (15 pp.).

[37] Kanaris, N., Grigoriadis, D., Kassinos, S., 2011. Three dimensional flow around a circular cylinder confined in a plane channel. Physics of Fluids, 23, 064106 (14 pp.).

[38] Uzun, A., Yousuff Hussaini, M., 2012. An application of delayed detached eddy simulation to tandem cylinder flow field prediction. Computers and Fluids, 60, 71-85.

[39] Sheard, G.J., Fitzgerald, M.J., Ryan, K., 2009. Cylinders with square cross-section: Wake instabilities with incidence angle variation. Journal of Fluid Mechanics, 630, 43-69.

[40] Subsalve USA corporation, http://www.subsalve.com/images/Subsalvecatalogweb2011.pdf//, Accessed on Jan, 2012.

[41] Centre for Operational Oceanographic Products and Services, http://oceanservice.noaa.gov, Accessed on June, 2012.

[42] National Weather Service Forecast Office, http://www.weather.gov/, Accessed on June, 2012.

[43] Prasanth, T.K., Behara, S., Singh, S.P., Kumar, R., Mittal, S., 2006. Effect of blockage on vortex-induced vibrations at low Reynolds numbers. Journal of Fluids and Structures, 22, 865–876.

[44] Prasanth, T.K., Mittal, S, 2008. Vortex-induced vibrations of a circular cylinder at low Reynolds numbers. Journal of Fluid Mechanics, 594, 463–491.

[45] Drescher, H., 1956. Messung der auf querangestromte Zylinder ausgeubten zeitlich veranderten Drucke. Zeitschrift fur Flugwissenschaften und Weltraumforschung, 4, 17–21.

[46] McGregor, D.M., Etkin, B.E., 1958. Investigation of the fluctuating pressures on a circular cylinder in an airstream. Physics of Fluids, 1, 162–164.

[47] Fung, Y.C., 1960. Fluctuating lift and drag acting on a cylinder in a flowat supercritical Reynolds numbers. Journal of the Aerospace Sciences, 27, 801–814.

[48] Schewe, G., 1983. On the force fluctuations acting on a circular cylinder in crossflow from subcritical up to transcritical Reynolds numbers. Journal of Fluid Mechanics, 133, 265–285.

[49] Blackburn, H.M., Melbourne, W.H., 1996. The effect of free-stream turbulence on sectional lift forces on a circular cylinder. Journal of Fluid Mechanics, 306, 267–292.

[50] Bearman, P.W., Wadcock, A.J., 1973. The interaction between a pair of circular cylinders normal to a stream. Journal of Fluid Mechanics, 61, 499–511.

[51] Sun, T.F., Gu, Z.F., He, D.X., Zhang, L.L., 1992. Fluctuating pressure on two circular cylinders at high Reynolds numbers. Journal of Wind Engineering and Industrial Aerodynamics, 41, 577–588.

[52] Dhiman A.K., Chhabra R.P, Eswaran, V., 2005. Flow and heat transfer across a confined square cylinder in the steady flow regime: Effect of Peclet number. International Journal of Heat and Mass Transfer, 48, 4598–4614.

[53] Dhiman A.K., Chhabra R.P, Eswaran, V., 2006. A numerical study on the forced convection heat transfer from an isothermal and isoflux sphere in the steady symmetric flow regime. International Journal of Heat and Mass Transfer, 49, 984–994.

[54] Smagorinsky, J., 1963. General circulation experiments with the primitive equations. I. The basic experiment. Monthly Weather Review, 91, 99–164.

[55] Lilly, D.K., 1992. A proposed modification of the Germano subgrid-scale closure model. Physics of Fluids, 4, 633–635.

[56] Germano, M., Piomelli, U., Moin, P., Cabot, W.H. Dynamic Subgrid-Scale Eddy Viscosity Model, Summer Workshop, Center for Turbulence Research, Stanford, CA 1996.

[57] Mylonas, D., Sayer, P., 2012. The hydrodynamic flow around a yacht keel based on LES and DES. Ocean Engineering, 46, 18–32.

[58] Shih T.H., Liou, W.W., Shabbir, A., Yang, Z., Zhu, J., 1995. A new k- eddy viscosity model for high Reynolds number turbulent flows. Computers and Fluids, 24, 227-38.

[59] Catalano, P., Wang, M., Iaccarino, G., Moin, P., 2003. Numerical simulation of the flow around a circular cylinder at high Reynolds numbers. International Journal of Heat and Fluid Flow, 24, 463–469.

[60] Huang, Z., Olson, J.A., Kerekes, R.J., Green, S.I., 2006. Numerical simulation of the flow around rows of cylinders. Computers and Fluids, 35, 485–491.

[61] Liu, Z.G., Liu, Y., Lu, J. Fluid–structure interaction of single flexible cylinder in axial flow. Computers and Fluids, 56, 143–151.

[62] Sagaut, p., 2001. Large-Eddy simulation for incompressible flows-An introduction. Springer-Verlag, Scientific computation series.

[63] Howe, M.S., Lauchle, G.C., Wang., 2001. Aerodynamic lift and drag fluctuations of a sphere. Journal of Fluid Mechanics, 436, 41-57.

[64] Hunt, J.C.R., Wray, A.A., Moin, P., 1988. Eddies, Stream, and Convergence Zones in Turbulent Flows. Center For Turbulence Research CTR-S88.

[65] Truesdell, C.A., 1954. The Kinematics of Vorticity. Indiana University Science Series; 19.

[66] Frana, K., Stiller, J., Grundmann, R., 2005. Taylor-Görtler Vortices in the Flow Driven by a Rotating Magnetic Field in a Cylindrical Container. Journal of Visualization, 8(4), 323-330.

[67] Ozcan, O., Meyer, K.E., Larsen, P.S., 2005. Measurement of mean rotation and strain-rate tensors by using stereoscopic PIV. Experiments in Fluids, 39, 771-783.

[68] Séverac, É., Poncet, S., Serre, É., Chauve, M., 2007. Large eddy simulation and measurements of turbulent enclosed rotor-stator flows. Physics of Fluids, 19, 085113 (17 pp.).

[69] Tanahashi, M., Hirayama, T., Taka, S., Miyauchi, T., 2008. Measurement of fine scale structure in turbulence by time-resolved dual-plane stereoscopic PIV. International Journal of Heat and Fluid Flow, 29, 792–802.

[70] Vernet, R., Thomas, L., David, L., 2009. Analysis and reconstruction of a pulsed jet in cross flow by multi-plane snapshot POD. Experiments in Fluids, 47, 707–720.

[71] Kunnen, R.P.J., Clercx, H.J.H., Geurts, B.J., 2010. Vortex statistics in turbulent rotating convection. Physical Review E, 82, 036306 (12 pp.)

[72] Stoesser, T., Kim, S.J., Diplas, P., 2010. Turbulent Flow through Idealized Emergent Vegetation. Journal of Hydraulic Engineering, 136, 1003-1017.

[73] Garrick, S.C., 2011. Effects of Turbulent Fluctuations on Nanoparticle Coagulation in Shear Flows. Aerosol Science and Technology, 45, 1272–1285.

[74] Kamkar, S.J., Wissink, A.M., Sankaran, V., Jameson, A., 2011. Feature-driven Cartesian adaptive mesh refinement for vortex-dominated flows. Journal of Computational Physics, 230, 6271–6298.

[75] Chang, K., Hughes, T.J.R., Calo, V.M., 2012. Isogeometric variational multiscale large-eddy simulation of fully-developed turbulent flow over a wavy wall. Computers and Fluids, 68, 94–104.

[76] Lee, G., Scalo, C., Piomelli, U., 2012. A simple technique for the visualization of eddy kinematics in turbulent flows. International Journal of Computational Fluid Dynamics, 26, 263–274.

[77] Yang, Y., Knudsen, S., 2012. Large-eddy simulations of the non-reactive flow in the Sydney swirl burner. International Journal of Heat and Fluid Flow, 36, 47–57.

[78] Krajnovi'c, S., Basara, B., 2009. Numerical Simulation of the Flow around a Tall Finite Cylinder Using LES and PANS. Progress in Turbulence III Springer Proceedings in Physics, 131, 15-118.

[79] Zhou, Y., Li, X., Fu, D., Ma, Y., 2007. Coherent structures in transition of a flat-plate boundary layer at Ma=0.7. Chinese Physics Letters, 22, 147-150.

[80] Paik, J., Sotiropoulos, F., 2010. Turbulent swirling flow through an abrupt axisymmetric expansion is investigated numerically using detached-eddy simulation at Reynolds numbers. International Journal of Heat and Fluid Flow, 31, 390–400.

[81] Omori, T., Jakirlic, S., Tropea, C., Obi, S., 2008. Shearless and sheared flow past a circular cylinder: Comparative analysis by means of LES. International Journal of Heat and Fluid Flow, 29, 703-720.

[82] Morton, C., Yarusevych, S., 2010. Vortex shedding in the wake of a step cylinder. Physics of Fluids, 22, 083602 (14 pp.).

[83] Kotouc, M., Bouchet, G., Dusek, J., 2009. Transition to turbulence in the wake of a fixed sphere in mixed convection. Journal of Fluid Mechanics, 625, 205-48.

[84] Dubief, Y., Delcayre, F., 2000. On coherent-vortex identification in turbulence. Journal of Turbulence, 1, 1-22.

[85] Howard, R.J.A., Pourquie, M., 2002. Large eddy simulation of an Ahmed reference model. Journal of Turbulence, 3, 1-18.

[86] Sohankar, A., 2006. Flow over a bluff body from moderate to high Reynolds numbers using large eddy simulation. Computers and Fluids, 35, 1154–1168.

[87] Paik, J., Escauriaza, C., Sotiropoulos, F., 2007. On the bimodal dynamics of the turbulent horseshoe vortex system in a wing-body junction. Physics of Fluids, 19, 045107 (pp. 20).

[88] David, L., Farcy, A., Alemdaroglu, N., 2008. Aerodynamic characteristics of flapping motion in hover. Experiments in Fluids, 44, 23–36.

[89] Dupont, S., Brunet, Y., 2009. Coherent structures in canopy edge flow: a large-eddy simulation study. Journal of Fluid Mechanics, 630, 93–128.

[90] Zhou, J., Zhong, S., 2009. Numerical simulation of the interaction of a circular synthetic jet with a boundary layer. Computers and Fluids, 38, 393–405.

[91] Zhou, J., Zhong, S., 2010. Coherent structures produced by the interaction between synthetic jets and a laminar boundary layer and their surface shear stress patterns. Computers and Fluids, 39, 1296–1313.

[92] Sujudi, D., Haimes, R., 1995. Identification of swirling flow in 3-D vector fields. American Institute of Aeronautics and Astronautics Journal. Technical report, 1-8.

[93] Chong, M.S., Perry, A.E., Cantwell, B.J., 1990. A general classification of three-dimensional flow fields. Physics of Fluids, 2, 765-777.

[94] Vallee, S., Andersson, H.I., Jenssen, C.B., 2002. Oblique vortex shedding behind tapered cylinders. Journal of Fluids and Structures, 16(4), 453-463.

[95] Gaster, M., 1969. Vortex shedding from slender cones at low Reynolds numbers. Journal of Fluid Mechanics, 38(3), 565-576.

[96] Corson, D., Jaiman, R., Shakib, F., 2009. Industrial application of RANS modelling: capabilities and needs. International Journal of Computational Fluid Dynamics, 23(4), 337–347.

[97] Achenbach, E., 1972. Experiments on the flow past spheres at very high Reynolds numbers. Journal of Fluid Mechanics, 54, 565-75.

[98] Clift, R., Grace, J.R., Weber, M.E., 1978. Bubbles Drops and Particles. New York: Academic Press, New York.

[99] Cantwell, B., Coles, D., 1983. An experimental study of entrainment and transport in the turbulent near wake of a circular cylinder. Journal of Fluid Mechanics, 136, 321-74.

[100] Heseltine, J.L. Flow around a circular cylinder with a free end. Thesis, University of Saskatchewan, August 2003.

[101] Stoica, P., Moses, R.L., 1997. Introduction to Spectral Analysis. Prentice-Hall, 24-26.

[102] Norman, A.K., McKeon, B.J., 2011. Unsteady force measurements in sphere flow from subcritical to supercritical Reynolds numbers. Experiments in Fluids, 51, 1439-1453.

Chapter 3

Flow Past an Accumulator Unit of an Underwater Energy Storage System: Three Touching Balloons in a Floral Configuration

A. R. Vasel-Be-Hagh, D. S.-K. Ting, R. Carriveau

Turbulence and Energy Laboratory, Lumley Centre for Engineering Innovation, University of Windsor, Ontario, Canada N9B 3P4

Vasel-Be-Hagh, A.R., Carriveau, R., Ting, D.S.-K., 2014. Flow past an Accumulator Unit of an Underwater Energy Storage System: Three Touching Balloons in a Floral Configuration. Journal of Marine Science and Application, 13(4), 467-476.

3.1 Introduction

Over the last decade the electricity market has changed drastically and renewable energy sources have been introduced as alternatives for fossil-fuel based electricity generation. However, renewable energy sources suffer from a number of challenges including their highly intermittent nature, low energy density, grid congestion and stability issues. Storage facilities have the potential to offer a solution to these challenges. One of the most efficient and environmentally safe storage technologies is compressed air energy storage (CAES), which is a modification of the basic gas turbine technology [1-2]. The application of this underground energy storage is, however, limited to the land based power stations [3]; while much of renewable resources are offshore [4]. Hence, a variant of the original CAES, underwater compressed air energy storage UW-CAES, designed

for offshore application is being built in a demonstration capacity at grid connection scale in Toronto Harbour [5-6]. In UW-CAES, the surplus electrical energy generated during the off-peak hours is converted to hydrostatic pressure by compressing air into submerged distensible accumulator units. The flexible balloons of the accumulator unit are anchored to the sea floor; hence, the stored air is pressurized by hydrostatic forces, ready to be released back to the surface to drive turbines to supply the electrical grid when needed. UW-CAES has also been studied by Pimm et al. [7] by performing an analysis of accumulator shape and cost. The study assumed an acting force normal to the surface of the balloon owing to the differential pressure acting across the surface. This analysis can be modified by taking into account the hydrodynamic loads exerted on the accumulator by the crossing flow. In a more recent study conducted at the European Marine Energy Centre in Orkney, Pimm et al. [8] discussed challenges associated with underwater accumulators focusing on tears occurring during the installation and operation. They also tested two different accumulators in a water tank and found a small leak causing the air hose and the accumulator to fill with water. The dynamic nature of the hydrodynamic loads produced by the crossing flow can severely affect the observed tears and leakages; hence, having insights into force characteristics of the crossing flow can be very useful in choosing a more durable material for manufacturing future balloons. Furthermore, providing a good estimate of hydrodynamic loading and structure of the flow is certainly one of the most demanding tasks to develop an optimal design for foundation, support structures and valve connections. It was the above-mentioned considerations that prompted the present study on flow over a floral unit of droplet shaped underwater balloons. There has been significant progress in the understanding of flow over bluff bodies over the last couple of decades. The focus, however, has been limited to flow over regular shapes like cylinders [9-15] and spheres [16-18]. A literature survey on flow over bluff bodies appeared to indicate a dearth of published research exploring the cross-flow past droplet-shaped bluff bodies. Hence, first, the basic case of flow over a single balloon was examined [19]. The current paper, however, explores the practical case of flow over three touching balloons in a floral configuration. The central aim of this paper is developing an understanding of the force characteristics and the structure of the flow over the accumulator unit of UW-CAES as an essential step to develop an efficient design.

3.2 Computational Details

The PF20000 model of professional (PF) lift bags manufactured by Subsalve USA Corporation is a suitable choice to perform as the accumulator unit of the UW-CAES system (Subsalve USA Corporation, [20]). In order to decrease computational expenses, dimensions of the PF20000 balloon were scaled down by a factor of 100. As the force coefficients are functions of the Reynolds number, the free stream velocity is scaled up 100 times to retain the same Reynolds number. Dimensions of the scaled balloon are presented in figure 3.1(a). The touching state of floral configuration of the balloons is illustrated in figure 3.1(b). The floral unit is symmetric about the X-axis (the flow direction); therefore, characteristics of the two downstream balloons are essentially identical. Hence, only one data set is presented for the downstream balloons. In this paper, the characteristic diameter used to define the Reynolds number is expressed as

$$D = \frac{6 \times V}{A} \tag{3.1}$$

where V and A are volume and surface area of a single balloon respectively. Accordingly, for the scaled down PF20000 balloon depicted in figure 3.1(a), the characteristic diameter D is 2.311×10^{-2}m.

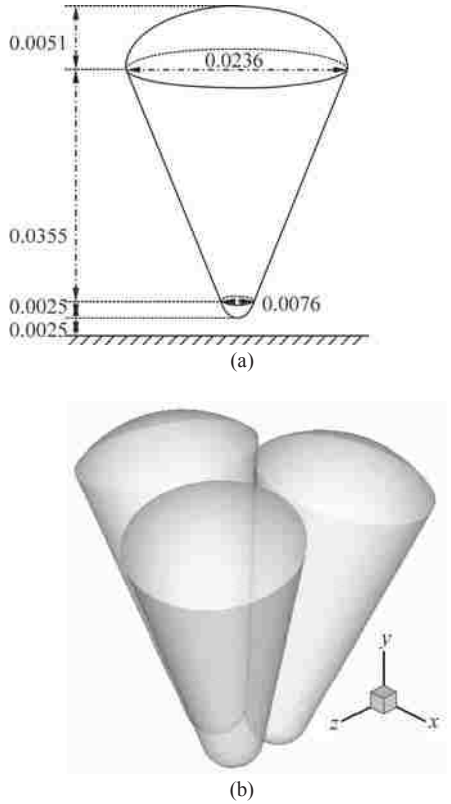

FIGURE 3.1: Dimensions and configurations of the balloons, x axis shows the streamwise direction; (a) scaled down PF20000 balloon; values are in meters (not to scale), (b) floral configuration of the touching balloons.

Dimensions of the computational domain are provided in terms of the characteristics diameter D in figure 3.2. As it is shown, length, height and width of the computational area are $40D$, $11D$ and $13.2D$ respectively. The balloon is located $7.7D$ downstream of the inlet boundary. There is an approximate distance of $0.1D$ between the lowest point of the floral unit and the solid bed. It should be mentioned that the reference of the coordinate system used in this study is fixed underneath the center of the unit on the bed surface; i.e., the lowest point of the unit is at (0, $0.1D$, 0). As is illustrated in figure 3.1(b), in the floral configuration studied, one of the balloons is located upstream and the other two are downstream, where the hypothetical line connecting the top of them is perpendicular to the streamwise direction. Of note, characteristics of the flow change with the angle of incidence.

The three boundary conditions applied in the current simulation are also described in figure 3.2. Mass-flow-inlet condition with mass flow rate of 888.5 kg/s is set at the inlet boundary, resulting

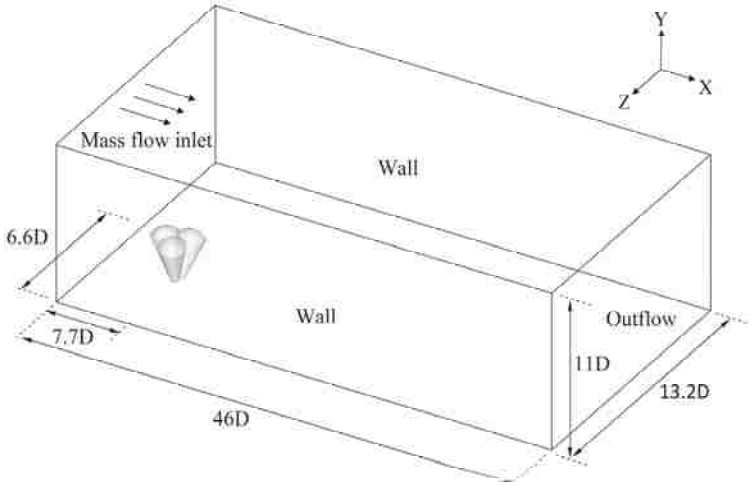

FIGURE 3.2: Boundary conditions and dimensions of the computational domain in terms of the characteristics diameter D.

in a Reynolds number of 2.3×10^5. The outflow boundary condition has a flow rate weighting of 1 at the outlet, as it is the only outlet of the domain. In the real application the accumulator unit is installed under deep water, therefore, to be in accordance with the real case a free surface condition should be applied on the top boundary of the computational domain. To avoid extra computational expenses the no slip condition was employed on the top boundary, due to the considerable depth this effect is expected to be small. The no slip condition is also applied at all solid-liquid interferences including side and bottom walls of the computational domain and the surface of the balloon, which is here assumed rigid (non-distensible). Regardless of the type, either pressure far-field, slip or no-slip; the simulation results should be independent of properly chosen side boundary conditions, since in the real scenario there are no boundaries around the accumulator. The literature has been largely focused on the no-slip boundary condition; verifying that if the blockage ratio (BR) is large enough, the effect of the slip boundary condition applied on the side-walls is negligible. This was our main motivation for using no-slip boundary condition.

Prasanth et al. [21] and Prasanth and Mittal [22] demonstrated that the effects of blockage ratio on the interactions between flow and bluff bodies are very significant at low Reynolds numbers so that the blockage ratio should be 1% or less. However, at Reynolds numbers larger than 100, the results for BR=1% and BR=5% were very close and almost independent of walls effect. At Reynolds numbers on the order of what was studied in the present paper (10^5) the blockage ratios are mostly chosen to be in the range of 3%–25% [23-29]. In the present paper, to ensure the negligibility of the effect of the no-slip boundary condition, the blockage ratio was set to be approximately 1.3% which is smaller than what others have been chosen for the similar cases. It should be mentioned that the blockage ratio was calculated as the ratio of frontal area of the floral unit and the cross sectional area of the computational domain.

3.3 Mesh

Due to the non-regular shape of the balloons, an unstructured mesh was generated in the proximity of boundaries. However, to reach a mesh-independent solution with a thoroughly unstructured mesh the number of cells would exceed the capacity of the available processors (4×2.4GHz Quad-Core Intel Xeon, supported by 24 GB RAM). To have an efficient control of the mesh density, the computational domain was divided into 18 blocks. An isometric view of the mesh is illustrated in figure 3.3(a). In the central block that contains the floral unit of the balloons an unstructured mesh was generated using the T-Grid type of Tet-hybrid cells (block 1, figure 3.3(b). In all other blocks the cooper type of hex-wedge cells was used to establish a structured mesh.

As the six blocks shown in figure 3.3(b) are meshed, the mesh size of the rest 12 blocks becomes constrained since each of them has three edges in common with the six blocks already meshed. Meldi et al. [30] demonstrated that a filter width of $\triangle = L/55$ is the limit for the correct application of Smagorinsky subgrid scale model in an LES simulation,

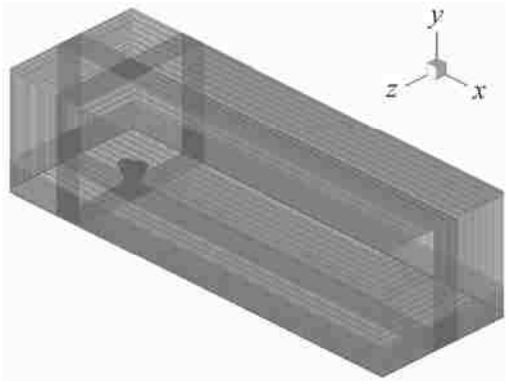

(a)

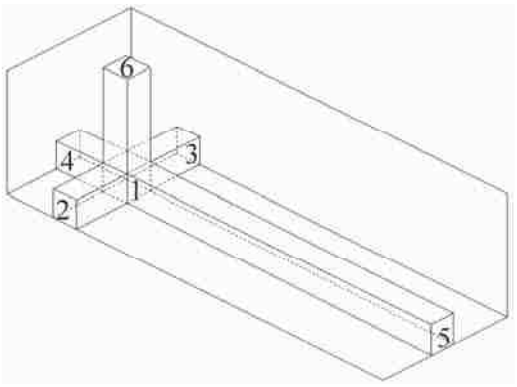

(b)

FIGURE 3.3: Meshing of the computational domain; (a) isometric view of the mesh through computational domain, (b) partitioning the computational domain to control mesh density.

where L is the large scale and in the present simulation is assumed to be the balloon height ($\approx 2D$) where D is the characteristic diameter. Accordingly, the central block with dimensions of $4D \times 4D \times 2D$ should contain more than $(4 \times 55/2) \times (4 \times 55/2) \times (2 \times 55/2) \approx 660{,}000$ cells to assure that the grid size is smaller than the LES filter width required for the Smagorinsky subgrid scale model (≈0.036D). As can be seen in figure 3.3(b), blocks 2–6 have two edges in common with the central block. As the common edges are already meshed, the grid size in these blocks can be controlled just in one direction through setting the maximum cell aspect ratio. It is highly recommended to avoid aspect ratios larger than 5. Accordingly, three fine, extra fine and extremely fine meshes were generated with maximum aspect ratios of 5, 4 and 3, respectively, resulting in total numbers of 6×10^6, 8×10^6 and 12×10^6 cells. The variation of the time averaged force coefficients with these three meshes are depicted in figure 3.4. As is observed, a fair mesh independency ceased when the number of cells exceeded approximately 8×10^6.

In the Fluent LES model, the wall boundary condition is implemented using the law-of-the-wall approach. Accordingly, there is a logarithmic relation between $u^+ = u/u_\tau$ and $y^+ = y \times u_\tau/\nu$ where $u_\tau = \sqrt{\tau_w/\rho}$ is the friction velocity in which τ_w and ρ are wall shear stress and density of the fluid respectively. Therefore, it seems there are no computational restrictions on the near wall mesh density. Here a very fine near-wall mesh spacing on the order of $y^+ = 1$ was generated as was recommended by Sagaut [31].

3.4 LES model

LES governs dynamics of large eddies by removing eddies with scales smaller than the grid spacing (or any other filter width) from unsteady Navier-Stokes equations. The filtered Navier–Stokes equations are as follows

$$\frac{\partial \overline{u}_i}{\partial \overline{x}_i} = 0 \tag{3.2}$$

$$\frac{\partial \overline{u}_i}{\partial t} + \overline{u}_j \frac{\partial \overline{u}_i}{\partial x_i} = -\frac{1}{\rho}\frac{\partial \overline{P}}{\partial x_i} + \frac{\partial}{\partial x_i}(2\nu S_{ij} - \tau_{ij}) \tag{3.3}$$

As it is seen, the filtering brings some additional unknown terms τ_{ij} namely subgrid scale (SGS) stresses which need to be determined through an SGS model. In the current paper, the SM model proposed by Smagorinsky [32] was applied to compute the SGS stresses. The main assumption of the SM model is the equality of the SGS with the product of an eddy-viscosity μ_t and the resolved rate of strain tensor S_{ij}:

$$\tau_{ij} - \frac{1}{3}\tau_{kk}\delta_{ij} = -2\mu_t \overline{S}_{ij} \tag{3.4}$$

where the rate of strain tensor S_{ij} and the eddy-viscosity μ_t are defined as

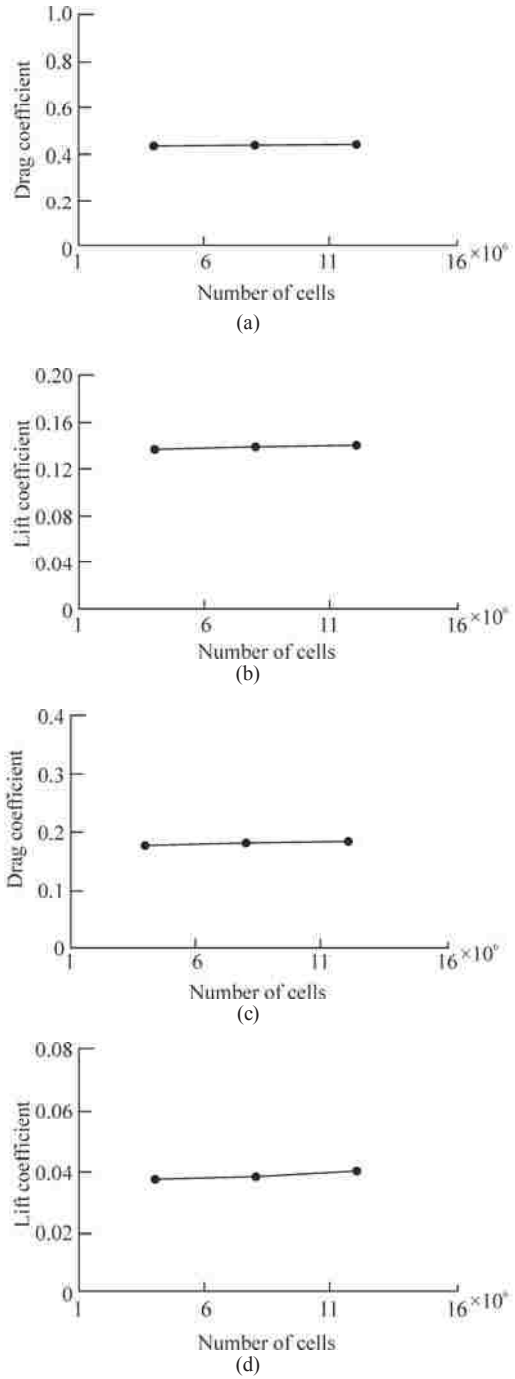

FIGURE 3.4: Mesh independence analysis; (a) drag coefficient of the upstream balloon versus total number of cells, (b) lift coefficient of the upstream balloon versus total number of cells, (c) drag coefficient of the downstream balloon versus total number of cells, (d) lift coefficient of the downstream balloon versus total number of cells.

$$\overline{S}_{ij} = 1/2((\frac{\partial \overline{u}_i}{\partial x_j}) + (\frac{\partial \overline{u}_j}{\partial x_i})) \tag{3.5}$$

$$\mu_t = \rho L_s^2 \mid \overline{S} \mid \tag{3.6}$$

in which $\mid \overline{S} \mid$ is computed via $\mid \overline{S} \mid = \sqrt{2\overline{S}_{ij}\overline{S}_{ij}}$. The mixing length L_s is defined by

$$L_s = min(\kappa d C_s V^{\frac{1}{3}}) \tag{3.7}$$

where κ, d and C_s are von Kármán constant, distance to the closest wall and Smagorinsky parameter respectively. The Smagorinsky parameter C_s can be kept constant, 0.1 is highly recommended [33] or dynamically computed during the simulation using the information provided by the smaller scales of the resolved fields (Lilly [34] and Germano et al. [35]). Mylonas and Sayer [36] found that the dynamic model gives a better prediction for the drag coefficient of a yacht keel when compared to their experiments. Thus, the dynamic model was adopted in this study.

3.5 Numerical Methodology and Verification

All nonlinear governing equations are linearized to a scalar system of equations through an implicit method. The Gauss-Siedel solver along with a segregated algebraic multi-grid (AMG) method is applied to solve this system of equations. The pressure implicit with split operator (PISO) algorithm is used for the pressure-velocity coupling. Compared to the other algorithms (for instance simple, simplec and coupled) the PISO algorithm requires more CPU to process; on the other hand, it significantly decreases the number of iterations before convergence occurs. PISO algorithm is also more proper for skewed cells which in meshing of the current complex geometry are unavoidable. In the LES turbulence model, physical diffusion is significantly affected by numerical diffusion; consequently, the bounded central differencing scheme would be a suitable approach to conduct the spatial discretization. However, in these schemes there is no numerical damping; therefore, the numerical fluctuations affect the physical ones. Fortunately, the Fluent code efficiently obviates this issue by changing the spatial discretization scheme from the central differencing to the upwind scheme for any oscillation with a wavelength less than twice the local grid spacing. This feature was the main motivation to conduct the current simulation using Fluent code. Furthermore, several researchers already verified the accuracy of the Fluent LES model in simulating flow over different bluff bodies [37-40]. In the current simulation, the Courant number was chosen to be 0.5 with a time step of $10^{-3}s$. The number of iterations for each time step was set to be 10. Using the 8–million–cell grid described in section 3, and running on a 4×2.4 GHz Quad–Core Intel Xeon system supported by 24 GB RAM, every second of real–time flow simulation required approximately 30 hours of CPU time.

3.6 Structure of the Flow

Consider the schematic motion of two typical particles a and b around a cylindrical surface element illustrated in figure 3.5(a). Since these particles are moving at the same linear and angular velocities $\omega = V/r$, the micro-scale line $\overline{ab}$ leaves the surface with no spin around X axis (see figure 3.5(a)). It simply moves side to side in the wake of the cylindrical surface. Figure 3.5(b) shows the motion of these particles around a surface element of a droplet-shaped body. In this case the particles are moving around unequal curves, consequently, the angular velocity of particle b is higher than the angular velocity of particle a. Hence, particle b turns around the surface ahead of particle a causing rotation of the line $\overline{ab}$. Therefore, the line $\overline{ab}$ leaving the leeward surface has a swirling motion around the flow direction, in addition to its sideward motion in the wake of the droplet-shaped body. The combination of such rotations on the surface elements can generate vortical cores on the leeward surface. These vortical cores swirl the flow and form vortex tubes downstream of the droplet shaped bluff body.

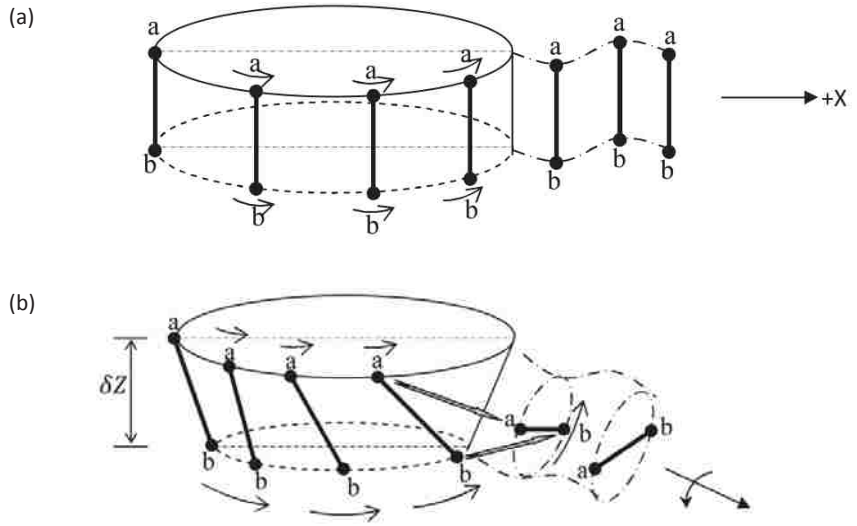

FIGURE 3.5: The schematic motion of two typical particles around the surface; (a) cylindrical surface element, (b) surface element of a droplet-shaped body.

Three-dimensional path lines colored by vorticity magnitude were used to examine the above-predicted swirling flows downstream of the droplet shaped balloons. The isometric, +X, +Y and +Z views of path lines downstream of the floral unit are illustrated in figure 3.6. The vortical cores on the leeward surface of the balloons and the resulting swirling flows are clearly observed in these contours. Sujudi and Haimes [41] predicted similar swirling flows downstream of an infinite slightly tapered surface by developing a mathematical algorithm based on the critical point theory. They proved mathematically that the structure of the vortical cores and the corresponding swirling flows are very coherent for strong swirls.

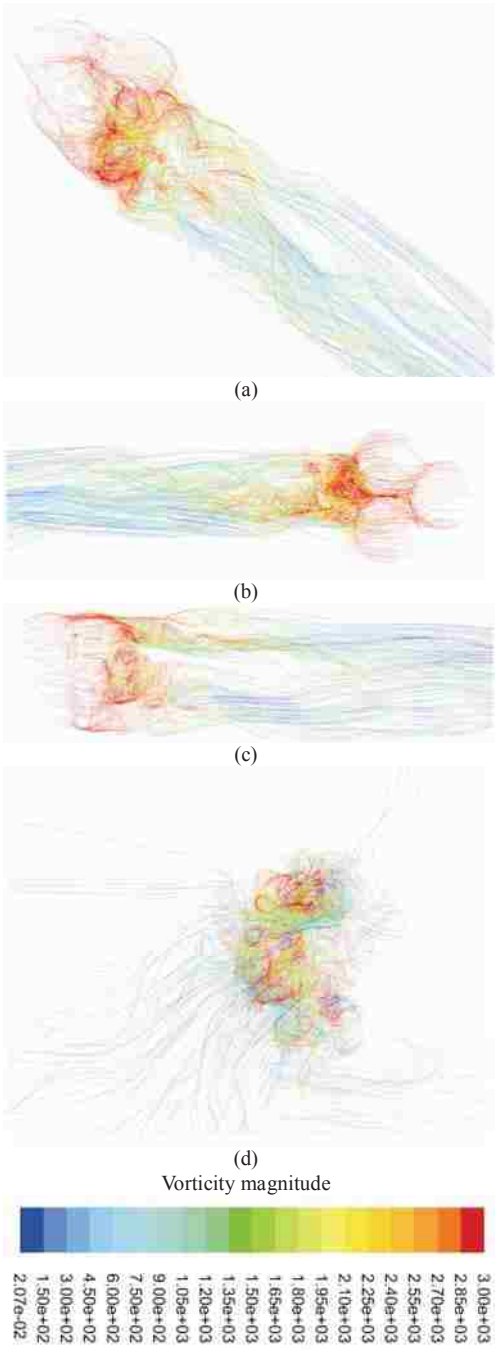

FIGURE 3.6: Three-dimensional pathlines downstream of the balloons in the closely spaced configuration, pathlines are colored by vorticity magnitude in 1/s; (a) isometric view, (b) top view, (c) side view, (d) back view.

Isosurfaces of the second invariant of the velocity gradient, namely the Q criterion proposed by Hunt et al. [42] are used to investigate the proposed vortical cores along the leeward surface of the balloon. The Q criterion is defined as

$$Q \equiv \frac{1}{2}({u_{i,i}}^2 - u_{i,j}u_{j,i}) = \frac{1}{2}(\parallel \Omega \parallel^2 - \parallel S \parallel^2) \tag{3.8}$$

where tensors Ω and S are the anti-symmetric and symmetric parts of the velocity gradient tensor ∇u respectively. Physically, Ω denotes vorticity rate and S represents the strain rate tensors. Therefore, in a pure irrotational straining motion $\nabla u = S$, and in the solid body rotation flow $\nabla u = \Omega$. The $\parallel \Omega \parallel$ term is the absolute value of the vorticity rate tensor Ω which is defined as $[Tr(\Omega\Omega^T]^{0.5}$, where Ω^T is transpose of Ω, and Tr, or the trace, is sum of the elements lying along the main diagonal. The term $\parallel S \parallel$ is defined similarly. Accordingly, if the strain rate is much higher than the vorticity rate ($\parallel S \parallel \gg \parallel \Omega \parallel$) shear flow is dominant. In contrast, if the rotation strength is much greater than the shear strength ($\parallel \Omega \parallel \gg \parallel S \parallel$), the flow will be highly rotational. The Q criterion can be expressed in a suitable non dimensional form by normalizing it by $\parallel S \parallel^2$. Hence the $f_{threshold}$ is defined as [43]

$$f_{threshold} = \frac{1}{2}(\frac{\parallel \Omega \parallel^2}{\parallel S \parallel^2} - 1) \tag{3.9}$$

Accordingly, irrotational flow occurs when $f_{threshold} \to -\frac{1}{2}$ and solid body rotation happens when $f_{threshold} \to \infty$. The highly coherent structure of the studied flow downstream of the balloons is illustrated in figure 3.7 for two fthreshold values of 20,000 and 5,000 respectively. The shedding swirling tube flows are clearly observed downstream of the floral unit.

Figure 3.8 illustrates the vorticity lines downstream of the floral unit of balloons. The solid lines and dashed lines, respectively, represent the positive (counter clock wise) and the negative (clock wise) values of vorticity. Five time-series snapshots are presented at each cross section to illustrate the dynamic of the flow. As is shown in figure 3.8(a), black lines with vorticity level in the range of 700–3 000 1/s are utilized to portray flow pattern on plane P_1. By moving toward downstream these lines gradually disappear so that on plane P_2 they have mostly faded (see figure 3.8(b)). As can be seen in panel (c), black lines are still observed on plane P_3, however, to show a better illustration blue lines with a lower vorticity level in the range 300–700 1/s are added to the vorticity contour. The values assigned to vorticity lines are arbitrary and one can use somewhat different ranges of vorticity magnitudes to portray the same flow pattern. Here, an effort was made to use vorticity levels that can describe the flow pattern as clearly as possible.

3.7 Force Characteristics

Force coefficients $F/0.5(\rho A_c U^a)$ are calculated using the maximum horizontal cross sectional area of a single balloon, i.e. $A_c = 7.81 \times 10^{-4} m^2$. Seeing that the force coefficients oscillate at high frequencies with time, they are simply presented in an interval of 2 seconds to enable a

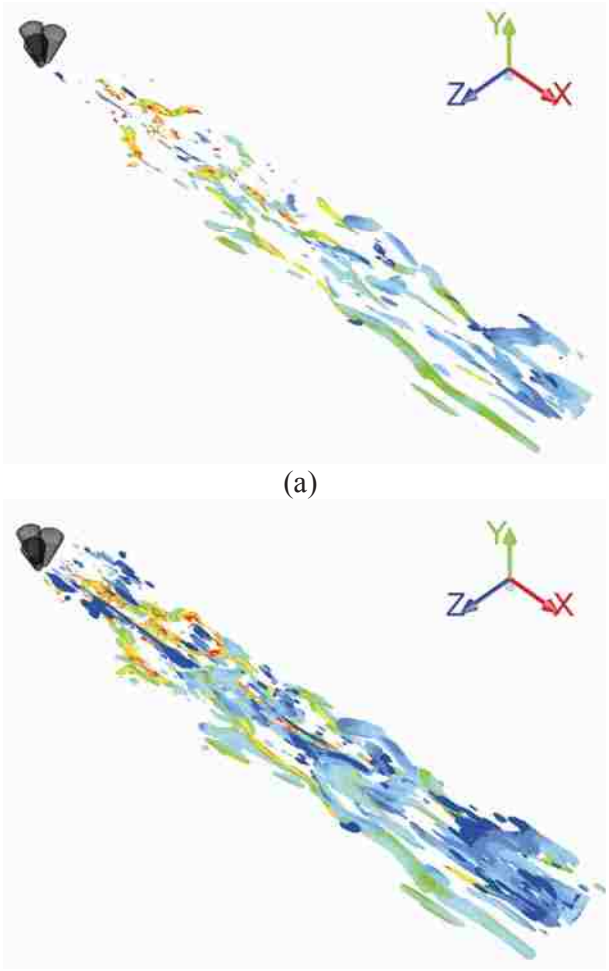

FIGURE 3.7: Cohesive structure of vortex tubes downstream of the balloons. Iso surfaces are colored by vorticity magnitude in the same range of figure 3.6. (a) $f_{threshold}$ of 20,000. (b) $f_{threshold}$ of 5,000.

closer observation. Time history of the drag coefficient of the balloons is illustrated in figure . According to panels (a) and (b), the mean values of the drag coefficient are 0.44 and 0.18 for the upstream and downstream balloons, respectively. In figure , panels (c) and (d) depict the time history of the lift coefficient of the upstream and downstream balloons with mean values of 0.14 and 0.04, respectively. The considerable difference between force coefficients of the upstream and downstream balloons is due to the closely spaced configuration of the balloons, i.e. the upstream balloon acts as a shield, protecting the downstream balloons from the direct flow. It is important to mention that figure shows statistically stationary behavior with a stable nature; confirming that the transient results have converged. The mean values of the drag and lift coefficients of the balloons are compared with those of a single balloon in tables 3.1 and 3.2 respectively. To put these values into perspective they are also compared with the values associated with the cylindrical and spherical bodies. It should be stressed that studies on these basic shapes are not under identical boundary conditions considered in this study, nonetheless, the closest ones are chosen.

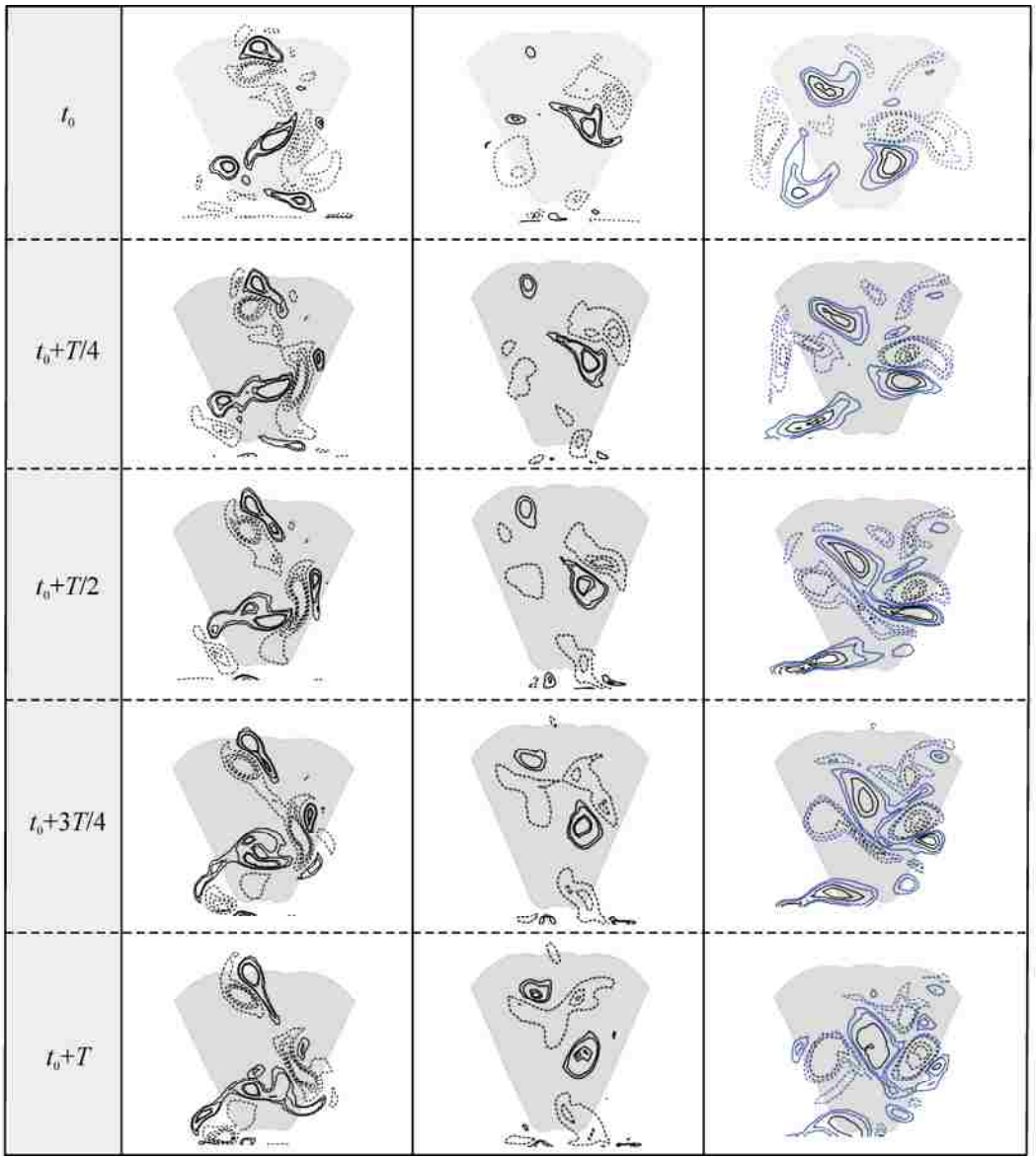

FIGURE 3.8: Time evolution of the flow pattern downstream of the floral unit of the touching balloons, vorticity level of the black and blue lines are in the range of 700–3 000 1/s, 300–700 1/s respectively; (a) plane P1 located at X=2D, (b) plane P2 located at x=4D, (c) plane P3 located at X=6D.

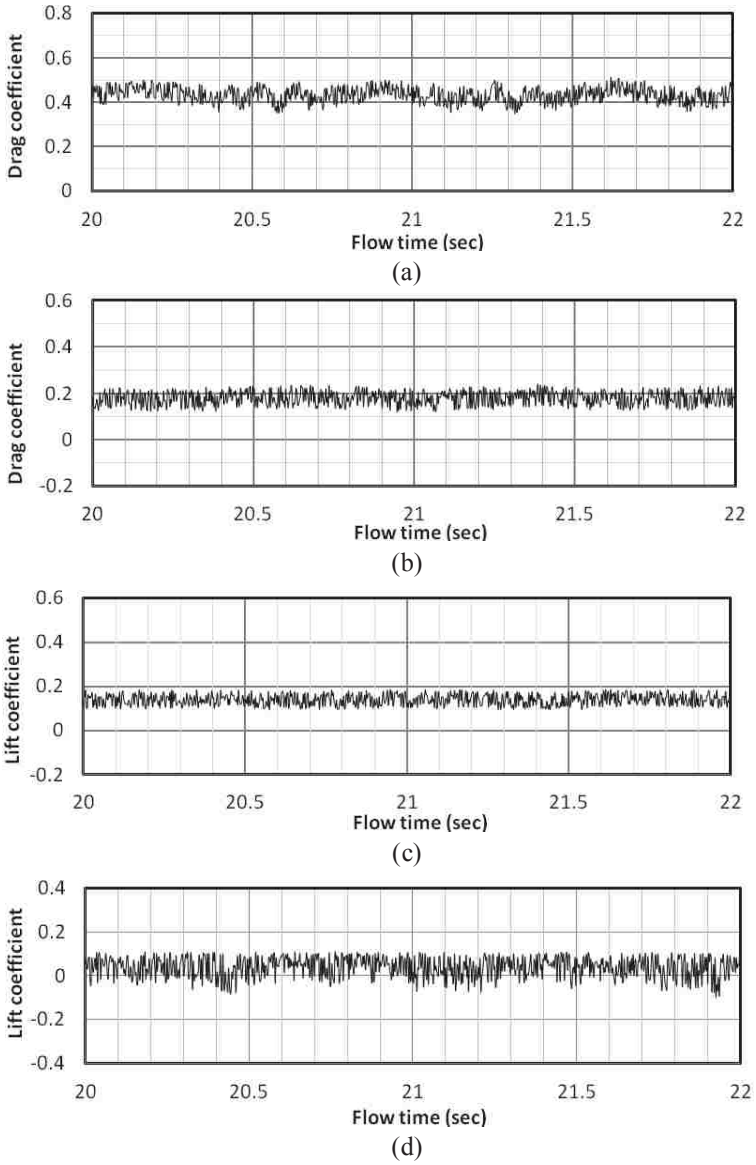

FIGURE 3.9: Time history of the drag coefficient and lift coefficient; (a) drag coefficient of the upstream balloon, (b) drag coefficient of the downstream balloon, (c) lift coefficient of the upstream balloon, (d) lift coefficient of the downstream balloon.

TABLE 3.1: The mean value of the drag coefficients applied on various bluff bodies at Re=2.3×10^5.

Single balloon (Vasel-Be-Hagh et al. [19])	Upstream balloon	Downstream balloon	Circular cylinder (Cantwell and Coles [46])	Sphere (Achenbach [45], Clift et al. [46])
0.69	0.44	0.18	$0.78 \leq C_D \leq 1.4$	0.51

TABLE 3.2: The mean value of the lift coefficients applied on various bluff bodies at Re=2.3×10^5.

Single balloon (Vasel-Be-Hagh et al. [19])	Upstream balloon	Downstream balloon	Circular cylinder (Cantwell and Coles [44])	Sphere (Achenbach [45], Clift et al. [46])
0.06	0.14	0.04	0	0

Power spectra density (PSD) of non-sinusoidal oscillations of the lift coefficients are presented in figure 3.10. Panels (a) and (b) respectively correspond to upstream and downstream balloons. These figures are plotted in log-log axes. The PSD were estimated using periodogram algorithm [47]. Two high peaks are observed in PSD of the downstream balloons at Strouhal numbers ($St = f.D/U$) of approximately 0.04 and 0.29 indicating the dominant frequencies at which the swirling-swinging tube flows are randomly shed off from the balloons. The upstream balloon is impeded by the downstream ones from generating any significant swirling tube flow to shed downstream.

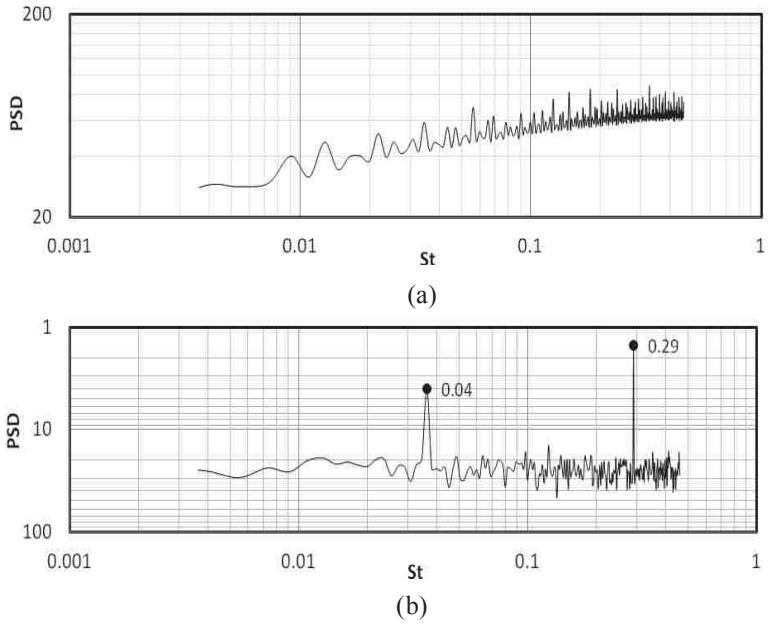

FIGURE 3.10: Power spectrum diagrams associated with the lift coefficients of the balloons; (a) upstream balloon, (b) downstream balloon.

3.8 Conclusions

Flow over a floral configuration of three touching energy storage balloons was simulated. The underwater balloons were assumed to be a droplet-shaped stationary bluff body and the free stream Reynolds number was set at 2.3×10^5. ere the key findings are summarized.

1) Flow around droplet-shaped bluff bodies generates shedding swirling-swinging tube flows. This may be attributed to the motion of fluid particles around non-equal circular sections while crossing the bluff body.

2) The swirling tube flows are found to be randomly swinging in different directions; sometimes interfering with and breaking up from each other.

3) The drag coefficient of the upstream and downstream balloons are lower than that of a single balloon when they are compared individually.

4) To compare the hydrodynamic efficiency of the floral unit of three touching balloons with a single balloon it is better to considering the touching floral unit as a single bluff body. According to Table 1, the drag coefficient of the unit is 0.8, which is not too much larger than that of a single balloon whereas it provides three times the storage capacity.

5) The frequency of the vortex tube shedding falls in the range of St $\approx$ 0–0.4 with a high peak at St $\approx$ 0.29 which is associated with the downstream balloons. The upstream balloon is blocked by the downstream ones from shedding any vortex tube.

References

[1] Denholm, P., Kulcinski, G.L., 2004. Life cycle energy requirements and greenhouse gas emissions from large scale energy storage systems. Energy Conversion and Management, 45(13-14), 2153-2172.

[2] Rahman, F., Rehman, S., Abdul-Majeed, M.A., (2012). Overview of energy storage systems for storing electricity from renewable energy sources in Saudi Arabia. Renewable and Sustainable Energy Reviews, 16(1), 274-283.

[3] Ibrahim, H., Ilinca, A., Perron, J., 2008. Energy storage systems–characteristics and comparisons. Renewable and Sustainable Energy Reviews, 12(5), 1221-1250.

[4] MacKay, D.J.C., 2008. Sustainable energy–without the hot air. Cambridge UIT Cambridge Ltd, Cambridge, England, 60-67.

[5] Cheung, B., Cao, N., Carriveau, R., Ting, D.S.-K., 2012a. Distensible air accumulators as a means of adiabatic underwater compressed air energy storage. International Journal of Environmental Studies, 69(4), 566-577.

[6] Cheung, B., Carriveau, R., Ting, D.S.-K., 2012b. Storing energy underwater. ASME Mechanical Engineering Magazine, 134(12), 38-41.

[7] Pimm, A.J., Garvey, S.D., Drew, R.J., 2011. Shape and cost analysis of pressurized fabric structures for subsea compressed air energy storage. Proceedings of the Institution of Mechanical Engineers, Part C: Journal of Mechanical Engineering Science, 225(5), 1027-1043.

[8] Pimm, A.J., Garvey, S.D., Jong, M., 2014. Design and testing of energy bags for underwater compressed air energy storage. Energy, 66, 496-508.

[9] Zhang, X., Su, Y.M., Yang, L., Wang, Z.L., 2010. Hydrodynamic performance of flapping-foil propulsion in the influence of vortices. Journal of Marine Science and Application, 9(2), 213-219.

[10] Lotfollahi Yaghin, M.A., Mojtahedi, A., Ettefagh, M.M., Aminfar, M.H., 2011. Experimental investigation of TARMAX model for modeling of hydrodynamic forces on cylinder-like structures. Journal of Marine Science and Application, 10(3), 281-288.

[11] Wang, S., Zhu, L., Zhang, X., He, G., 2011. Flow past two freely rotatable triangular cylinders in tandem arrangement. Journal of Fluids Engineering, 133(8), 081202-02.

[12] Peng, Y.F., Sau, A., Hwang, R.R., Yang, W.C., Hsieh, C.M., 2012. Criticality of flow transition behind two side-by-side elliptic cylinders. Physics of Fluids, 24(3), 1-36.

[13] Lam, K., Lin, Y.F., Zou, L., Liu, Y., 2012. Numerical study of flow patterns and force characteristics for square and rectangular cylinders with wavy surfaces. Journal of Fluids and Structures, 28(1), 359-377.

[14] Shimada, K., Ishihara, T., 2012. Predictability of unsteady two-dimensional k-ϵ model on the aerodynamic instabilities of some rectangular prisms. Journal of Fluids and Structures, 28, 20-39.

[15] Vasel-Be-Hagh, A.R., Ting, D.S.-K., Carriveau, R., 2013a. Correlating flow pattern with force coefficients in air flow past a tandem unit of three circular cylinders. International Journal of Fluid Mechanics Research, 40(3), 235-253.

[16] Taneda, S., 1978. Visual observations of the flow past a sphere at Reynolds numbers between 104 and 106. Journal of Fluid Mechanics, 85(1), 187-192.

[17] Constantinescu, G.S., Squires, K.D., 2003. LES and DES investigations of turbulent flow over a sphere at Re = 10,000. Flow, Turbulence and Combustion, 70(1-4), 267-298.

[18] El Khoury, G.K., Andersson, H.I., Pettersen, B., 2010. Cross flow past a prolate spheroid at Reynolds number of 10000. Journal of Fluid Mechanics, 659, 365-374.

[19] Vasel-Be-Hagh, A.R., Ting, D.S.-K., Carriveau, R., 2013b. Numerical simulation of flow past an underwater energy storage balloon. Computers and Fluids, 88, 272-286.

[20] Subsalve USA Corporation, 2012. Underwater lift bags. Available from *www.subsalve.com/images/Subsalve* [read on 07.06.2012].

[21] Prasanth, T.K., Behara, S., Singh, S.P., Kumar, R., Mittal, S., 2006. Effect of blockage on vortex-induced vibrations at low Reynolds numbers. Journal of Fluids and Structures, 22(6-7), 865-876.

[22] Prasanth, T.K., Mittal, S., 2008. Vortex-induced vibrations of a circular cylinder at low Reynolds numbers. Journal of Fluid Mechanics, 594, 463-491.

[23] Drescher. H., 1956. Messung der auf querangestromte zylinder ausgeubten zeitlich veranderten drucke. Zeitschrift fur Flugwissenschaften und Weltraumforschung, 4, 17-21.

[24] McGregor, D.M., Etkin, B.E., 1958. Investigation of the fluctuating pressures on a circular cylinder in an airstream. Physics of Fluids, 1(2), 162-164.

[25] Fung, Y.C., 1960. Fluctuating lift and drag acting on a cylinder in a flow at supercritical Reynolds numbers. Journal of the Aerospace Sciences, 27(11), 801-814.

[26] Schewe, G., 1983. On the force fluctuations acting on a circular cylinder in crossflow from subcritical up to transcritical Reynolds numbers. Journal of Fluid Mechanics, 133(1), 265-285.

[27] Blackburn, H.M., Melbourne, W.H., 1996. The effect of free-stream turbulence on sectional lift forces on a circular cylinder. Journal of Fluid Mechanics, 11, 267-292.

[28] Bearman, P.W., Wadcock, A.J., 1973. The interaction between a pair of circular cylinders normal to a stream. Journal of Fluid Mechanics, 61(3), 499-511.

[29] Sun, T.F., Gu, Z.F., He, D.X., Zhang, L.L., 1992. Fluctuating pressure on two circular cylinders at high Reynolds numbers. Journal of Wind Engineering and Industrial Aerodynamics, 41(1-3), 577-588.

[30] Meldi, M., Lucor, D., Sagaut, P., 2011. Is the Smagorinsky coefficient sensitive to uncertainty in the form of the energy spectrum? Physics of Fluids, 23(12), 1-14.

[31] Sagaut, P., 2006. Large eddy simulation for incompressible flows–An introduction. 3rd edition. Springer, Berlin Heidelberg, 1-556.

[32] Smagorinsky, J., 1963. General circulation experiments with the primitive equations. Monthly Weather Review, 91(3), 99-164.

[33] Chen, H.L., Dai, S.S., Li, J., Yao, X.L., 2009. Three-dimensional numerical simulation of the flow past a circular cylinder based on LES method. Journal of Marine Science and Application, 8(2), 110-116.

[34] Lilly, D.K., 1992. A proposed modification of the Germano subgrid-scale closure method. Physics of Fluids A: Fluid Dynamics, 4(3), 633-635.

[35] Germano, M., Piomelli, U., Moin, P., Cabot, W.H., 1991. A dynamic subgrid-scale eddy viscosity model. Physics of Fluids A, 3(7), 1760-1765.

[36] Mylonas, D., Sayer, P., 2012. The hydrodynamic flow around a yacht keel based on LES and DES. Ocean Engineering, 46, 18-32.

[37] Vakil, A., Green, S.I., 2009. Drag and lift coefficients of inclined finite circular cylinders at moderate Reynolds numbers. Computers and Fluids, 38(9), 1771-1781.

[38] Vakil, A., Green, S.I., 2011. Two-dimensional side-by-side circular cylinders at moderate Reynolds numbers. Computers and Fluids, 51(1), 136-144.

[39] Bao, Y., Huang, C., Zhou, D., Tu, J., Han, Z., 2012. Two-degree-of-freedom flow-induced vibrations on isolated and tandem cylinders with varying natural frequency ratios. Journal of Fluids and Structures, 35(1), 50-75.

[40] Liu, Z.G., Liu, Y., Lu, J., 2012. Fluid-structure interaction of single flexible cylinder in axial flow. Computers and Fluids, 56, 143-151.

[41] Sujudi, D., Haimes, R., 1995. Identification of swirling flow in 3-D vector fields. Cambridge, USA, Technical Report No. AIAA 95-1715, 1-8.

[42] Hunt, J.C.R., Wray, A.A., Moin, P., 1988. Eddies, streams, and convergence zones in turbulent flows. Center for Turbulence Research, Stanford University, technical report No. CTR-S88.

[43] Kamkar, S.J., Wissink, A.M., Sankaran, V., Jameson, A., 2011. Feature-driven Cartesian adaptive mesh refinement for vortex-dominated flows. Journal of Computational Physics, 230(16), 6271-6298.

[44] Cantwell, B., Coles, D., 1983. An experimental study of entrainment and transport in the turbulent near wake of a circular cylinder.Journal of Fluid Mechanics, 136, 321-374.

[45] Achenbach, E., 1972. Experiments on the flow past spheres at very high Reynolds numbers. Journal of Fluid Mechanics, 54(3), 565-575.

[46] Clift, R., Grace, J.R., Weber, M.E., 1978. Bubbles, drops, and particles Academic Press Inc, New York, United States, 97-137.

[47] Stoica, P., Moses, R., 1997. Introduction to spectral analysis. Prentice Hall Inc, Upper Saddle River, New Jersey, USA, 25-26.

Chapter 4

Flow over Submerged Energy Storage Balloons in Closely and Widely Spaced Floral Configurations

A. R. Vasel-Be-Hagh, D. S.-K. Ting, R. Carriveau

Turbulence and Energy Laboratory, Lumley Centre for Engineering Innovation, University of Windsor, Ontario, Canada N9B 3P4

Vasel-Be-Hagh, A.R., Carriveau, R., Ting, D.S.-K., 2015. Flow over Submerged Energy Storage Balloons in Closely and Widely Spaced Floral Configurations. Ocean Engineering, 95, 59-77.

4.1 Introduction

The renewable energy industry in general, and the wind energy in particular, has made significant progress in recent years. Wind energy production in the USA experienced a 28 fold increase from 1998 to 2011 with production capacity reaching 46,919 MW (Statistics of wind energy in USA, [1]). In the same period, the wind energy production capacity in Canada increased to 5265 MW, i.e. more than 210 times what was produced at the beginning of the year 1998 (Statistics of wind energy in Canada, [2]). Despite this significant expansion, many notable challenges still remain. One of which includes the efficient management of supply and demand. That is, in contrast to fossil-fueled power plants, prevalent renewables like wind and solar are inherently intermittent and peak supply is often temporally out of phase with peak demand. Furthermore,

grid congestion and stability issues can prevent the delivery of power to the grid [3]. Energy storage plants are viable options to overcome these issues and make intermittents dispatchable. One of the most efficient and environmentally friendly technologies is compressed air energy storage (CAES), which is driven by a modification of basic gas turbine technology [4]. CAES boasts a potentially long service life of approximately 40 years and high energy efficiency of 71% [5]. However, the application of this underground storage system is limited to regulation of the onshore wind power stations [6] while a significant portion of the wind-based power is generated by the offshore wind farms across the world, e.g. Denmark is generating up to 30% of its total electric power by offshore wind farms [7]. To add to this, North America is currently gearing up to make a significant entry into offshore wind. Subsequently, a new energy storage system based on CAES for application in the seas has been developed [8-11]. In this storage plant, namely under water CAES or UWCAES, the surplus electrical energy generated in the off-peak hours is utilized to compress air into submerged distensible accumulators. The accumulators are moored to the sea floor; hence, the stored air is under hydrostatic pressure, ready to be released back to the surface to drive turbines to supply the electrical grid when needed (see figure 4.1). A successful Pilot Experiment in Lake Ontario [10] has lead to design and construction of two planned demonstration facilities to be deployed at fresh and salt water sites.

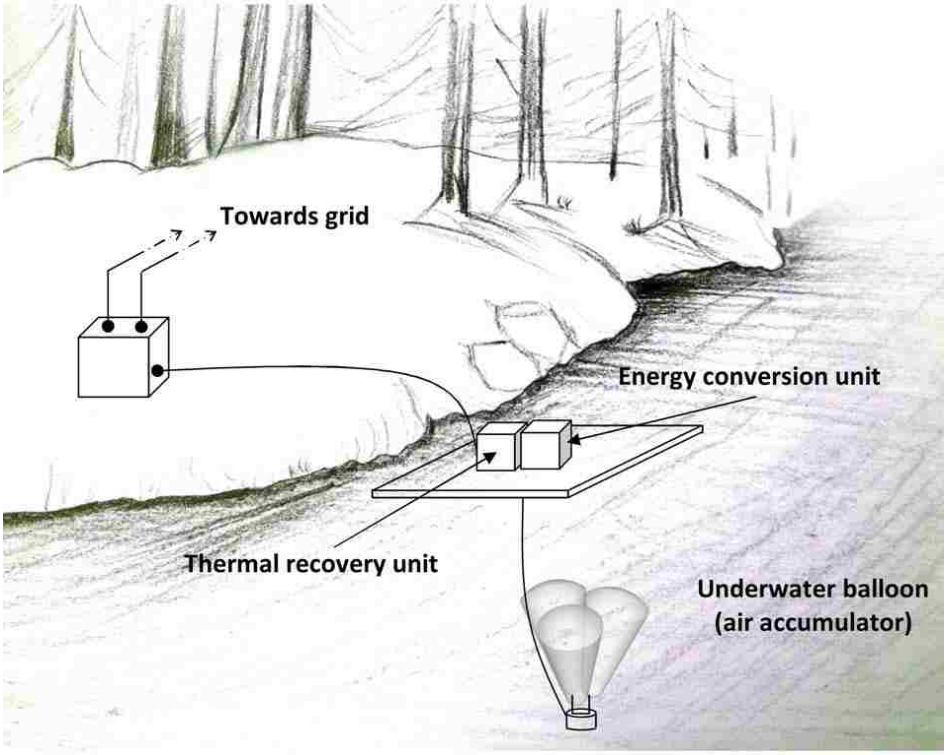

FIGURE 4.1: Typical underwater compressed air energy storage plant; the accumulator unit consists of three distensible balloons arranged in floral configuration.

To perform the role of distensible energy accumulator marine salvage balloons were chosen for their market availability and robust nature. The PF20000 model of Professional (PF) lift bags manufactured by SUBSALVE USA CORPORATION were chosen as the base accumulator unit of the UWCAES system owing to their optimal size and flexible rigging points. The general

droplet shape of PF lift balloons with various sizes are compared with an average human body in figure 4.2. To develop more innovative and cost-effective designs for the foundations and support structures of the accumulator units, it is necessary to provide a credible estimate of hydrodynamic loading [12-13]. There has been a significant progress in understanding of fluid-structure interactions over the last couple of decades. The focus, however, has been limited to flow over circular cylinders [14-22], square cylinders [23-26], rectangular cylinders [27-30] and elliptical cylinders [31]; these are all primarily two-dimensional studies. There are also several three-dimensional studies but they are mostly concerned with the flow over regular shapes such as spheres [32-36], circular cylinders [37-42] and square cylinders [43]. Our review on flow over bluff bodies appeared to indicate a dearth of published research exploring the cross-flow over droplet-shaped bluff bodies. Hence, at the first step, the fundamental case of flow over a single isolated balloon was studied [44] and then the current numerical study was carried out to examine the practical case of flow over floral units of balloons. Developing a good understanding of the force characteristics and the structure of this flow is an essential part of this project. Due to the absence of any experimental evidence, simulations were carried out using both URANS and LES turbulence models to validate the results. To assert the verification of the numerical methodology, the turbulence model features were discussed as well as the numerical code qualifications. Grid independence was assessed for both URANS and LES simulations separately. Furthermore, for the LES simulation the grid size was compared with LES filter width, and y^+ in close proximity to the balloons surfaces was set to be in accordance with what is recommended for an LES simulation in the literature.

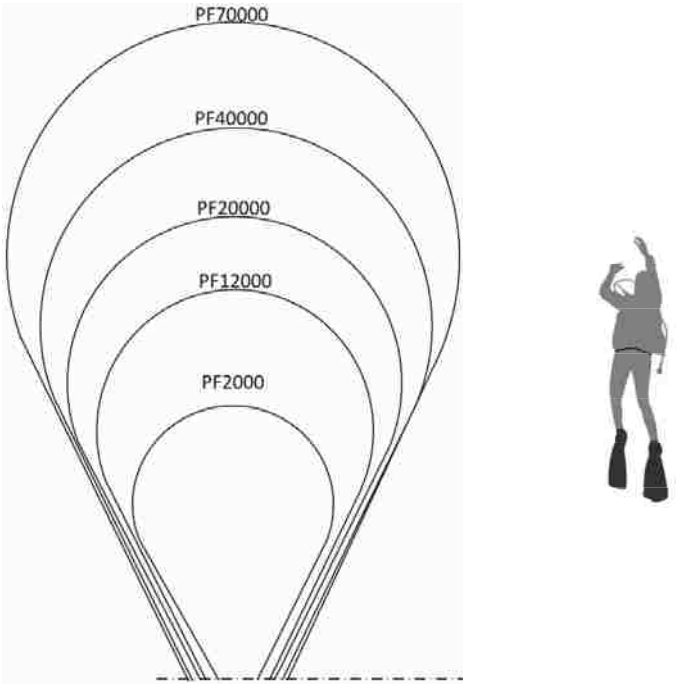

FIGURE 4.2: An approximate comparison between dimensions of different underwater balloons of the professional (PF) series manufactured by SUBSALVE USA CORPORATION. The PF20000 model was applied in the present application.

4.2 Computational Details

In order to decrease computational expenses, dimensions of the PF20000 balloon are scaled down by a factor of 100. As the force coefficients are functions of Reynolds number, the free stream velocity is scaled up 100 times to retain the same Reynolds number. Dimensions of the scaled balloon are presented in figure 4.3. Original dimensions of the PF20000 balloon are reported in inches in the Subsalve USA Corporation manual [45]; therefore, in figure 4.3 the scaled dimensions are presented in both meters and inches (inch values in brackets) to ensure the decimal accuracy.

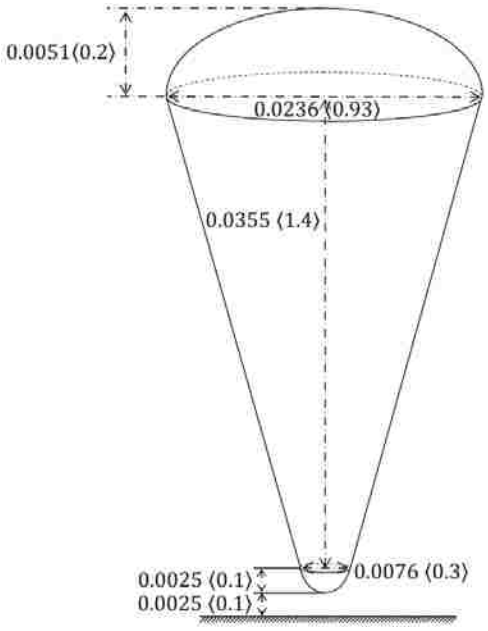

FIGURE 4.3: Scaled down PF20000 balloon. Values are in meters, the bracketed values are in inches.

In figure 4.4, panels (a) and (b) respectively depict two limiting states of closely and widely spaced floral configurations of the balloons. The symmetry axis of each balloon is limited through external supports to make an angle of $\theta = 10°C$ and $\theta = 30°C$ with the vertical direction. The dimensions of the supports are negligible compared to the balloons dimensions; therefore, their influence is expected to be minimal. For the two cases considered in this study, the floral units of the balloons are perfectly symmetric about X-axis (the flow direction); therefore, all characteristics of the two downstream balloons are identical. Accordingly, only one data set is presented for both of them.

In this paper, the characteristic diameter used to define the Reynolds number is expressed as

$$D = \frac{6 \times V}{A} \tag{4.1}$$

where V and A are volume and surface area of a single balloon respectively. Accordingly, for the scaled down PF20000 balloon depicted in figure 4.3, the characteristic diameter D is

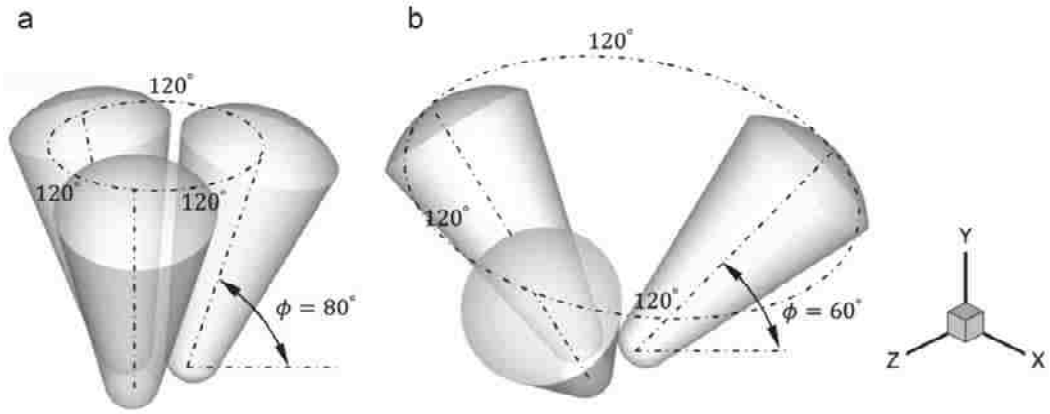

FIGURE 4.4: (a) Closely spaced configuration of the balloons, (b) widely spaced configuration of the balloons. Water flows in the X direction.

2.311×10^{-2}m $\langle 0.91 \rangle$. Dimensions of the computational domain are provided in terms of the characteristics diameter D in figure 4.5. As is shown, length, height and width of the computational area are $40D$, $11D$ and $13.2D$ respectively. The balloon is located $7.7D$ downstream of the inlet boundary. There is an approximate distance of $0.1D$ between the lowest point of the floral unit and the solid bed. It should be mentioned that the reference of the coordinate system used in this study is fixed underneath the center of the unit on the bed surface; accordingly the center of the bottom of the unit is at $(0, 0.1D, 0)$.

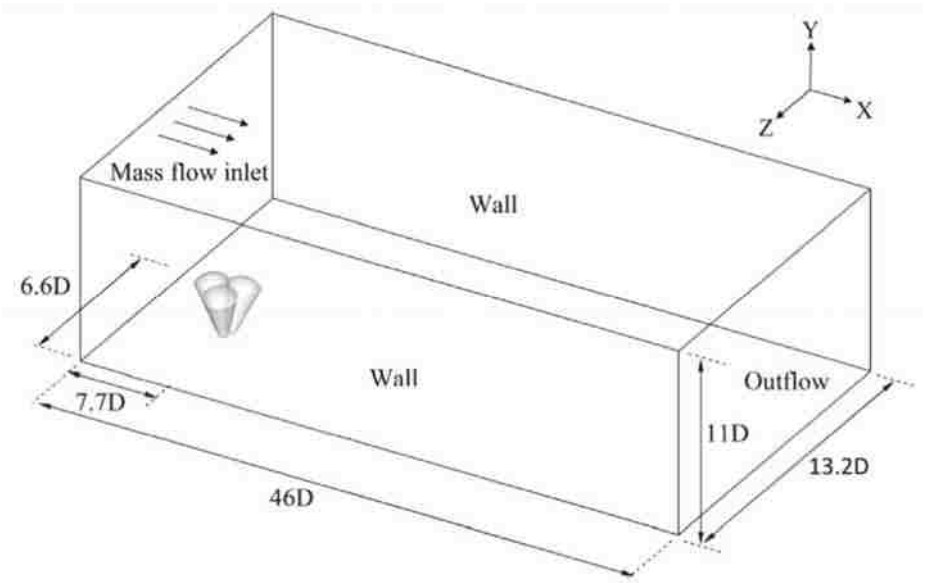

FIGURE 4.5: Boundary conditions and dimensions of the computational domain in terms of the characteristics diameter D.

The three boundary conditions applied in the current simulation are also described in figure 4.5. Mass-flow-inlet condition with mass flow rate of 888.5 kg/s is set at the inlet boundary, resulting

in a Reynolds number of 2.3×10^5. The outflow boundary condition has a flow rate weighting of 1 used at the outlet of the computational domain, as it is the only outlet of the domain. In the real application the accumulator unit is installed under deep water, therefore, to be in exact accordance with the real case a free surface condition should be applied on the top boundary of the computational domain. However, because of the considerable depth of water, this boundary condition is not expected to significantly affect the physical behavior of the flow over the balloons. Consequently, to avoid extra computational expenses of this boundary condition we employed the no slip condition on the top boundary. The no slip boundary condition is also applied at all solid-liquid interferences including side and bottom walls of the computational domain and the surface of the balloon, which is here assumed rigid (non-distensible). According to figure 4.5, the blockage ratios of the closely and widely spaced configurations are 1.7 and 2.4% respectively; indicating the negligible effect of the no slip boundary condition of the side walls on the physics of the flow around the balloons.

4.3 Numerical Methodology

The present numerical simulation was conducted using both URANS k–ω and LES Dyna–SM turbulence models to assess the validity of results. In the LES turbulence model physical diffusion is significantly affected by numerical diffusion, consequently, the central differencing is a suitable approach to conduct the spatial discretization. However, in the central differencing scheme there is no numerical damping, therefore, the numerical fluctuations affect the physical ones. Fortunately, the Fluent code obviates this issue by changing the spatial discretization scheme from the central differencing to one the upwind schemes for any oscillation with a wavelength less than twice the local grid spacing. This feature was the main motivation to conduct the current simulation with the Fluent code. Moreover, several researchers already verified the accuracy of the Fluent LES and URANS models in simulating flow over different bluff bodies, e.g. [46-60]. The LES and URANS models used in the present work were similar to those described in Vasel-Be-Hagh et al. [44]. See Vasel-Be-Hagh et al. [44] for details about governing equations and numerical methodology.

4.4 Mesh

To have an efficient control of the mesh density the present computational domain was divided into 27 blocks. In the central block that contains the floral unit of the balloons an unstructured mesh was generated using the T–Grid type of Tet–hybrid cells, dimensions of this block was set to be $4D \times 4D \times 2D$ where D is the characteristic diameter. In all other blocks the cooper type of hex-wedge cells was used to establish a structured mesh. This mesh was created using GAMBIT 2.3.16. Isometric, +X, +Y and +Z views of the mesh are illustrated in figure 4.6.

Separate mesh-independence analyses were carried out for both closely and widely spaced cases to validate the accuracy of the computations done by URANS and LES models. The mesh study

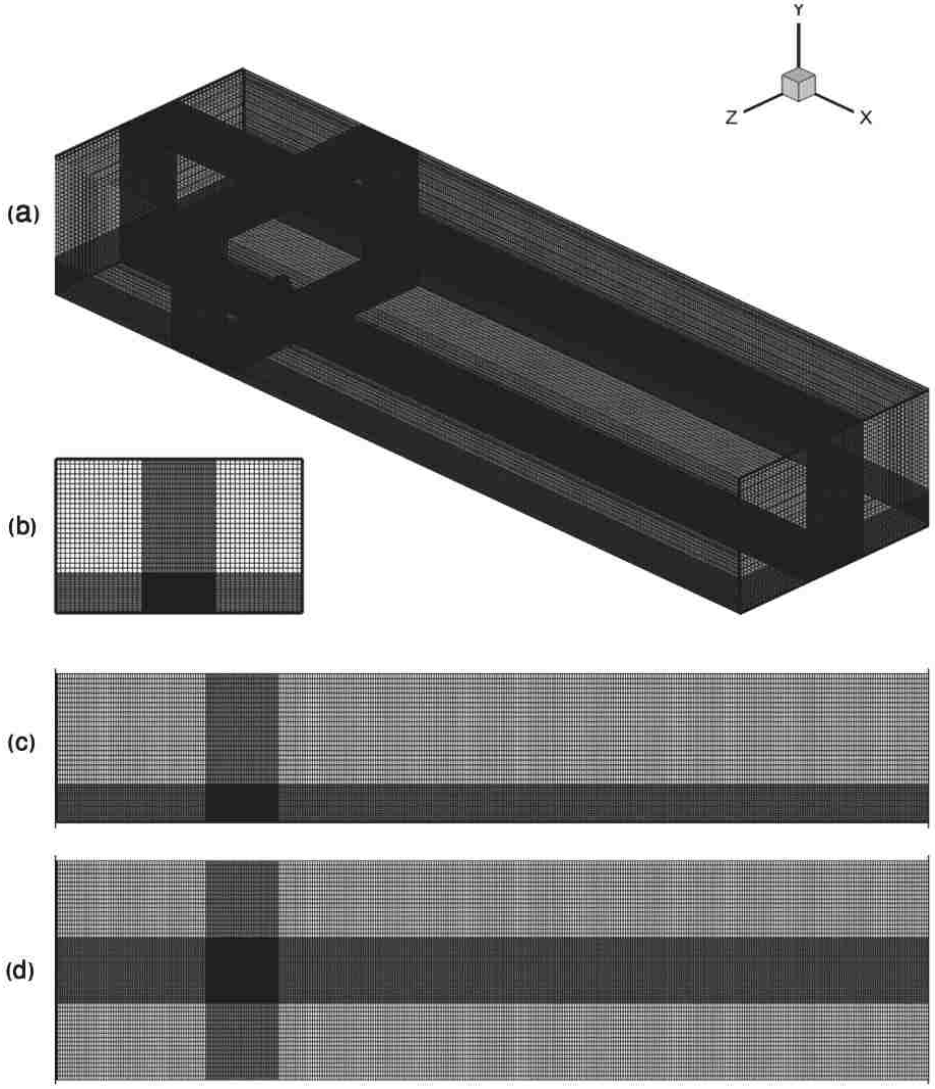

FIGURE 4.6: Panels (a), (b), (c) and (d) illustrate isometric, +X, +Y and +Z views of the mesh respectively.

was conducted by calculating the mean force coefficients of each balloon for different numbers of cells.

Figure 4.7 depicts the effect of the mesh density on the force coefficients of the balloons in the closely spaced configuration. Panel (a) depicts the effects of mesh density on the force coefficients calculated by URANS turbulence model. The drag coefficient of the upstream balloon appeared to be more sensitive compared to the other force coefficients; however, beyond 3.1 million cells it is almost independent of cell size. Hence, a mesh with 3.6 million cells was generated for the URANS simulation of flow over the closely spaced configuration. Panel (b) shows the variation of the force coefficients calculated by LES turbulence model with mesh density. Meldi et al.[61] demonstrated that a filter width of $\triangle = L/55$ is the limit for the correct application of Smagorinsky subgrid scale model where L is the large scale and approximately equals to the balloon height ($\approx$2D) in the current case. Accordingly, the central block with dimensions of $4D \times 4D \times 2D$ should contain

approximately $(4 \times 55/2) \times (4 \times 55/2) \times (2 \times 55/2) \approx 660{,}000$ cells to assure that the grid size is smaller than the LES filter width required for the Smagorinsky subgrid scale model. Other blocks have two edges in common with the central one, so the grid size in those blocks can be controlled just in one direction. Generating cells in those blocks with aspect ratios of 5, 4 and 3 respectively ends in the total number of 6, 8 and 12 million cells. As is observed in panel (b), beyond 6 million cells the force coefficients of the balloons do not significantly vary with mesh size, accordingly, grid with 7.8 million cells was used to conduct the LES simulation of flow over the closely spaced case. In figure 4.7(b) only the last three meshes with approximately 6, 8 and 12 million cells fulfil the Meldi et al.'s [61] criterion.

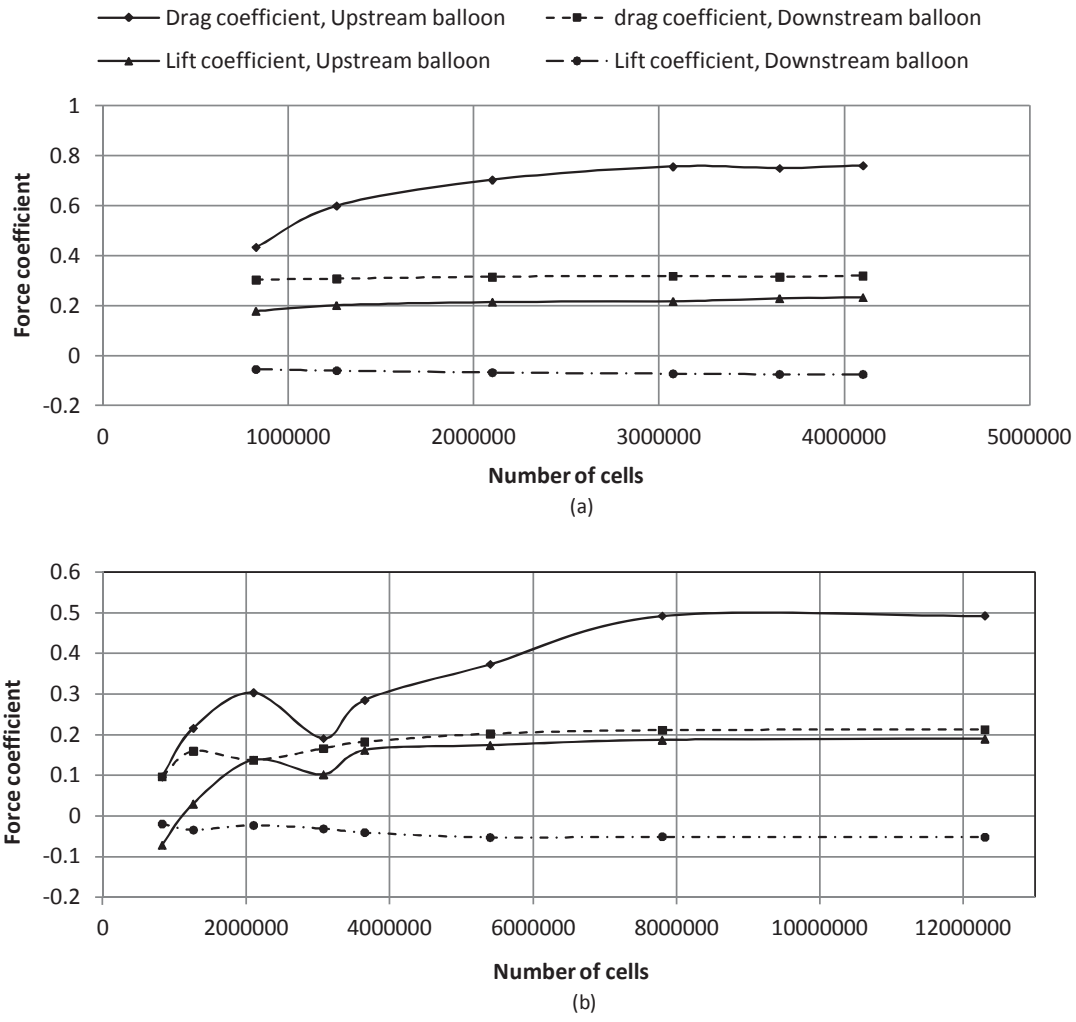

FIGURE 4.7: Mesh independence study for the closely spaced configuration; (a) force coefficients predicted by URANS k-ω versus number of cells, (b) force coefficients predicted by LES Dyna–SM versus number of cells.

Figure 4.8 illustrates variation of the force coefficients of the balloons with mesh refinement for the widely spaced configuration. Panel (a) illustrates the force coefficients calculated by URANS versus total number of cells. As is observed the absolute value of the force coefficients initially increases with number of cells, however, once the number of cells goes beyond approximately 3

million force coefficients tends toward constant values. Hence, mesh with 3 million cells was used to conduct the URANS simulation of flow over the widely spaced case. Panel (b) presents LES predictions of the force coefficients in different mesh densities. The LES mesh was generated similar to the closely spaced case; the mesh independency was achieved once the number of cells exceeds 6 million. So the mesh with 7.8 million cells was applied for the LES simulation of the flow around widely spaced case.

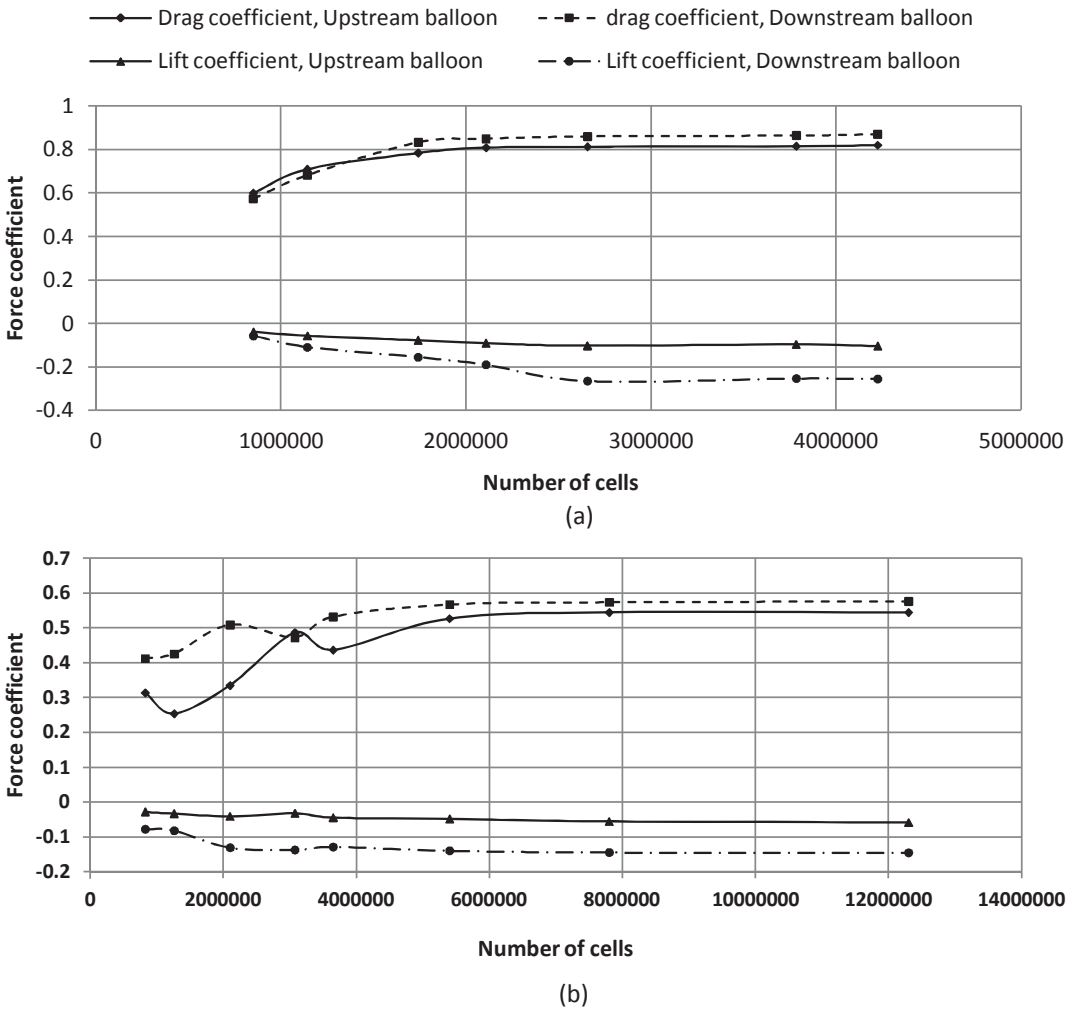

FIGURE 4.8: Mesh independence study for the widely spaced configuration; (a) force coefficients predicted by URANS k–ω versus number of cells, (b) force coefficients predicted by LES Dyna–SM versus number of cells.

In the LES model of the Fluent code the wall boundary condition is implemented using the law-of-the-wall approach. Accordingly, there is a logarithmic relation between $u^+ = u/u_\tau$ and $y^+ = y \times u_\tau/\nu$ where $u_\tau = \sqrt{\tau_w/\rho}$ is the friction velocity. In which τ_w and ρ are wall shear stress and density of the fluid respectively. Therefore, there are no computational restrictions on the near wall mesh density, however, it is strongly recommended to use mesh spacing on the order of $y^+ = 1$ [62]. In the current LES simulations, a mesh with a y^+ of approximately 1 was adopted near the balloons surfaces. The URANS simulations were conducted utilizing a mesh with a

near wall density on the order of $y^+ \approx 30$. Figure 4.9 shows a close up of the present mesh on a two-dimensional plane perpendicular to the Y axis at Y=0.3D. In this figure, the unstructured mesh in the near vicinity of one of the downstream balloons is illustrated. The non-uniformity of the structured mesh density in the two neighboring regions is due to their connections to the unstructured cells.

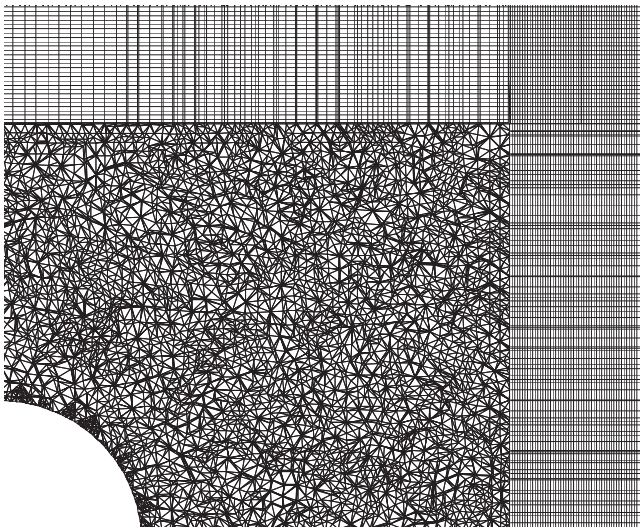

FIGURE 4.9: Two-dimensional view of the local mesh near the vicinity of one of the balloons. Plane is perpendicular to the Y axis at Y=0.3D.

4.5 Results and Discussion

In this section, the structure of the flow downstream of the floral unit of the balloons is taken into consideration first, and then force characteristics predicted by LES and K–ω turbulence models are compared and discussed. Before discussing the structure of the flow it is first worthwhile to recall that the flow patterns presented herein are associated with the scaled down geometry given in §4.2, not the full size balloon in the real application. Although force characteristics are only functions of Reynolds number, flow pattern details may change with scaling even if the Reynolds number remains constant.

4.5.1 Structure of the Flow

The discussion below tries to provide some insights into underlying physics of the flow pattern by considering the motion of fluid particles around the balloon. Consider the schematic motion of two typical particles a and b around a cylindrical surface element illustrated in figure 4.10(a). Since these particles are moving at the same linear and angular velocities $\omega = V/r$, the $\overline{ab}$ line leaves the surface with no spin on X axis; it simply moves side to side in the wake of the cylindrical surface. Figure 4.10(b) shows the motion of these particles around a surface element of a droplet–shaped body. In this case the particles are moving around unequal curves,

consequently, the angular velocity of particle b is higher than the angular velocity of particle a. So particle b turns around the surface ahead of particle a, and gradually rotates the $\overline{ab}$ line. Therefore, the $\overline{ab}$ line leaving the leeward surface has a swirling motion in addition to its sideward motion in the wake of the droplet-shaped body. This Coriolis effect on the surface elements can generate vortical cores on the leeward surface. These vortical cores swirl the flow and form shedding vortex tubes downstream of the bluff body. In the case of a spherical surface, the link $\overline{ab}$ tends to rotate about both X and Y axes; this leads to the formation of vortex rings downstream of the sphere. These vortex rings are well described by Howe et al. [63].

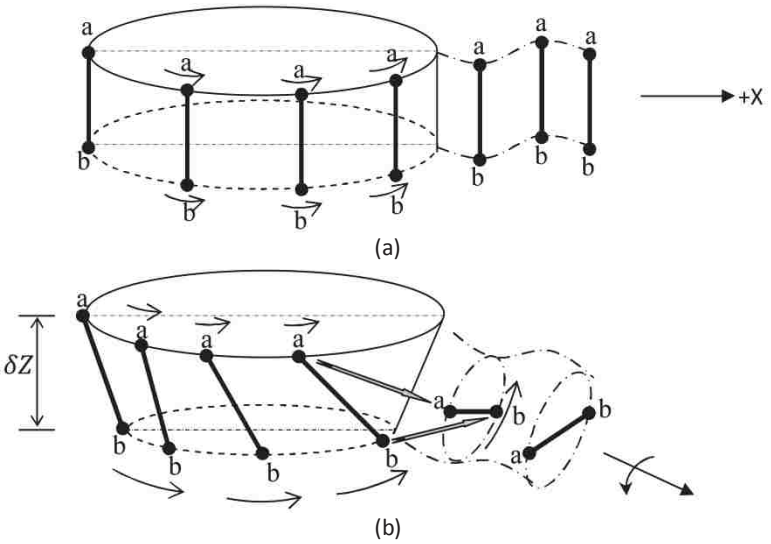

FIGURE 4.10: The schematic motion of two typical particles around the surface; (a) cylindrical surface element, (b) surface element of a droplet-shaped body.

Iso-surfaces of the second invariant of the velocity gradient, namely the Q criterion proposed by Hunt et al. [63] are used to investigate these vortical cores on the leeward surface of the balloons. The Q criterion is defined as

$$Q \equiv \frac{1}{2}({u_{i,i}}^2 - u_{i,j}u_{j,i}) = \frac{1}{2}(\parallel \Omega \parallel^2 - \parallel S \parallel^2) \tag{4.2}$$

where tensors Ω and S are the anti-symmetric and symmetric parts of the velocity gradient tensor ∇u respectively. Physically, Ω denotes vorticity rate and S represents the strain rate tensors. Therefore, in a pure irrotational straining motion $\nabla u = S$, and in the solid body rotation flow $\nabla u = \Omega$. The $\parallel \Omega \parallel$ term is the absolute value of the vorticity rate tensor Ω which is defined as $[Tr(\Omega\Omega^T]^{0.5}$, where Ω^T is transpose of Ω, and Tr, or the trace, is sum of the elements lying along the main diagonal. The term $\parallel S \parallel$ is defined similarly. Accordingly, if the strain rate is much higher than the vorticity rate ($\parallel S \parallel \gg \parallel \Omega \parallel$) shear flow is dominant. In contrast, if the rotation strength is much greater than the shear strength ($\parallel \Omega \parallel \gg \parallel S \parallel$), the flow will be highly rotational. Truesdell [65] defined a kinematic vorticity number in the non-dimensional form of $N_k = \parallel \Omega \parallel / \parallel S \parallel$ to evaluate the degree of rotation. Accordingly, for a kinematic vorticity

number of zero $N_k = 0$, the flow is irrotational, and if it approaches infinity $N_k \to \infty$ a solid body rotational flow occurs.

Instantaneous +X, +Y and isometric views of iso-surfaces of the Q criterion are illiustrated in figure 4.11 in the range of $1 \times 10^6 \leq Q \leq 3 \times 10^6$ for the closely spaced configuration. Panel (a) shows the iso-surface associated with Q=3×10^6 indicating a highly rotational region on the leeward surface of the downstream balloons (the circled region). In this region the kinematic vorticity number N_k is roughly 3200 indicating that the flow tends toward rigidly rotating. As it is depicted in panel (b), when Q criterion is decreased to 2×10^6 some other highly rotational cores with the kinematic vorticity number N_k of approximately 2500 are revealed on the lower part of the backside surface of the downstream balloons. The next strongly rotational core is observed roughly at the middle of the leeward surface of them as illustrated by the iso-surface of Q=3×10^6, see panel (c). The kinematic vorticity number N_k is around 1300 in this region.

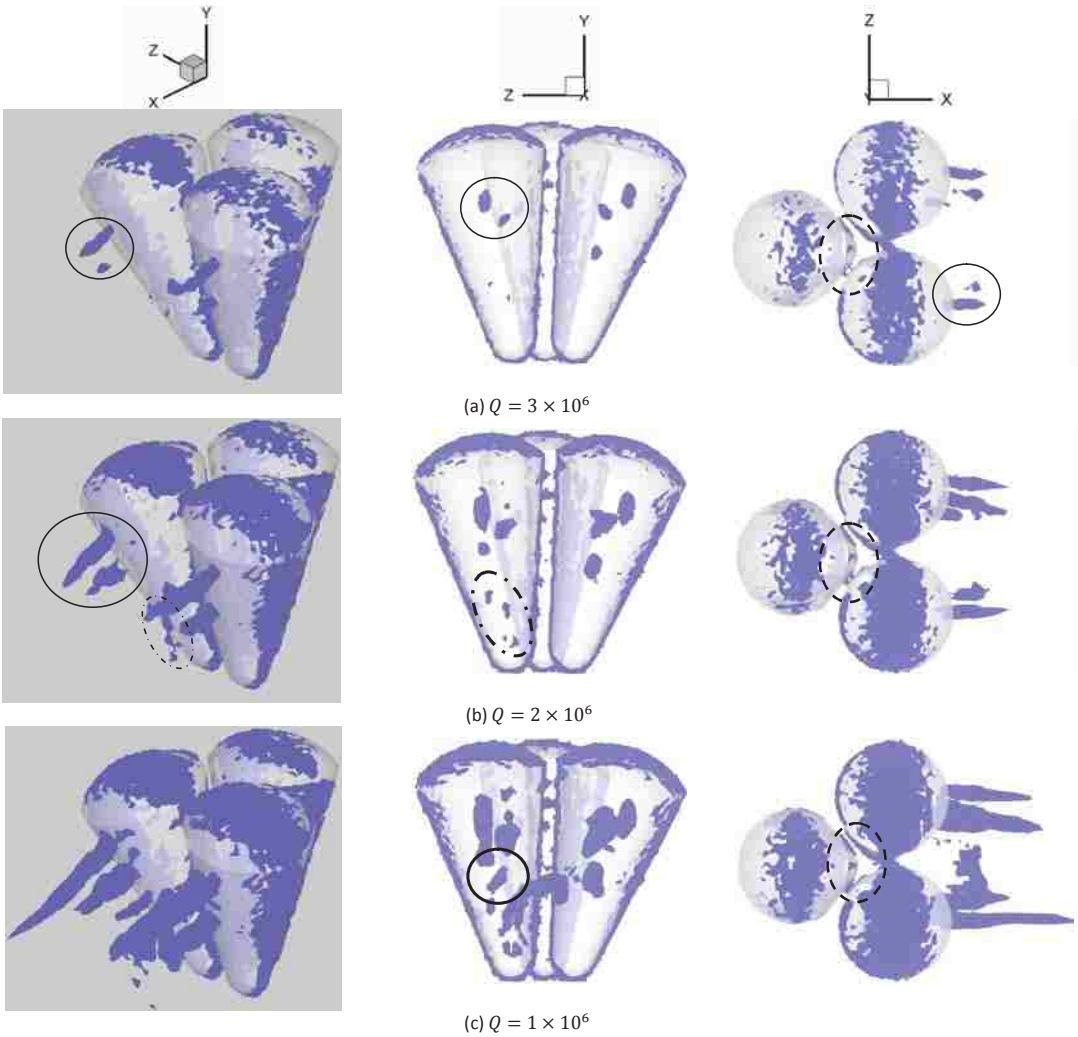

FIGURE 4.11: Q criterion iso-surfaces downstream of the closely spaced configuration of the balloons.

Figure 4.12 depicts instantaneous iso-surfaces of the Q criterion downstream of the widely spaced configuration of the balloons in the same range of Q as the closely spaced case, i.e. $1 \times 10^6 \leq$ Q $\leq 3 \times 10^6$. Panel (a), associated with value of Q=3×10^6, shows two side-by-side highly rotaional cores on the top of the leeward surface of the upstream balloon. In addition, two other vortical cores are observed on the surface of the each of the downstream balloons; one on the top and the other one on the middle of the backside. In these regions the kinematic vorticity number N_k is indicating that the flow could be approaching rigid body rotation. When the Q criterion is decreased to 2×10^6 another highly rotational core with the kinematic vorticity number N_k of approximately 1750 is reveald on the backside of the downstream balloons between two previous ones (see panel (b)). The next strongly rotational region on the lower part of leeward surface of the downstream balloons is shown in panel (c) through iso-surface of Q= 1×10^6. The kinematic vorticity number N_k is around 1200 in this region. The existence of the observed swirling flows had been already predicted by Sujudi and Haimes [64]. They developed a mathematical algorithm based on critical point theory to identify the center of three-dimensional swirling flows. The critical points are defined as points where the stream line slope is indeterminate and the velocity is zero relative to appropriate observer [65]. They tested their algorithm for flow past an infinite tapering surface and found several vortical cores on or very close to the surface. They also showed the corresponding swirling flows. They mathematically proved that the structure of the vortical cores and the correspond swirling flows are very coherent for strong swirls.

To put the strength of the vortical cores identyfied in the current study into perspective, their Q criterion values should be considered in comparison with those of well known classical flows. Hence, the literature was examined for Q criterion studies of related geometries. Many researchers who used Q criterion iso-surfaces to identify vortical flows did not report the value correspond to those iso-surfaces [66-73]. They simply used the Q criterion iso surfaces to qualitatively show the structure of the flow. However, there were several studies in which the Q value was given. Although the given values are arbitrary and one can use different Q values to illustrate the same flow pattern; these values should be on the same order of magnitude as used in these studies. For instance, Krajnovic and Basara [74] studied flow around a finite circular cylinder at a Reynolds number of 2×10^4 and reported a value of Q=1.3×10^5 for the most rotational regions, i. e. at edges of the free end. Zhou et al. [75] studied the flat-plate boundary layer transition process at Reynolds number of 5×10^4 through representing isosurfaces of Q=10. Paik and Sotiropoulos [76] used Q criterion isosurfaces with value of 50 to depict vortices in turbulent swirling flow through an abrupt axisymmetric expansion at Re=3×10^4. Omori et al. [77] illustrated the vortex structure in shearless and sheared flow past a circular cylinder at Re of 3800 by means of isosurfaces of Q=10. Morton and Yarusevych [78] and Kotou et al. [79] calculated a Q criterion on the order of 10^{-3} for flow over a step circular cylinder and a sphere at Reynolds numbers of 300 and 400 respectively. For more reviews, see [80-87]. According to the available literature, the Q criterion in the close vicinity of the leeward surface of the balloons is orders of magnitude larger than what has been reported for the classical cases indicating that the flow downstream of the balloon is significantly more rotational.

The vortical cores detected on the leeward surfaces of the balloons generate shedding vortex tubes. These vortex tubes swirl the flow downstream of the balloons. Instantaneous three-dimensional pathlines serve as useful visual aids in the pattern analysis of these turbuent swirling

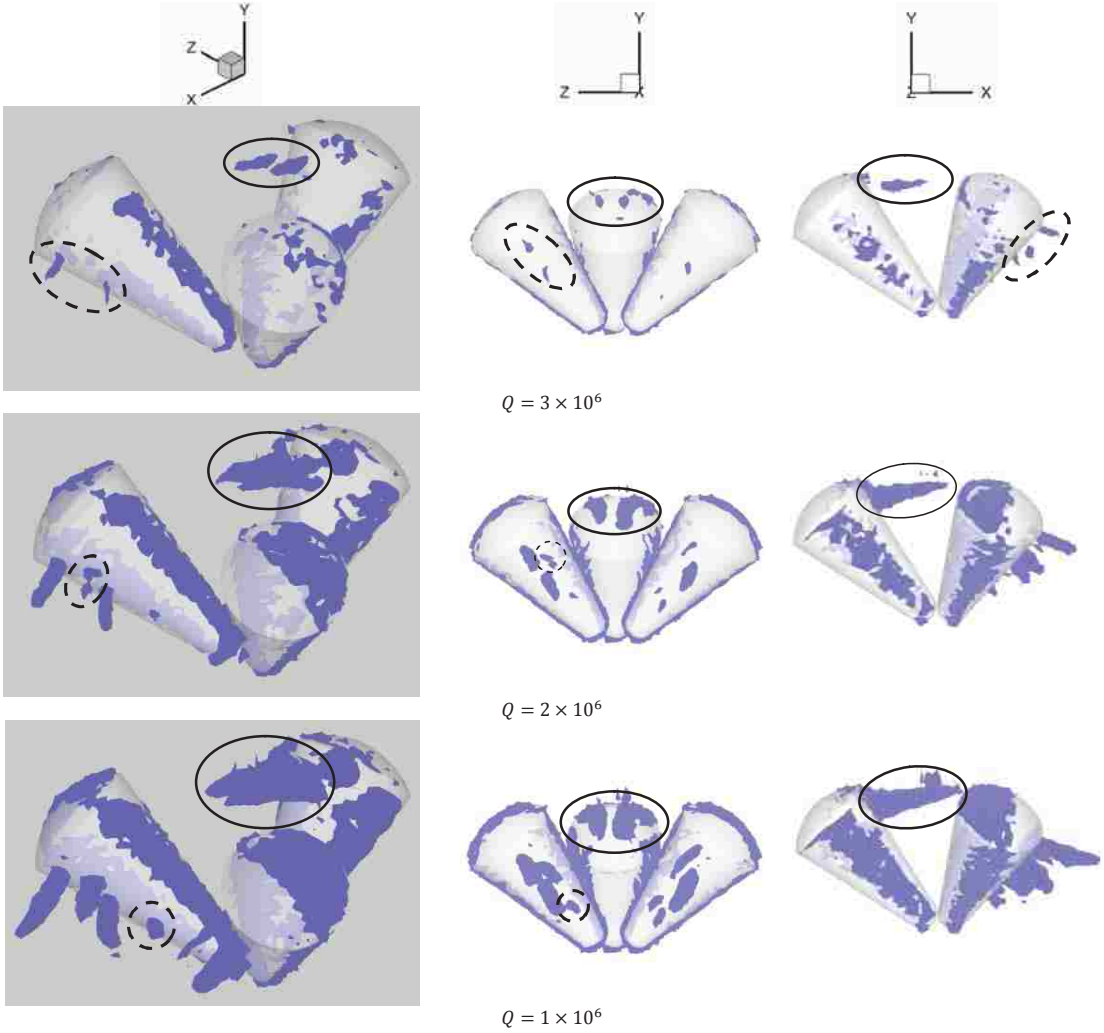

FIGURE 4.12: Q criterion iso-surfaces downstream of the widely spaced configuration of the balloons.

flows. Pathlines correspond to the closed and wide configurations are respectively illustrated in figures 4.13 and 4.14. Pathlines are coloured by vorticity magnitude. The strongest swirling tube flows generated by the exteremly vortical cores illustrated in figures 4.11 and 4.12 are clearly observed here.

As can be seen in figure 4.13, in the closely spaced configuration, the upstream balloon is impeded by the downstream ones from generating any significant swirling tube flow. On the other hand, the downstream balloons produce several swirling tube flows which are appear to be randomly moving in different directions. It is observed that these swirling motions are mostly sourced from the middle and top of the leeward surface of the downstream balloons, where vortical cores are more concentrated (see figure 4.11). In contrast to the closely spaced case, in the wide configuration of the balloons, two side by side swirling tube flows are observed on the top of the leeward surface of the upstream balloon (see figure 4.14). Compared to the closed configuration,

two swirling tube flows generated by the each of the downstream balloons are moving wider, with less effect on each other (see figures 4.13(d) and 4.14(d)).

Accompanying these swirling motions in which fluid particles perform full rotations around the vortex tubes axes, there are also some partial revolving motions due to the change of the swirling tube flows direction. The swirling tube flows are found to be randomly moving in different directions sometimes interfering with, and breaking up from each other. Although the directions of these flows are always changing chaotically, their sources appear fixed on the leeward surface of the balloon, i.e. a kind of three-dimensional non-ordered swinging motion. To visualize the swinging motion of the tube flows it would be more revealing if we look at the time evolution of the tube flows cross sections. Hence, vorticity lines are depicted on four vertical planes (P_1,...,P_4) parallel to the Y–Z reference plane, that is at X=$2D$, $3D$, $4D$ and $5D$ downstream of the floral units of the balloons. These two-dimensional contours on the planes perpendicular to the flow direction illustrate the cross sections of the swirling tube flows, which due to their turbulent dynamic nature are non-circular loops.

Figure 4.15 illustrates the vorticity lines downstream of the closed configuration of the floral unit of the balloons. The solid lines and dashed lines, respectively, represent the positive (counter clock wise) and the negative (clock wise) values of vorticity. Five time-series snapshots are presented at each cross section to illustrate the flow pattern evolution. As is shown in figure 4.15(a), black lines with vorticity levels in the range of $2000 \sim 4500$ 1/s are utilized to portray flow pattern on the plane P_1. By moving in the downstream direction, these lines gradually disappear so that on the plane P_2 they are mostly faded (see figure 4.15(b)). Consequently, blue lines with a lower vorticity level in the range of $1500 \sim 2000$ 1/s are used to depict flow pattern on the plane P_2. As can be seen in panel (c), blue lines are still observed on plane P_3, however, to show a better illustration of flow pattern evolution red lines with vorticity level in the range of $1100 \sim 1500$ are added to the vorticity contour on this plane (see figure 4.15(d)). The assigned values are arbitrary and one can use different vorticity magnitudes to portray the flow pattern, however, they will be around the same range. Here, an effort was made to use vorticity levels that can describe the flow pattern as clearly as possible.

The two-dimensional vorticity contours downstream of the wide configuration of the balloons are illustrated in figure 4.16. Like the closely spaced case, five instantaneous snapshots of flow pattern are presented for each cross section, however, in these snapshots the vorticity level of the black, blue and red lines are in the narrower ranges of $1500 \sim 2300$ 1/s, $1000 \sim 1500$ 1/s and $700 \sim 1000$ 1/s respectively. In figure 4.16(a) flow pattern is portrayed on the plane P_1 through black lines. These lines slowly fade away as we move downstream so that at plane P_2 black lines have mostly disappeard. Therefore, as it is shown in figure 4.16(b), blue lines with a lower vorticity level are utilized to illustrate flow pattern on the plane P_2. According to figure 4.16(c), black lines are barely visible on the plane P_3, however, blue lines are still observed. By moving a little farther downstream, blue lines have mostly faded and black line vortices have completely dissipated (see figure 4.16(d)), consequently red lines with a lower level of vorticity were added to show the weaker vortices. Progressively decreasing vorticity levels can be used as we move downstream to trace the flow pattern until the vortices are dissipated.

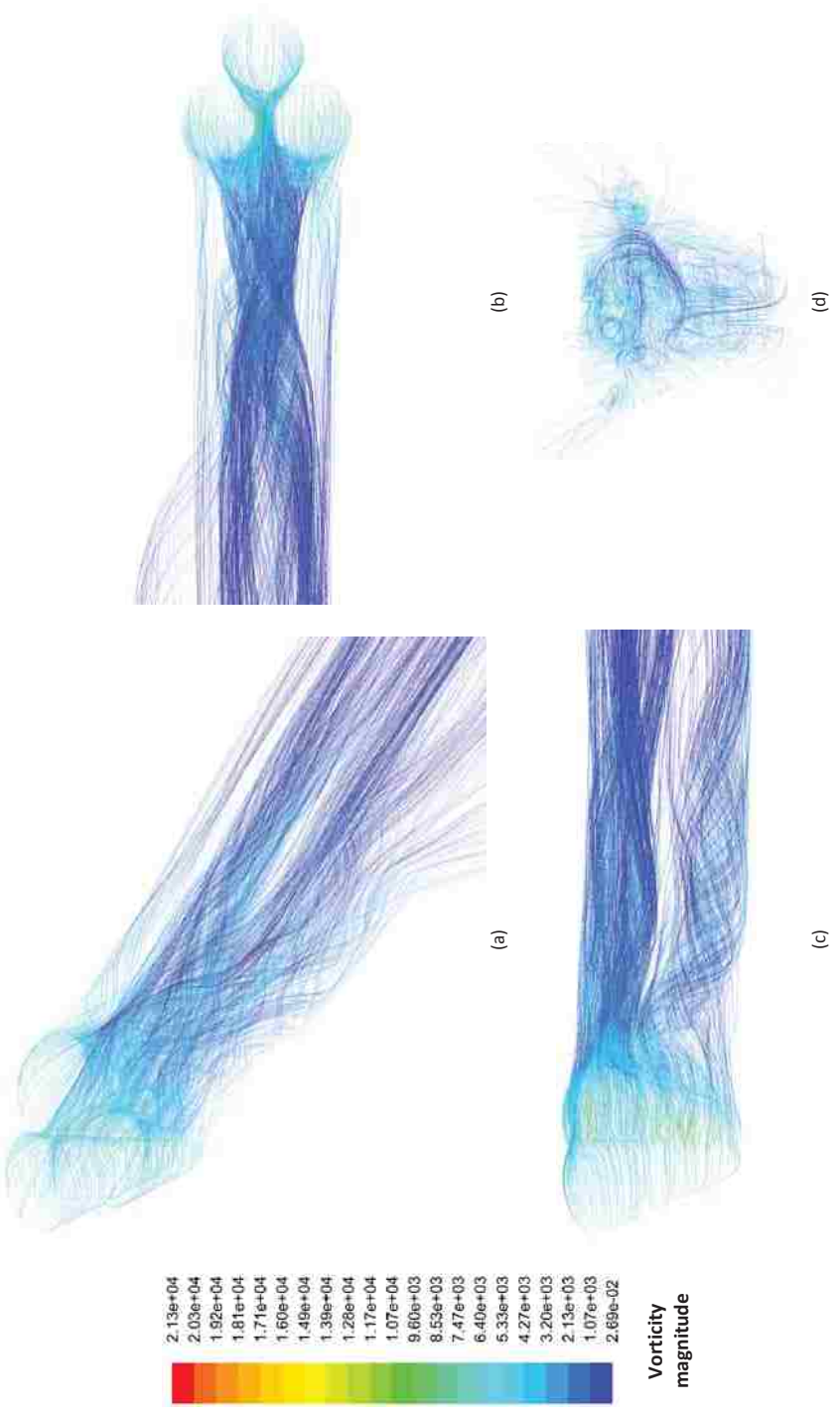

FIGURE 4.13: Three-dimensional pathlines downstream of the balloons in the closely spaced configuration. Pathlines are colored by vorticity magnitude in 1/s.

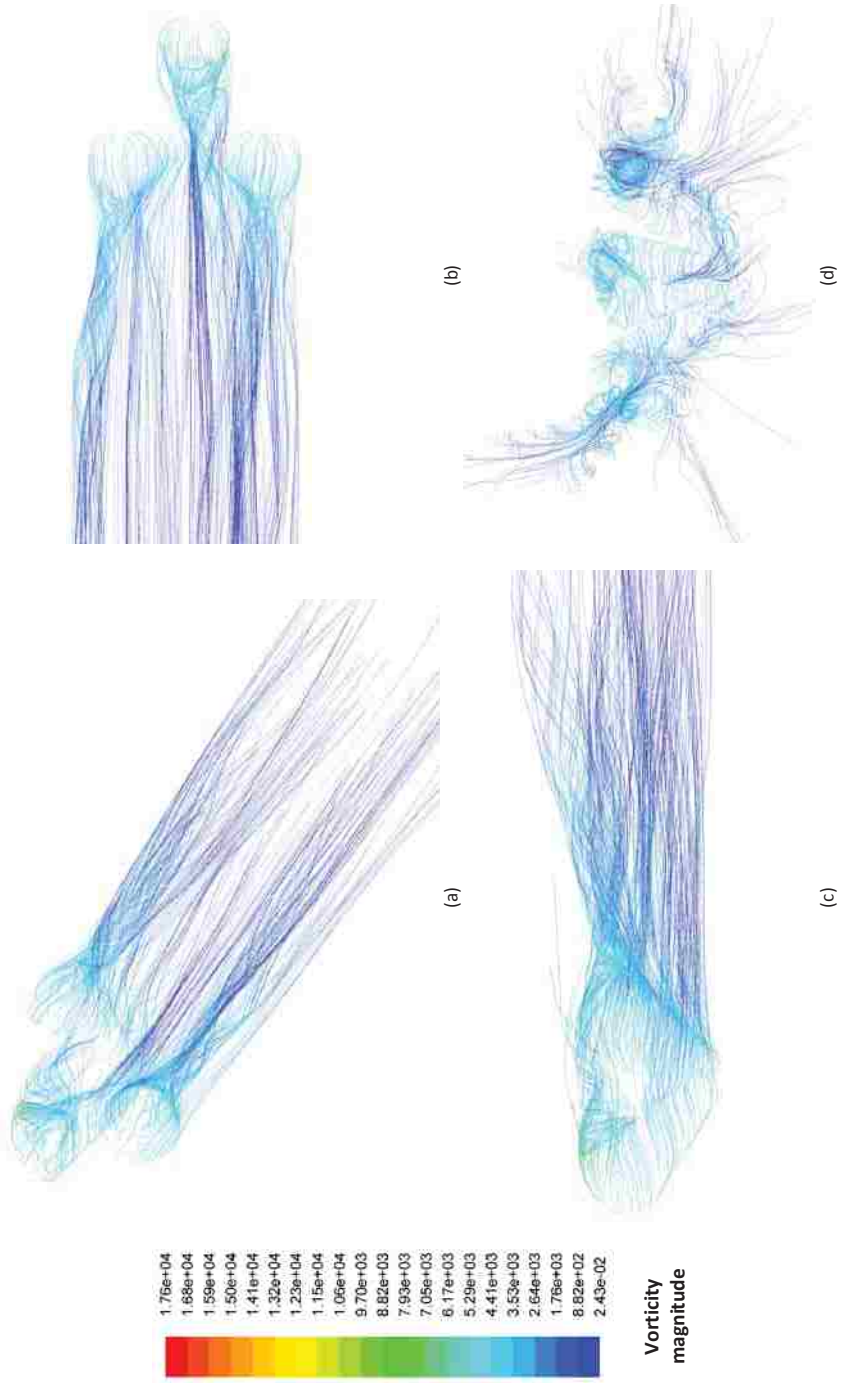

FIGURE 4.14: Three-dimensional pathlines downstream of the balloons in the widely spaced configuration. Pathlines are colored by vorticity magnitude in 1/s.

The irregular chaotic time evolutions illustrated in figures 4.15 and 4.15 represent the turbulent swinging motions of the swirling tube flows in random directions. Basically, the balloons cause two simultaneous movements in the crossing fluid flow; fluid particles are rotating in vortices depicted in figures 4.15 and 4.15, at the same time they are in chaotic translations described in the time-series snapshots.

4.5.2 Force Characteristics

Force characteristics are calculated using two turbulence models; URANS with sub model of k–ω, and LES with sub-grid model of Dyna–SM. Force coefficients $F/0.5(\rho A_c U^a)$ are calculated using the maximum vertical cross sectional area of a single balloon, i.e. $A_c = 7.81 \times 10^{-4} m^2 \langle 1.1 \rangle$.

4.5.2.1 URANS Results

Figures 4.17 and 4.18 illustrate URANS prediction of the force coefficient time histories correspond to the closed and wide configurations respectively. These figures indicate that URANS gives an almost steady periodic prediction for the force coefficients; after some initial instabilities, all cases go into weak steady oscillations with very small amplitudes in the order of 10^{-2} and low frequencies in the range of $St \approx 10^{-3} \sim 10^{-2}$. To enable a closer observation, all force coefficients have been magnified between 15 and 20s times in figures 4.17 and 4.18. This steady priodic prediction seems to be far away from the turbulent nature of such high-Reynolds number flow crossing the complex arrangement of three droplet shaped bluff bodies. This failure to capture the flow oscillations is due to a limitation of the URANS turbulence model that is the governing equations are only resolved for the mean values, and all turbulence length scales are modeled through sub models. Accordingly, the mean values provided by URANS should be considered reliable even in such high Reynolds numbers. Catalano et al. [88] examined this by studying flow over a single circular cylinder at Reynolds numbers of 5×10^5 and 10^6. They showed that the mean values of the force coefficients obtained by URANS k–ω and also LES are in good accordance with the experimental results for their bluff body flow.

In figure 4.17, panels (a) and (b) depict the URANS prediction for the time history of the drag coefficients respectively correspond to the upstream and downstream balloons in the closely spaced configuration. Accordingly, the mean values of the upstream and downstream balloons drag coefficients are approximately 0.76 and 0.32. This considerable difference is due to the closed arrangement of the balloons, i.e. in the closely spaced arrangement, the upstream balloon acts as a shield and protects the downstream balloon from the flow; this causes the drag coefficient of the downstream balloons to significantly decrease. Panels (c) and (d) illustrate the time convergence history of the lift coefficients of the upstream and downstream balloons respectively. The mean values of the lift coefficient of the upstream and downstream balloons are 0.23 and -0.08; similar to the drag coefficient, the lift coefficient of the upstream balloon is larger than the downstream one. The negative sign indicates the downward direction.

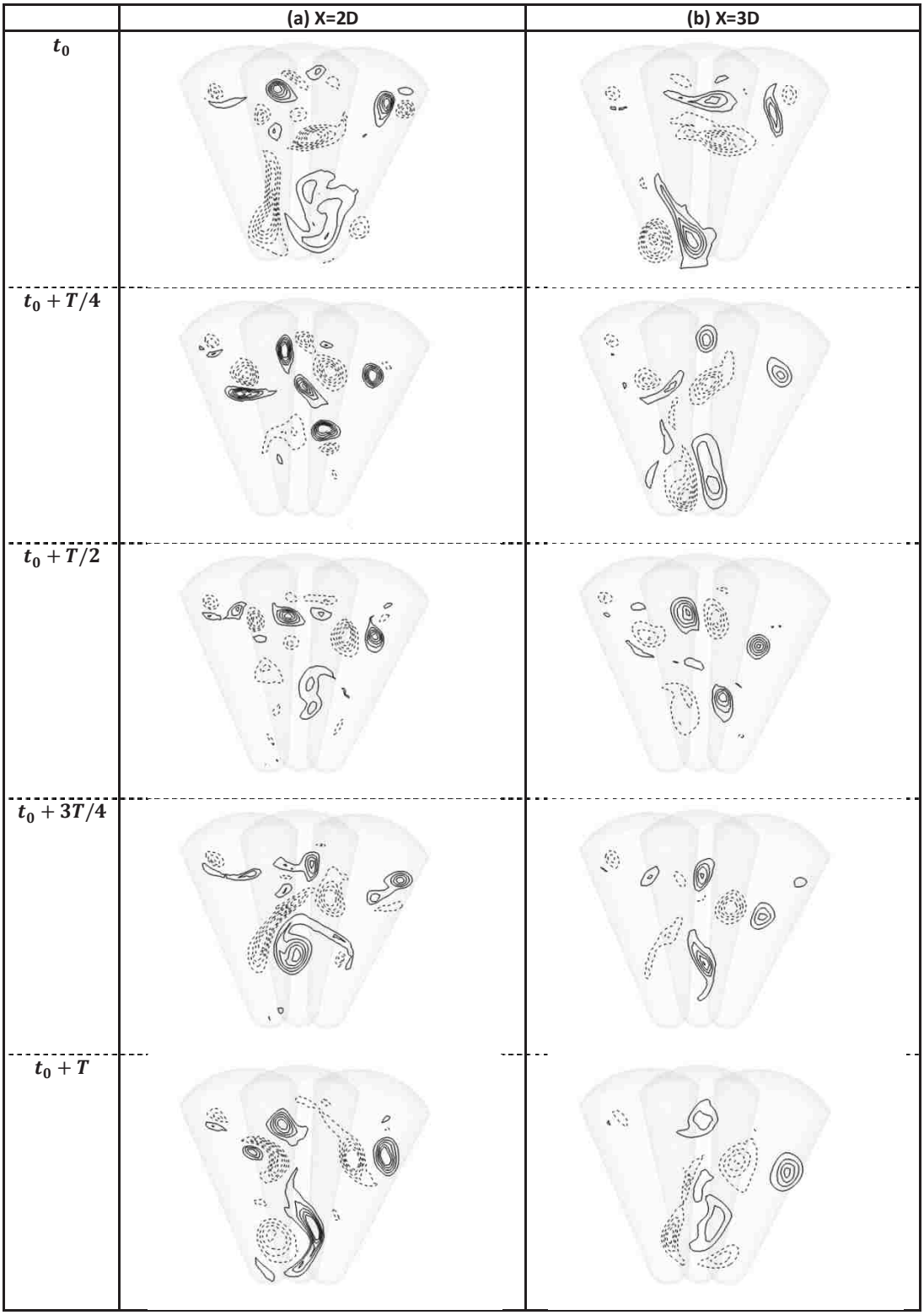

FIGURE 4.15: Time evolution of the flow pattern downstream of the floral unit of the balloons in the closely spaced configuration. Vorticity level of the black, blue and red lines are in the range of 2000∼4500 1/s, 1500∼2000 1/s and 1100∼1500 1/s respectively; (a) plane P_1 located at $X = D$, (b) plane P_2 located at $X = 2D$, (c) plane P_3 located at $X = 3D$, (d) plane P_4 located at $X = 4D$.

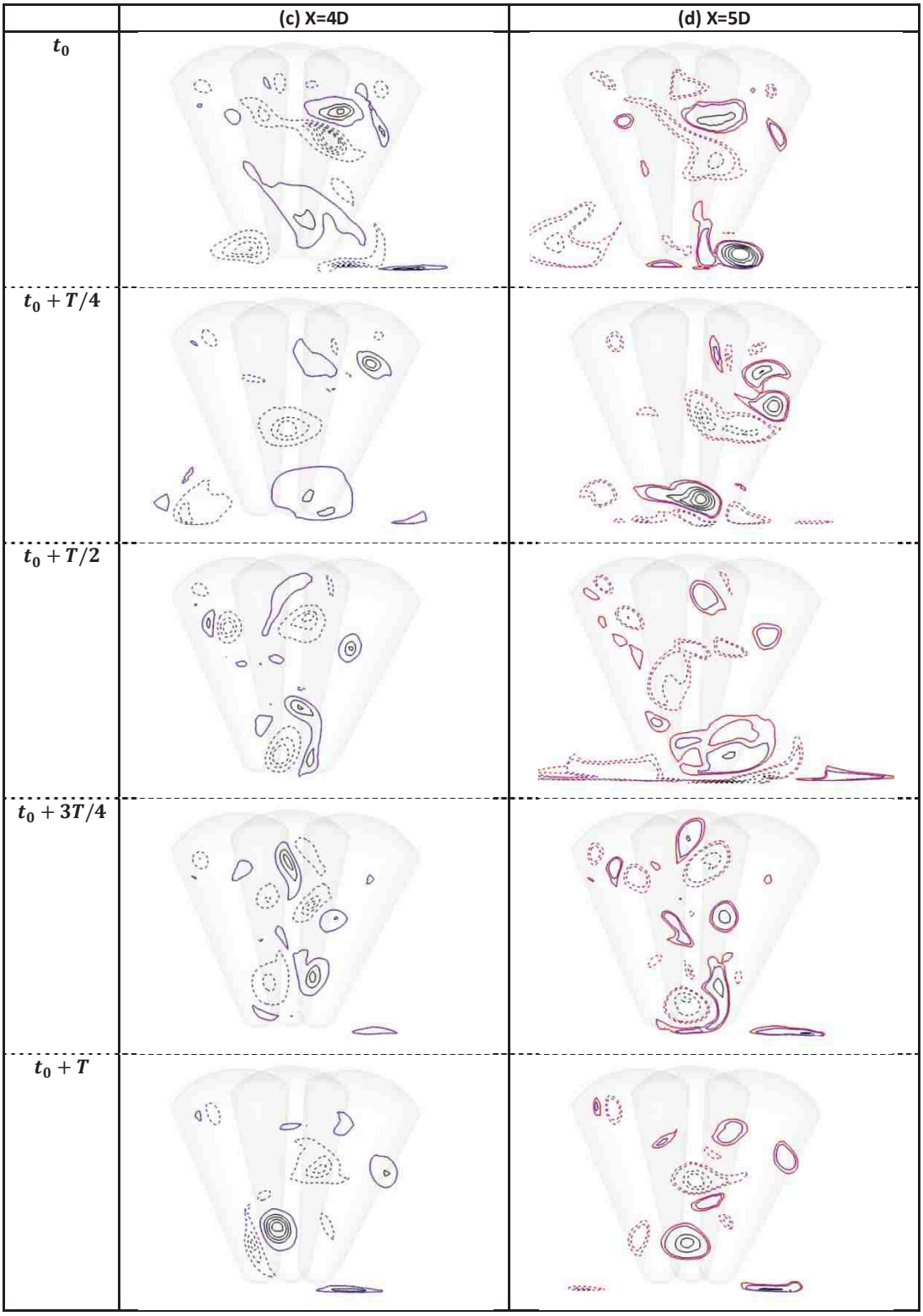

FIGURE 4.15: (continued)

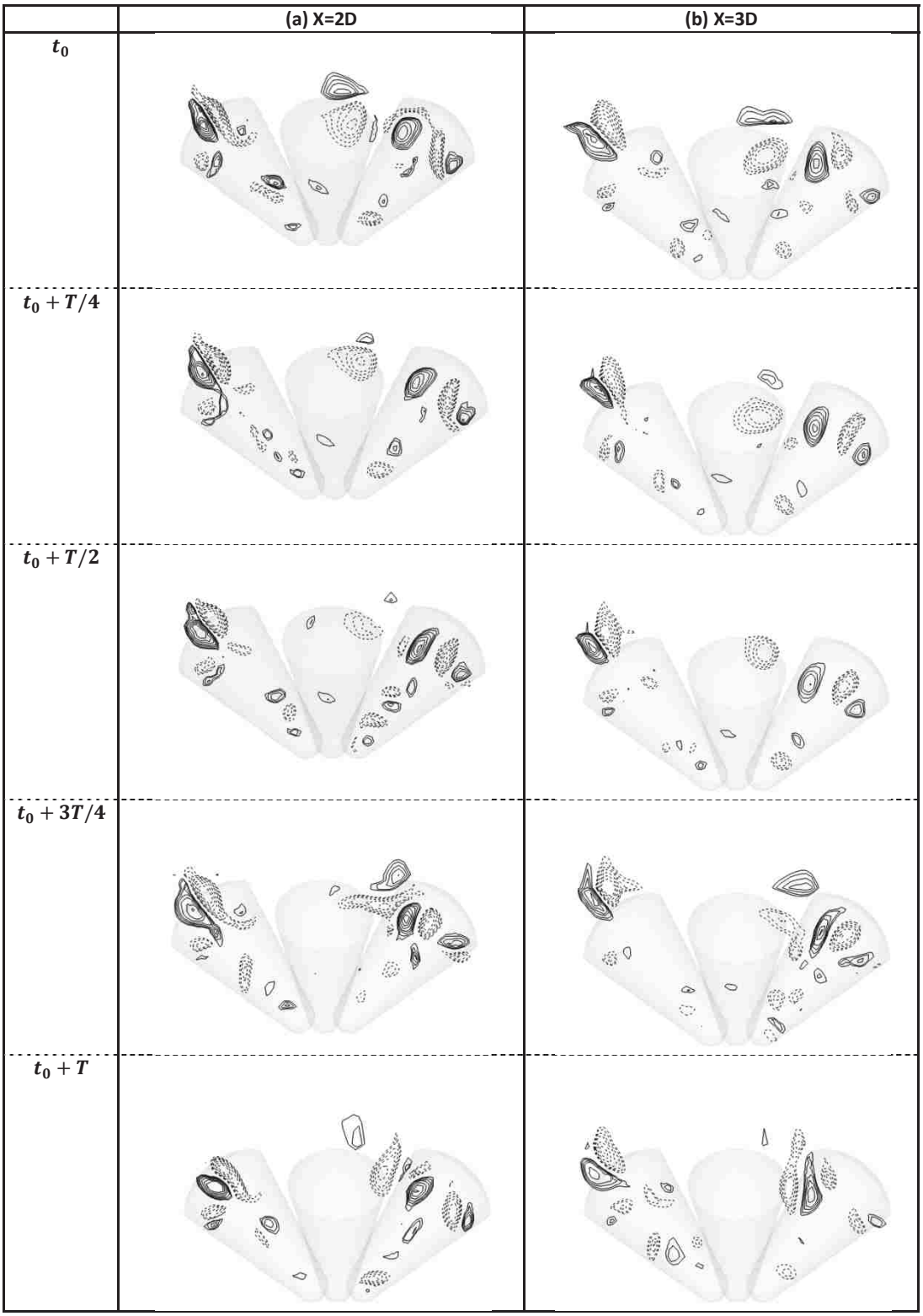

FIGURE 4.16: Time evolution of the flow pattern downstream of the floral unit of the balloons in the widely spaced configuration. Vorticity level of the black, blue and red lines are in the range of 1500∼2300 1/s, 1000∼1500 1/s and 700∼1000 1/s respectively; (a) plane P_1 located at $X = D$, (b) plane P_1 located at $X = 2D$, (c) plane P_1 located at $X = 3D$, (d) plane P_1 located at $X = 4D$.

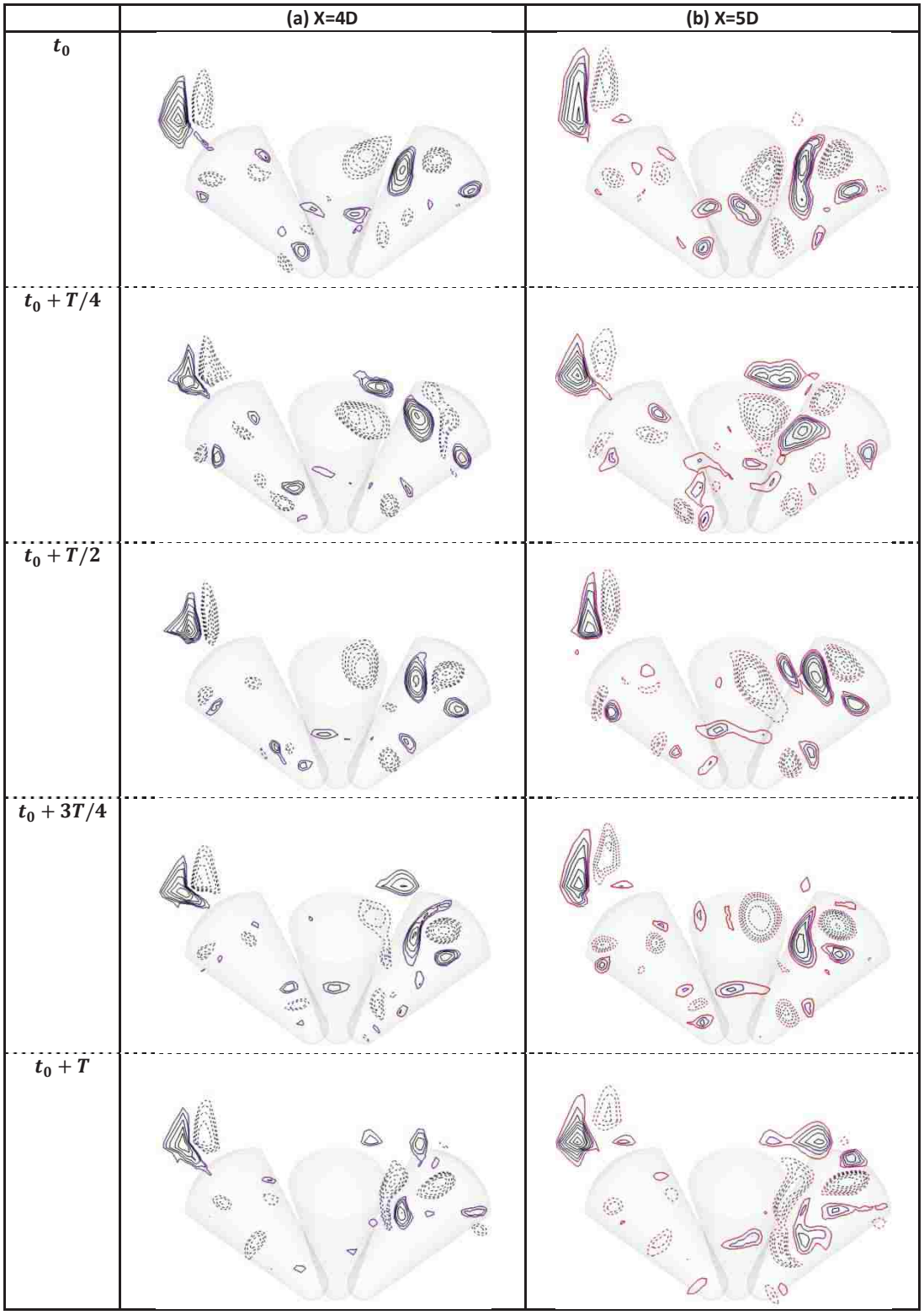

FIGURE 4.16: (continued)

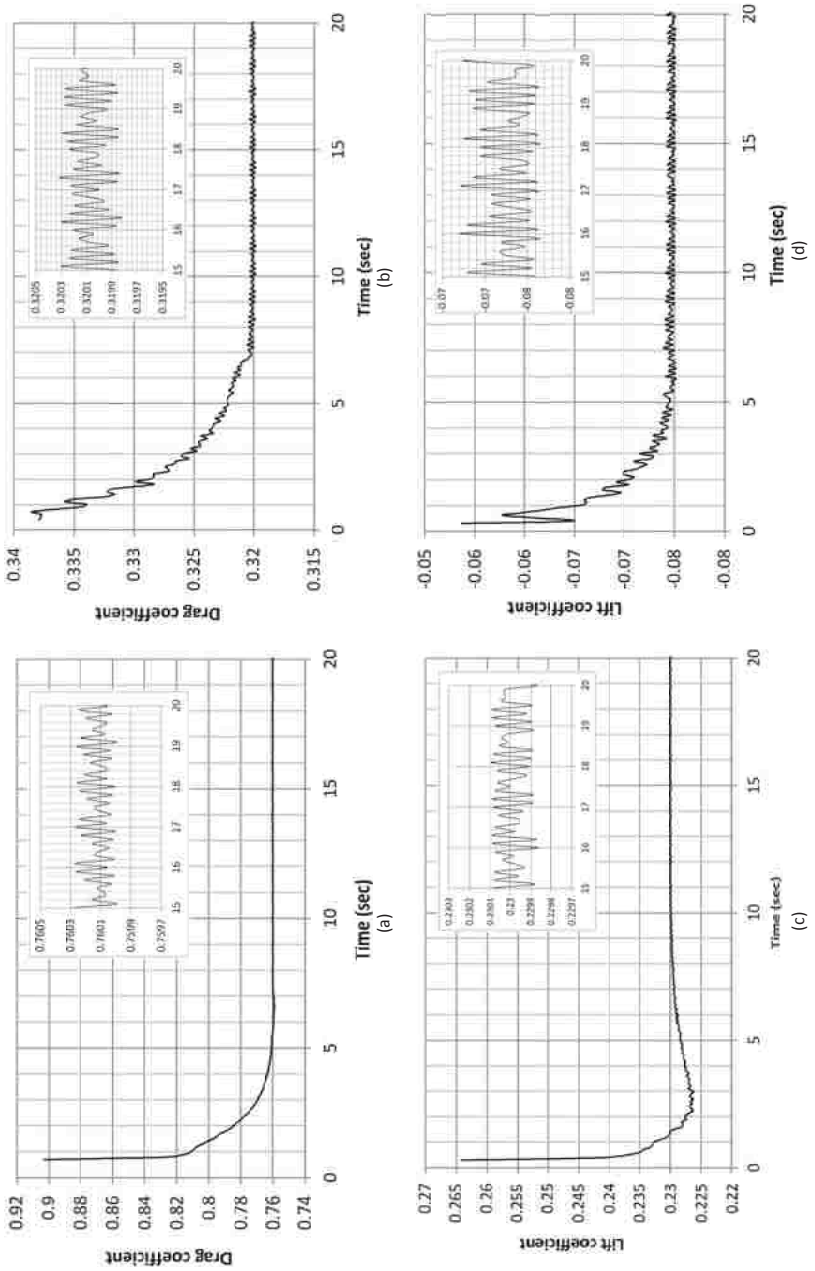

FIGURE 4.17: URANS prediction for the time history of the force coefficients correspond to the balloons in the closely spaced configuration; (a) drag coefficient of the upstream balloon, (b) drag coefficient of the downstream balloon, (c) lift coefficient of the upstream balloon, (d) lift coefficient of the downstream balloon in Y direction.

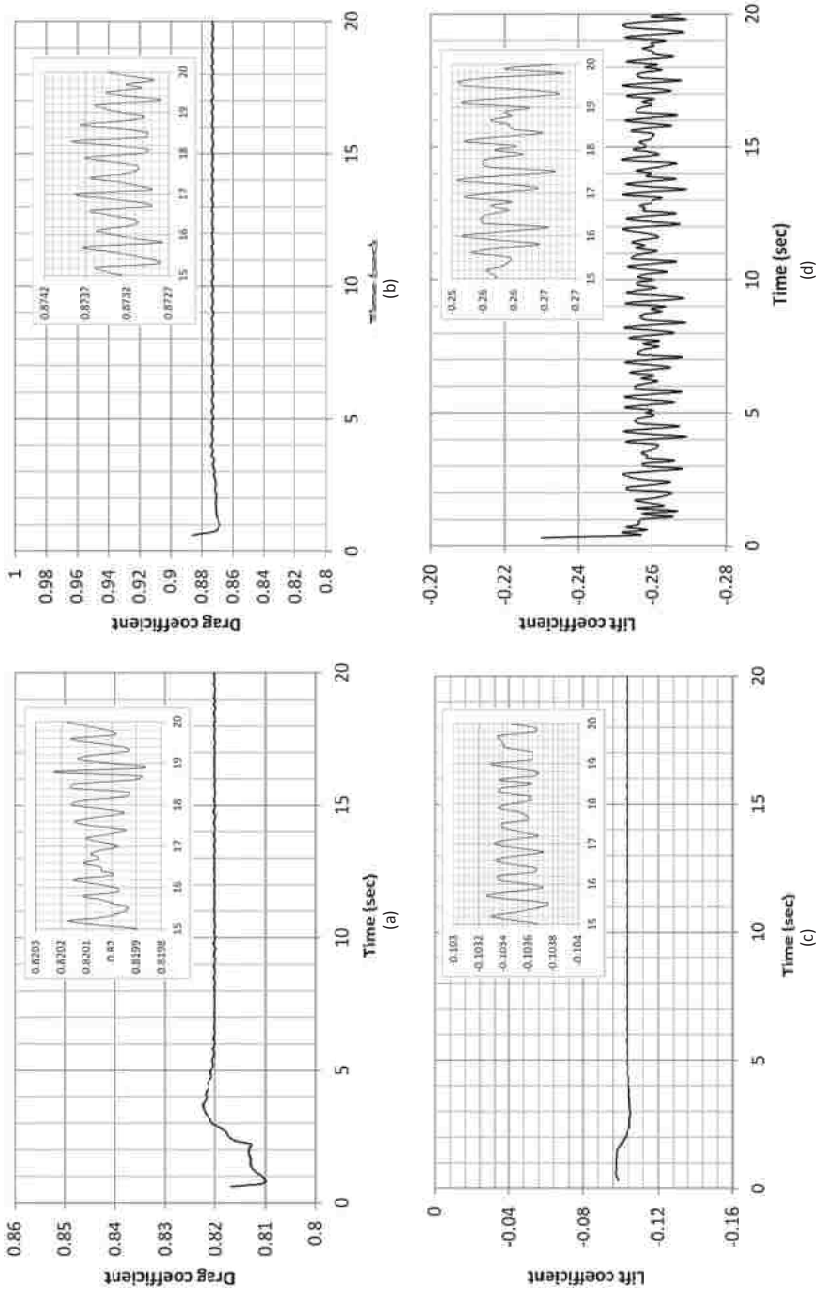

FIGURE 4.18: URANS prediction for the time history of the force coefficients correspond to the balloons in the widely spaced configuration; (a) drag coefficient of the upstream balloon, (b) drag coefficient of the downstream balloon, (c) lift coefficient of the upstream balloon, (d) lift coefficient of the downstream balloon.

4.5.2.2 LES Results

In contrast to URANS, in the LES turbulence model the large scale eddies which contain most of energy and fluxes and are significantly affected by the flow conditions are directly resolved and just the small scale eddies with a more universal nature are modeled. Consequently, as is seen in figures 4.19 and 4.20, the fluctuations in the flow over the floral units of the balloons and the resulting oscillations in the force coefficients were captured well by the LES simulation. It is observed that against the URANS results which were well organized and periodic (see figures 4.17 and 4.18), the LES results display broadband turbulence characteristics; with an amplitude of approximately 10 times larger than what was captured by the URANS. It is important to point out that both figures 4.19 and 4.20 show statistically stationary behaviour with a stable nature; confirming that the transient results have converged.

The mean values of the force coefficients predicted by the LES simulation are compared with those obtained by the URANS in table 4.1. From this table one can see that the mean values predicted by URANS are larger compared to those of LES. As was mentioned in Vasel-Be-Hagh et al. [44], the unavoidable discrepancy between mean values of the force coefficient predicted by URSANS and LES is attributed to three main reasons. Firstly, the mesh generated for LES model is different from the URANS mesh. Secondly, URANS model is originally based on the time averaged Navier-Stokes equations, whereas the LES model solves the spatially filtered Navier-Stokes. The third reason is the difference between stress tensors of URANS and LES models. These values are also compared with the values associated with the single balloon [44]. In the widely spaced configuration, drag coefficient of the balloons are almost equal. In the closely spaced configuration, however, the drag coefficient of the downstream balloon is much lower than that of the upstream balloon; this can be attributed to the shield effect of the upstream balloon. If we look at the floral unit of the balloons as a single bluff body, we can say that the total drag coefficient of the widely spaced configuration ($\approx$1.68) is much larger than the toatl drag coefficient of the closely spaced configuration ($\approx$0.91), while the energy storage capacity is the same. To put these values into perspective, they can be compared to force coefficients of the cylindrical and spherical bodies. It should be stressed that studies on these basic shapes are not under the same boundary conditions considered in the present study, nonetheles, the closest ones are chosen. In contrast with the balloons, the lift coefficient of single sphere and single cylinder is zero. This is owing to the asymmetric shape of the balloons about the X-Z plane. Concerning the drag coefficient, Achenbach [89] and Clift et al. [90] measured a value of C_D=0.51 for a single sphere and Cantwell and Coles [91] reported a range of $0.78 \leq C_D \leq 1.43$ for a single circular cylinder with different end conditions at a Reynolds number of 2.3×10^5. As was mentioned in Vasel-Be-Hagh et al. [44], drag coefficient of the single balloon is between drag coefficient of sphere and cylinder.

TABLE 4.1: Comparison of the time averaged force coefficients of the balloons.

	Closely spaced configuration		Widely spaced configuration		Single balloon
	Upstream balloon	Downstream balloon	Upstream balloon	Downstream balloon	
	Lift				
LES: Dyna-SM	0.19	-0.05	-0.06	-0.15	0.06
URANS: k-ω	0.23	-0.08	-0.10	-0.26	0.13
	Drag				
LES: Dyna-SM	0.49	0.21	0.54	0.57	0.69
URANS: k-ω	0.76	0.32	0.82	0.87	0.98

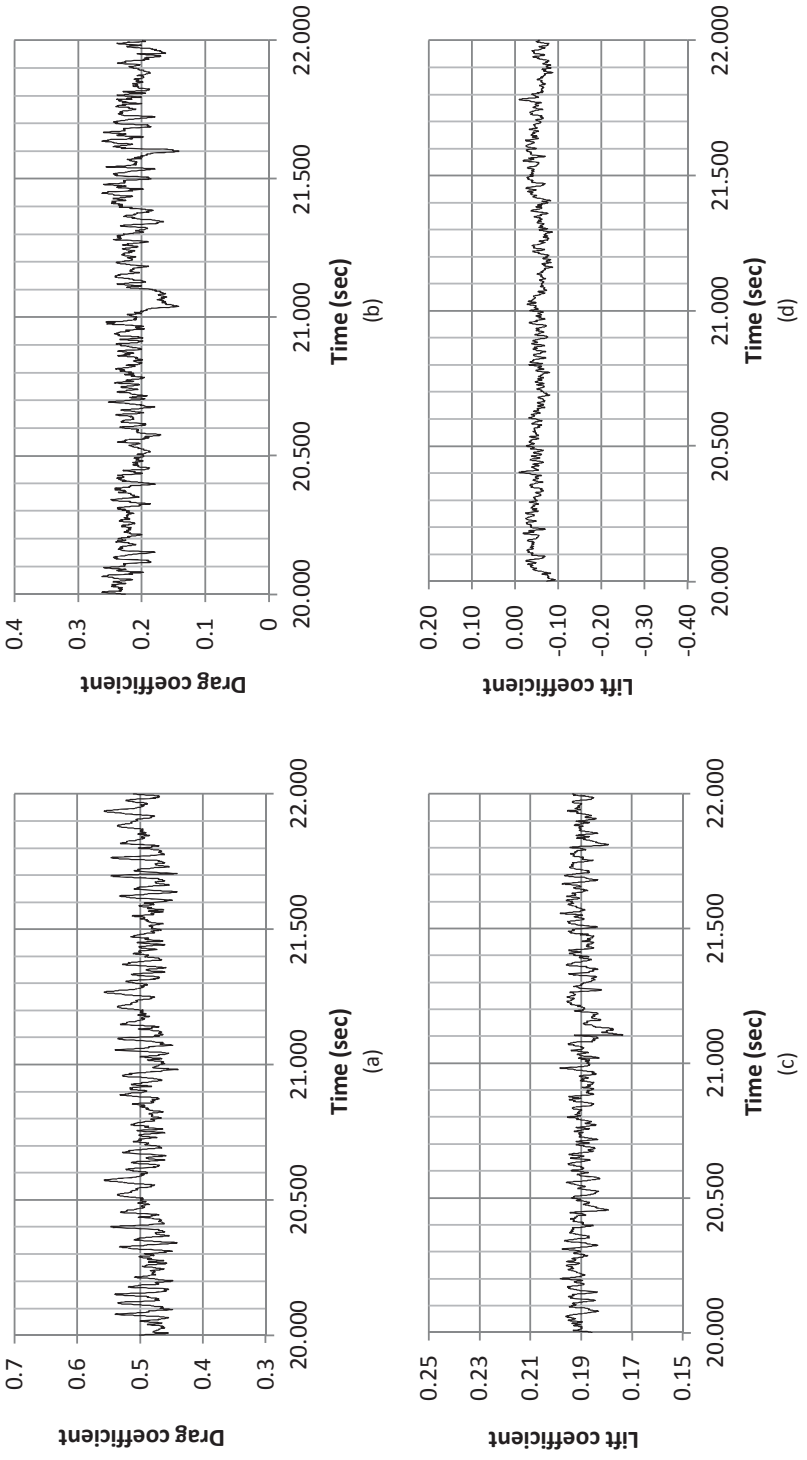

FIGURE 4.19: LES prediction for the Time convergence history of the force coefficients correspond to the balloons in the closely spaced case; (a) drag coefficient of the upstream balloon, (b) drag coefficient of the downstream balloon, (c) lift coefficient of the upstream balloon, (d) lift coefficient of the downstream balloon.

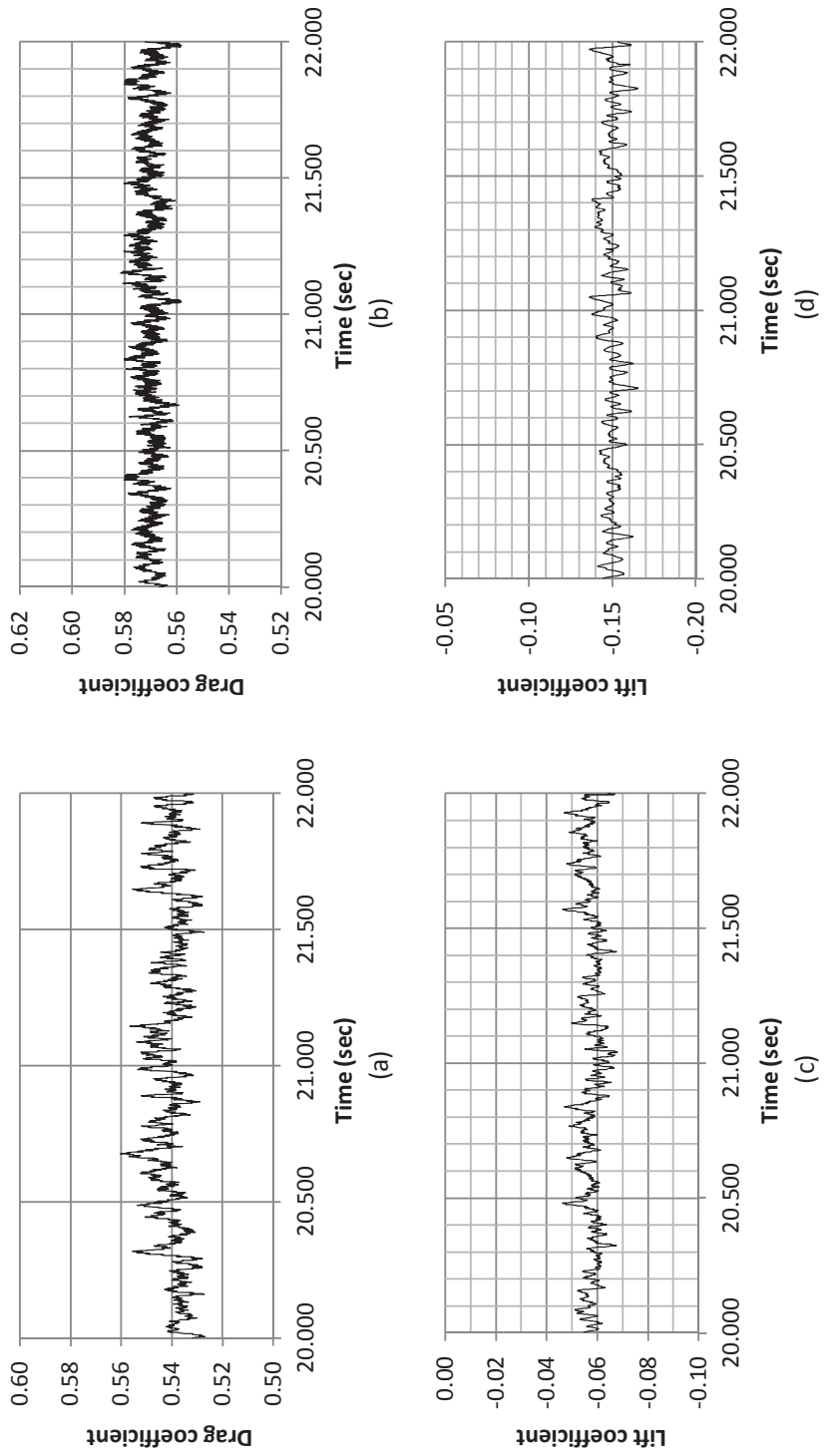

FIGURE 4.20: LES prediction for the Time convergence history of the force coefficients correspond to the balloons in the widely spaced case; (a) drag coefficient of the upstream balloon, (b) drag coefficient of the downstream balloon, (c) lift coefficient of the upstream balloon, (d) lift coefficient of the downstream balloon.

Power spectra of non-sinusodial oscillations of the lift coefficients are presented in figures 4.21 and 4.22 for the closely and widely spaced configurations respectively. These figures are plotted on log-log axes. In each figure panels (a) and (b) display the power spectrum associated with the lift coefficients of the upstream and downstream balloons respectively. These power spectra were estimated using periodogram algorithm [92]. For both widely and closely spaced cases the Strouhal number ($St = f.D/U$) falls in the range of 0.01∼1.3. Some high- and low-peaks are observed in this range indicating the dominant frequencies in which the vortex tubes are shed randomly from the balloons. In power specrum of the closely spaced configuration shown in figure 4.21, a high-peak is observed at approximately $St \approx 0.15$. Some other low-peaks are also observed at larger Strouhal numbers. Power specrtra associated with the lift coefficients of the widely spaced configuration are illustrated in figure 4.22. Panel (a) shows one strong peak at Strouhal numbers of 0.52 in power spectrum of the upstream balloon lift coefficient; however, it is not appeard in the power spectra of the lift coefficient of the downstream balloons. In table 4.2, Strouhal numbers of the balloons in both widely and closely spaced configurations are compared with those of single balloon, cylinders and spheres. As can be seen, the vortex shedding frequency of the balloons in widely spaced configuration are very close to that of a single balloon, however, it seems it is too much lower for the closely spaced configuration.

TABLE 4.2: Comparison of the Strouhal number of the balloons with published data for cylinders and spheres.

		St	Re
Balloon	Wide configuration	0.52	230,000
	Close configuration	0.15	
	Single balloon [44]	0.45 and 0.65	
Cylinder	Schewe [93]	0.43	230,000
	Saghafian et al.[94]	0.30	230,000
Sphere	Kiyaetal.[95]	0.19	100,00
	Constantinescu and Squires [96]	1-1.3	430,000
	Norman and McKeon [97]	0.2	100,000

4.6 Conclusion

Flow over two limiting configurations of three underwater balloons of an underwater compressed air energy storage plant was simulated using URANS and LES turbulence models. Some details about the force characteristics and the structure of the flow around such droplet-shaped bluff bodies were disclosed. The major findings of the study are summarized as follows:

- When flow crosses a droplet-shaped bluff body, fluid particles move around non-equal circles. This Coriolis–type effect leads to the generation of rotational cores on the leeward surface of the body which produces tube shedding flows.
- The swirling tube flows also tend to have random precessing or swinging motions.
- The turbulent shedding of the vortex tubes occurs at different Strouhal numbers in the range of 0.01∼1.3. The dominant frequency for the widely spaced configuration occurs at

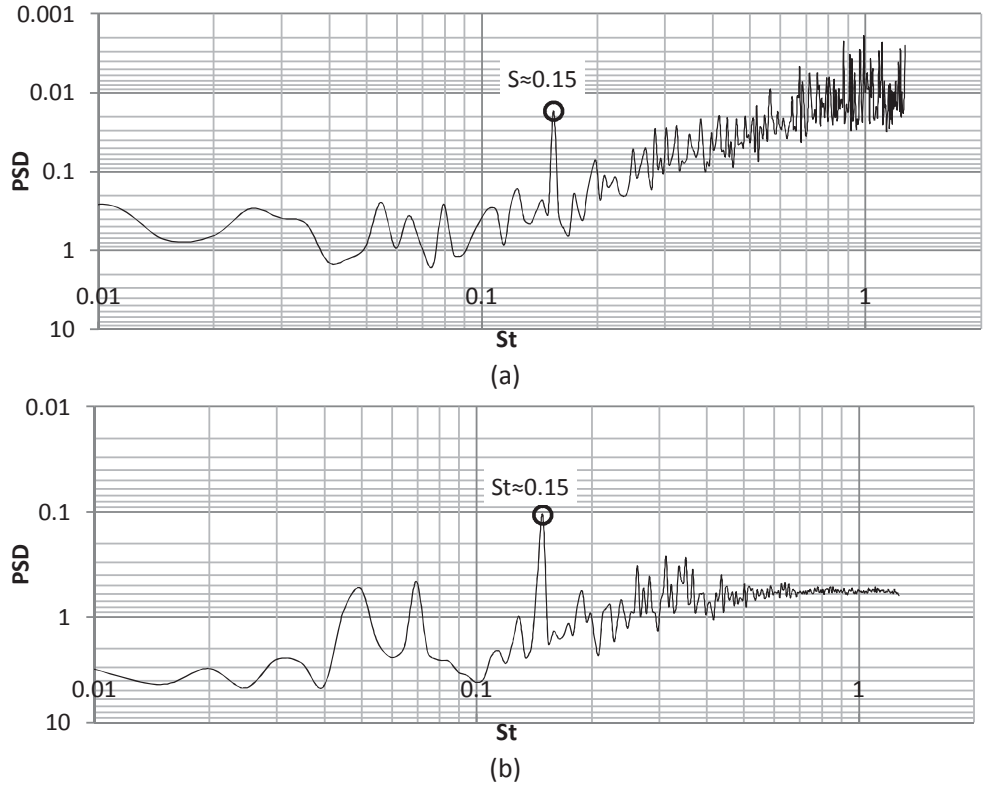

FIGURE 4.21: Power spectrum diagrams associated with the force coefficients of the balloons in the closely spaced configuration; (a) power spectrum of the lift coefficient of the upstream balloon, (b) power spectrum of the lift coefficient of the downstream balloon.

$St \approx 0.52$ which is close to that of a single balloon. For the closely spaced configuration a high-peak at $St \approx 0.18$ is observed.

- The URANS model predicted larger force coefficients than the LES. However, time history of the force coefficients indicates that LES has a better description of turbulence nature of the present flow.
- In the case of closely spaced configuration, the drag coefficient of the upstream balloon is larger than the drag coefficient of the downstream ones, whereas for the widely spaced configuration the drag coefficient of the downstream balloons is larger than that of the upstream one.
- The total drag coefficient of the wide unit is approximately 1.8 times the total drag coefficient of the closed unit. The total drag coefficients of both wide and closed units of three balloons are smaller than three times the drag coefficient of a single balloon, while the storing capacity is the same.
- The hydrodynamic modeling presented here is a potentially useful prediction of flow structures and forces that could affect the installation of submerged energy storage accumulators. Such information will be essential for the design of moorings and system rigging

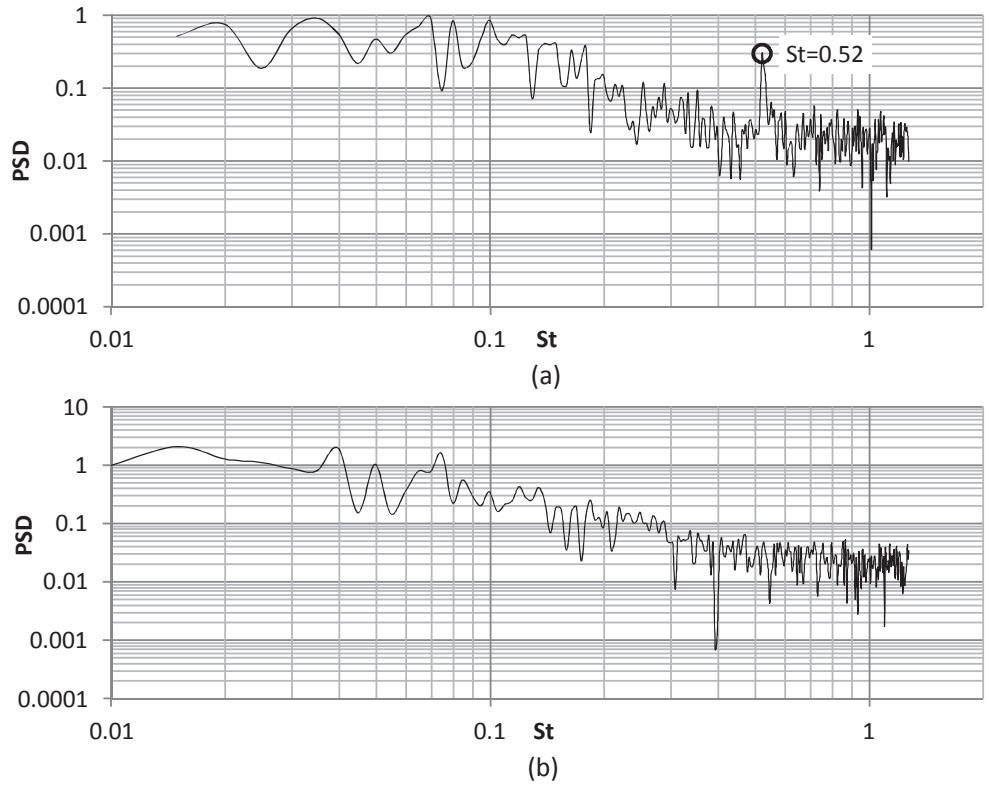

FIGURE 4.22: Power spectrum diagrams associated with the force coefficients of the balloons in the widely spaced configuration; (a) power spectrum of the lift coefficient of the upstream balloon, (b) power spectrum of the lift coefficient of the downstream balloon.

critical for the installation of this technology. Further, these results represent a contribution to the currently sparse literature available on flow around droplet shaped bodies.

Acknowledgements

This work is made possible by Natural Sciences and Engineering Research Council of Canada, and the Ontario Centres of Excellence. The lead author is most grateful to the Ontario Trillium Foundation for an Ontario Trillium Scholarship. Sincerest thanks are also due to Mrs. Nooshin Younesi for her invaluable help in preparing some figures of this paper

References

[1] Statistics of wind energy in USA. Buc, France: The Wind Power. **[Link]**

[2] Statistics of wind energy in Canada. Buc, France: The Wind Power. **[Link]**

[3] Safaei, H., Keith, D.W., Hugo, R.J., 2013. Compressed air energy storage (CAES) with compressors distributed at heat loads to enable waste heat utilization. Applied Energy, 103, 165–179.

[4] Rahman, F., Rehman, S., Abdul-Majeed, M.A., 2012. Overview of energy storage systems for storing electricity from renewable energy sources in Saudi Arabia. Renewable Sustainable Energy Review, 16, 274–283.

[5]Denholm, P., Kulcinski, G.L., 2004. Life cycle energy requirements and greenhouse gas emissions from large scale energy storage systems. Energy Conversion and Management, 45, 2153–72.

[6]Ibrahim, H., Ilinca, A., Perron, J., 2008. Energy storage systems characteristics and comparisons. Renewable Sustainable Energy Review, 12, 1221–50.

[7]Robb, D., 2010. Could CAES answer wind reliability concerns. Power, 154, 58–61.

[8]Pimm, A.J., Garvey, S.D., 2009. Analysis of flexible fabric structures for large-scale subsea compressed air energy storage. Journal of Physics: Conference Series, 181, 012049.

[9] Pimm, A.J., Garvey, S.D., Drew, R.J., 2011. Shape and cost analysis of pressurized fabric structures for subsea compressed air energy storage. Proceedings of the Institution of Mechanical Engineers Part C Journal of Mechanical Engineering Science, 225, 1027-1043.

[10] Cheung, B., Cao, N., Carriveau, R., Ting, D.S-K., 2012(a). Distensible air accumulators as a means of adiabatic underwater compressed air energy storage. International Journal of Environmental Studies, 69, 566-577.

[11] Cheung, B., Carriveau, R., Ting, D.S-K., 2012(b). Storing energy underwater. Mechanical Engineering Magazine (ASME), 134, 38-41.

[12] Graff, W.J., 1981. Introduction to offshore structures; design, fabrication, installation. Houston: Gulf Publishing Company.

[13] Haritos, N., 2007. Introduction to the Analysis and Design of Offshore Structures–An Overview. EJSE Special Issue: Loading on Structures, 55-65.

[14] Mureithi, N.W., Price, S.J., Païdoussis, M.P., 1994. The post-hopf-bifurcation response of a loosely supported cylinder in an array subjected to cross-flow, part I: experimental results. Journal of Fluids and Structures, 8, 833-852.

[15] Sumner, D., Price, S.J., Paidoussis, M.P., 1999. Tandem cylinders in impulsively started flow. Journal of Fluids and Structures, 13, 955-965.

[16] Akosile, O.O., Sumner, D., 2003. Staggered circular cylinders immersed in a uniform planar shear flow. Journal of Fluids and Structures, 18, 613-633.

[17] Zhang, C., Pettigrew, M.J., Mureithi, N.W., 2007. Vibration excitation force measurements in a rotated triangular tube bundle subjected to two-phase cross flow. Journal of Pressure Vessel Technology, 129, 21-27.

[18] Yang, X., Zheng, Z.C., 2010. Nonlinear spacing and frequency effects of an oscillating cylinder in the wake of a stationary cylinder. Physics of Fluids, 22, 043601.

[19] Sarkar, S., Sarkar, S., 2010. Vortex dynamics of a cylinder wake in proximity to a wall. Journal of Fluids and Structures, 26, 19-40.

[20] Griffith, M.D., Leontini, J., Thompson, M.C., Hourigan, K., 2011. Vortex shedding and three-dimensional behaviour of flow past a cylinder confined in a channel. Journal of Fluids and Structures, 27, 855-860.

[21] Bao, Y., Huang, C., Zhou, D., Tu, J., Han, Z., 2012. Two-degree-of-freedom flow-induced vibrations on isolated and tandem cylinders with varying natural frequency ratios. Journal of Fluids and Structures, 35, 50-75.

[22] Mureithi, N.W., Païdoussis, M.P., Price, S.J.,1994b. The post-hopf-bifurcation response of a loosely supported cylinder in an array subjected to cross-flow. Part II: Theoretical model and comparison with experiments. Journal of Fluids and Structures, 8, 853–876.

[23] Kumar, S., Gonzalez, B., Probst, O., 2011. Flow past two rotating cylinders. Physics of Fluids, 23, 014102.

[24] Huang, R.F., Lin, B.H., Yen, S.C., 2010. Time-averaged topological flow patterns and their influence on vortex shedding of a square cylinder in cross flow at incidence. Journal of Fluids and Structures, 26, 406-29.

[25] Mahbub Alami, M., Zhou, Y., Wang, XW., 2011. The wake of two side-by-side square cylinders. Jounal of Fluid Mechanics, 669, 432-471.

[26] Bao, Y., Wu, Q., Zhou, D., 2012. Numerical investigation of flow around an inline square cylinder array with different spacing ratios. Computers & Fluids, 55, 118-131.

[27] Lin M.Y., Huang L.H., 2010. Vortex shedding from a submerged rectangular obstacle attacked by a solitary wave. Jounal of Fluid Mechanics, 651, 503-18.

[28] Lam, K., Lin, Y.F., Zou, L., Liu, Y., 2012. Numerical study of flow patterns and force characteristics for square and rectangular cylinders with wavy surfaces. Journal of Fluids and Structures, 28, 359-377.

[29] Maiti, D.K., 2012. Numerical study on aerodynamic characteristics of rectangular cylinders near a wall. Ocean Engineering, 54, 251–260.

[30] Tian, X., Ong, M.K., Yang, J., Myrhaug, D., 2013. Unsteady RANS simulations of flow around rectangular cylinders with different aspect ratios. Ocean Engineering, 58, 208–216.

[31] Peng, Y.F., Sau, A., Hwang, R.R., Yang, W.C., Chih-Min Hsieh, 2012. Criticality of flow transition behind two side-by-side elliptic cylinders. Physics of Fluids, 24, 034102.v

[32] Taneda, S., 1978. Visual observations of the flow past a sphere at Reynolds numbers between 10^4 and 10^6. Jounal of Fluid Mechanics, 85, 187–192.

[33] Constantinescu, G.S., Squires, K.D., 2000. LES and DES investigation of turbulent flow over a sphere. Technical Report AIAA Paper 2000-0540, 1-11.

[34] Yoon, D.H., Yang, K.S., 2009. Characterization of flow pattern past two spheres in proximity. Physics of Fluids, 21, 073603.

[35] El Khoury, G.K., Andersson, H.I., Pettersen, B., 2010. Crossflow past a prolate spheroid at Reynolds number of 10000. Jounal of Fluid Mechanics, 659, 365-374.

[36] Dixona, A.G., Taskina, M.E., Nijemeisland, M., Stitt, E.H., 2011. Systematic mesh development for 3D CFD simulation of fixed beds: Single sphere study. Computers & Chemical Engineering, 35, 1171–1185.

[37] Sumner, D., Heseltine, J.L., 2008. Tip vortex structure for a circular cylinder with a free end. Journal of Wind Engineering and Industrial Aerodynamics, 96, 1185-1196.

[38] Li, H., Sumner, D., 2009. Vortex shedding from two finite circular cylinders in a staggered configuration. Journal of Fluids and Structures, 25, 479-505.

[39] Adaramola, M.S., Sumner, D., Bergstrom, D.J., 2010. Effect of velocity ratio on the streamwise vortex structures in the wake of a stack. Journal of Fluids and Structures, 26, 1-18.

[40] Zhou, T., Wang, H., Razali, S.F.M., Zhou, Y., Cheng, L., 2010. Three-dimensional vorticity measurements in the wake of a yawed circular cylinder. Physics of Fluids, 22, 015108.

[41] Kanaris, N., Grigoriadis, D., Kassinos, S., 2011. Three dimensional flow around a circular cylinder confined in a plane channel. Physics of Fluids, 23, 064106.

[42] Uzun, A., Yousuff Hussaini, M., 2012. An application of delayed detached eddy simulation to tandem cylinder flow field prediction. Computers & Fluids, 60, 71-85.

[43] Sheard, G.J., Fitzgerald, M.J., Ryan, K., 2009. Cylinders with square cross-section: Wake instabilities with incidence angle variation. Jounal of Fluid Mechanics, 630, 43-69.

[44] Vasel-Be-Hagh, A.R., Carriveau, R., Ting, D.S.-K., 2013. Numerical simulation of Flow Past an Underwater Energy Storage Balloon. Computers & Fluids, 88, 272-286.

[45] Subsalve USA Corporation manual, 2012. Underwater lift bags. **[Link]** [read on 07.06.2012].

[46] Lei, C., Cheng, l., Kavanagh, L., 2000. A finite difference solution of the shear flow over a circular cylinder. Ocean Engineering, 27, 271–290.

[47] Hatipoglu, F., Avci, I., 2003. Flow around a partly buried cylinder in a steady current. Ocean Engineering, 30, 239–249.

[48] Catalano, P., Wang, M., Iaccarino, G., Moin, P., 2003. Numerical simulation of the flow around a circular cylinder at high Reynolds numbers. International Journal of Heat and Fluid Flow, 24: 463–469.

[49] Huang, Z., Olson, J.A., Kerekes, R.J., Green, S.I., 2006. Numerical simulation of the flow around rows of cylinders. Computers & Fluids, 35, 485–491.

[50] Shao, J., Zhang, C., 2008. Large eddy simulations of the flow past two side-by-side circular cylinders. International Journal of Computational Fluid Dynamics, 22, 393–404.

[51] Vakil, A., Green, S.I., 2009. Drag and lift coefficients of inclined finite circular cylinders at moderate Reynolds numbers. Computers & Fluids, 38, 1771–1781.

[52] Unal, U.O., Atlar, M., Goren, O., 2010. Effect of turbulence modelling on the computation of the near-wake flow of a circular. Ocean Engineering, 37, 387–399.

[53] Singha, S., Sinhamahapatra, K.P., 2010. Flow past a circular cylinder between parallel walls at low Reynolds numbers. Ocean Engineering, 37, 757–769.

[54] Vakil, A., Green, S.I., 2011. Two-dimensional side-by-side circular cylinders at moderate Reynolds numbers. Computers & Fluids, 51, 136-44.

[55] Dixona, A.G., Taskina, M.E., Nijemeisland, M., Stitt, E.H., 2011. Systematic mesh development for 3D CFD simulation of fixed beds: Single sphere study. Computers & Chemical Engineering, 35, 1171–1185.

[56] Mylonas, D., Sayer, P., 2012. The hydrodynamic flow around a yacht keel based on LES and DES. Ocean Engineering, 46, 18–32.

[57] Liu, Z.G., Liu, Y., Lu, J., 2012. Fluid–structure interaction of single flexible cylinder in axial flow. Computers & Fluids, 56, 143–151.

[58] M. Balogha , A. Parenteb, C. Benoccic. 2012. RANS simulation of ABL flow over complex terrains applying an Enhanced k-ϵ model and wall function formulation: Implementation and comparison for fluent and OpenFOAM. Journal of Wind Engineering and Industrial Aerodynamics, Volumes 104–106, Pages 360–368

[59] Tuling, S., Dala, L., Toomer, C., 2013. Lee-Side Flow Structures of Very Low Aspect Ratio Cruciform Wing–Body Configurations. J Spacecraft Rockets 50(6), 1134-49.

[60] Aissa, M., Bouabdallah, A., Oualli, H., 2014. Radial deformation frequency effect on the three-dimensional flow in the cylinder wake. Journal of Fluids Engineering, 137(1), 1-11

[61] Meldi, M., Lucor, D., Sagaut, P., 2011. Is the Smagorinsky coefficient sensitive to uncertainty in the form of the energy spectrum?. Physics of Fluids, 23, 125109.

[62] Sagaut, P., 2001.Large-eddy simulation for incompressible flows – an introduction, Scientific computationseries.Springer-Verlag.

[63] Howe, M.S., Lauchle, G.C., Wang, J., 2001. Aerodynamic lift and drag fluctuations of a sphere. Jounal of Fluid Mechanics, 436, 41-57.

[64] Sujudi, D., Haimes, R., 1995. Identification of swirling flow in 3-D vector fields. Technical Report AIAA Paper 95-1715, 1-8.

[65] Chong, M.S., Perry, A.E., Cantwell, B.J., 1990. A general classification of three-dimensional flow fields. Physics of Fluids, 2, 765-777.

[66] Frana, K., Stiller, J., Grundmann, R, 2005. Taylor-Görtler vortices in the flow Driven by a rotating magnetic Field in a cylindrical container. Journal of Visualization, 8(4), 323-330.

[67] Tanahashi, M., Hirayama, T., Taka, S., Miyauchi, T., 2008. Measurement of fine scale structure in turbulence by time-resolved dual-plane stereoscopic PIV. International Journal of Heat and Fluid Flow, 29, 792–802.

[68] Vernet, R., Thomas, L., David, L., 2009. Analysis and reconstruction of a pulsed jet in cross flow by multi-plane snapshot POD. Experiments in Fluids, 47, 707–720.

[69] Kunnen, R.P.J., Clercx, H.J.H., Geurts, B.J., 2010. Vortex statistics in turbulent rotating convection. Physical Review E, 82, 036306.

[70] Garrick, S.C., 2011. Effects of turbulent fluctuations on nanoparticle coagulation in shear flows. Aerosol Science and Technology, 45, 1272–1285.

[71] Lee, G., Scalo, C., Piomelli, U., 2012. A simple technique for the visualization of eddy kinematics in turbulent flows. International Journal of Computational Fluid Dynamics, 26, 263–274.

[72] Yang, Y., Knudsen, S., 2012. Large-eddy simulations of the non-reactive flow in the Sydney swirl burner. International Journal of Heat and Fluid Flow, 36, 47–57.

[73] Chang, K., Hughes, T.J.R., Calo, V.M., 2012. Isogeometric variational multiscale large-eddy simulation of fully-developed turbulent flow over a wavy wall. Computers & Fluids, 68, 94–104.

[74] Krajnovi'c, S., Basara, B., 2009. Numerical simulation of the flow around a tall finite cylinder using LES and PANS. Progress in Turbulence III, Springer Proceedings in Physics, 131, 15-118.

[75] Zhou, Y., Li, X., Fu, D., Ma, Y., 2007. Coherent structures in transition of a flat-plate boundary layer at Ma=0.7. Chinese Physics Letters, 22, 147-150.

[76] Paik, J., Escauriaza, C., Sotiropoulos, F., 2007. On the bimodal dynamics of the turbulent horseshoe vortex system in a wing-body junction. Physics of Fluids, 19, 045107.

[77] Omori, T., Jakirlic, S., Tropea, C., Obi, S., 2008. Shearless and sheared flow past a circular cylinder: comparative analysis by means of LES. International Journal of Heat and Fluid Flow, 29, 703-720.

[78] Morton, C., Yarusevych, S., 2010. Vortex shedding in the wake of a step cylinder. Physics of Fluids, 22, 083602.

[79] Kotouc, M., Bouchet, G., Dusek, J., 2009. Transition to turbulence in the wake of a fixed sphere in mixed convection. Jounal of Fluid Mechanics, 625, 205-48.

[80] Dubief, Y., Delcayre, F., 2000. On coherent-vortex identification in turbulence. Journal of Turbulence, 1, 1-22.

[81] Howard, R.J.A., Pourquie, M., 2002. Large eddy simulation of an Ahmed reference model. Journal of Turbulence, 3, 1-18.

[82] Sohankar, A., 2006. Flow over a bluff body from moderate to high Reynolds numbers using large eddy simulation. Computers & Fluids, 35, 1154–1168.

[83] Paik, J., Sotiropoulos, F., 2010. Turbulent swirling flow through an abrupt axisymmetric expansion is investigated numerically using detached-eddy simulation at Reynolds numbers. International Journal of Heat and Fluid Flow, 31, 390–400.

[84] Kurtulus, D.F., David, L., Farcy, A., Alemdaroglu, N., 2008. Aerodynamic characteristics of flapping motion in hover. Experiments in Fluids, 44, 23–36.

[85] Dupont, S., Brunet, Y., 2009. Coherent structures in canopy edge flow: a large-eddy simulation study. Jounal of Fluid Mechanics, 630, 93–128.

[86] Zhou, J., Zhong, S., 2009. Numerical simulation of the interaction of a circular synthetic jet with a boundary layer. Computers & Fluids, 38, 393–405.

[87] Zhou, J., Zhong, S., 2010. Coherent structures produced by the interaction between synthetic jets and a laminar boundary layer and their surface shear stress patterns. Computers & Fluids, 39, 1296–1313.

[88] Catalano, P., Wang, M., Iaccarino, G., Moin, P., 2003. Numerical simulation of the flow around a circular cylinder at high Reynolds numbers. International Journal of Heat and Fluid Flow, 24: 463–469.

[89] Achenbach, E., 1972. Experiments on the flow past spheres at very high Reynolds numbers. Jounal of Fluid Mechanics, 54, 565-75.

[90] Clift, R., Grace, J.R., Weber, M.E., 1978. Bubbles drops and particles. New York: Academic Press, New York.

[91] Cantwell, B., Coles, D., 1983. An experimental study of entrainment and transport in the turbulent near wake of a circular cylinder. Jounal of Fluid Mechanics, 136, 321-74.

[92] Stoica, P., Moses, R.L., 1997. Introduction to spectral analysis, Prentice-Hall, 24-26.

[93] Schewe, G., 1983. On the force fluctuations acting on a circular cylinder in cross flow from subcritical up to transcritical Reynolds numbers. Jounal of Fluid Mechanics, 133, 265–285.

[94] Saghafian, M., Stansby, P.K., Saidi, M.S., Apsley, D.D., 2003. Simulation of turbulent flows aound a circular cylinder using nonlinear eddy–viscosity modeling steady and oscillatory amient flows. Journal of Fluids and Structures, 17, 1213–1236.

[95] Kiya, M., Ishikawa, H., Sakamoto, H., 2001. Near wake instabilities and vortex structures of three dimensional bluff bodies: ma review. Journal of Wind Engineering and Industrial Aerodynamics, 89, 1219–1232.

[96] Constantinescu, G.S., Squires, K.D., 2004. Numerical investigations of flow over a sphere in the subcritical regimes. Physics of Fluids, 16, 1449-1466.

[97] Norman, A.K., McKeon, B.J., 2011. Unsteady force measurements in sphere flow from subcritical to supercritical Reynolds numbers. Experiments in Fluids, 51, 1439-1453.

Chapter 5

A Balloon Bursting Underwater

A. R. Vasel-Be-Hagh, R. Carriveau and D. S.-K. Ting

Turbulence and Energy Laboratory, Lumley Centre for Engineering Innovation, University of Windsor, Ontario, Canada N9B 3P4

Vasel-Be-Hagh, A.R., Carriveau, R., Ting, D.S.-K., 2015. A Balloon Bursting Underwater. Journal of Fluid Mechanics, 769, 522 - 540.

5.1 Introduction

There is a fundamental difference in the physics of vortex rings depending on whether they are buoyant or not. According to Reynolds [1], the impulse P of a non-buoyant vortex ring in a viscous fluid is constant. Hence, considering Turner's impulse equation $P{=}\rho\Gamma\pi R^2$ and the fact that vortex rings expand as they advance, the circulation Γ of a non-buoyant vortex ring decreases with time [2]. In the case of buoyant vortex rings, also called vortex ring bubbles, impulse increases under the action of the buoyancy force; therefore, the circulation remains constant. Non-buoyant vortex rings have been extensively studied for more than a century, the buoyant vortex rings, however, have received relatively less attention. Nevertheless, a number of seminal theoretical [2-5], experimental [2-3] and numerical [6-7] contributions have been made concerning the general properties and the stability of buoyant vortex rings. One of the latest studies on the vortex ring bubbles was the lattice Boltzmann simulation conducted by Cheng et al. [7]. The main motivation of their study was to assess whether the ring bubble continues to expand while the rise velocity decreases, as was predicted by Turner [2], Walters and Davidson [3], Pedley [4] and Lundgren and Mansour [6], or, ultimately a steady state is achieved at which the ring radius and rise velocity become constant, as was predicted by Joseph et al. [5]. They found that, in contrast to Joseph et al.'s [5] prediction, the ring radius increases and the rising velocity decreases with time until the vortex ring becomes unstable and breaks down into small spherical cap bubbles. For further investigation, we extended the model proposed by Sullivan

et al. [8] to include buoyant vortex rings, and unexpectedly, achieved a steady state solution suggesting that similar to the spherical bubbles, the vortex ring bubbles eventually attain a constant velocity, as was predicted by Joseph et al. [5]. This implication prompted us to experimentally assess whether the modified model matches with reality or not. Another major motivation for the present work was the conspicuous lack of an investigation concerning the flow produced by the bursting of balloons used increasingly in maritime energy storage and salvage applications. According to the literature (e.g. Sullivan et al. [8]; Walker et al.[9]; Hershberger et al. [10]; Gan et al. [11]) the common technique for the generation of a vortex ring bubble is the rapid ejection of fluid into a water tank through an orifice exit. In other words, the initial source of energy is kinetic, whereas the vortex ring bubbles studied herein are powered by the potential energy initially stored in the underwater balloons. Beyond this, an investigation exploring high-Bond-number vortex rings was not evident in the literature. A secondary motivation for the present work was to address this gap by studying vortex rings up to Bo=1000 produced by large balloons bursting in a 25-m^3 water tank.

Before the subject of a balloon bursting underwater can be discussed, it is important first to briefly review some basic characteristics of buoyant vortex rings described in the literature. Then, the dynamics of vortex ring bubbles will be characterized through a semi analytical model based on the concept of drag. Afterwards, the setup and procedure of the experiment are described. At the end, results are presented and discussed.

5.2 Buoyant vortex rings

Turner developed one of the earliest analytical theories about vortex ring bubbles by invoking two fundamental assumptions [2]. First, vorticity generated on the bubble surface was assumed to be confined within a region which never extends to the symmetry axis of the vortex ring; therefore, no vorticity is canceled due to diffusion across the axis of symmetry (OO' in figure 5.1). As sketched in figure 5.1, a region of rotational flow rising along with the vortex ring was postulated; Turner illustrated this moving region via a shadowgraph picture of a buoyant vortex ring, see Turner ([2], figure 7). Second, Turner assumed that no vorticity was diffused across the boundary of the bulk fluid region $\boldsymbol{B}$, that is, no vorticity was lost to a wake [2]. In view of the aforementioned assumptions, circulation remains constant since vorticity is constant, and, the viscous effect is negligible in the force balance since there is no momentum loss in a viscous wake. These assumptions also underlay some later theoretical and numerical analyses such as those of Walters and Davidson [3], Pedley [4] and Lundgren and Mansour [6]. Turner predicted that a ring bubble expands radially as it rises [2];

$$R_T = (R_0^2 + \frac{Ft}{\pi\Gamma})^{\frac{1}{2}} \tag{5.1}$$

where R_0 is the initial radius of the vortex ring, t stands for time and F is defined as $g\Omega(\rho\text{-}\rho\prime)/\rho$ in which Ω is volume of the vortex ring, ρ is the density of water and $\rho\prime$ is the density of air. The rising velocity, however, decreases as

$$u_T = \frac{c\Gamma}{R_T} \tag{5.2}$$

where c is constant. In the present paper, §5.5.2, a comparison is drawn with the expansion of the vortex ring bubble generated by the bursting balloon and those given by equation 5.1. In addition to this analytical theory, Turner also performed some experiments and realized the rather unexpected conclusion that for a given circulation, increasing the buoyancy force decreases the rising velocity [2]. Furthermore, he found that increasing the buoyancy force gives a greater rate of expansion; our mathematical model presented in §5.3.2 confirms this observation by demonstrating that the ring expansion is basically caused by the buoyancy force.

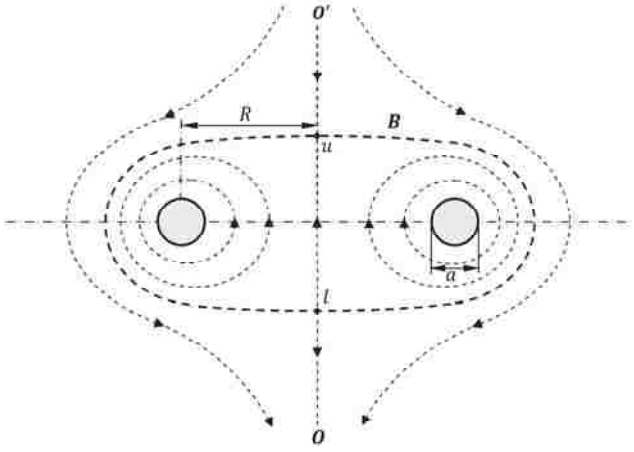

FIGURE 5.1: $\boldsymbol{B}$ is the boundary of the bulk fluid carried along with the vortex ring; within this region the flow is rotational whereas the ambient flow is irrotational. The shape of the boundary $\boldsymbol{B}$ depends on the ratio R/a where R and a respectively represent the ring and core radii; at R/a<14, it looks like an oblate spheroid, as R/a increases points u and l approach each other and eventually meet at R/a=86 forming a toroidal region.

Turner's [2] findings on the general properties of a vortex ring were later confirmed by Pedley's [4] analytical solution. Pedley [4] demonstrated that the vortex ring radius increases as t and the rising velocity decreases as $t^{-\frac{1}{2}}$ which is in accordance with equation 5.2. Besides tracing these properties, he investigated the stability of the vortex ring and predicted that the vortex ring will eventually break up since the stabilizing influence of the circulation decreases as the velocity at the bubble surface decreases through the action of viscosity. Further to this, the destabilizing effect of surface tension increases as the diameter of the core decreases with the vortex ring expansion. He expressed the critical time t_c, the time at which a vortex ring breaks down, as

$$t_c = \frac{3\Gamma}{16\pi\nu}\left(\frac{\rho a^3}{T}\right)^{\frac{1}{2}} \tag{5.3}$$

Equation 5.3 is valid only if the Weber number $We{=}\rho\Gamma^2/4\pi^2 a\,T$ is much larger than unity. In this equation, T stands for the surface tension of water in contact with air, and, ρ and ν are density and viscosity of water respectively. It must be considered that equation 5.3 is an implicit

function since a is the core radius at the critical time and must be written in terms of t_c by combining ring volume $\Omega{=}2\pi R(\pi a^2)$ with equation 5.1. For the vortex ring bubbles produced by bursting balloons we found a trend similar to that predicted by equation 5.3, i.e. as the circulation increases the bubble becomes more stable (see §5.5).

Similar to the Turner's [2] theory, constant circulation is an essential assumption for Pedley's [4] analysis. By deriving a similarity scale, Pedley demonstrated that the time required for vorticity to diffuse to the ring symmetry axis or to the boundary of the rotational flow region $\boldsymbol{B}$ (see figure 5.1) is on the order of a^2/ν which is much greater than the critical time t_c. Hence, before the vorticity starts being cancelled across the symmetry axis or being swept off into a wake, the vortex ring becomes unstable and breaks down; upholding the assumption of vorticity conservation and, consequently, constant circulation. The assumption of constant circulation was also experimentally verified by Walters and Davidson [3]. They generated three vortex ring bubbles with volumes of 21, 43 and 88 cm^3 by rapidly releasing a jet of air at the bottom of a water tank. The circulations associated with these bubbles are reproduced in figure 5.2; relative standard deviation of each case is approximately 7% indicating that the circulation can be considered roughly constant. In addition to experiments, Walters and Davidson [3] applied the initial-motion theory to analytically investigate motion of a vortex ring bubble, assuming it is initially spherical and starts from rest. They found a rough approximation of the circulation in terms of the initial volume Ω_0 as

$$\Gamma = 3g^{\frac{1}{2}}\Omega_0^{\frac{1}{2}}. \tag{5.4}$$

As illustrated in figure 5.2, the circulation obtained from equation 5.4 is roughly in accordance with their experimental measurements; we also found satisfactory agreement between circulations of bubbles produced by the bursting balloons and values determined from equation 5.4 (see §5.5.1). In addition to the circulation, Walters and Davidson [3] investigated the rising velocity. According to them, the bubble starts rising with twice the acceleration of gravity, however, as it travels upward it slows down.

Although numerical simulation of the generation and the translation of an air core vortex ring is technically challenging, a few in-depth CFD analyses such as those of Lundgren and Mansour [6] and Cheng et al. [7] have been performed, revealing interesting details of the phenomenon. Lundgren and Mansour [6] conducted a two-stage numerical simulation using a boundary integral method. In the first stage, it was observed that a liquid jet penetrated through the bubble from below until it impinged on the upper surface and generated a toroidal geometry. Owing to the complicated physics involved in the impingement, they could continue the simulation just until the liquid jet penetrated very close to the upper surface. Then, the second stage of the simulation started from a toroidal bubble, the initial circulation of which was determined from the first stage. Lundgren and Mansour [6] improved Turner's [2] results by solving the force balance equation,

$$\rho A\frac{\mathrm{d}\overrightarrow{u}}{\mathrm{d}t} = \rho\Gamma\widehat{e_t}\times\overrightarrow{u} + \rho A g\,\widehat{e_z} + \overrightarrow{F_T} \tag{5.5}$$

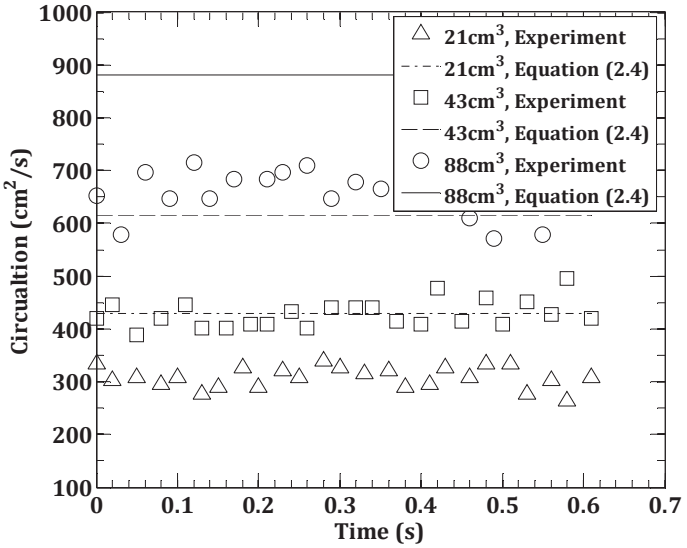

FIGURE 5.2: .
Maximum deviation corresponds to the case of 88 for which relative standard deviation is approximately 7% indicating that circulation can be considered almost constant.]Circulation associated with three vortex ring bubbles with initial volumes of 21, 43 and 88 cm^3; markers represent experimental results and lines correspond to the analytical prediction given by equation 5.4 [3]. Maximum deviation corresponds to the case of 88 for which relative standard deviation is approximately 7% indicating that circulation can be considered almost constant.

where $\overrightarrow{u}$ is velocity of an arbitrary point on the perimeter of the ring relative to the rising velocity of the ring. The left-hand side of equation 5.5 represents the inertia and the right-hand side terms are Kutta-Joukowski lift, buoyancy and surface tension forces respectively. Having no viscous force in the force balance equation is supported by the aforementioned assumptions made by Turner [2]; also see the note by Sirakov et al. [12] on irrotational viscous flow. Solving equation 5.5 yields,

$$R = R_T - \frac{1}{\Gamma^2}\frac{4}{9}\frac{\sin\tau}{R_T^{\frac{1}{2}}R_0^{\frac{3}{2}}} \tag{5.6}$$

where $\tau=\frac{3}{4}\Gamma^2(R_T^3\text{-}R_0^3)$. Equation 5.6 corrects the Turner's [2] radius (equation 5.1) by introducing a sinusoidal term, note the inverse effect of the initial condition (R_0) on the amplitude of oscillations. Although this equation suggests no phase difference in oscillations of the fluid particles located on the ring perimeter, it seems to be related to the azimuthal waves described by Krutzsch [13] and Maxworthy [14]; this was confirmed by Lundgren in a private communication. We believe the energy consuming oscillations described by equation 5.6 may be a reason for the continuous decrease in the rising velocity of a vortex ring bubble.

5.3 Model

In this section, the model developed by Sullivan et al. [8] is first recapitulated and then reformulated to be applicable for buoyant vortex rings. At the outset, consider equations 5.7 to 5.9 respectively for impulse P, energy E and velocity V of vortex rings

$$P = \rho\Gamma\pi R^2, \tag{5.7}$$

$$E = \frac{1}{2}\rho\Gamma^2 R \times (\ln(\frac{8R}{a}) - \alpha), \tag{5.8}$$

$$V = \frac{\Gamma}{4\pi R} \times (\ln(\frac{8R}{a}) - \beta). \tag{5.9}$$

Parameters α and β depend on the core models; for the viscous cores they are 2.040 and 0.558 while for the solid rotating cores they are 7/4 and 1/4 respectively.

5.3.1 Sullivan et al.'s model [8]

Based on their experiments, Sullivan et al. [8] constructed a mathematical model for vortex rings generated by fast injection of fluid via a piston/cylinder mechanism, namely a vortex gun. Accordingly, the momentum of the fluid displaced by the piston P_P was assumed to be equal to the impulse of the vortex ring P_V. Using equation 5.7

$$\rho\Gamma\pi R^2 = \rho\pi {R_0}^2 L V_P \tag{5.10}$$

where R_0, L, V_P and R are the initial radius of the piston, length of the cylinder, velocity of the piston and radius of the vortex ring respectively. Thus, the circulation can be expressed in terms of vortex gun parameters as

$$\Gamma = \frac{{R_0}^2 L V_P}{R^2} \tag{5.11}$$

suggesting that the circulation increases with the volume of the cylinder and the velocity of the piston.

In addition to the circulation, Sullivan et al. [8] modeled the slowing down of the vortex ring by considering the concept of drag. Drag force causes the impulse of the vortex ring to decrease given by

$$\frac{dP}{dt} = -D_f = -C_d \times \frac{1}{2}\rho V^2 \times 4\pi a R \tag{5.12}$$

where C_d is the drag coefficient, V is the rise velocity, a is the radius of the core and R is the radius of the vortex ring. Combining equations 5.7, 5.9 and 5.12 yields the following homogeneous differential equation

$$\frac{dV}{dt} = \frac{\Lambda a}{2\pi R^2} C_d V^2 \tag{5.13}$$

in which $\Lambda = ln(8R/a) - \beta$. Solving equation 5.13 for the rise velocity yields

$$V = \frac{V_0}{1 + V_0 ct} \tag{5.14}$$

where V_0 is the initial velocity of the vortex ring and c is the decay coefficient defined as $c = \Lambda a C_d / 2\pi R^2$. One fundamental assumption to obtain equation 5.14 is that the radius of the vortex ring does not vary as it travels through the fluid. It is noteworhty that for long times equation 5.14 agrees with the Maxworthy's [14] prediction that the rising velocity decreases as t^{-1}.

5.3.2 Modified model

Unlike the approach adopted by Sullivan et al. (2008), it is not possible to construct a model for a vortex ring bubble produced by an underwater bursting balloon through the impulse equation (equation 5.7), since there is no moving piston to equate its momentum to the initial impulse of the vortex ring. Instead, one can assume that the initial energy of the vortex ring bubble is approximately equal to the potential energy of compressed air stored in the underwater balloon. Assuming an isothermal compression process, the potential energy stored in the balloon is given by

$$U_c = P_0 \Omega_0 ln(\frac{P_{amb}}{P_0}) \tag{5.15}$$

where P_0, Ω_0 and P_{amb} are initial pressure of the balloon, initial volume of the balloon and ambient pressure respectively. Equating this to equation 5.8

$$\frac{1}{2}\rho\Gamma^2 R(ln(8R/a) - \alpha) = P_0 \Omega_0 ln(\frac{P_{amb}}{P_0}) \tag{5.16}$$

Considering $P = \rho g h$ and $\Omega = 4\pi r^3/3$, equation 5.16 can be written as

$$\Gamma = (\frac{8\pi g}{3} \times \frac{{r_0}^3 (h_0 + h_{amb}) ln(\frac{h_{amb}}{h_0})}{R_0 \Lambda\prime})^{\frac{1}{2}} \tag{5.17}$$

where $\Lambda\prime = ln(8R_0/a) - \alpha$, h_0 is the initial depth of the underwater balloon, h_{amb} is the atmospheric pressure in meter of water and r_0 is equal to the radius of a perfect sphere with the same volume of the balloon, namely equivalent radius. An interesting analogy can be drawn between equations 5.11 and 5.17. Equation 5.11 suggests that the circulation of the vortex ring produced via a piston/cylinder mechanism depends on the displacement volume of the cylinder and the velocity of the piston, whereas according to equation 5.17, the circulation of the vortex ring produced by an underwater bursting balloon depends on the volume of the balloon and the depth at which the balloon bursts. Therefore, the effect of balloon volume is similar to the effect of cylinder volume and the effect of bursting depth is similar to the effect of piston velocity;

both cause the circulation to increase. Moreover, equation 5.17 agrees well with equation 5.4 demonstrating that the circulation of the vortex ring is a function of $\Omega_0^{\frac{1}{2}}$.

To model the slowing down of the vortex ring we add the buoyancy force F_B to the Sullivan et al's. [8] force balance equation (equation 5.12) to give the following inhomogeneous differential equation

$$\frac{dP}{dt} = -D_f + F_B = -C_f \times \frac{1}{2}\rho V^2 \times 4\pi aR + F_B \tag{5.18}$$

in which C_f is the force coefficient representing all effective forces including viscous force, Kutta-Joukowski lift force, surface tension force etc. – except buoyancy force. We can start solving equation 5.18 from the assumption made by Sullivan et al. [8] that the radius of the vortex ring does not significantly change with time. Accordingly, the rise velocity converges to the constant value of $V{=}\sqrt{\pi ag/c_f}$ for long times. Although this solution qualitatively confirms the solution offered in Joseph et al. [5], it is in contrast with our preliminary experimental observations. The disparity is owed to the assumption of constant radius. To resolve this, the radius is considered to be a time dependent variable. The circulation, however, is assumed to be constant on the basis of equations 5.17 and 5.4. The validity of this assumption is further confirmed by our experimental measurements presented in §5.5.1. Combining equation 5.18 with equations 5.7 and 5.9 under the assumption of constant circulation yields

$$\frac{dR}{dt} = C_1 \frac{(ln(C_2 R\sqrt{R}) - \frac{1}{4})^2}{R^2\sqrt{R}} + \frac{C_3}{R} \tag{5.19}$$

where $C_1 = -\sqrt{6}\Gamma C_f/48\sqrt{\pi^5}$, $C_2 = 4\sqrt{6\pi}$ and $C_3 = F_B/2\pi\Gamma$. All parameters appearing in equation 5.19 including those with dimension of length, time, velocity, circulation and force are normalized using r_0, $(r_0/g)^{1/2}$, $(gr_0)^{1/2}$, $(gr_0^3)^{1/2}$ and $\rho g r_0^3$ respectively, where ρ is density of water, g is the gravitational acceleration and r_0 is the equivalent radius. Although equation 5.19 is highly non-linear with no general solution, one can produce a semi-analytical solution using perturbation technique (see Chapter 6); then, substituting the calculated radius into equation 5.9 yields the rise velocity. As a preliminary analysis, basic scaling can be used to qualify the solution of equation 5.19 by estimating the order of magnitude of each term. Note that the value of the dimensionless radius R in equation 5.19 is always larger than unity, i.e. the radius of the vortex ring bubble is always larger than the equivalent radius of the balloon r_0. Therefore, on the right-hand side, the order of magnitude of the second term, i.e. buoyancy term, is significantly greater than the order of magnitude of the first term, i.e. viscous term, since the exponent of radius in the denominator of the second term is smaller than that of the first term. It is worth mentioning that the disparity between the order of magnitude of the viscous term and the order of magnitude of the buoyancy term on the right hand side of equation 5.19 increases with time, since these terms are inversely correlated to the ring radius and the vortex ring bubble expands as it rises. It is now noteworthy to recall equation 5.5. Lundgren and Mansour [6] did not include a drag force in this equation on the basis of Pedley's [4] theory that the vortex ring bubble is predicted to become unstable before the vorticity generated at the bubble surface diffuses through the boundary of the rotational region (see figure 5.1). Comparing the order of magnitude of the right hand side terms of equation 5.19 reveals that even if the vorticity

diffuses into the surrounding fluid, the effect of the drag force is minimal in comparison with the buoyancy force. Equating the order of magnitude of the left hand side of equation 5.19 with the order of magnitude of the dominant term of the right hand side of this equation yields

$$\frac{\Delta R}{t} \sim \frac{C_3}{R}, \tag{5.20}$$

therefore,

$$\Delta R \sim \frac{F_B t}{2\pi\Gamma R}. \tag{5.21}$$

One immediate outcome of equation 5.21 is the direct relation between expansion of the vortex ring and buoyancy force. Accordingly, buoyancy force is what causes the radius of the vortex ring to increase; this clearly reveals why the radius of the non-buoyant vortex rings studied by Sullivan et al. [8] did not increase with time. One important point to consider is that although no buoyancy force acts on the non-buoyant vortex rings, they still radially expand as they advance. According to equation 5.19, this expansion occurs under the action of viscous force and inertia and is considerably lower than the radial expansion of a similar buoyant vortex ring. Solving equation 5.21 for radius R yields

$$R \sim \ R_0 + (\ R_0 + \frac{F_B t}{\pi\Gamma})^{\frac{1}{2}}. \tag{5.22}$$

This order of magnitude is in good agreement with Turner's [2] radius equation (equation 5.1; $R = (\ R_0^2 + \frac{Ft}{\pi\Gamma})^{\frac{1}{2}}$). More is said regarding equations 5.17, 5.19, 5.21 and 5.22 in the results and discussion section (§5.5).

5.4 The experiment

The experiments reported in this study were conducted in a large plexiglass tank that was 4.2 m long, 2.5 m wide and 2.4 m high. The experimental setup is sketched in figure 5.3. As illustrated in this figure, an air-filled balloon (#1) was gently pulled down via a thin nylon line (#2) which was attached to a winch (#3) through a pulley system (#4). Once impressed on the sharp pin (#5), the balloon burst and a vortex ring bubble was produced; a hypodermic needle with outer diameter of 0.4 mm was chosen to perform as the pin. Similar to Hershberger et al. [10], all the experimental data were obtained photographically. Three cameras (#6-8) with speed of 60 frames per second at high resolution of 1080P were configured above and on two orthogonal sides of the tank to record the generation and the motion of the vortex ring bubble. The videos were then analyzed frame by frame using MATLAB image processing toolbar to deduce the elevation and dimensions of the vortex ring bubble. The rate of expansion $\frac{\mathrm{d}R}{\mathrm{d}t}$ was calculated using the measured ring radius, and the rising velocity V was obtained from the measured elevation. Substituting the rising velocity and the dimensions of the ring in equation 5.9 yields circulation as

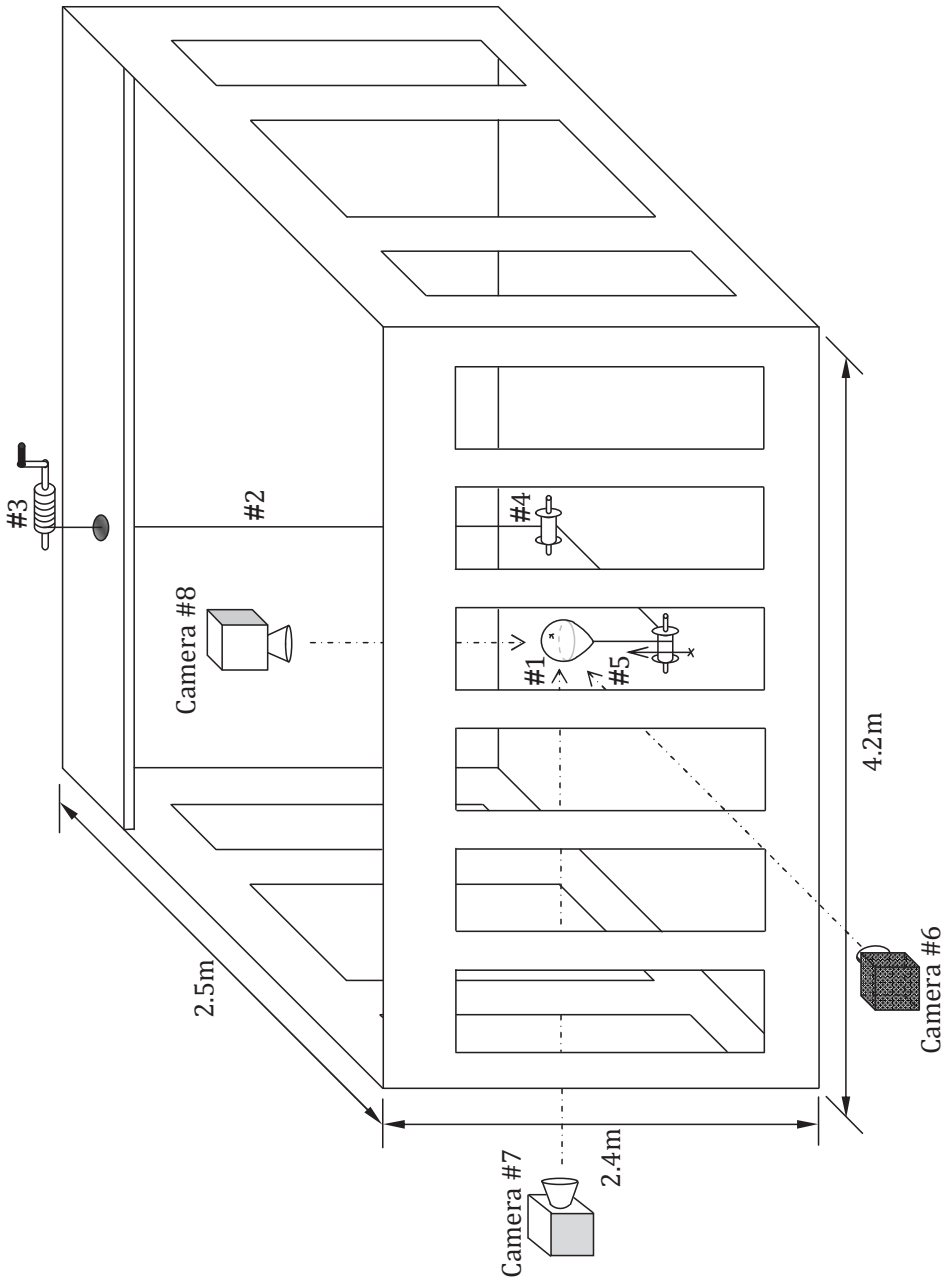

FIGURE 5.3: Sketch of the experimental setup; #1: balloon, #2: nylon line, #3: winch, #4: pulley system, #5: sharp needle, #6-8: cameras.

$$\Gamma = 4\pi R \times V \times (\ln(\frac{8R}{a}) - \frac{1}{4})^{-1}. \tag{5.23}$$

Similar to equation 5.19, all measured parameters including those with the dimension of length, time, velocity, acceleration and circulation were made dimensionless using r_0, $(r_0/g)^{1/2}$, $(gr_0)^{1/2}$, g and $(gr_0^3)^{1/2}$ respectively, where g is the gravitational acceleration and r_0 is the equivalent radius of the balloon.

The reciprocal of dimensionless surface tension, the so-called Bond number, given by

$$Bo = S^{-1} = \frac{\rho g r_0^2}{T} \tag{5.24}$$

was chosen as the independent variable, where T=72.8×10^{-5} N/cm is water-air surface tension at 20°C. Results were reported for Bond numbers 225±14, 500±10, 750±9 and 1000±7, respectively associated with initial volumes of approximately 334, 946, 1740 and 2676 cm^3. Given uncertainties were obtained from standard deviation of ten individual measurements at a 95% confidence level. The initial volume of each balloon was measured through three independent approaches; Archimedes principle, the displacement volume of the balloon inflation pump through utilization of the Boyle-Mariotte law, and finally MATLAB image processing. The average of the three measurements was considered to represent the initial volume. Note that alternatively, one could use dimensionless surface tension $S = T/(\rho g R_0^2)$ instead of Bond number; therefore, Bond numbers 225, 500, 750 and 1000 could be replaced by dimensionless surface tensions of 0.0040, 0.0020, 0.0013 and 0.0010, respectively.

5.5 Results and Discussion

When a sufficiently large air-filled balloon quickly bursts underwater, a vortex ring bubble will be generated. Note that no vortex ring can be produced if the balloon is not large enough, since the associated small bubble will be easily suppressed by the punctured balloon. Likewise, if the air is released slowly, for instance if the balloon is ripped by a blunt pin, no vortex ring will be generated either, even if the balloon is large; this is similar to the case of tilting an inverted beaker as described by Lundgren and Mansour [6]. To ensure that the wall effects are negligible, the largest vortex ring bubbles included in this study were set to be approximately 2700 cm^3 with an associated dimensionless surface tension of S=0.0010. This leads to a sufficiently low blockage ratio of approximately 1% assuming the vortex ring and the bulk fluid region rising along with it is a bluff body. The smallest vortex ring bubbles we could produce in the tank described in figure 5.3 were approximately 335 cm^3 with an associated dimensionless surface tension of S=0.0040. This is much larger than those generated with previous techniques; for instance, Walters and Davidson [3] generated vortex rings with volume of 21 cm^3 by rapidly releasing a jet of air at the bottom of a water tank. In the conventional techniques the required upward momentum to generate a vortex ring is provided by an external source, for instance a moving piston; therefore, even very small vortex rings can be generated if the input momentum has been sufficiently increased. However, the input momentum of a vortex ring generated by a

bursting balloon is provided through the buoyancy force; when the initial volume of the balloon was less than approximately 335 cm^3 the buoyancy force appeard to be insufficient to provide the momentum required for the vortex ring generation.

For the case of S=0.0040, the vortex ring appeared markedly unstable and broke down into small spherical cap bubbles after approximately 2.5 sec at an elevation of approximately z=1.25m above the initial level of the balloon. According to Cheng et al. [7] the number of spherical cap bubbles that a vortex ring bubble breaks into is equal to the number of the azimuthal waves generated on the ring perimeter. In Cheng et al.'s [7] simulation, the number of waves was set to be 8, in our experiments; however, it appeared to vary from run to run. Vortex ring bubbles with dimensionless surface tension of S=0.0020, however, did not break down before reaching the free surface at z=2m. By decreasing the dimensionless surface tension to S=0.0013 and then to S=0.0010 vortex ring bubbles appeared to become progressively more stable and stronger, indicating that the lower dimensionless surface tension (i.e. higher Bond number) causes the lifetime of the vortex ring to increase. In other words, the lifetime of vortex rings appears to be limitted by the amount of surface tension instability. This trend is consistent with equation 5.3 proposed by Pedley [4], but in contrast with data reported by Cheng et al [7]. According to Cheng et al. [7], as the Bond number decreases, the vortex ring becomes more stable and its lifetime increases. It must be mentioned that their simulation was conducted over a very different range of $30 \leq Bo \leq 100$ which is notably smaller than the Bond number of the vortex ring bubbles studied herein. The vortex ring instability can also be attributed to the oscillations described by equation 5.6. The amplitude of those destructive oscillations is directly proportional to the dimensionless surface tension; therefore, when the dimensionless surface tension increases, the vortex ring will be subjected to stronger oscillations, consequently, it will not survive as long. The azimuthal waves described by Krutzsch [13] and Maxworthy [14] could be cited as another reason for vortex ring breakdown. In addition, the process of destabilization is presumably accelerated by the external influences, for instance, the punctured balloon; which is entrained by the vortex and subsequently marks ring rotations at the bubble surface as it travels with it. There is also slight distortion caused by the pin at the instant of bursting.

In the following sections the radius, the trajectory, the circulation, the rise velocity and the energy balance of the vortex ring bubbles generated by a bursting balloon are investigated over the range of S=0.0010-0.0040.

5.5.1 Circulation

In contrast to the vortex ring guns where the circulation is produced by viscous separation at the exit hole [14], the circulation associated with a vortex ring produced by a bursting balloon is generated by the inertial process of the toroid formation through which a gravitationally driven liquid tongue penetrates into the droplet shaped bubble from the bottom, impinges on the upper surface and escapes out of the bubble; this makes the fluid rotate around an imaginary axis forming the vortex ring bubble. Figure 5.4 attempts to illustrate the described process via a time-sequence of frames; panel (a) corresponds to the moment right after the bursting, and panel

(j) shows the approximate moment at which the vortex ring is formed. Due to opaque surface of the bubble it is difficult to visualize the penetrating tongue.

Figure 5.5 compares circulations associated with different dimensionless surface tensions; these values are calculated using equation 5.24. It is observed that circulation increases as the Bond number, i.e. the balloon size, increases. This observation agrees well with what was predicted by equation 5.17 according to which at a specific depth the circulation of the vortex ring directly depends on the initial volume of the balloon. In other words, a greater initial potential energy causes circulation to increase. This is logically consistent with the case of vortex ring gun where circulation increases with the speed of the piston, i.e. higher initial kinetic energy (Sullivan et al. [8]). In other words, regardless of the technique used to produce the vortex ring, circulation is a direct function of initial energy. As is seen, at a specific dimensionless surface tension, circulation is approximately constant with respect to time; maximum relative standard deviation is approximately 6% which is lower than that associated with Walters and Davidson's [3] measurements (see figure 5.2). Measured circulations are compared with those estimated by equation 5.4; fairly good agreement is found. The disparity can be attributed to the basic assumption made in the derivation of this equation that the bubble is initially spherical, whereas in our experiments the bubble was initially droplet shaped. It is of note to mention that the experimental results here compare much better with equation 5.4 than those of Walters and Davidson [3], this is likely due to the completely different test conditions and vortex generation techniques (see figiure 5.2). As is observed in figure 5.5, measured circulations are also consistent with those of equation 5.17. The overestimation is due to the assumption underlying this equation; that the initial potential energy stored in the balloon entirely converts to the kinetic energy of the vortex ring. In other words, viscous dissipation from the moment of bursting (see figure 5.4(a)) to the moment of vortex ring formation (see figure 5.4(j)) is not taken into account. Hence, calculating the difference between the energy associated with the measured initial circulation and the energy associated with the circulation estimated through equation 5.17 yeilds the amount of energy dissipated during the vortex ring formation process. For dimensionless surface tension of 0.0010, almost 50% of the initial potential energy stored in the balloon was found to be dissipated during the vortex ring bubble formation, this value was increased to 70% for dimensionless surface tension of 0.0040.

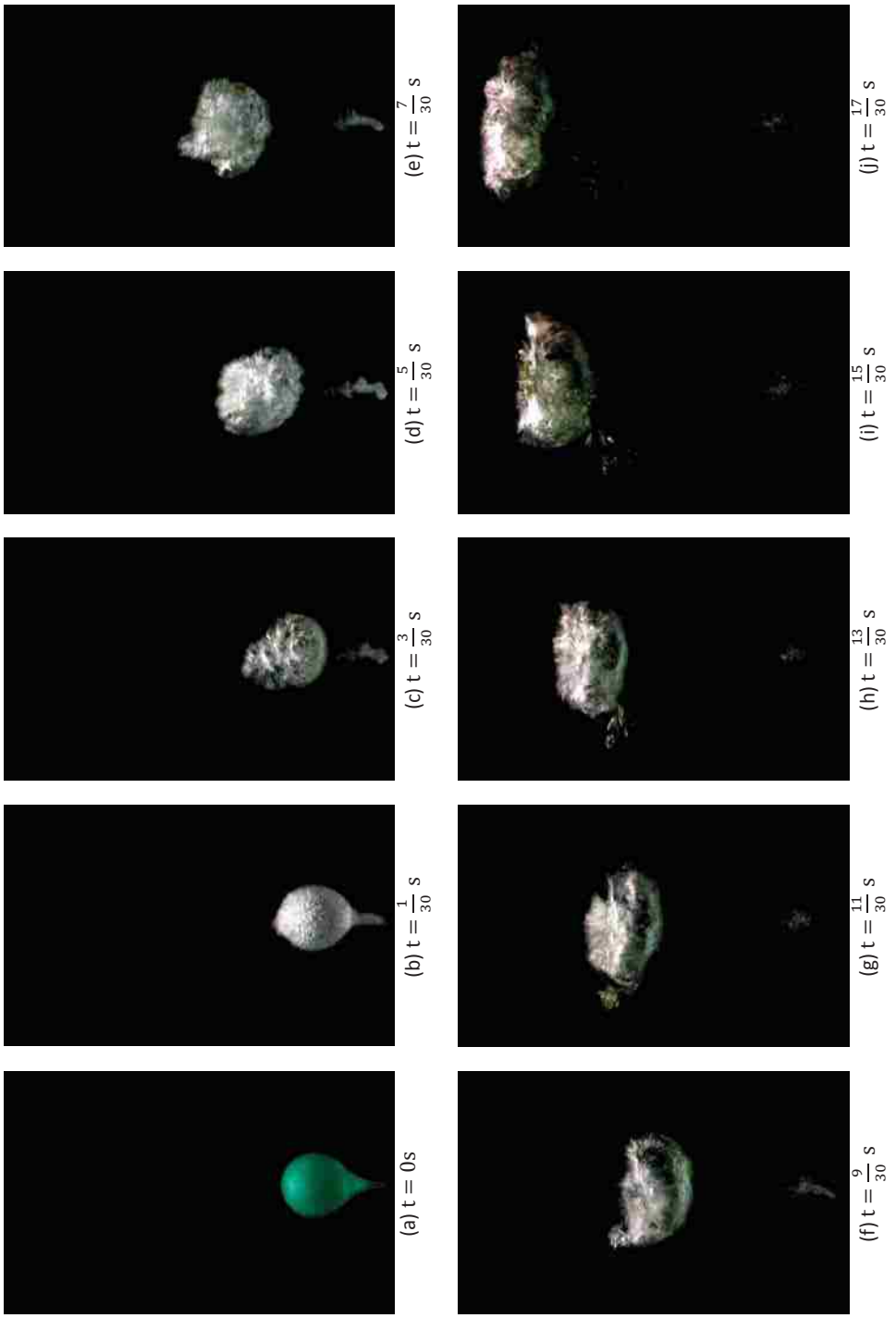

FIGURE 5.4: Vortex ring bubble formation, S=0.0010.

5.5.2 Radius

The effect of dimensionless surface tension on the radius of vortex ring bubbles is illustrated in figure 5.6. As is observed in panel (a), at a fixed dimensionless surface tension, the vortex ring radius increases with time. Panels (b) to (e) compare measured ring radius with the Turner's [2] radius (equation 5.1); a good qualitative agreement is observed. Measured data were also compared with the order of magnitude given by equation 5.22; although this equation was obtained from a very simple basic-scaling analysis it appeared to predict the ring radius as well as the Turner's [2] equation. Although the experiment was carefully controlled to minimize the effect of the initial conditions the repeatability needs to be assessed by estimating the precision of individual measurments. Error bars shown in panels (b) to (e) represent precision of ten individual measurments at a 95% confidence level. For visual clarity, error bars are shown only on typical data points. As is suggested by equation 5.21 the radial expansion of the vortex ring bubbles is essentially due to the buoyany force. According to equation 5.21, one expects to see a one order-of-magnitude change in the rate of expansion by increasing the dimensionless surfcae tension from 0.0010 to 0.0040 since the buoyancy force decreases approximately 10 times. It is observed that the dimensionless radius increases with the dimensionless surface tension; the rate of expansion, however, appeared to remain constant. This is due to the inverse correlation of circulation with the rate of expansion; as was observed in figure 5.5, circulation increases with the buoyancy force. In addition to equation 5.21, the underlying physics of the ring expansion can also be explained using equation 5.6 proposed by Lundgren and Mansour [6]. Considering the upward buoyancy force and the radially inward surfaces tension force, a downward component of the Kutta-Joukowski lift force must exist, since the bubble rises with a negative acceleration (see equation 5.2). As is illustrated in figure 5.7, to have a downward Kutta-Joukowski lift force there must be a radial velocity component u_R demonstrating the radial expansion of vortex ring bubbles.

It is worthwhile to mention that the small fluctuations of the ring radius observed in figure 5.6 can be attributed to the azimuthal waves described by Krutzsch [13] and Maxworthy [14]. The mentioned fluctuations are more considearble at lower dimenionless surface tensions, particularly at early times. Figure 5.8 tries to give a visual impression of these waves on the perimeter of vortex ring bubble through a time-series of snapshots at S=0.0010. Panel (a) represents the approximate moment at which the azimuthal waves were visualised for the first time, and panel (n) depicts the vortex ring at the moment that the free surface starts bowing; beyond this moment the vortex ring will be affected by the free surface (free surface is not shown in the figure). Note that the bubble depicted in figure 5.8 corresponds to early times of the vortex ring illustrated in figure 5.4.

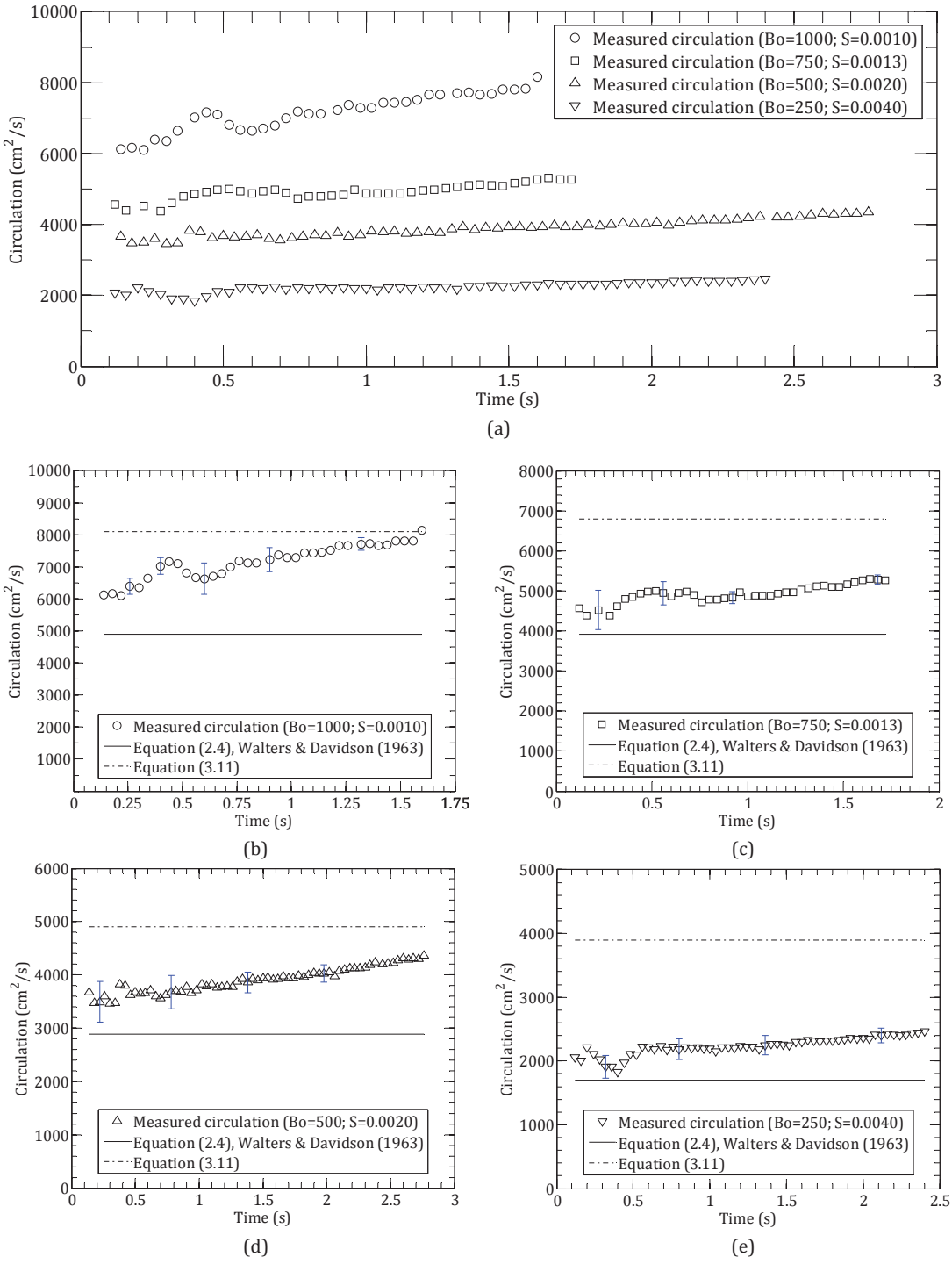

FIGURE 5.5: Circulation associated with dimensionless surface tensions ranging from S=0.0010 to S=0.0040; markers represent measured values, solid lines show values estimated through equation 5.4 and dash-dot lines correspond to those predicted by equation 5.17.

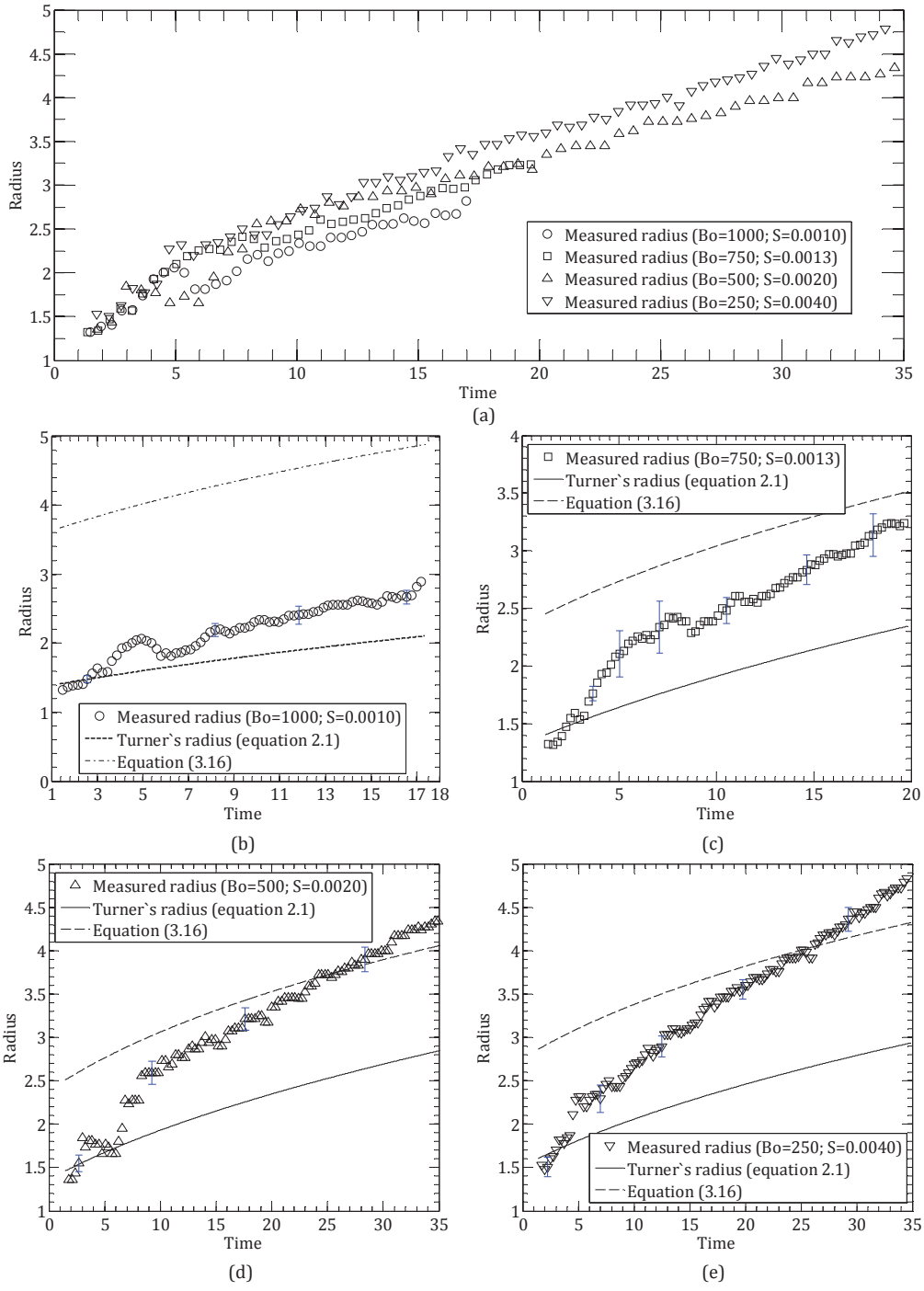

FIGURE 5.6: (a): Influence of dimensionless surface tension on the dimensionless vortex ring radius, (b) to (e): comparing measured radius of vortex ring bubbles with values predicted by equations 5.1 and 5.22.

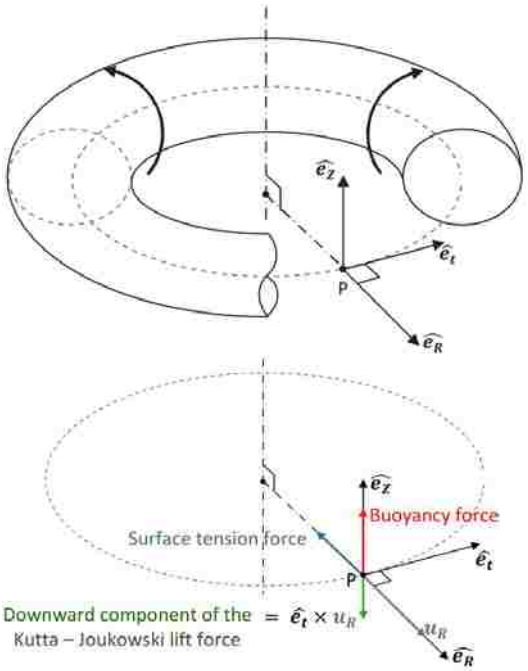

FIGURE 5.7: The radial expansion of the vortex ring bubble, u_R, leads in a downward Kutta-Joukowski lift force, $\widehat{e_t} \times u_R$, which is necessary to balance the buoyancy force and inertia effect.

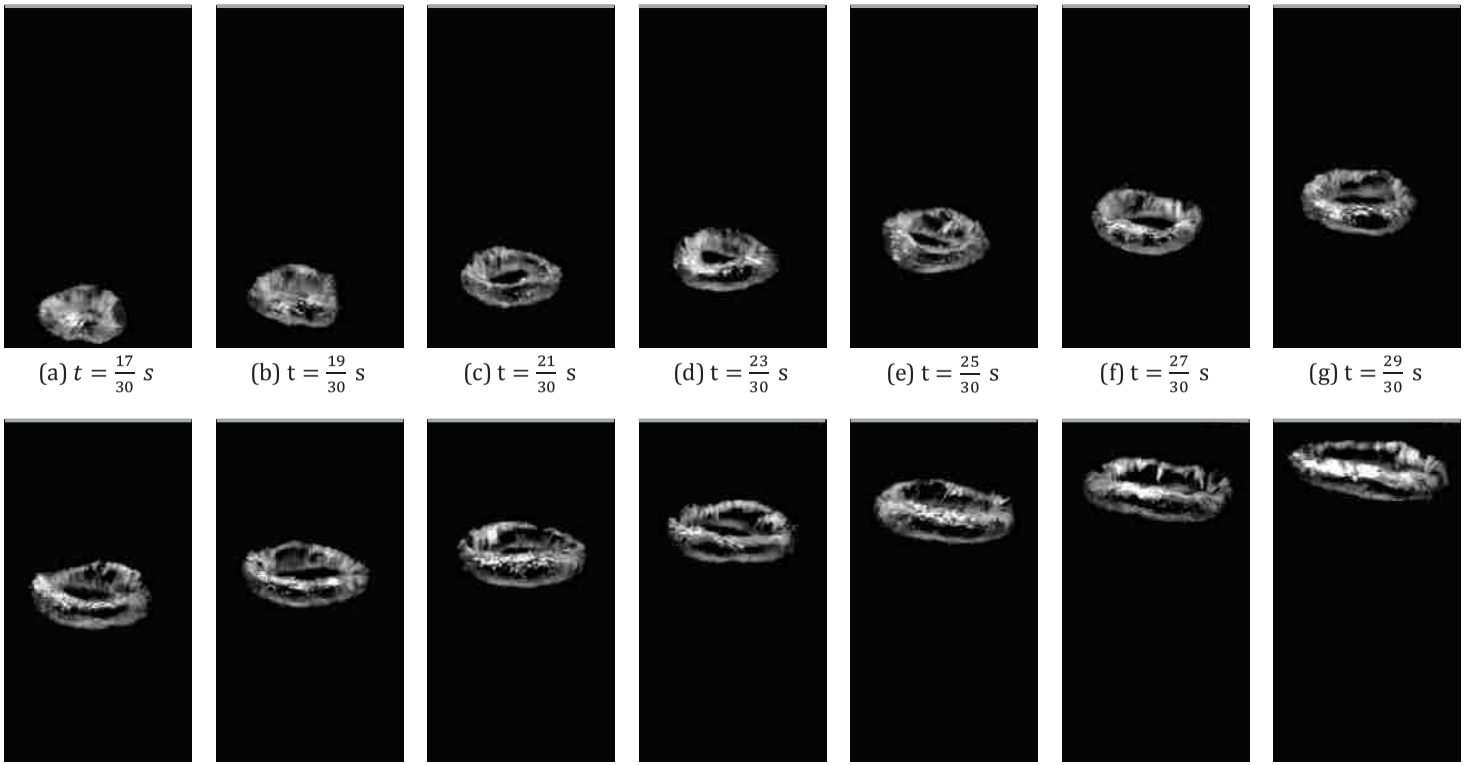

FIGURE 5.8: Translation of the vortex ring bubble corresponding to the case of S=0.0010. This corresponds to later times of the vortex ring illustrated in figure 5.4.

5.5.3 Trajectory

Figure 5.9 illustrates trajectory of the core centre of the vortex ring bubble at the dimensionless surface tensions studied herein. Note that the elevation and radius of each case have been made dimensionless using the corresponding equivalent radius r_0 (see §5.4). As is observed, the trajectory of each case is roughly linear; the slope slightly decreases with the dimensionless surface tension. According to figure 5.9, as the dimensionless surface tension increases, the vortex ring bubble forms at a higher dimensionless elevation. Similarly, the larger dimensionless surface tension leads to a larger initial dimensionless radius.

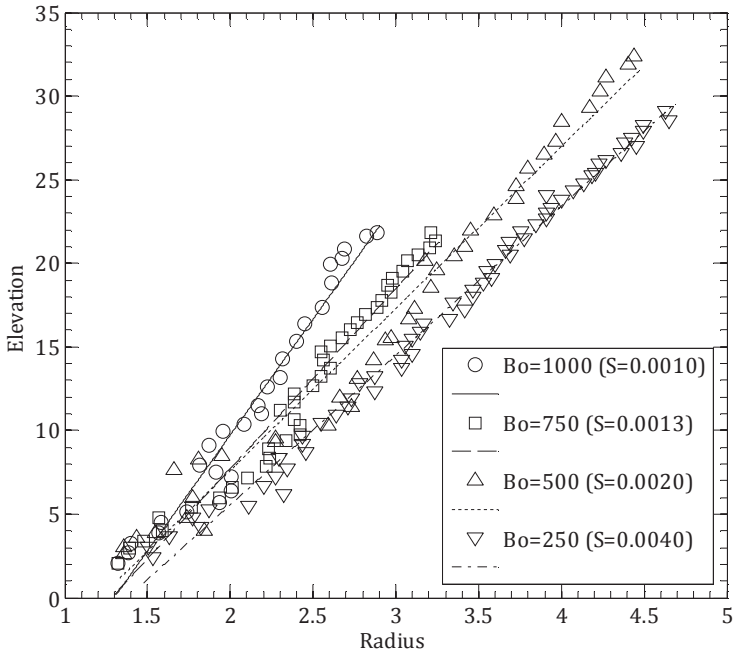

FIGURE 5.9: Effect of dimensionless surface tension on the trajectory of the core centre.

5.5.4 Rise Velocity

Figure 5.10 illustrates the effect of dimensionless surface tension on dimensionless rising velocity. As is observed, rise velocity increases as the dimensionless surface tension decreases. It is also observed that at a fixed dimensionless surface tension, rise velocity decreases with time. This trend is in agreement with Hick's equation (equation 5.7). According to Hick's equation, and considering the fact that vortex rings expand as they rise, rising velocity decreases with time. The velocity reduction illustrated in figure 5.10 also agrees with Turner's [2] velocity u_T (equation 5.2). A similar trend is observed in Walters and Davidson's [3] experiments and Cheng et al.'s [7], simulations.

A number of physical factors can be listed for the slowing down of vortex ring bubbles. This can be attributed to energy consuming oscillations described by equation 5.6; the energy of the oscillations is supplied from mechanical energy of the vortex ring, therefore, the total mechanical

energy of the vortex ring decreases with time, causing deceleration. A similar interpretation can be made for those azimuthal waves visualised in figure 5.4; waves extract energy from the vortex ring bubble, slowing its motion. Another suggestion is the entrainment process [14]. Velocity depends upon the amount and distribution of vorticity, and due to the entrainment process, the vorticity generated at the bubble surface is distributed over a larger region of the bulk fluid as the bubble rises. This may cause continuous reduction in rise velocity. Viscous dissipation also is likely to be influential on the deceleration of the vortex ring bubbles.

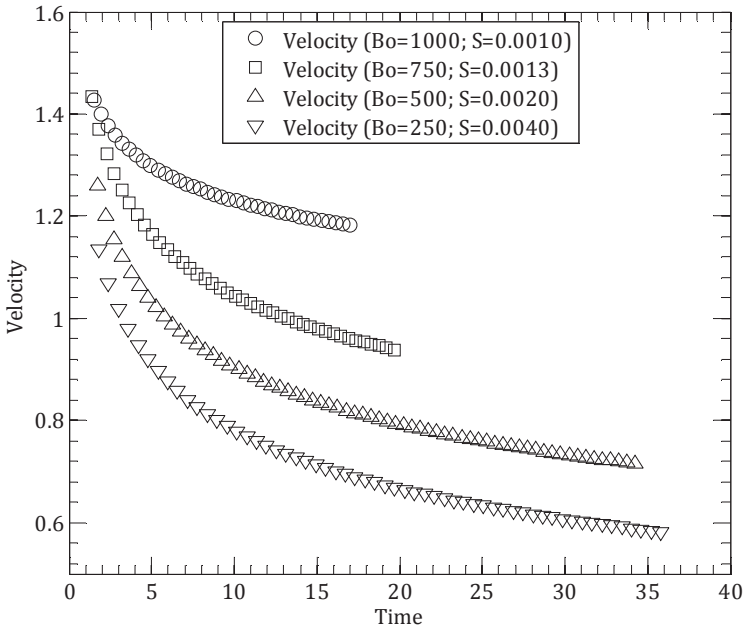

FIGURE 5.10: Effect of dimensionless surface tension on dimensionless rising velocity.

5.6 Conclusion

We examined some of the basic dynamic features and stability characteristics of vortex ring bubbles. The primary motivations for this work were investigating flow generated by a balloon bursting underwater, modifying Sullivan et al.'s [8] drag-based model to include buoyant vortex rings and studying large vortex rings with Bond numbers up to 1000. Notable observations from the conditions studied are summarized as follows:

- A basic scaling analysis demonstrated that the significant radial expansion of vortex ring bubbles is essentially due to the buoyancy force. The effect of buoyancy in the momentum balance was found to be much greater than the effect of the viscous force, the difference was found to increase with time.
- An expression for the circulation was obtained according to which the circulation increases with the volume of the balloon and the depth at which the balloon bursts. Comparing the measured circulations with those predicted by this expression demonstrates the considerable viscous dissipation through the vortex ring formation process.

- For dimensionless surface tension of 0.0010, almost 50% of the initial potential energy stored in the balloon was found to be dissipated during the vortex ring bubble formation, this value was increased to 70% for dimensionless surface tension of 0.0040.
- Vortex ring bubbles were found to have a finite lifetime. As the dimensionless surface tension decreased, the structure of vortex ring bubble became more coherent and it survived longer.
- It was observed that vortex ring bubbles expand as they rise. The rate of expansion appeared to remain approximately constant with respect to dimensionless surface tension.
- Non-dimensional radius was found to be larger as dimensionless surface tension increased.
- Circulation appeared to be inversely proportional to dimensionless surface tension. However, for a given dimensionless surface tension, it was approximately constant with respect to time. Vortex ring bubbles were found to decelerate as they rise. The rising velocity was faster at lower dimensionless surface tensions.
- The trajectory of the core centre of vortex ring bubbles were found to be approximately linear; with line slope slightly decreasing with dimensionless surface tension.

Acknowledgements

The authors are deeply indebted to Professor Timothy J. Pedley, Professor Tom Lundgren and Professor Russell Donnelly for their helpful comments. This work is made possible by the Natural Sciences and Engineering Research Council of Canada and the Ontario Trillium Foundation.

References

[1] Reynolds, O., 1876. On the resistance encountered by vortex rings and the relation between the vortex rings and the streamlines of a disk. Nature, 14, 477-479.

[2] Turner, J. S., 1957. Buoyant vortex rings. Proceedings of the Royal Society A: Mathematical, Physical and Engineering Sciences, 239, 61-75.

[3] Walters, J. K., Davidson, J. F. 1963 The initial motion of a gas bubble formed in an inviscid liquid. Journal of Fluid Mechanics, 17, 321-336.

[4] Pedley, T. J., 1968. The toroidal bubble. Journal of Fluid Mechanics, 32, 97-112.

[5] Joseph, D., Funada, T., Wang, J., 2007. Potential Flows of Viscous and Viscoelastic Liquids. Cambridge University Press.

[6] Lundgren, T. S., Mansour, N. N., 1991. Vortex ring bubbles. Journal of Fluid Mechanics, 224, 177-196.

[7] Cheng, M., Lou, J., Lim, T. T., 2013. Motion of a bubble ring in a viscous fluid. Physics of Fluids, 25, 1-19.

[8] Sullivan, I. S., Niemela, J. J., Hershberger, R. E., Bolster, D., Donnelly, R. J., 2008. Dynamics of thin vortex rings. Journal of Fluid Mechanics, 609, 319-347.

[9] Walker, J. D. A., Smith, C. R., Cerra, A. W., Doligalski, T. L., 1987. The impact of a vortex ring on a wall. Journal of Fluid Mechanics, 181, 99-140.

[10] Hershberger, R. E., Bolster, D., Donnelly, R. J., 2010. Slowing of vortex rings by development of kelvin waves. Physical Review E, 82, 036309.

[11] Gan, L., Dawson, J. R., Nickels, T. B., 2012. On the drag of turbulent vortex rings. Journal of Fluid Mechanics, 709, 85-105.

[12] Sirakov, B. T., Greitzer, E. M., Tan, C. S., 2005. A note on irrotational viscous flow. Physics of Fluids, 17 (10), 1-3.

[13] Krutzsch, C. H., 1939. Ber eine experimentell beobachtete erscheinung an wirbelringen bei ihrer translatorischen bewegung in wirklichen ssigkeiten. Annalen der Physik–Berlin, 427 (6), 497-523.

[14] Maxworthy, T., 1972 The structure and stability of vortex rings. Journal of Fluid Mechanics, 51, 15-32.

Chapter 6

On the Drag of Buoyant Vortex Rings

A. R. Vasel-Be-Hagh[1], R. Carriveau[1], D. S.-K. Ting[1] and J. S. Turner[2]

1 Turbulence and E nergy Laboratory, Lumley Centre for Engineering Innovation, University of Windsor, Ontario, Canada N9B 3P4

2 Research School of Earth Sciences, Australian National University, Canberra, A. C. T. 0200, Australia

Vasel-Be-Hagh, A. R., Carriveau, R., Ting, D. S.-K. and Turner, J. S. 2015 On the Drag of Buoyant Vortex Rings. Physical Review Letters, under review.

6.1 Introduction

Vortex rings are categorized into buoyant and non-buoyant groups depending on whether they contain a fluid lighter than the surrounding fluid. Drag of non-buoyant vortex rings has been extensively studied by Gan et al. [1]; however, there is a dearth of published research concerning the drag of buoyant vortex rings – although their other overall properties (e.g. circulation, radius, velocity of rise, stability, lifetime etc.) have been widely investigated [2-5]. One of the earliest analytical theories about buoyant vortex rings, also called vortex ring bubbles or toroidal bubbles, was developed by Turner [3], predicting that a rising buoyant vortex ring expands radially as

$$R_T = (R_0^2 + \frac{Ft}{\pi\Gamma})^{1/2} \tag{6.1}$$

where R_T, namely Turner's radius, is the radius of the toroid at time t, R_0 is the initial radius of the toroid, Γ is the circulation and F is defined as $g\,V(\rho\text{-}\rho')/\rho$ in which V is the volume of

the toroid, ρ is density of water and ρ' is density of air. Equation. (6.1) was devised under two fundamental assumptions:

I. As sketched in figure 6.1, a region of rotational flow rising along with the vortex ring was postulated. Turner [3] assumed that no vorticity diffuses across the boundary of this region $\boldsymbol{B}$; that is, no vorticity is lost to a wake.

II. Vorticity generated on the surface of the vortex ring was assumed to be confined within a region which never extends to the symmetry axis (OO' in figure 6.1). In other words, no vorticity is cancelled due to diffiusion across the axis of symmetry.

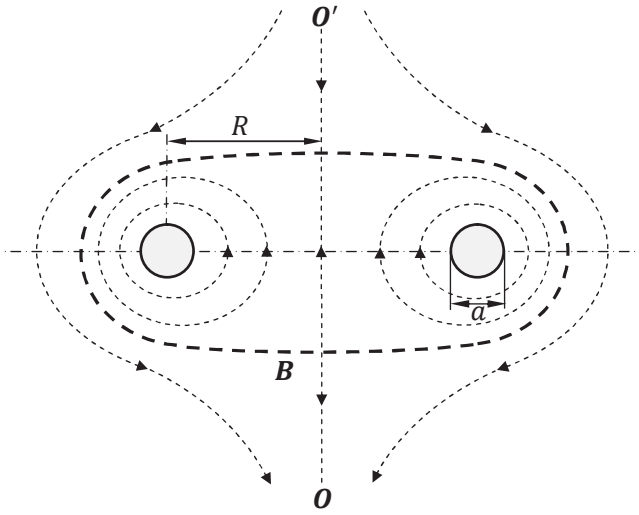

FIGURE 6.1: Schematic sketch of a cross-section through centre of a vortex ring; $\boldsymbol{B}$ is the boundary of the bulk fluid carried along with the vortex ring; within this region flow is rotational whereas the ambient flow is irrotational.

These assumptions also underlay some later theoretical and numerical analyses such as those of Walters & Davidson [4] and Pedley [5]. In view of Turner's assumptions, circulation of buoyant vortex rings remains constant since vorticity is constant, and, the viscous effect is negligible since there is no momentum loss in a viscous wake. In other words, buoyancy is assumed to be the only effective force on the buoyant vortex rings. In a recent study Vasel-Be-Hagh et al. [6] (chapter 5), we proposed a drag-based model to take into account the effect of a viscous force in addition to the effect of a buoyancy force on the radial expansion of buoyant vortex rings. The idea was inspired by the model proposed by Hershberger et al. [7] for non-buoyant vortex rings. Our model was developed on the basis of a force balance equation according to which the impulse of a buoyant vortex ring increases under the action of buoyancy whilst the drag force causes the impulse to decrease as given by

$$\frac{dP}{dt} = F_B - D_f = F_B - C_d \times \frac{1}{2}\rho V^2 \times 4\pi aR \tag{6.2}$$

where F_B is the buoyancy force, C_d is the drag coefficient, V is the rise velocity, a is the radius of the core and R is the radius of the toroid. Consider the following classical equations, respectively for impulse P and velocity V of vortex rings:

$$P = \rho\Gamma\pi R^2 \tag{6.3}$$

$$V = \frac{\Gamma}{4\pi R} \times (\ln(\frac{8R}{a}) - \beta) \tag{6.4}$$

where parameter β depends on the core models; for viscous cores it is 0.558 while for solid rotating cores it is 0.25. Combining Eq. (6.2) with Eqs. (6.3) and (6.4) yields the following nonlinear nonhomogeneous differential equation

$$\frac{dR}{dt} = -C_1 \frac{(ln(C_2 R\sqrt{R}) - \frac{1}{4})^2}{R^2\sqrt{R}} + \frac{C_3}{R} \tag{6.5a}$$

$$R(0) = R_0 \tag{6.5b}$$

where $C_1 = \sqrt{6}\Gamma C_d/48\sqrt{\pi^5}$, $C_2 = 4\sqrt{6\pi}$ and $C_3 = F_B/2\pi\Gamma$. Equation 6.5b is the initial condition for equation 6.5a in which R_0 is the initial radius of the toroid. All parameters appearing in equations 6.5a and 6.5b including those with dimensions of length, time, velocity, circulation and force are normalized using r_0, $(r_0/g)^{1/2}$, $(gr_0)^{1/2}$, $(gr_0^3)^{1/2}$ and $\rho g r_0^3$ respectively, where ρ is the density of water, g is the gravitational acceleration and r_0 is equal to the radius of a perfect sphere enclosing the same volume of air as the initial toroidal bubble. In our recent study [6] (chapter 5), basic scaling was used as a preliminary analysis to qualify the solution of equation 6.5a by estimating the order of magnitude of each term. In the present letter, we propose a semi-analytical solution to this equation using a perturbation technique. This solution introduces a first-order perturbation modification to Turner's radius. It is noteworthy to mention that the modifying term includes the unkown drag coefficient. Substituting the experimentally measured radius into the proposed equation yields the drag coefficient of the associated buoyant vortex ring.

6.2 Model

Considering C_1 as the perturbation parameter, i.e. $\epsilon = C_1$, radius R can be represented by the following expansion in the first-order approximation

$$R = \Re_0 + \epsilon\Re_1 + O(\epsilon^2) \tag{6.6}$$

where $\Re_0$ is the zeroth-order solution and $\epsilon\Re_1$ is the first-order perturbation correction. Substituting equation (6.2) into equations 6.5a and 6.5b, expanding the resulting equations in a power series of ϵ through Taylor series, and equating to zero the terms of zeroth- and first-order in ϵ yields two sets of simpler equations as

$$\frac{\mathrm{d}\Re_0}{\mathrm{d}t} = \frac{C_3}{\Re_0} \tag{6.7a}$$

$$\Re_0(0) = R_0 \tag{6.7b}$$

and

$$\frac{\mathrm{d}\Re_1}{\mathrm{d}t} + \frac{C_3}{\Re_0^2}\Re_1 = -\frac{(ln(C_2\Re_0\sqrt{\Re_0}) - 0.25)^2}{{\Re_0}^2\sqrt{\Re_0}} \tag{6.8a}$$

$$\Re_1(0) = 0 \tag{6.8b}$$

note that all terms including second- and higher-order in ϵ are neglected. Equations 6.7b and 6.8b are initial conditions for equations 6.7a and6.8a respectively. Solving equation 6.7a, the zeroth-order solution is $\Re_0 = (I_1 + 2 \times C_3 t)^{1/2}$. By substituting $C_3 = F_B/2\pi\Gamma$ and implementing the initial condition given by equation 6.7b, we obtain

$$\Re_0 = (R_0^2 + \frac{F_B t}{\pi\Gamma})^{1/2} \tag{6.9}$$

Equation 6.9 is Turner's radius; i.e., $\Re_0 = R_T$. Substituting equation 6.9 into equation 6.8a, and solving equation 6.8a using the initial condition given by equation 6.8b gives

$$\Re_1 = -\frac{1907}{250}\frac{t}{R_T} \tag{6.10}$$

It should be indicated that the term $[ln(C_2\Re_0\sqrt{\Re_0}) - 0.25]^2$ was simply curve fitted with $[7.755\Re_0^{0.75}]$. The goodness of the curve fitting was evaluated through coefficient of determination defined as 1-SS_{res}/SS_{tot}, where SS_{res} and SS_{tot} are the sum of squares of residuals and the total sum of squares respectively. A fairly good value of 0.9947 was obtained for the coefficient of determination in the range of $1 \leq R \leq 5$, i.e. the fit explains 99.47% of the total variation in the data about the average; the value of the coefficient of determination decreases as radius R grows beyond 5. It is worth noting that without this curve fitting we cannot find any general solution for equation 6.8a. Solving equation 6.9 for t and substituting into equation yields

$$\Re_1 = -\frac{1551}{200}\frac{1}{2C_3}R_T[1 - (\frac{R_0}{R_T})^2] \tag{6.11}$$

therefore,

$$\epsilon\Re_1 = -\Lambda[1 - (\frac{R_0}{R_T})^2]R_T \tag{6.12}$$

where $\Lambda = \alpha\Gamma^2 C_d/F_B$ in which $\alpha = 0.0711$ is a constant and C_d, as yet unknown, stands for the drag coefficient. Substituting equations 6.9 and 6.12 into equation , we obtain

$$R = R_T - \Lambda[1 - (\frac{R_0}{R_T})^2]R_T \tag{6.13}$$

Accordingly, the radius of the buoyant vortex ring R includes two terms; the first term, R_T, represents the effect of the buoyancy and the second term, $\Lambda[1 - (\frac{r_0}{R_T})^2]R_T$, describes the effect of the viscosity. Equation 6.13 indicates that the Turner's radius overestimates the actual radius of buoyant vortex rings since it does not take into account the viscous dissipation. In fact, the viscous force causes the rate of expansion to decrease, since it acts downward in the opposite direction of the buoyant force. Defining η as the ratio of the viscous term to the buoyant term, we find

$$\eta = \Lambda[1 - (\frac{R_0}{R_T})^2] \tag{6.14}$$

Figure 6.2 illustrates the variation of η with respect to time. As is observed, the ratio of the viscous term to the buoyancy term increases asymptotically to $\Lambda = \alpha\Gamma^2 C_d/F_B$ as the vortex ring rises. This can be attributed to the diffusion of the vorticity generated on the vortex ring surface through the rotational area, and probably, over its bounadry $\boldsymbol{B}$ sweeping off into the initially irrotational region (see figure 6.1). In figure 6.2, the value of Λ is still unknown, since the drag coefficient C_d of the vortex ring cannot be calculated through pure analytical analysis. Solving equation 6.13 for Λ, we obtain

$$\Lambda = \frac{1 - \frac{R}{R_T}}{1 - (\frac{R_0}{R_T})^2} \tag{6.15}$$

To determine the value of Λ we need to conduct experiments and measure the radius of the vortex ring. Plugging the measured radius R into equation 6.15 yeilds Λ; consequently, the drag coefficient C_d can be deduced since $\Lambda = \alpha\Gamma^2 C_d/F_B$ or $C_d = \Lambda F_B/\alpha\Gamma^2$.

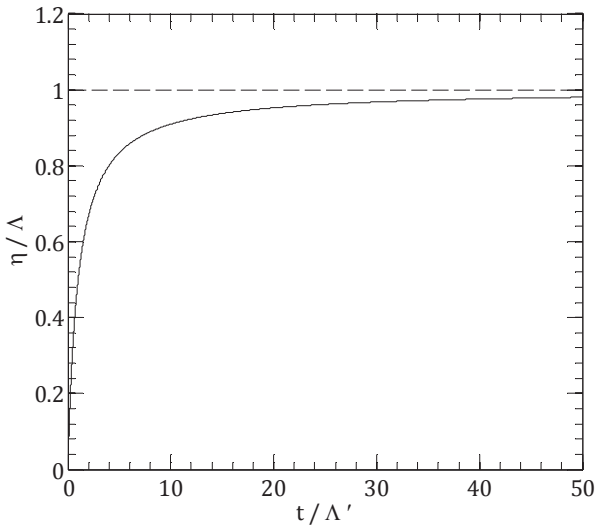

FIGURE 6.2: Time history of the ratio of the viscous term to the buoyant term; $\Lambda = \alpha\Gamma^2 C_d/F_B$ and $\Lambda' = R_0\pi\Gamma/F_B$. The effect of the viscous term increases with time.

6.3 The experiment

The experiment reported in this study was conducted in a Plexiglas tank that was 0.8 m long, 0.8 m wide and 2.4 m high. The experimental setup is sketched in figure 6.3. As illustrated in this figure, compressed air passes through a pressure regulator (1) to a solenoid valve (2). The solenoid valve is controlled by a programable logic controler (PLC) (3). Over a short period of time δt, the PLC opens the solenoid valve and air flow pushes the cap (4) against the force of the spring (5). Once the cap is lifted, presurized air bursts out through the small opening on the flexible membrane (6) and produces a buoyant vortex ring (7). Similar to Hershberger et al. [**?**], all the experimental data were obtained photographically. Three cameras with speed of 60 f.p.s. at a resolution of 1080P were configured above and on two orthogonal sides of the tank to

record the generation and the motion of the vortex ring bubble. The videos were then analysed frame by frame using the MATLAB image processing toolbar to deduce the time history of the elevation and dimensions of the vortex ring bubble. The rising velocity V was obtained as the first derivative of measured elevation. Substituting the rising velocity and the dimensions of the vortex ring bubble into equation 6.4 yields circulation as

$$\Gamma = 4\pi R \times V \times (\ln(\frac{8R}{a}) - \beta)^{-1} \tag{6.16}$$

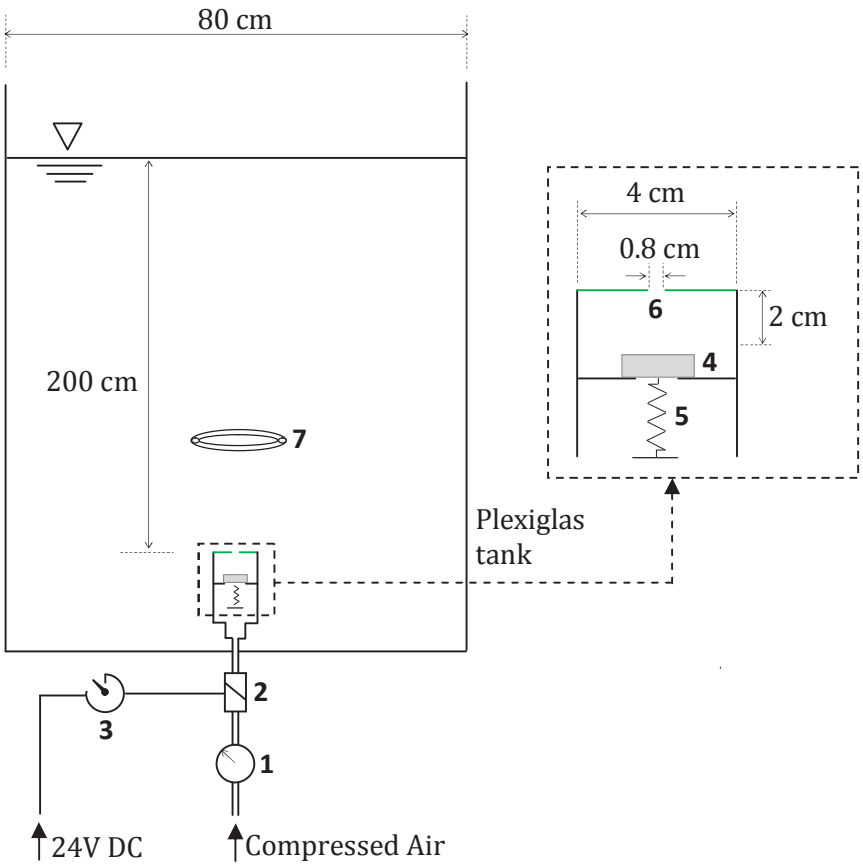

FIGURE 6.3: Apparatus; (1) pressure regulator, (2) solenoid valve, (3) PLC, (4) cap, (5) spring, (6) small opening on a membrane, (7) vortex ring.

6.4 Results and Discussion

The vortex ring is characterized by the reciprocal of dimensionless surface tension, the Bond number, given as $Bo = \rho g {r_0}^2/T$, where T is water-air surface tension. Using the experimental setup described in figure 6.3, the Bond number of the vortex ring can be controlled by the inlet pressure of the air flow, the duration of release through the solenoid valve, the diameter of the opening and the height of water over the vortex ring generator. The vortex ring bubble studied herein was generated at a supplied pressure of 20 psi (almost 138 kPa) over a duration of 0.1

s while the diameter of the opening was 0.08 m and the height of water over the membrane was set to be 1.5 m; leading to a Bond number of 85±5. It should be mentioned that the air-water surface tension was assumed to be $T = 72.8 \times 10^{-5} Ncm^{-1}$ since water temperature was approximately 20 $^{\circ}C$. The given precision uncertainty was obtained from the standard deviation of ten individual measurements at a 95% confidence level.

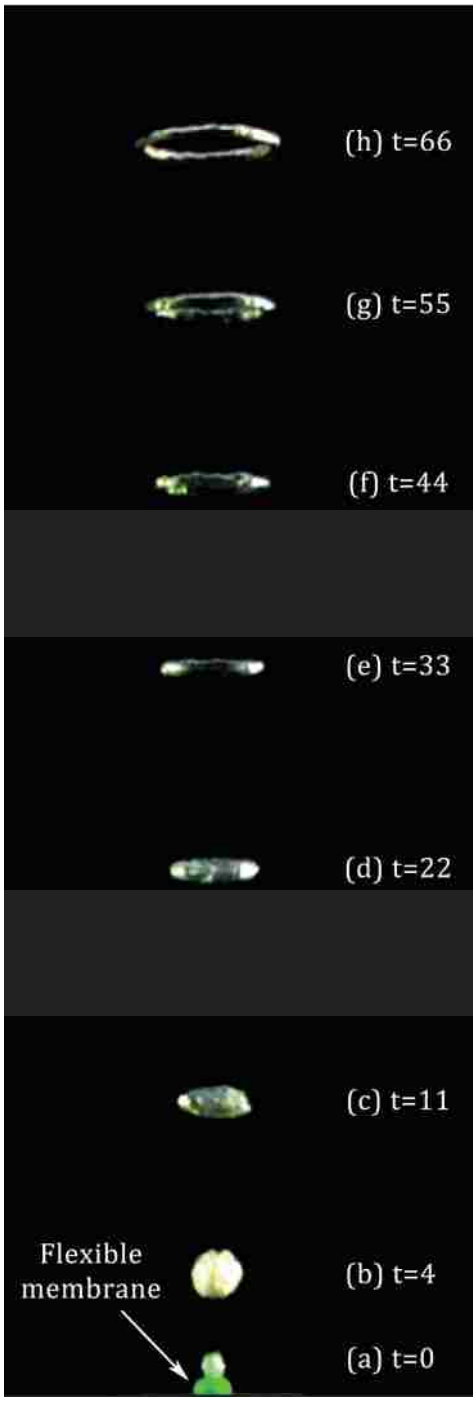

FIGURE 6.4: Formation and translation of the vortex ring bubble corresponding to Bo=85. Values are dimensionless.

Figure 6.4 attempts to illustrate the formation and translation of the buoyant vortex ring corresponding to Bo=85. Figure 6.4(a) represents the approximate moment that the pressurized air burst out through the small opening on the flexible membrane (green surface), figure 6.4(b) coresponds to the moment at which the vorex ring was formed, and figure 6.4(h) depicts the vortex ring at the moment that the free surface starts bowing; beyond this moment the vortex ring will be affected by the free surface (free surface is not shown in the figure). As is clearly observed, the buoyant vortex ring expands radially as it rises. The time history of the radius of the mentioned vortex ring bubble is plotted in figure 6.5. To ensure the negligibility of the free surface tension, the radius was not measured beyond t=50. Although the experiment was carefully controlled to minimize the uncertainties, the repeatability needs to be assessed by estimating the precision of individual measurements. Error bars shown in figure 6.4 represent precision of ten individual measurements at a 95% confidence level. Figure 6.4 compares the experimentally observed radius with that predicted by the Turner's equation (equation 6.1). As is observed, measured radius is smaller than the Turner's radius; the disparity increases as the vortex ring bubble rises. As time goes by, the vorticity produced by the vortex ring diffuses through the ambient flow; consequently, the effect of viscosity becomes more noticeable, and the measured values reported here diverge from the radii reported by Turner. Time history of the circulation associated with the vortex ring described in figure 6.5 is illustrated in figure 6.6. The data presented in this figure is calculated using equation 6.16 assuming a solid rotating core. It can be seen that circulation is approximately constant with respect to time with an average value of 6.54. Here it is noteworthy to mention again that circulation and all other parameters have been made dimensionless using terms explained below equations 6.5a and 6.5b. Substituting the Turner's and measured radii reported in figure 6.5 into equation 6.15 yields $\Lambda = \alpha\Gamma^2 C_d/F_B$; then, using circulation given in figure 6.6 the drag coefficient of a buoyant vortex ring at Bond number of approximately 85 can be deduced as is shown in figure 6.7. We observe that the time history of the drag coefficient is approximately constant with a relative standard deviation of 12% and an average value of $C_d = 0.31$.

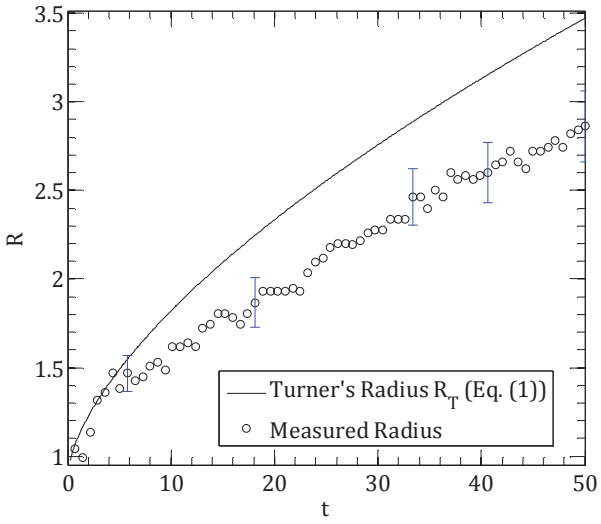

FIGURE 6.5: Radius of a buoyant vortex ring at $Bo = 85$; values are dimensionless. Solid line shows Turner's radius (equation 6.1) and circles represent measured values

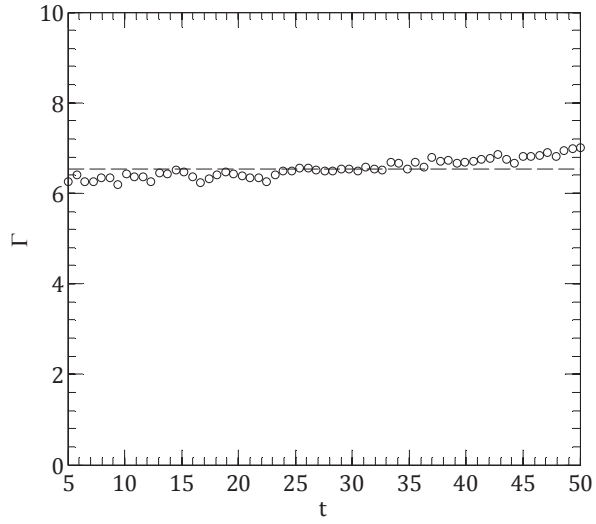

FIGURE 6.6: Circulation of a buoyant vortex ring at $Bo = 85$; values are dimensionless. Dashed line shows the average circulation of approximately 6.54.

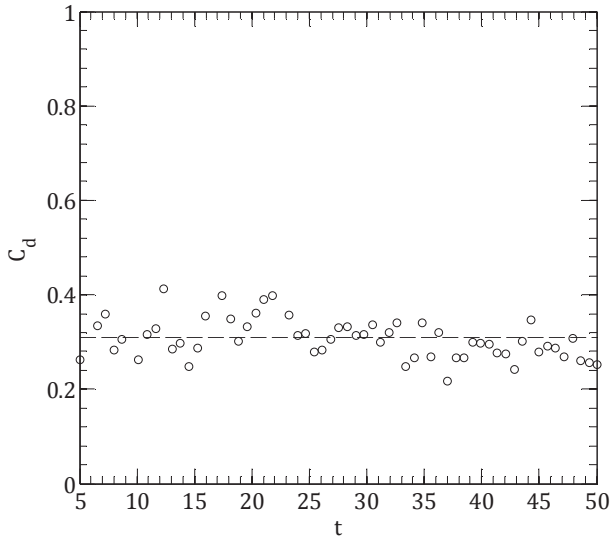

FIGURE 6.7: Drag coefficient of a buoyant vortex ring at $Bo = 85$; values are dimensionless. Dashed line shows the average drag coefficient of approximately 0.31.

References

[1] Gan, L., Dawson, J. R., Nickels, T. B., 2012. On the drag of turbulent vortex rings. Journal of Fluid Mechanics, 709, 85-105.

[2] Lundgren, T. S., Mansour, N. N., 1991. Vortex ring bubbles. Journal of Fluid Mechanics, 224, 177-196.

[3] Turner, J. S., 1957. Buoyant vortex rings. Proceedings of the Royal Society A: Mathematical, Physical and Engineering Sciences, 239, 61-75.

[4] Walters, J. K., Davidson, J. F. 1963. The initial motion of a gas bubble formed in an inviscid liquid. Journal of Fluid Mechanics, 17, 321-336.

[5] Pedley, T. J., 1968. The toroidal bubble. Journal of Fluid Mechanics, 32, 97-112.

[6] Vasel-Be-Hagh, A.R., Carriveau, R., Ting, D.S.-K., 2015. A Balloon Bursting Underwater. Journal of Fluid Mechanics, 769, 522-540.

[7] Hershberger, R. E., Bolster, D., Donnelly, R. J., 2010. Slowing of vortex rings by development of kelvin waves. Physical Review E, 82, 036309.

Chapter 7

Conclusion

The present research was carried out as a part of developing an underwater compressed air energy storage plant (see §1.1). The research was conducted in two preliminary and three primary phases.

7.1 Preliminary Phases

The objective of phase I was reviewing the existing energy storage plants; this literature survey let to proposing two new energy storage technologies described in Appendices A and B. The purpose of phase II was to become familiar with the ANSYS-Fluent and post-processing softwares by simulating flow over regular bluff bodies, for instance, flow over circular cylinders (see Appendix C)

7.2 Primary Phases

In three primary phases, flow over underwater balloons (phases III and IV) and flow produced by an underwater bursting balloon (phase V) were investigated. The major findings of the primary phases are summarized here.

7.2.1 Flow over Underwater Balloons

Flow over underwater balloons was investigated numerically at Reynolds number of 2.3×10^5. Reynolds number was calculated based on the physical properties of water at $15°C$, mean velocity of approximately 0.11 m/s and dimensions of the PF20000 lift bag manufactured by SUBSALVE USA CORPORATION (see figures 2.1 and 2.2).

Strouhal number and force coefficients of a single isolated balloon, three balloons in widely spaced floral configuration, three balloons in closely spaced floral configuration and three touching balloons in a floral configuration are compared in tables 7.1 and 7.2. The URANS model failed to capture the turbulent nature of the flow (see figures 2.12, 4.17 and 4.18); however, its predictions of the mean values were in reasonable agreement with those of the LES model. It was observed that at the studied Reynolds number the mean drag coefficient of a single balloon was smaller than the drag coefficient of a cylinder and larger than the drag coefficient of a sphere. The total drag coefficient of the wide unit is approximately 1.8 times the total drag coefficient of the closed unit, and the total drag coefficient of the closed unit is approximately 1.1 times the total drag coefficient of the touching configuration. The total drag coefficients of all three floral units of three balloons are smaller than three times the drag coefficient of a single balloon, while the storing capacity is the same. Unlike cylindrical and spherical bluff bodies, the lift coefficient of the balloon is not zero, which is due to its non-symmetric shape about the X-Z plane.

When flow crosses a droplet-shaped bluff body, fluid particles move around non-equal radius circles. This causes a rotation about the flow direction, leading to the generation of vortex tubes. The swirling tube flows were found to be fluctuating around in a highly turbulent manner. The vortex tubes were directly contacting and interacting with each other.

7.2.2 Flow Produced by a Balloon Bursting Underwater

Underwater balloons of various scales play a significant role in maritime applications including aircraft recovery, boat salvage, marine construction, offshore oil field diving, explosive ordinance disposal systems and underwater energy storage. In any such application, balloon rupture is conceivable owing to potential internal overpressure or collision with a sharp object or debris; this is what prompted phase VI of this study on underwater bursting balloons. According to our experiments, when a sufficiently large air–filled balloon bursts underwater, a buoyant vortex ring, also called vortex ring bubble or toroidal bubble, is produced. We examined some of the basic dynamic features and stability characteristics of vortex ring bubbles produced by underwater bursting balloons. The effect of dimensionless surface tension on characteristics including rise velocity, rate of expansion, circulation, trajectory, and lifetime of the vortex ring bubble was investigated. Results showed reasonable agreement with the literature of vortex rings produced by conventional approaches. It was observed that as the dimensionless surface tension increased, the rise velocity, the circulation and consequently the stability of the vortex ring bubble increased; however, the rate of expansion tends toward constant values. A semi analytical model was proposed by modifying the drag–based model presented by Sullivan et al. [9] to make it applicable for buoyant vortex rings. The modiffied model suggests that the vortex ring expansion is essentially due to the buoyancy force. An expression was also obtained for the circulation in terms of the initial volume of the balloon and the depth at which the balloon bursts. Comparing the measured circulations with those predicted by this expression demonstrates the considerable viscous dissipation through the vortex ring formation process. For dimensionless surface tension of 0.0010, almost 50% of the initial potential energy stored in the balloon was found to be dissipated during the vortex ring bubble formation, this value was increased to 70% for dimensionless surface tension of 0.0040.

.

Table 7.1: Comparison of the Strouhal number of the balloons with published data for cylinders and spheres.

		St	Re
Balloons	Single isolated	0.45 and 0.65	Re=230,000
	Wide configuration	0.52	
	Close configuration	0.15	
	Touching configuration	0.29	
Cylinder	Schewe [1]	0.43	Re=230,000
	Saghafian et al.[2]	0.3	Re=230,000
Sphere	Kiya et al.[3]	0.19	Re=100,000
	Constantinescu and Squires [4]	1-1.13	Re=430,000
	Norman and McKeon [5]	0.2	Re=100,000

.

Table 7.2: Comparison of the time averaged force coefficients of the balloons with published data for cylinders and spheres.

	Single Balloon	Widely spaced configuration		Closely spaced configuration		Three touching balloons		Circular cylinder Cantwell and Coles [6]	Sphere Achenbach, [7], Clift et al. [8]
		Upstream balloon	Downstream balloon	Upstream balloon	Downstream balloon	Upstream balloon	Downstream balloon		
	Lift								
LES: Dyna-SM	0.06	-0.06	-0.15	0.19	-0.05	0.14	0.04	0	0
URANS: K–ω	0.13	-0.1	-0.26	0.23	-0.08	-	-		
	Drag								
LES: Dyna-SM	0.69	0.54	0.57	0.49	0.21	0.44	0.18	078-1.4	0.51
URANS: K–ω	0.98	0.82	0.87	0.76	0.32	-	-		

Extending from the mentioned semi-analytical model, an expression was derived for the ring radius to be used to determine the drag coefficient of buoyant vortex rings. First, the vortex ring bubble is experimentally visualized and the ring radius is photographically measured. Second, the circulation of the vortex ring bubble is calculated through equation 6.16. Substituting measured radius into equation 6.15, we obtain Λ. And then, the drag coefficient is deduced using $C_d = \Lambda F_B/\alpha\Gamma^2$. To give further clarification, the drag coefficient of a vortex ring bubble was calculated at a Bond number of approximately 85 (see chapter 6). It was observed that the time history of the drag coefficient is approximately constant with a relative standard deviation of 12% and an average value of $C_d = 0.31$. The same procedure can be applied to determine the drag coefficient of vortex ring bubbles at other Bond numbers.

References

[1] Schewe, G., 1983. On the force fluctuations acting on a circular cylinder in cross flow from subcritical up to transcritical Reynolds numbers. Jounal of Fluid Mechanics, 133, 265–285.

[2] Saghafian, M., Stansby, P.K., Saidi, M.S., Apsley, D.D., 2003. Simulation of turbulent flows aound a circular cylinder using nonlinear eddy–viscosity modeling steady and oscillatory amient flows. Journal of Fluids and Structures, 17, 1213–1236.

[3] Kiya, M., Ishikawa, H., Sakamoto, H., 2001. Near wake instabilities and vortex structures of three dimensional bluff bodies: ma review. Journal of Wind Engineering and Industrial Aerodynamics, 89, 1219–1232.

[4] Constantinescu, G.S., Squires, K.D., 2004. Numerical investigations of flow over a sphere in the subcritical regimes. Physics of Fluids, 16, 1449-1466.

[5] Norman, A.K., McKeon, B.J., 2011. Unsteady force measurements in sphere flow from subcritical to supercritical Reynolds numbers. Experiments in Fluids, 51, 1439-1453.

[6] Cantwell, B., Coles, D., 1983. An experimental study of entrainment and transport in the turbulent near wake of a circular cylinder. Jounal of Fluid Mechanics, 136, 321-74.

[7] Achenbach, E., 1972. Experiments on the flow past spheres at very high Reynolds numbers. Jounal of Fluid Mechanics, 54, 565-75.

[8] Clift, R., Grace, J.R., Weber, M.E., 1978. Bubbles drops and particles. New York: Academic Press, New York.

[9] Sullivan, I. S., Niemela, J. J., Hershberger, R. E., Bolster, D., Donnelly, R. J., 2008. Dynamics of thin vortex rings. Journal of Fluid Mechanics, 609, 319-347.

Appendix A

Energy Storage Using Weights Hydraulically Lifted above Ground

A. R. Vasel-Be-Hagh, D. S.-K. Ting, R. Carriveau

Turbulence and Energy Laboratory, Lumley Centre for Engineering Innovation, University of Windsor, Ontario, Canada N9B 3P4

Vasel-Be-Hagh, A.R., Carriveau, R., Ting, D.S.-K., 2013, Energy storage using weights hydraulically lifted above ground. International Journal of Environmental Studies, 70(5), 792-799.

A.1 Introduction

A smarter grid, an overarching goal of electrical industry, is an intelligent, highly reliable and secure electrical grid. Among those countries in North America, Europe and the Middle East which have been striving towards the smarter grids, Italy has achieved the highest penetration [1]. Because there is a gap between the current status of electrical grids and the absolute definition of smart grid, it is more appropriate to speak of "emerging smart grids". Much effort is still needed to close the gap. Figure A.1 summarizes the five major characteristics of a smart grid.

To run a smart grid, the demand should be managed via reliable-response hardware switches operated by software platforms that encourage end consumers to decrease their demand at peak hours. A smart grid must also be capable of self diagnosing and troubleshooting. In a smart grid, all assets must operate nearest their optimum points and all procedures ought to be as efficient as possible. A smart grid must facilitate power generation from a wide range of energy

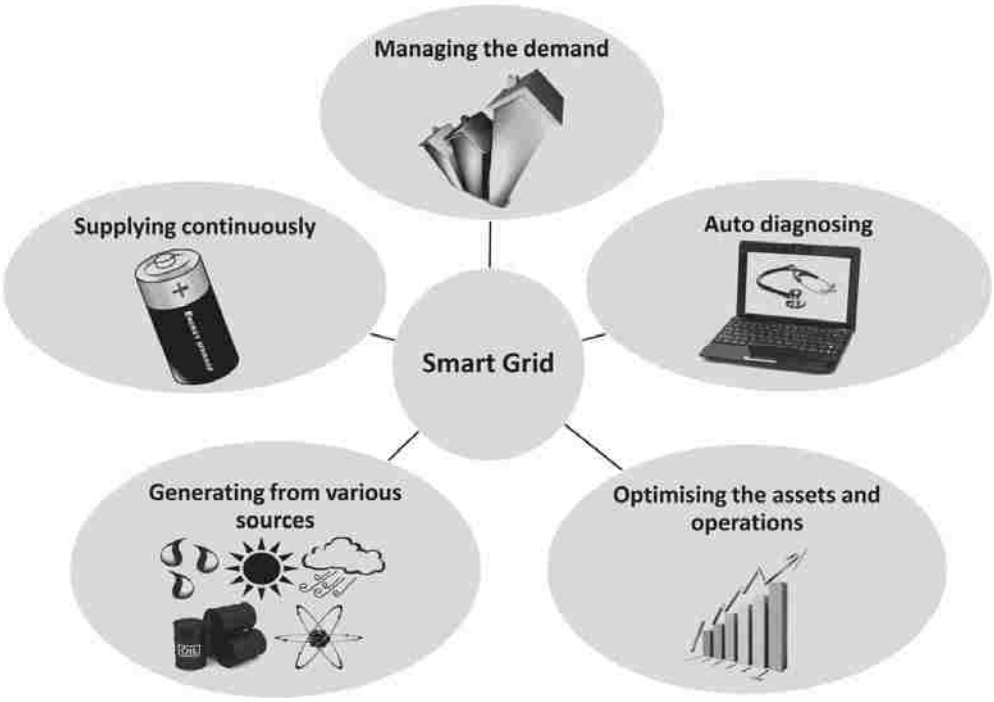

FIGURE A.1: Key characteristics of smart grid.

sources including fossil fuels, nuclear energy and renewable sources. Although the renewable energy sources have taken up a relatively small portion of the total energy supply, nonetheless, they are rapidly growing. For instance, wind energy production in the USA experienced a 28-fold increase from 1998 to 2011 with production capacity reaching 46,919MW [2]. In the same period, the wind energy production capacity in Canada increased to 5265MW, i.e. more than 210 times what was produced at the beginning of 1998 [3]. Considering this significant development rate, a smart grid needs to integrate renewable energy sources into the power supply system.

There are, however, many notable challenges associated with renewable energies; which make them non-dispatchable. Prevalent renewables like wind and solar are inherently intermittent; therefore, peak supply is often temporally out of phase with peak demand. In addition, even if peak production and demand coincide, high instability and grid congestion issues can prevent the delivery of the generated power to the grid. These problems can be overcome. One solution is to support the power generated from renewable sources via fast ramping power supplies called 'peakers'. These are driven by fossil fuels; therefore, they are only used under significant demands.

Energy storage systems are an even better solution to the problem of intermittency. Energy storage can be more efficient and more environmental friendly than standard peakers. In addition to facilitating the integration of renewable resources into the grid, energy storage is a necessary component of a smart grid to secure a continuous supply of power. Storage technologies can be grouped into chemical, electrical and mechanical systems.

Chemical and electrical technologies fall outside the scope of the present paper and will not be discussed. Primary mechanical technologies include flywheels, compressed air and pumped hydro energy storage. Among these, the pumped hydro energy storage is the most mature and the most commonly used energy storage; nearly 99capacity currently installed around the globe falls into this category [4,5]. Despite this wide application, some challenges remain. These must be addressed. This paper proposes a novel design which may effectively remove some of these outstanding challenges. First, conventional pumped energy storage is reviewed and major issues associated with that are highlighted and then, the suggested solution is introduced.

A.2 Conventional Pumped Hydro Energy Storage

The earliest technological advances of this storage system were made in 1910; today, efforts continue to enhance its quality and performance [6,7]. This energy storage choice is widespread because it offers several major advantages including no standby losses, reliable power production, simple construction, cost-effective maintenance and operational environmental friendliness. Pumped hydro energy storage is about converting electrical energy to potential energy by pumping water from a low level reservoir to a high level reservoir. The water of the high level reservoir is then released to the lower one through turbine generators to produce electricity. This mechanism has the following drawbacks:

- Without significant natural elevation differences, towered water tanks are required. This can be cost prohibitive even at small scales. That is why most existing cases are found in mountainous areas [7–9].
- The amount of potential energy stored in water is limited by the size of the reservoir and the altitude of the available highland; it is not practical to install the storage reservoir at any desirable altitude.
- The system is not flexible, i.e. it is impossible to balance constantly the storage capacity with the available surplus electrical power. The energy storage is designed specifically to operate at a fixed capacity which is typically not needed in practice. Hence, the energy storage often operates away from its optimum point.
- It is not easy to expand the storage capacity and upgrade an installed system.
- Long piping is required. For instance, in the system designed by Anagnostopoulos and Papantonis [10], a 3250m long piping was needed.

In an effort to tackle these challenges, the present paper proposes re-imagined pumped hydro energy storage. The design is investigated in detail, in the following sections.

A.3 Hydraulically Lifted Weights Energy Storage

Similar to the conventional pumped hydro energy storage, the proposed hydraulically lifted weight-energy storage (HLW-ES) accumulates excess electrical power in the form of potential

energy. Relying on the premise that a denser material has a larger capacity for storing potential energy $U = m.g.h$, the present energy storage adaptation accumulates the surplus electricity in weights several times denser than water, and thus it has a higher storage capacity per unit footprint. The heavy weights are elevated via hydraulic forces exerted by pumped water. Figure A.2 gives a general view in detail of the method. Table A.1 summarizes the main components of the system.

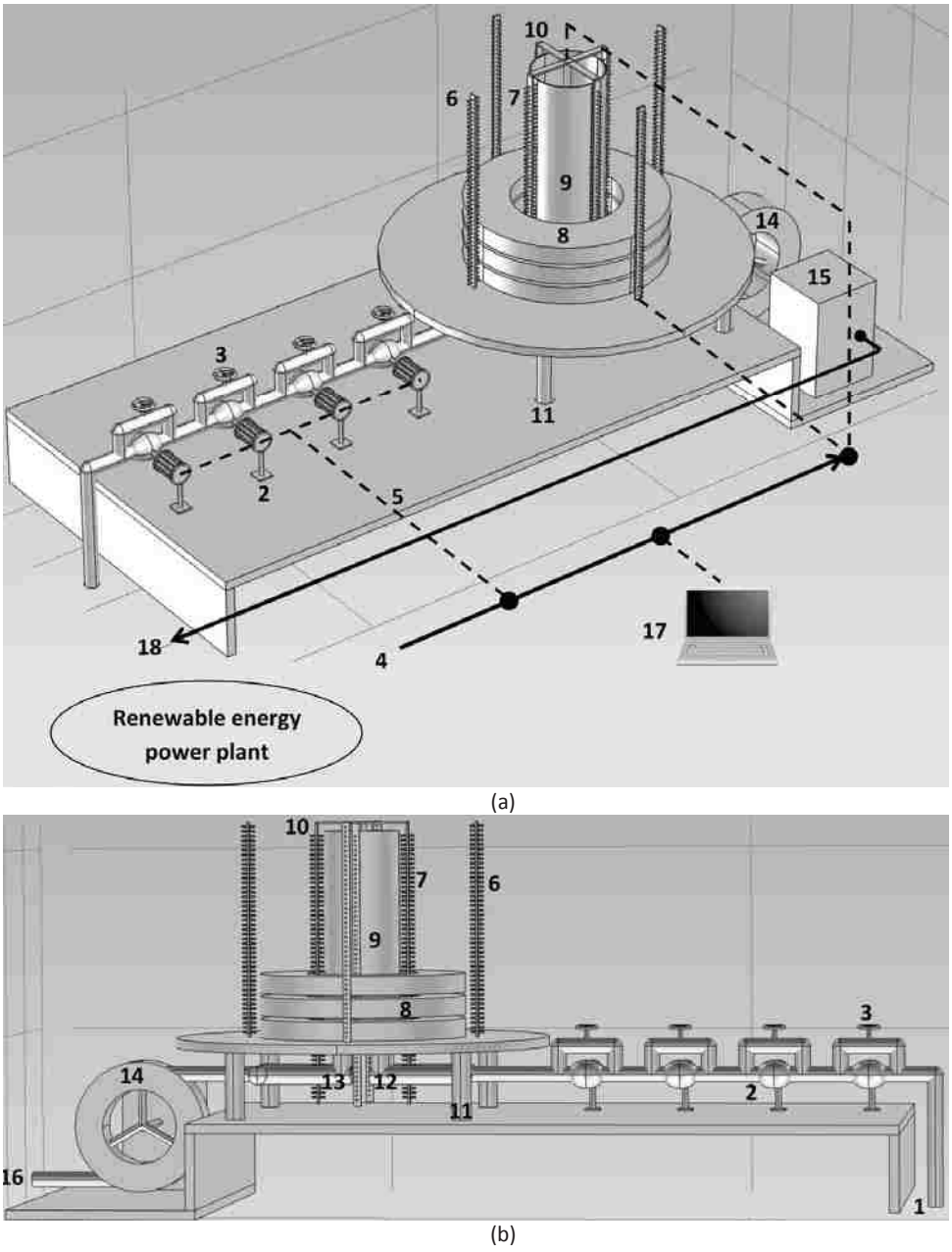

FIGURE A.2: The general view of the proposed HLW-ES; (a) isometric view, (b) side view.

The present energy storage operates as follows. The surplus electricity generated at off-peak hours is used to drive gear pumps (2) to pump water from a low level reservoir into the main

Table A.1: Main components of the proposed HLW-ES.

1	Inlet pipe from the low level reservoir	10	Weight transferring arms
2	Pumps	11	Platform columns
3	Bypass	12	Inlet of the main tank
4	Surplus electrical power line	13	Outlet of the main tank
5	Data and power connections	14	Turbine
6	Outer auto control pins	15	Generator
7	Inner auto control pins	16	Outlet pipe to the low level reservoir
8	External heavy weights	17	Data control centre
9	Main tank	18	Electrical outlet of the energy storage

tank (9). The main tank (9) is a cylinder sealed with a piston. The piston is connected to several heavy weights (8) through an automated clutching system including inner (7) and outer (6) auto control pins, weight transferring arms (10) and data control centre (17). The data control centre activates the external weights, one by one with increasing surplus energy to be stored.

In other words, when the surplus energy exceeds the first threshold, the inner pins grab the next external weight and at the same time the outer pins leave it; therefore, the weight is transferred to the piston through the weight transferring arms (10) and the capacity of the storage will increase. During the reverse process of releasing the stored energy back into the grid, the data control centre manages the inner auto pins to leave the external weights, as many as required, to balance the storage capacity with the input electrical power. The data control centre also manages operation of the gear pumps and balances the number of active pumps with respect to the acting external weights.

The effect of each external weight on flexibility of the system is similar to what a small backup tank does in the conventional pumped hydro storage. But, adding an external weight to the present energy storage is much easier than installing a small tank at a higher elevation. During peak demand, the pressurized water will be released to the hydro turbine (14) to provide the required power. The discharge rate can be controlled by managing the number of the active weights, i.e. weights can be added to accelerate discharge.

The unique features of the proposed energy storage can be highlighted as follows:

- It is not necessary to be installed at high altitude; thus, it significantly reduces the height limitation.
- With reduced height, corresponding pipe length is considerably reduced.
- With on-ground operation, the cost of installation and maintenance is much lower.
- The storage is scalable; capacity can be varied by altering weights to meet the need. Dividing the total external weight into more specific sub-weights further increases the flexibility of the storage.
- The discharge process occurs under a constant pressure condition for any set capacity.
- This system is designed to ramp rapidly, thus to respond to near-real time changes in demand.

A.4 Typical HLW-ES

In this section the dimensions and weights of the proposed energy storage are deduced to provide a storing capacity approximately equal to the mini pumped hydro energy storage designed by Manolakos et al. [8].

Manolakos et al. [8] designed a hybrid renewable energy power plant comprising of a wind turbine and solar panels in order to provide for the energy needs of Merssini village on Donoussa Island in the Aegean Sea. The system was supported by a storage solution consisting of batteries and a micro hydraulic plant. The micro hydraulic power plant operates like a conventional pumped hydro storage, i.e. after the batteries are fully charged the surplus power is used to pump water from a low level reservoir to a storage tank of 100m^3. The head difference between the low level reservoir and the storage tank was 97 m. Accordingly, the maximum storage capacity was $U = m.g.H = \rho.V.g.H = 1000 \times 1000 \times 9.8 \times 97 = 95\text{MJ}$.

To provide this storage capacity using the proposed HLW–ES, a cylindrical tank with a diameter of 4m and a height of 10m resulting in a volume of 124m^3 is selected. The tank is installed on a platform with a height of 4 m. As shown in figure A.3, the total external loading is provided by three ring-shaped iron weights initially located at heights of 0, 1.2 and 2.4m above the platform surface. Dashed lines show the initial position of the piston inside the tank.

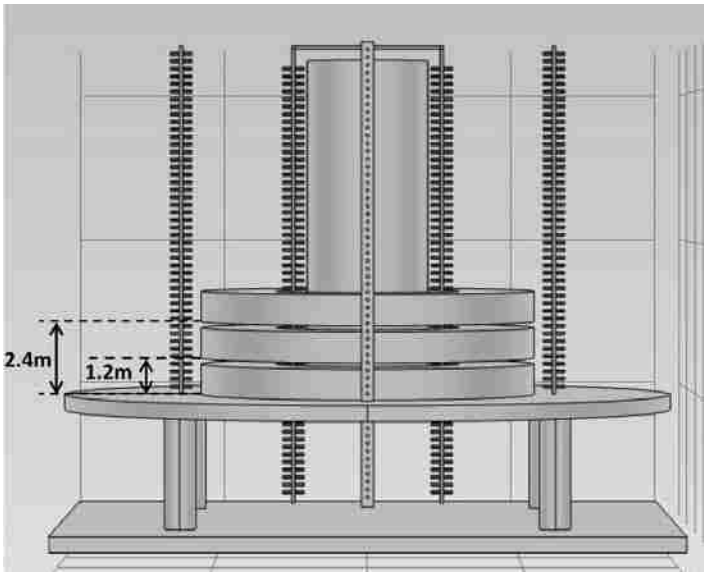

FIGURE A.3: A completely discharged HLW-ES with three external weights proposed for the 95 MJ hybrid renewable energy power plant installed in Merssini village, Greece.

The thickness T_w, the inner radius R_i and the outer R_o radius of each weight are 1, 3 and 5.5m, respectively. There is an initial distance of 0.2m between the weights. Table A.2 summarizes the characteristics of the HLW–ES proposed for the current case.

Figure A.4 illustrates a complete charge cycle of the above described HLW-ES. Panel (a) shows the completely discharged state where the weights are at rest at their initial locations. Dashed

TABLE A.2: Characteristics of the HLW-ES proposed for the 95 MJ Merssini plant.

Tank height	H_T	10 m
Tank diameter	D_T	4 m
Tank volume	V_T	m^3
Platform height	H_P	4 m
Number of weights	N_W	3
Weights material	ρ	7870 kg/m^3
Weights thickness	T_W	1 m
Weights inner radius	R_i	3 m
Weights outer radius	R_o	5.15 m

lines show the piston location inside the cylindrical tank. Once the piston reaches 2.4m above the base of the tank, the outer auto pins release the top weight to the inner ones; transferring its weight to the piston through the weight transferring arm. At the same time, the data control centre activates the second gear pump (see panel (b)).

In panel (c), the piston and the first weight are at a height of 4.4m above the platform surface. At this moment, the second weight is added to the total elevating mass and simultaneously the third pump is turned on. Panel (d) illustrates the energy storage after an additional 2 m elevation increase. As shown in this panel, the piston and the first weight are at 6.4 m and the second weight is 3.2 m above the platform surface. At this moment the final weight is secured and the fourth pump is activated. Any time during the charging process, if the surplus electrical power decreases below the required value to run the energized pumps, the weights are returned to the outer auto pins as the associated pumps are shut down to decrease the capacity to an appropriate value. Whenever the electric grids require energy from the storage, the aforementioned process is reversed.

As an effect of the maximum height of each weight (see panel (e)) and density of iron, ρ = 7870 kg/m^3, storage capacities of the first, second and third weights are 32, 24 and 15 MJ, respectively. These are approximately equal to capacity of water tanks with volumes of 34, 25 and 16m^3 at altitude of 97 m. The iron piston with diameter of D_p=2.5 m and thickness of T_p=1m adds a storing capacity of 15 MJ to the energy storage. With regard to the potential energy of the water inside the tank, the maximum capacity of the energy storage is 95 MJ.

According to the data reported by Manolakos et al. [8], for the conventional pumped water energy storage installed in Merssini village, the average amount of water inside the storage tank was less than 50flexibility of the conventional storage, the water must always be pumped through the long piping of the system to the altitude of 97 m; therefore, approximately 50electricity is wasted. If the energy storage proposed here were applied instead, the data control centre would set the weights and pumps to reach half of the maximum storage capacity; this would result in next to zero waste.

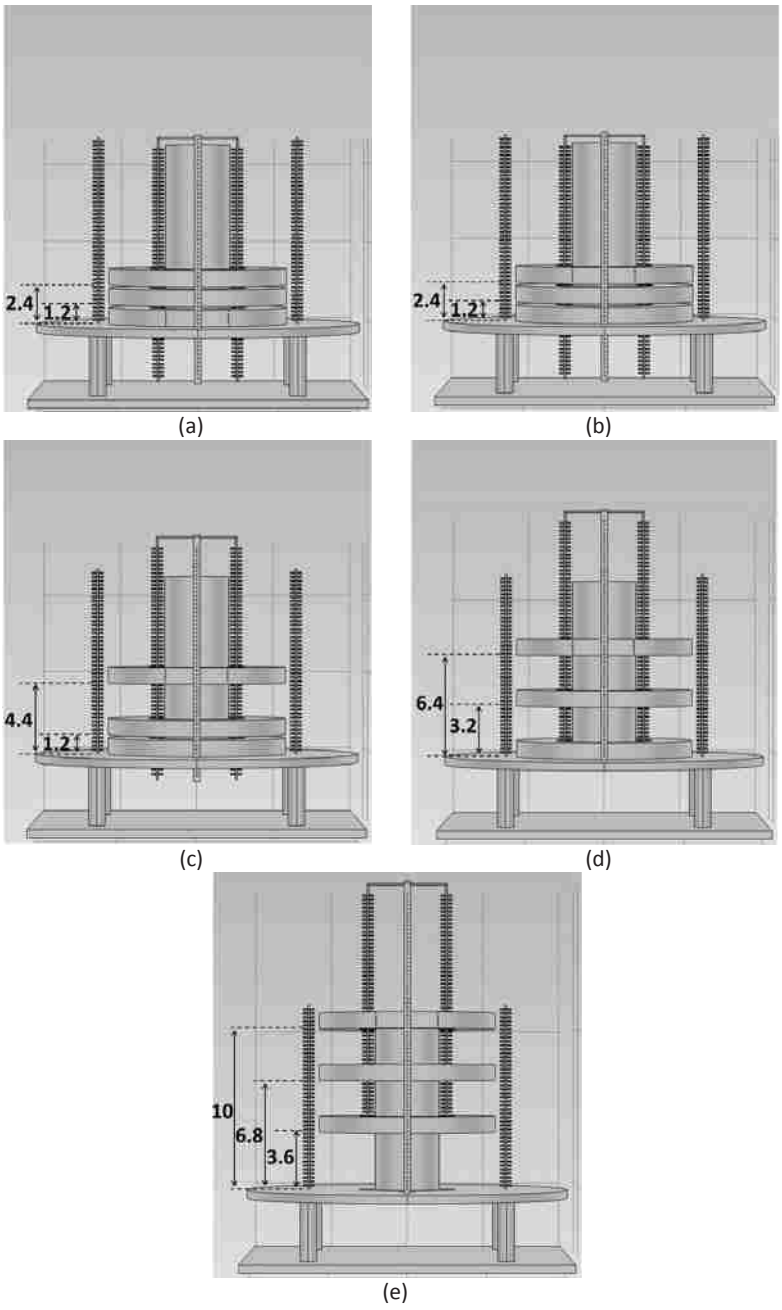

FIGURE A.4: A complete charge cycle of the HLW-ES proposed for the 95 MJ Merssini plant. All dimensions are in metres.

A.5 Conclusion

A new pumped hydro energy storage was proposed. In contrast to the conventional pumped hydro energy storage where surplus power is stored as elevated water, the proposed energy storage applies pumped water to elevate weights several times heavier than water. This provides a considerable operational flexibility since weights and consequently gear pumps can be balanced in accordance with the instantaneous excess electrical power. The discharge rate can be also controlled by the external weight; discharge can occur very rapidly via activation of the external weights. This allows the storage to adjust quickly to the fluctuating demand. Beyond this, the suggested solution has inherent installation and maintenance advantages. For instance, it does not need to be constructed at high altitudes, and so, no tall water tank tower and long piping are needed. Consequently, capital and maintenance costs can be significantly reduced.

Acknowledgements

This work is made possible by the Natural Sciences and Engineering Research Council of Canada. The lead author is most grateful to the Ontario Trillium Foundation for an Ontario Trillium Scholarship.

References

[1] Smart from the Start, 2010. Roundtable Discussion Paper (London: PricewaterhouseCooper).

[2] The wind power, 2012. wind turbines and wind farms database, general data, USA.

[3] The wind power, 2012. Wind Turbines and Wind Farms Database, General Data, Canada.

[4] Electric Power Research Institute EPRI, 2010. Electric Energy Storage Technology Options: A White Paper Primer on Applications, Costs, and Benefits, (Palo Alto, CA: EPRI).

[5] Rangoni, B., 2012. A contribution on electricity storage: the case of hydro-pumped storage appraisal and commissioning in Italy and Spain. Utilities Policy, 23, 31–39.

[6] Kuan, T., 1989. Basic planning analysis of pumped-storage (PhD thesis). Colorado, USA: Civil Engineering Department, Colorado State University.

[7] Buenoa, C., Carta, Jose A., 2006. Wind powered pumped hydro storage systems, a means of increasing the penetration of renewable energy in the Canary Islands. Renewable and Sustainable Energy Reviews, 10, 312–340.

[8] Manolakos, D., Papadakis, G., Papantonis, D., Kyritsis, S., 2001. A simulation-optimisation programme for designing hybrid energy systems for supplying electricity and fresh water through desalination to remote areas case study: the Merssini village, Donoussa island, Aegean Sea, Greece. Energy, 26, 679–704.

[9] Manolakos, D., Papadakis, G., Papantonis, D., Kyritsis, S., 2004. A stand-alone photovoltaic power system for remote villages using pumped water energy storage. Energy, 29, 57–69.

[10] Anagnostopoulos, J., Papantonis, D., 2008. Simulation and size optimization of a pumped–storage power plant for the recovery of wind-farms rejected energy. Renewable Energy, 33, 1685–1694.

Appendix B

Underwater Compressed Air Energy Storage Improved through Vortex Hydro Energy

A. R. Vasel-Be-Hagh, D. S.-K. Ting, R. Carriveau

Turbulence and Energy Laboratory, Lumley Centre for Engineering Innovation, University of Windsor, Ontario, Canada N9B 3P4

Vasel-Be-Hagh, A.R., Carriveau, R., Ting, D.S.-K., 2014, Underwater compressed air energy storage improved through Vortex Hydro Energy. Sustainable Energy Technologies and Assessments, 7, 1-5.

B.1 Introduction

The intermittent nature of major renewable energy sources causes system stability issues and supply–demand synchronization challenges. An environmentally friendly solution to the intermittency issue is energy storage. Among existing technologies, Compressed Air Energy Storage CAES remains one of the most efficient ones. The application of this underground storage system is, however, limited to terrestrial constraints [2]; while much of wind's momentum is moving offshore. Hence, a variant of the original CAES, UWCAES, designed for offshore application is being built in a demonstration capacity at grid connection scale in Toronto Harbour [3]. In this system, the surplus electrical energy generated in the off-peak hours is used to run compressors to charge submerged distensible balloons by compressed air. The balloons are moored to the sea floor; thusly, the submerged air is maintained at pressure by hydrostatic forces, ready to be released back to the surface to drive turbines to supply the electrical grid when needed.

Considering the potential significance of UWCAES for offshore power production, any improvement in the round-trip efficiency will increase the benefits of the technology. One effective approach is to design the underwater accumulators to be power generating to harvest underwater kinetic energy to make up for round-trip losses. One of the most efficient hydro energy converters is the Vortex Induced Vibration Aquatic Clean Energy VIVACE which harvests the hydrokinetic energy of river and ocean currents via vortex induced vibration VIV [1]. Building on the promise of the VIVACE, the present technical note proposes a power generating UWCAES variant that couples the original design detailed by authors of the current note [3] with the VIVACE concept developed by Bernitsas et al. [1].

B.2 Coupled Underwater Compressed Air Energy Storage–Vortex Hydro Energy (UWCAES–VHE)

In the proposed hybridization a charged compressed air accumulator also plays a second role as an active energy converter. The SP20000 model of the flexible enclosed cylindrical lift bags manufactured by SUBSALVE USA CORPORATION [4] is a suitable choice to perform as the accumulator–converters (A–C) for this hybrid system (see figure B.1). The proposed coupled UWCAES–VHE is illustrated in figure B.2; 1^{st}, 2^{nd}, (n-1)th and nth A–Cs are shown in the figure. To evade the effects of the upstream A–Cs on the VIV of the downstream ones each A–C should be placed in a staggered pattern off the wake of the upstream one. Key components of this system are summarized in table B.1.

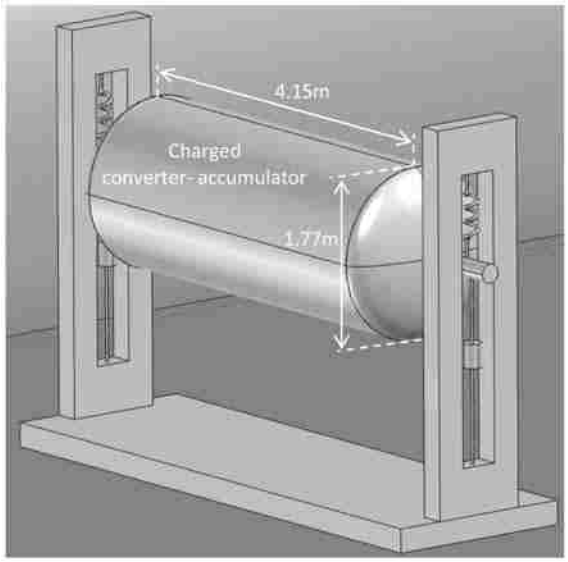

FIGURE B.1: A charged SP20000 balloon performing as the A–C of the coupled UWCAES–VHE.

The potential energy stored in a charged A–C can be calculated through

Table B.1: Key components of the coupled UWCAES–VHE.

1	Compressor unit	7	Wires to transit electrical power
2	Starter supply	8	AC convertor
3	A charged A–C	9	Output lines of the A–Cs
4	Pressure line from compressor tothe A–Cs	10	Pressure line from A–Cs to turbine
5	A discharged A–C	11	Turbine
6	DC collector	12	Generator

$$U = P_{A-C}V_{A-C} \times Ln(\frac{P_{atm}}{P_{A-C}}) \tag{B.1}$$

where P_{A-C} and V_{A-C} are the internal pressure and volume of each A–C in the charged state. By assuming a charging pressure of 8 atm, the potential energy stored in each charged A–C described in

Figure B.1 will be approximately 20 MJ; therefore, even in the case of no water current and, thus, no power generation, a very small scale of the proposed power generating energy storage with seven hundred A–Cs is able to supply approximately 3000 American houses for one hour. Note that the vortex hydro power plant presently installed in the Detroit River contains 13,100 conventional converters with length and diameter of 20 m and 1 m respectively [1].

B.3 Effects of the UWCAES–VHE Coupling on Storage Capability

B.3.1 Charging

The charging sequence of a coupled UWCAES–VHE including n cylindrical accumulator–converters (A–C) is as follows. First, the compressor unit (see figure B.2; 1) is driven by the surplus electrical power of the grid Ps to compress air into the first A–C (see figure B.2; 3) through the high pressure piping (see figure B.2; 4). Due to the deformation of the uncharged flexible balloons in cross flow, A–C is locked during the charging process; when the inside pressure exceeds the desirable value to prevent deformation it becomes unlocked to freely traverse up and down, a fully mechanical locking mechanism can be applied to prevent any extra electrical power consumption. The kinetic energy of the oscillating A–C is then delivered to the direct electrical current collector (see figure B.2; 6) and the alternative electrical current convertor (see figure B.2; 8) through the power transmission wires (see figure B.2; 7).

Then the power generated by the first A–C, $P_{G,A--C}$, contributes to charging of the second A–C, therefore, the second A–C is charged by a larger power of $P_2 = P_s + P_{G,A--C}$, where $P_{G,A--C} = \eta_{VHE} \times P_{max,VHE}$ in which η_{VHE} is the VHE conversion efficiency which indicates the harvestable portion of the maximum available power $P_{max,VHE} = \frac{1}{2}\rho U^3 DL$; note that $P_{max,VHE}$ is not affected by the aspect ratio of the converter. Following the same logic, the ith A–C is charged by $P_i = P_s + (i-1)P_{G,A-C} = P_s + (i-1)\eta_{VHE} \times P_{max,VHE}$ this is significantly larger than the charging power of the ith stationary accumulator of a conventional

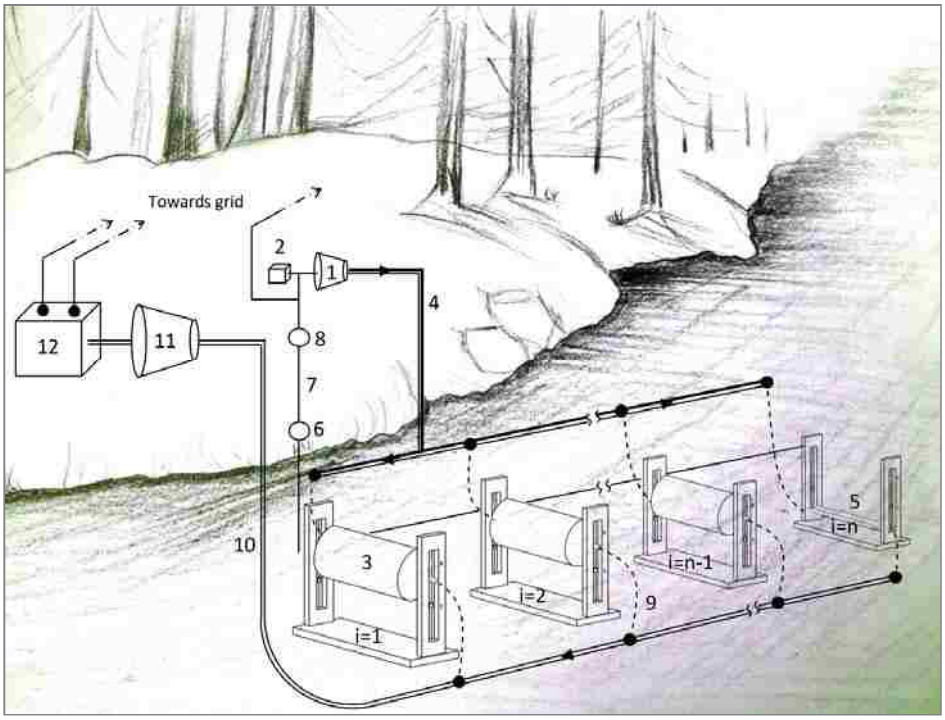

FIGURE B.2: Overview of the coupled UWCAES–VHE.

UWCAES ($P_i = P_s$). Therefore, the total charging time for a coupled UWCAES–VHE including n cylindrical A–Cs is considerably reduced to

$$\triangle_{UWCAES-VHE} = \sum_{i=1}^{i=n} \frac{E_{stored}}{n \times (P_s + (i-1)\eta_{VHE} \times P_{max,VHE})} \tag{B.2}$$

in which E_{stored} is the total storage capacity of the energy storage. Due to the term $(i-1)\eta_{VHE} \times P_{max,VHE}$ in the denominator of equation B.2, the total charging duration of the coupled UWCAES–VHE is much shorter than that of a conventional UWCAES, $\triangle_{UWCAES-VHE} = \sum_{i=1}^{i=n} \frac{E_{stored}}{n \times P_s}$.

B.3.2 Discharging

The ratio between the electrical energy delivered from energy storage to the grid and the electrical energy used to charge the storage can be called roundtrip efficiency η_{Rt}. The roundtrip efficiency of a conventional UWCAES with n stationary accumulator is $\eta_{Rt,UWCAES} = \frac{\sum_1^n E_{ACC,A-C}}{E_{stored}}$; where $E_{ACC,A-C}$ is the accessible energy of each charged accumulator and E_{stored} is the total stored energy during charging (i.e. the energy inputted into the energy storage).

In the proposed coupled UWCAES–VHE, the energy delivered to the grid while discharging the i^{th} accumulator–converter is $E_{ACC,A-C} + \frac{E_{ACC,A-C}}{P_{dis}}(n-i)(\eta_{VHE} \times P_{max,VHE})$ where P_{dis} is the discharge rate and $\frac{E_{ACC,A-C}}{P_{dis}}(n-i)(\eta_{VHE} \times P_{max,VHE})$ is the power generated by the $(n-i)$

charged A–Cs during discharge of the i^{th} A-C, note that $(i-1)$ A–Cs have been already discharged and no longer contribute to power generation (see figure B.3). Therefore, the roundtrip efficiency of the UWCAES–VHE is

$$\eta_{Rt,UWCAES-VHE} = \frac{\sum_1^n (E_{ACC,A-C} + \frac{E_{ACC,A--C}}{P_{dis}}(n-i)(\eta_{VHE} \times P_{max,VHE}))}{E_{stored}} \tag{B.3}$$

By substituting $\eta_{Rt,UWCAES} = \frac{\sum_1^n E_{ACC,A-C}}{E_{stored}}$ into equation B.3, it is simplified as

$$\eta_{Rt,UWCAES-VHE} = \eta_{Rt,UWCAES} \times \frac{1}{n} \times \sum_1^n (1 + (n-i)\frac{P_{max,VHE}}{P_{dis}}\eta_{VHE}) \tag{B.4}$$

Equation B.4 indicates that the increase in the roundtrip efficiency is a function of the VHE conversion efficiency, number and dimensions of the accumulator–converters (A–C) and discharging rate.

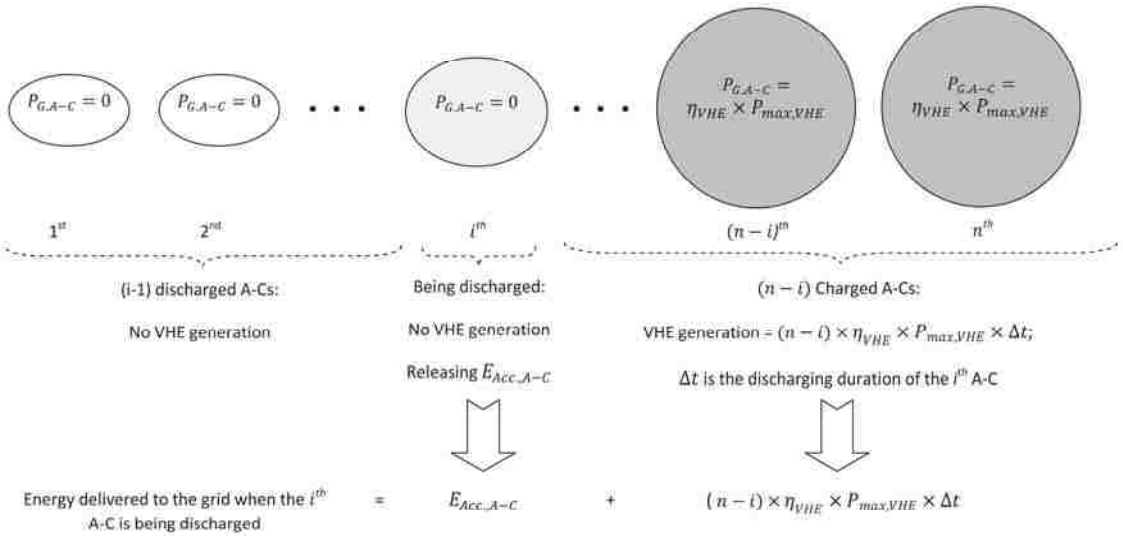

FIGURE B.3: Energy delivered to the grid when the ith A–C is being discharged.

B.3.3 Typical UWCAES–VHE

To further clarify, charging time and roundtrip efficiency of a typical UWCAES–VHE are deduced and compared to the conventional UWCAES presented by Cheung et al. [3]; the average surplus electrical power provided by the grid, the compressor unit, storing capacity and installation conditions such as depth are assumed to be identical.

According to Cheung et al. [3], the electrical energy required to run the compressor unit of an UWCAES including 150 stationary droplet-shaped accumulators with a total volume of 7500 m3 is approximately 6.5 MWh. Considering the roundtrip efficiency of approximately $\eta_{Rt,UWCAES}$= 65%; almost 4.2 MWh of the stored energy can be released into the grid. Assuming an average

surplus electrical power of $P_s = 1$ MW, it takes $\triangle_{UWCAES} = 6.5$ h to fully charge the energy store.

According to figure B.1, the volume of each A–C of the proposed UWCAES–VHE is approximately 10.2 m^3. Consequently, to provide a storage capacity equal to the conventional UWCAES presented by Cheung et al. [3], a UWCAES–VHE with 736 A–Cs is taken into consideration. Assuming free stream velocity of 1 m/s, fluid mechanical power for each A–C is $P_{max,VHE} = \frac{1}{2}\rho U^3 DL = 3.7$ KW, therefore, equation B.2 is written as

$$\triangle_{UWCAES-VHE} = \sum_{i=1}^{i=736} \frac{6.5}{736 \times (1000 + (i-1)\eta_{VHE} \times 3.7)} \tag{B.5}$$

So, the charging time of the UWCAES–VHE is a function of conversion efficiency of the A–Cs. Figure B.4 shows variation of charging time DUWCAES–VHE with conversion efficiency η_{VHE}. Bernitsas et al. [1] measured conversion efficiencies of η_{VHE}=24% and 37% respectively for oscillating mass ratios of 10.3 and 3.3 where mass ratio is defined as $m^* = m_c/m_a$ in which m_c and $m_a = \rho_{water}\pi D^2/4$ are mass of the oscillating cylinder and added mass respectively. It is observed that at η_{VHE} =37 % charging length of the UWCAES–VHE is approximately 4.5 h which is almost 2 h less than that of the conventional UWCAES under the same condition. The charging length would be ideally reduced to roughly 3.2 h if it was possible to improve the conversion efficiency of the accumulator–convertors to η_{VHE}=100 %.

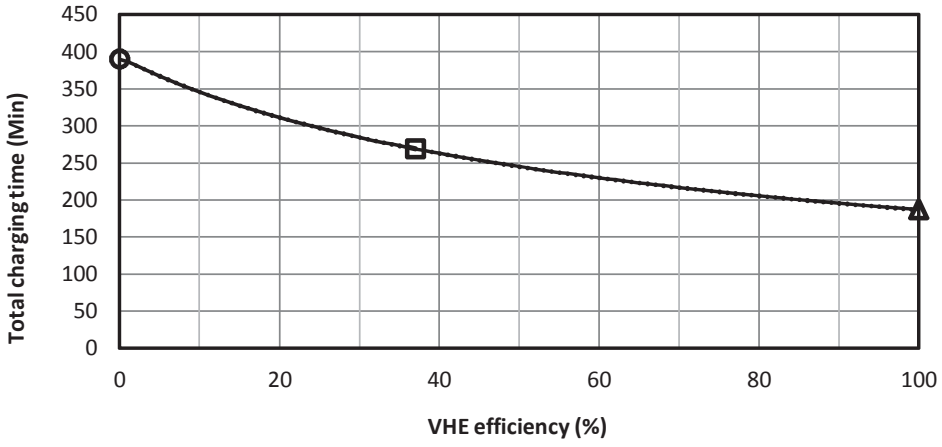

FIGURE B.4: Total charging length versus VHE conversion efficiency; circle: conventional UWCAES, square: UWCAES–VHE with η_{VHE}=37%, triangle: UWCAES–VHE with η_{VHE}=100%.

According to equation B.4 and considering $\eta_{Rt,UWCAES}$ =65%, the roundtrip efficiency of the typical UWCAES–VHE presented in this section is related to the VHE efficiency through $\eta_{Rt,UWCAES-VHE}(\%) = 65\% \times \frac{1}{736} \times \sum_1^{736}(1 + 0.0037(736 - i)\eta_{VHE}(\%))$ this equation can be accurately fitted by $\eta_{Rt,UWCAES-VHE}(\%) = 65\% + 0.885 \times \eta_{VHE}(\%)$ which is illustrated in figure B.5. As can be seen, at η_{VHE}= 0, i.e. conventional UWCAES, the roundtrip efficiency is almost 65%, however, at $\eta_{VHE} = 37\%$, i.e. coupled UWCAES–VHE, the roundtrip efficiency is

increased to 97.7%. According to equation B.4, approximately 34% of the energy released during one complete discharge of the abovedescribed typical system is generated by the A–Cs and the rest is the grid surplus power stored in the A–Cs.

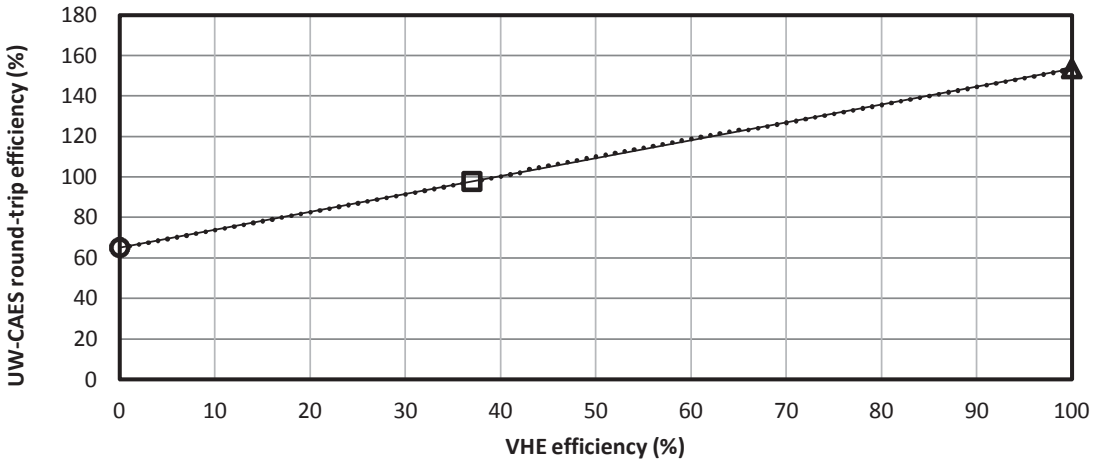

FIGURE B.5: Roundtrip efficiency of the UWCAES–VHE versus VHE conversion efficiency; circle: conventional UWCAES, square: UWCAES–VHE with η_{VHE}=37%, triangle: UWCAES–VHE with η_{VHE}=100%.

Conversion efficiency of the A–Cs of the typical UWCAES–VHE studied in the current section was assumed to be 37%; this value was measured by Bernitsas et al. [1] for a typical conventional VHE converter described in table B.2. Considering the close relationship between conversion efficiency of a VHE converter and its structural features, A–Cs of the UWCAES–VHE are expected to provide higher efficiencies than conventional VHE converters. To better appreciate this expectation, it is worth briefly reviewing some basic characteristics of VIV.

.

TABLE B.2: Specifications of a typical conventional VIVACE converter [5].

Parameter	Description	Value
$m_{cylinder}$	Mass of bare cylinder	2.5350 kg
$L_{cylinder}$	Length of cylinder	0.914 m
$D_{cylinder}$	Diameter of cylinder	0.0889 m
m_{osc}	Total oscillating mass including spring mass	9.784 kg
m_a	Added mass	5.6707 kg
m^*	Mass ratio	1.7250

.

VIV is described by response displacement $y(t)$ and response frequency f_0 respectively defined as amplitude and frequency of the oscillations of the bluff body. Response displacement $y(t)$ and response frequency f_0 are functions of mass ratio m^* and reduced velocity $U^* = U/(f_n D)$ where U, D and f_n respectively are free stream velocity, diameter of the oscillating cylinder and natural frequency of the oscillating cylinder which is defined as [6]

$$f_n = \sqrt{k/(m + m_a)}/2\pi \tag{B.6}$$

where m_a is added mass

$$m_a = \rho_{water}.\pi.D^2/4 \tag{B.7}$$

To maximize the power output, the VHE converter must operate under lock-in condition. To understand the lock-in, it is required to define the Strouhal f_s and excitation f_v frequencies. Strouhal frequency f_s is the frequency of the vortex shedding in the stationary state, and excitation frequency f_v is the vortex shedding frequency of the oscillating cylinder. At a specific mass ratio m^*, while the reduced velocity approaches the value of $\frac{1}{St}$, i.e. $\frac{U}{f_s D}$, the vortex shedding frequency f_v increases and locks into the response frequency. This phenomenon is called lock–in and causes a large increase in response displacement that is a jump in the mechanical power of the oscillating cylinder. Flow retains the lock-in condition within a specific range of reduced velocity called synchronization region. Once reduced velocity exceeds the upper limit of the synchronization region, the response displacement quickly drops down, i.e. a significant decrease in the power converted by the VIVACE converter. From Williamson and Govardhan [6], a significant increase in frequency, displacement and in the range of synchronization occurs as mass ratio is reduced. This is one reason that Bernitsas et al. [1] stated ". . .the length of each VIVACE cylinder has to be long enough to ensure low m^*. . .". As is seen, the mass ratio of the typical conventional converter described in table B.2 is 1.725. For the proposed coupled VHE–UWCAES, scaled to the dimensions of the typical conventional VIVCAE described in table B.2, using the same material of the SP20000 model of cylindrical accumulator, and assuming a stored air pressure of 800 kPa and water temperature of $12°C$ the oscillating mass is approximately 8 kg. This results in a lower mass ratio of 1.4; this provides a wider synchronization envelope with higher VIV amplitude and frequency; this may increase the overall conversion efficiency of the VHE converter to values higher than 37% and consequently, may lead to round trip efficiencies beyond 97.7%.

B.4 Conclusions

By replacing the stationary, droplet shaped accumulators of conventional UWCAES with cylindrical accumulators that are free to oscillate in response to vortex induced vibrations; a power generating UWCAES is introduced. The power generated by the oscillating accumulators effectively compensates for UWCAES energy losses such that the roundtrip efficiency of the energy storage is significantly increased. For the UWCAES–VHE considered here, the storage efficiency sees a nearly 1 percent increase per each percent of VHE conversion efficiency. Thus, at η_{VHE}=37% the roundtrip efficiency of the energy storage is improved to approximately $\eta_{Rt,UWCAES}$=97.75%. The hybridization of these technologies also leads to a reduced storage system charging time through the power generated by the oscillating accumulators. Finally, the UWCAES–VHE coupling also positively affects the efficiency of the VIVACE converters. The

lower mass ratio of the coupled VIVACE–UWCAES, the reduced velocity range of VIV, the reduced velocity range of lock-in and the response displacement are effectively improved leading to higher volume energy density, footprint energy density, and conversion efficiency.

Acknowledgements

This work is made possible by Natural Sciences and Engineering Research Council of Canada, the Ontario Centres of Excellence and the Ontario Trillium Foundation.

References

[1] Bernitsas, M.M., Raghavan, K., Ben-Simon, Y., Garcia, E.M.H., 2008. VIVACE vortex induced vibration aquatic clean energy: a new concept in generation of clean and renewable energy from Fluid Flow. Journal of Offshore Mechanics and Arctic Engineering, 130, 1–15.

[2] Ibrahim, H., Ilinca, A., Perron, J., 2008. Energy storage systems characteristics and comparisons. Renewable and Sustainable Energy Reviews, 12, 1221–50.

[3] Cheung, B., Cao, N., Carriveau, R., Ting, D.S.-K., 2012. Distensible air accumulators as a means of adiabatic underwater compressed air energy storage. International Journal of Environmental Studies, 69, 566–77.

[4] Subsalve USA Corporation, 2011. **[Link]**

[5] Bernitsas, M.M., Park, H., Kumar, R.A., 2012. Selective roughness in the boundary layer to suppress flow-induced motions of circular cylinder at $30,000 \leq Re \leq 120,000$. Journal of Offshore Mechanics and Arctic Engineering, 134, 1–7.

[6] Williamson, C.H.K., Govardhan, R., 2004. Vortex-induced-vibrations. Annual Review of Fluid Mechanics, 36, 413–55.

Appendix C

Correlating Flow Pattern with Force Coefficients in Air Flow past a Tandem Unit of Three Circular Cylinders

A. R. Vasel-Be-Hagh, D. S.-K. Ting, R. Carriveau

Turbulence and Energy Laboratory, Lumley Centre for Engineering Innovation, University of Windsor, Ontario, Canada N9B 3P4

Vasel-Be-Hagh, A.R., Carriveau, R., Ting, D.S.-K., 2015. Correlating Flow Pattern with Force Coefficients in Air Flow past a Tandem Unit of Three Circular Cylinders, International Journal of Fluid Mechanics Research, 40(3), 235-253.

C.1 Introduction

Over the last few decades, much attention has been devoted to the study of flow past cylindrical structures, including one or two cylinders. The most extensively investigated is the flow past a single circular cylinder. Despite these existing comprehensive studies, flow around one single cylinder is still a very active research area and new discoveries about this kind of flow are still being reported [1–5]. Also, many experimental and numerical investigations have examined flow around two cylinders for different configurations including inclined configuration [6], closely [7], moderately and widely [8, 9] spaced staggered configuration for different incidence schemes ($0° < \alpha < 90°$), tandem ($\alpha = 0°$) configuration [10], side by side ($\alpha = 90°$) configuration [11], etc. In many applications that utilize cylinder–like structures, flow must proceed around more

than two cylinders, like different combinations of three cylinders. Compared to single and double cylinder investigations, there is a relative dearth of three cylinder studies in the literature.

Lam and Cheung [12] were the first to conduct an experimental study on flow past three circular cylinders. Other researchers followed with different arrangements and Reynolds numbers ranges as summarized in table C.1. It is clear that flow around three cylinders has not been extensively studied and many aspects are not well documented, particularly at low Reynolds number which sees application in some micro scale structures like micro heat exchangers, micro UAVs (unmanned aerial vehicle), planes which fly at very low speed at high altitudes for climate studies etc. The current paper is an attempt to further our understanding on laminar flow around three closely spaced circular cylinders in tandem through computational simulation. This study is conducted at different Reynolds numbers ranging from 20 to 300 in increments of 20. The spacing ratio is fixed at L/D=2.

C.2 Geometry and Boundary Conditions

The schematic diagram of computational domain is shown in figure C.1. As this figure shows, the cylinders are arranged in tandem configuration with spacing ratio of L/D=2. The diameter of each cylinder is set to be 1 inch. These cylinders are mounted in a channel in a way that the center of the second cylinder (the middle one) is placed 20 inches downstream of the inlet boundary. Also the width and length of the channel are 30 and 70 inches respectively.

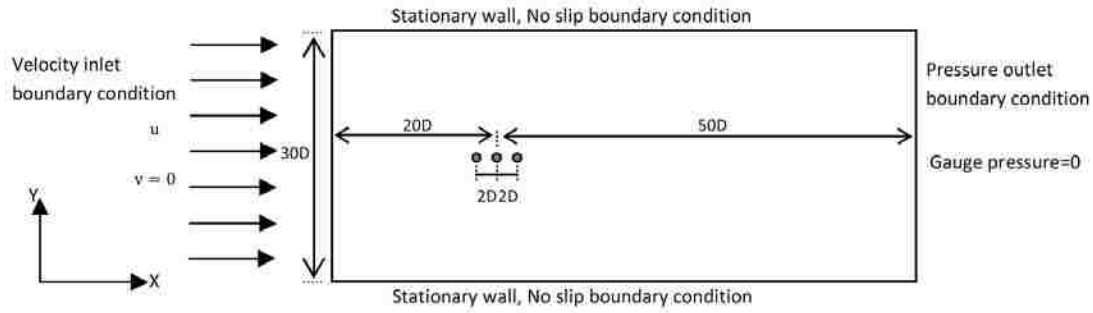

FIGURE C.1: Geometry of computational domain and boundary conditions.

In this simulation, three kinds of boundary condition are implemented. No slip boundary condition is chosen for the channel and cylinders walls which all are stationary. Also velocity inlet and pressure outlet boundary conditions are set at inlet and outlet of the channel respectively. The y–component of the incoming flow velocity is zero and its x–component magnitude varies from 0.453 to 6.8 in/s depending on the Reynolds number which is calculated based on the cylinder diameter and air properties at standard temperature and pressure. The gauge pressure at outlet boundary is set at zero.

TABLE C.1: The calculated and measured results for the flow around three cylinders.

Researcher	Re	Arrangement	Calculated/Measured Data	Approach
Lam and Cheung [12]	(2.1... 2.5) $\times 10^3$	Equilateral-triangular	vortex shedding frequency	Experimental
Sayers [13]	10^4	Equilateral-triangular	Vortex shedding frequency	Experimental
Tatsuno et al. [14]	6.2 $\times 10^4$	Equilateral-triangular	Variation of force coefficients with incidence angle, Local C_p for some different spacing ratio	Experimental
Guillaume and Rue [15]	(2.5...4.4) $\times 10^3$	Side-by-side	Hot-wire power spectra versus frequency, Local C_p for some different spacing ratio Local C_p, distribution of mean velocity, Reynolds normal stresses and shear stress,	Experimental
Zhang and Zhou [16]	300 and 1500	Side-by-side	Hot-wire power spectra versus Strouhal number, Vorticity contour	Experimental
Wu et al. [17]	(100...300)	Equilateral-triangular	Drag coefficient, time-mean Nusselt number and isotherms for different spacing ratiosand Re numbers	Numerical
Harichandan and Roy [18]	100 and 200	Tandem side-by-side	Force coefficient and Strouhal number for different spacing ratio	Numerical
Bao et al. [19]	1.4 $\times 10^4$	Equilateral-triangular	Force coefficient and Strouhal number	Numerical

C.3 Mesh–Independence Analysis

To have an efficient mesh for the geometry described in previous section, different kinds of cells were checked; however, a combination of quad and triangular cells appeared to be less sensitive to the total number of cells and performed a faster convergence speed. Accordingly, for the current simulation the quadrilaterals method is used to generate mesh in the near vicinity of cylinders and the rest of the computational domain is meshed using triangles (see figure C.2). This mesh was created using ANSYS Workbench 12.0. Vakiland Green [6] used such combination of quad and triangular cells for a two dimensional simulation of side-by-side circular cylinders. Some other researchers employed only triangular cells to mesh other configurations of circular cylinders; Bao et al. [19] used triangular cells to mesh over three cylinders with equilateral triangular arrangement and Sharman et al. [20] used them to mesh two tandem cylinders.

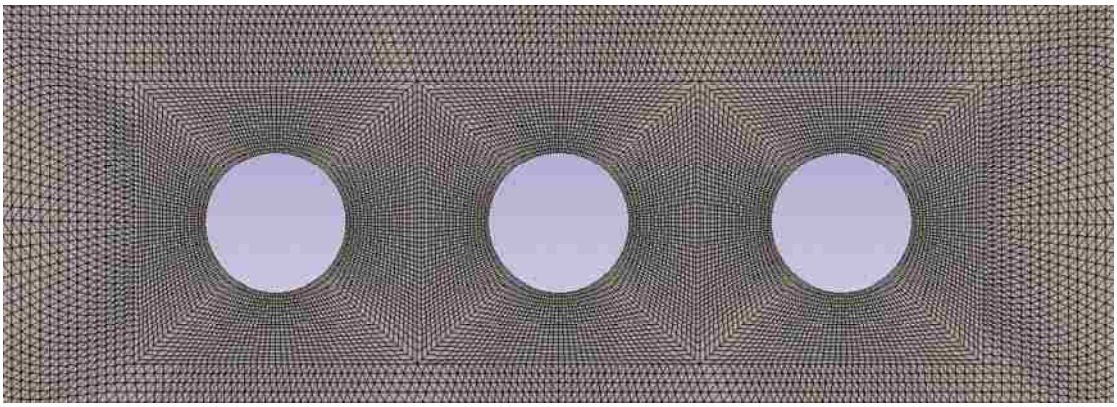

FIGURE C.2: Mesh with 123000 cells used for the current study.

To establish the accuracy of the results, a mesh-independence analysis is conducted by calculating the drag coefficient of cylinders for different number of cells. Figure C.3 depicts effects of mesh density on drag coefficient at Re = 150. As can be seen, by initial refinement of the relatively coarse mesh, the drag coefficient of the cylinders significantly varies; the third cylinder appears to be most sensitive to meshing. However, beyond 123000 elements the drag coefficient of each cylinder is nearly constant and a further mesh refinement has negligible effect on it. Accordingly, the mesh with 123000 elements is used in this simulation.

C.4 Solution

The simulation reported in this paper is carried out using the conservation of mass and momentum equations which for unsteady, laminar, and incompressible flow with constant fluid properties are respectively described by

$$\nabla . V = 0, \tag{C.1}$$

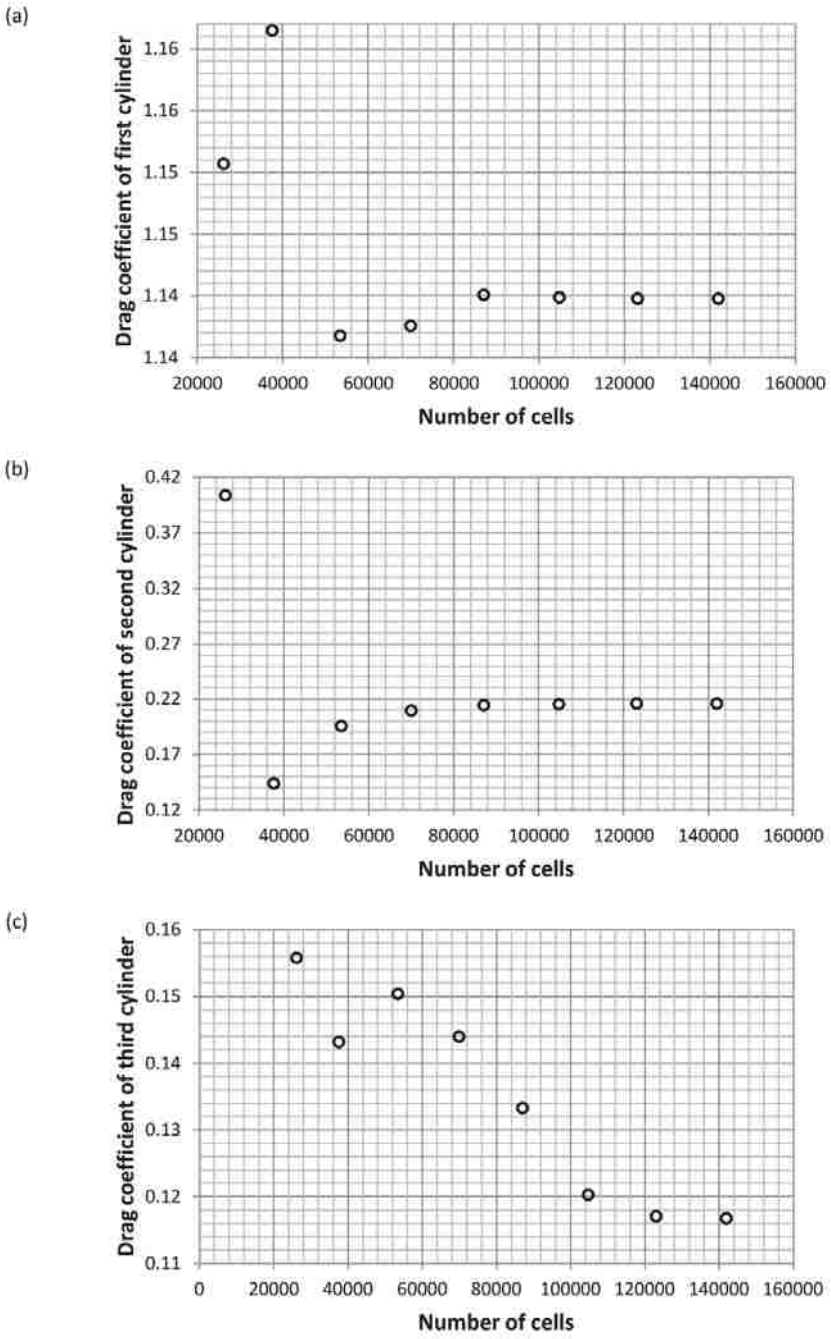

FIGURE C.3: Drag coefficient of cylinders vs. number of cells; (a) the 1^{st} cylinder, (b) the 2^{nd} cylinder, (c) the 3^{rd} cylinder.

$$\frac{\partial V}{\partial t} + V.\nabla V = -\frac{1}{\rho}\nabla p + \nu\nabla^2 V, \tag{C.2}$$

where V, p, ρ and ν are the fluid velocity vector, pressure, density and kinematic viscosity. It is assumed that the computational domain is two dimensional and no body force exists. A second order implicit method is applied to provide the transient solution of equations C.1 and C.2 using Fluent 12.0.16 software. It should be mentioned that this software uses finite volume method to discretize governing equations. In this simulation the solution was considered converged when the total residuals for the continuity and momentum equations were equal to 10^{-8}.

C.5 Results and Discussion

In this section results of the simulation are discussed for Reynolds numbers from 20 up to 300 in two parts. At first, the mean force coefficients of all three cylinders are discussed. Then, the time evolution of the lift coefficient and Strouhal number are studied to isolate the critical Reynolds number for which the flow becomes unsteady.

C.5.1 Force Coefficients

The simulation reveals that no lift force is acting on the cylinders, and the cylinders are only affected by the drag force which includes two components; pressure viscous force.Figure C.4 shows pressure, viscous and total drag coefficients of first, second, and third cylinders versus Reynolds number. The C_D–Re relationship may be described by a power law curve fit,

$$C_D = aRe^b + c, \tag{C.3}$$

where C_D stands for drag coefficient. The magnitude of parameters a, b, and c are summarized in table C.2.

TABLE C.2: Constant parameters of equation C.3.

	First cylinder			Second cylinder			Third cylinder		
C	a_1	b_1	c_1	a_1	b_1	c_1	a_1	b_1	c_1
Pressure drag coeff., C_p	10.230	-1.079	0.848	5.634	-0.035	-4.944	1.668	-0.667	0
Viscous drag coeff., C_f	5.477	-0.613	0	3.490	-0.791	-0.066	3.266	-0.817	0
Total drag coeff., C_D	11.72	-0.745	0.865	3.312	-0.314	-0.901	4.811	-0.749	0

Figure C.4(a) shows drag coefficients of the first cylinder. It is observed that the pressure coefficient is higher than its viscous counterpart and it makes up the major portion of total drag coefficient. For this cylinder, the difference between pressure and viscous drag coefficients is constantly increasing so that the viscous share of total drag coefficient decreases from 41 to 15% with increasing Re from 20 to 300.

Figure C.4(b) is related to the second cylinder. As this diagram illustrates, while the Re number goes from 20 to 300, both pressure and viscous drag forces decrease. More can be learned about

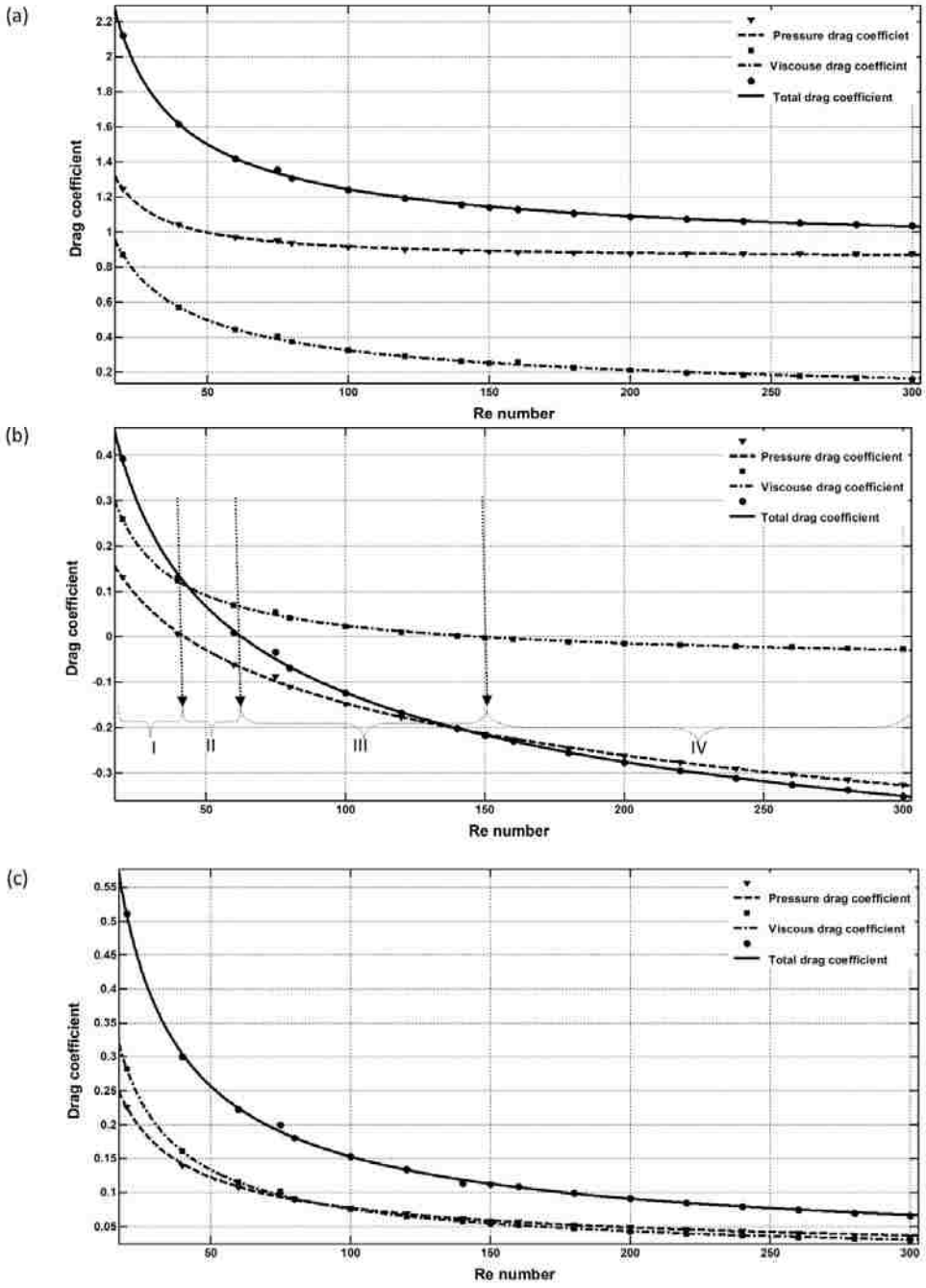

FIGURE C.4: Drag coefficients versus the Reynolds number; (a) the 1^{st} cylinder, (b) the 2^{nd} cylinder, (c) the 3^{rd} cylinder.

these forces by studying the pressure and velocity distribution in the near vicinity of this cylinder in four separate parts, as follows.

I: $20 \leq$ **Re** ≤ 42**.** In this range of Re, the total pressure close to the upstream half of cylinder surface is higher than the downstream one. So, as it is shown in figure C.4(b), when Re is lower than 42 the pressure coefficient is positive, i. e., the pressure drag force points towards the downstream direction. This is better observed in figure C.5 by examining the pressure contour around cylinders at Re of 20.

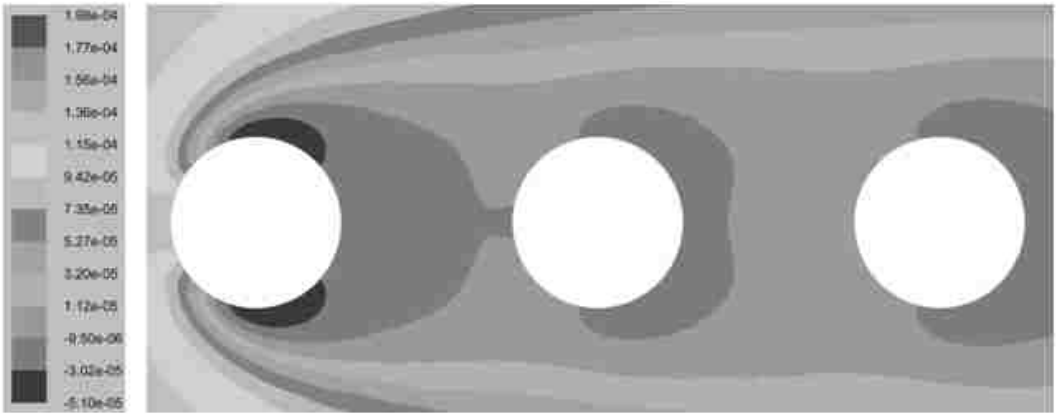

FIGURE C.5: Pressure contour at Re = 20 (the values are in Pa).

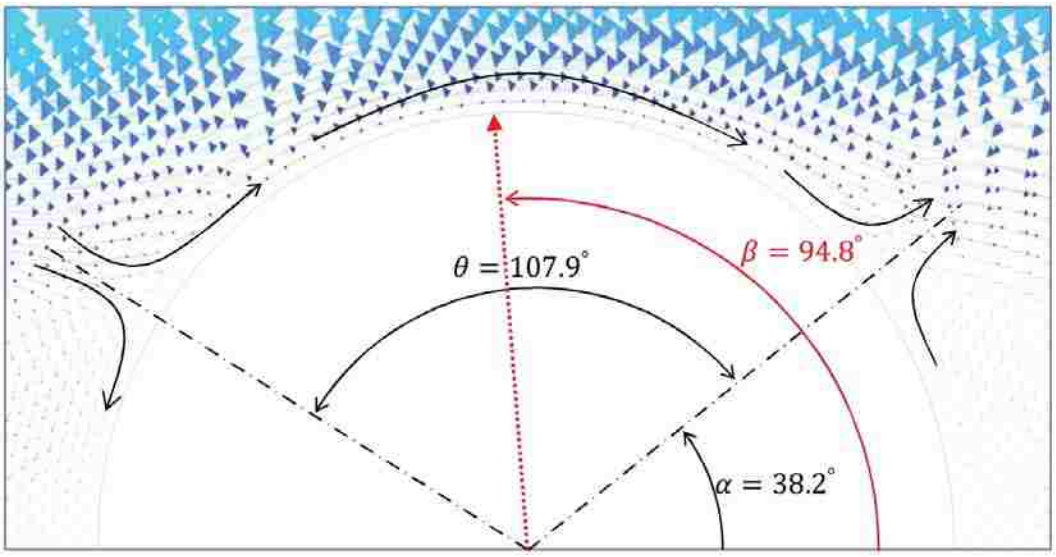

FIGURE C.6: Flow near the surface of second cylinder at Re = 20, $\theta = 107.9°$ and $\beta = 94.8°$.

According to the flow direction close to the surface of the second cylinder, three different zones are always observed on its surface (see figure C.6). On the middle zone flow goes downstream and on the two other ones flow reverses back toward upstream. Figure C.6 illustrates this for Re of 20. This figure shows only the top half of cylinder, the lower half is identical to the top. In this figure, θ is the central angle delineating the surface zone for which the flow is

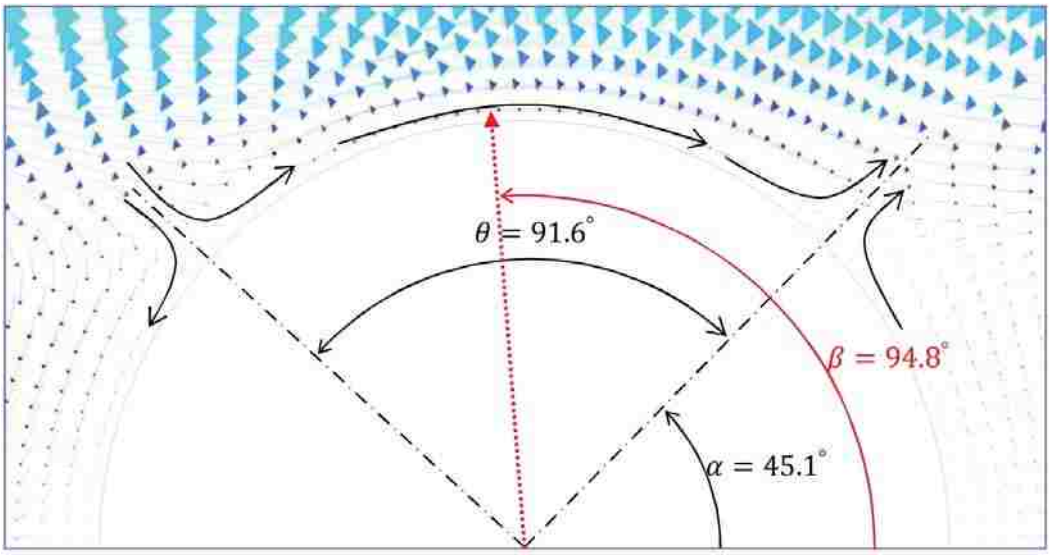

FIGURE C.7: Flow near the surface of second cylinder at Re = 42, $\theta = 91.6°$ and $\beta = 94.8°$.

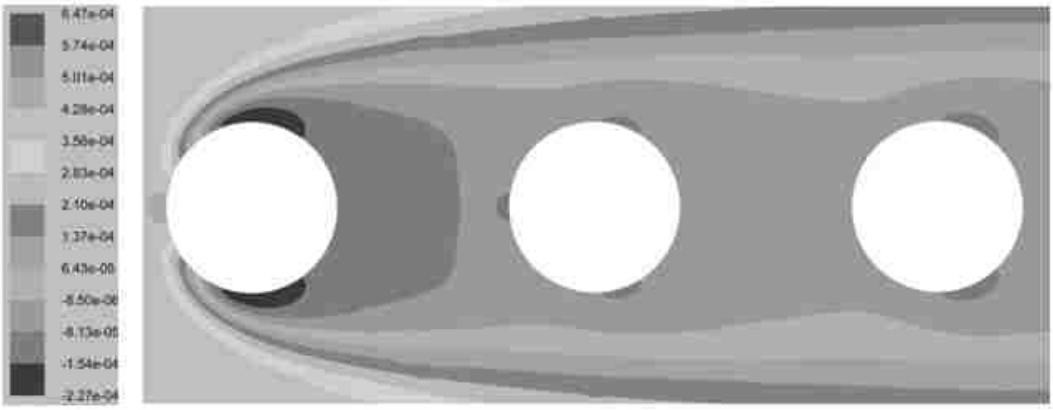

FIGURE C.8: Pressure contours at Re = 42 (the values are in Pa).

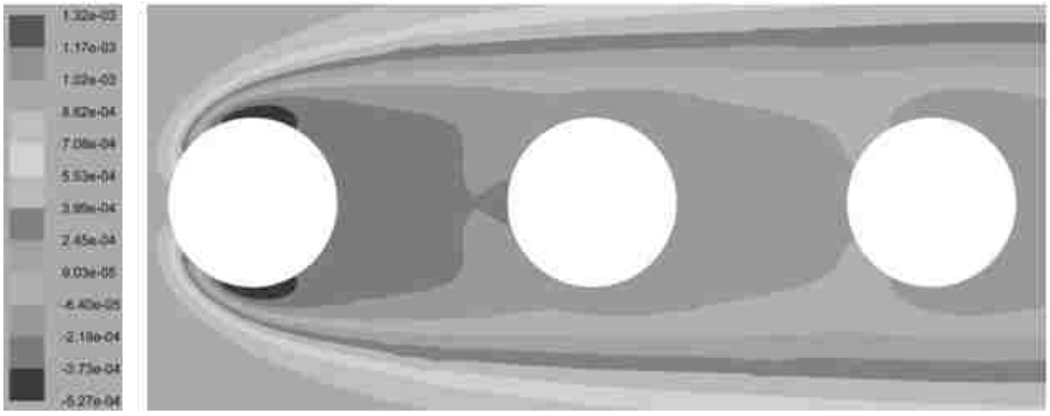

FIGURE C.9: Pressure contours at Re = 60 (the values are in Pa).

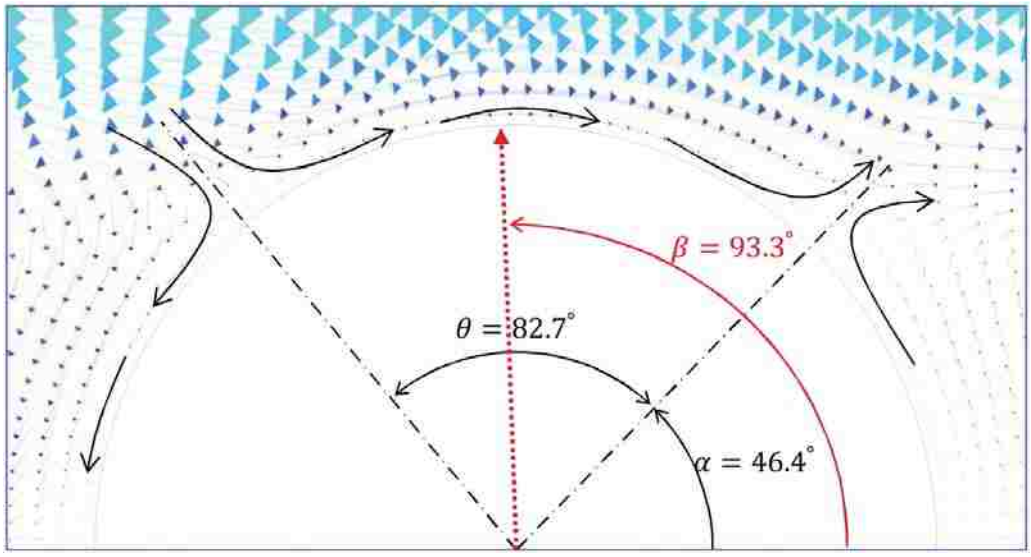

FIGURE C.10: Flow near the surface of second cylinder at Re = 63, $\theta = 82.7°$ and $\beta = 93.3°$.

headed toward downstream, and β is the center of the angular sector where the shear stress rises to its maximum magnitude. This specific location is shown with a dashed arrow in figure C.6. When Re is between 20 and 42, the specific location β in which the shear stress is at its maximum magnitude is identified on the middle zone. Further, the area of this zone is larger than summation of the two other ones, i.e., $\theta > 90°$. Consequently, the component of viscous force which is toward downstream is greater than the other component which is oriented in the upstream direction. Accordingly, net result goes toward downstream and viscous drag coefficient is positive (see figure C.4(b)). It is observed that for the case of Re = 20 in figure C.6, θ is 107.9° which amounts to 60 percent of the total surface. In this case, the region where shear stress is maximised is limited to angular locations of $\beta = 94.8° \pm 15°$. When Re is increased to 42, shear stress is maximised at angular location of $\beta = 94.8° \pm 16°$ and θ decreases to 91.6° (see figure C.7). This leads the reduction of the viscous force component which is shown in figure C.4(b).

II: $42 \leq$ **Re** ≤ 63**.** Figure C.8 depicts the pressure distribution around the second cylinder for Reynolds number of 42. It is observed that the total pressure at the back of the second cylinder approaches that of its frontal area, leaving viscous drag as the only force acting on the second cylinder.

With further increase in Re, the back pressure increases beyond the pressure at the frontal area. So the direction of pressure force changes toward upstream, as shown in figure C.4(b), i.e., the pressure drag coefficient becomes negative. In other words, Re of 42 represents a turning point for the pressure drag force. Figure C.9 provides an example of such a case. This figure shows the pressure distribution around the cylinders at Re of 60. It is seen that the pressure on the rearward half of second cylinder surface is higher than that at the front.

The velocity vectors near the surface of the second cylinder are shown in figure C.10 at Re of 63. It is observed that with increasing Re from 42 to 63, the downstream bound flow sector decreases

in size from $\theta = 91.6°$ to $82.7°$ and the maximum shear stress region becomes more limited from $\beta = 94.8° \pm 16°$ to $\beta = 93.3° \pm 10.5°$. This leads to a reduction of viscous drag coefficient as shown in figure C.4(b). However, this coefficient is still positive, and the net viscous drag force is oriented downstream and is still larger than the pressure drag force.

III: $63 \leq$ **Re** ≤ 150**.** Beyond Re of 63, the downward viscous force decreases to such an extent that it becomes equal to the upward pressure force, consequently, at Re = 63 the total drag force on the second cylinder is zero. Similar to the trend observed in the previous section, increase of Reynolds number from 63 to 150 decreases the size of the downstream bound flow sector from $\theta = 82.7°$ to $65.5°$, producing a decline in the viscous drag force. On the other hand, the pressure contours indicate that increasing Re widens the difference between pressure level at back and front of the second cylinder. Consequently, the pressure drag coefficient increases; see figure C.4(b). Accordingly, the magnitude of pressure force becomes larger than viscous one and the direction of total drag force changes toward upstream. Thus, Re of 63 represents a critical point where the total drag coefficient changes from positive to negative, i.e., crosses the zero value.

Next, flow near the surface of the second cylinder is examined and illustrated in figure C.11 for a Reynolds number of 100. In this case θ is reduced to 70.8°, however, the region of maximised shear stress is still contained at $\beta = 93.3° \pm 16°$ and extended into the θ domain. Here the positive component of the viscous drag force is larger than the negative one. Accordingly, the net viscous drag force remains oriented in the downstream direction and the viscous drag coefficient remains positive.

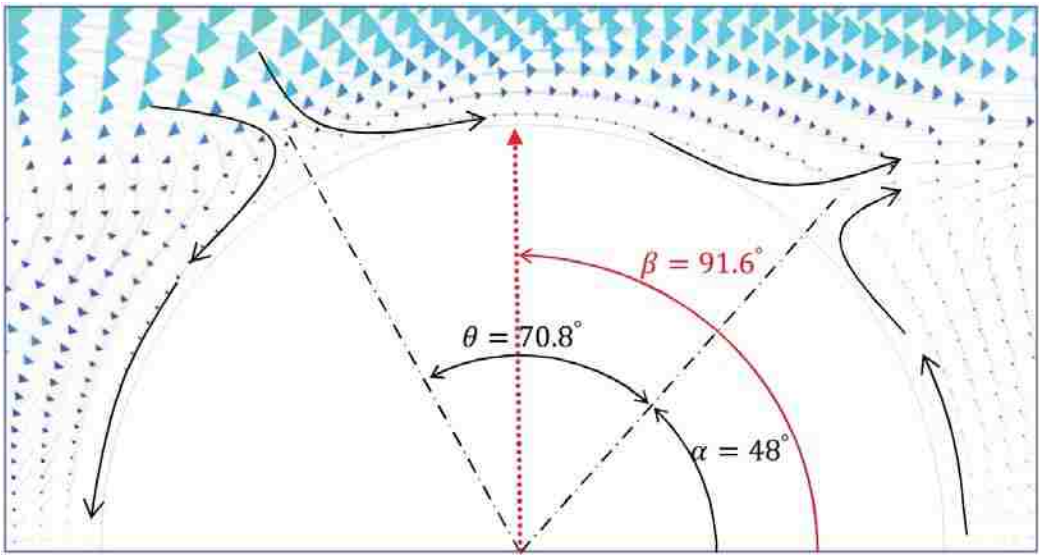

FIGURE C.11: Flow near the surface of second cylinder at Re = 100, $\theta = 70.8°$ and $\beta = 91.6°$.

IV: $150 \leq$ **Re** ≤ 300**.**

As the Reynolds number exceeds 150, the sector on which the viscous force is oriented downstream decreases to 60.5°. It is observed that in this case the upstream and downstream viscous force components are equal. So, as it is observed in figure C.5(a), at Reynolds number of 150

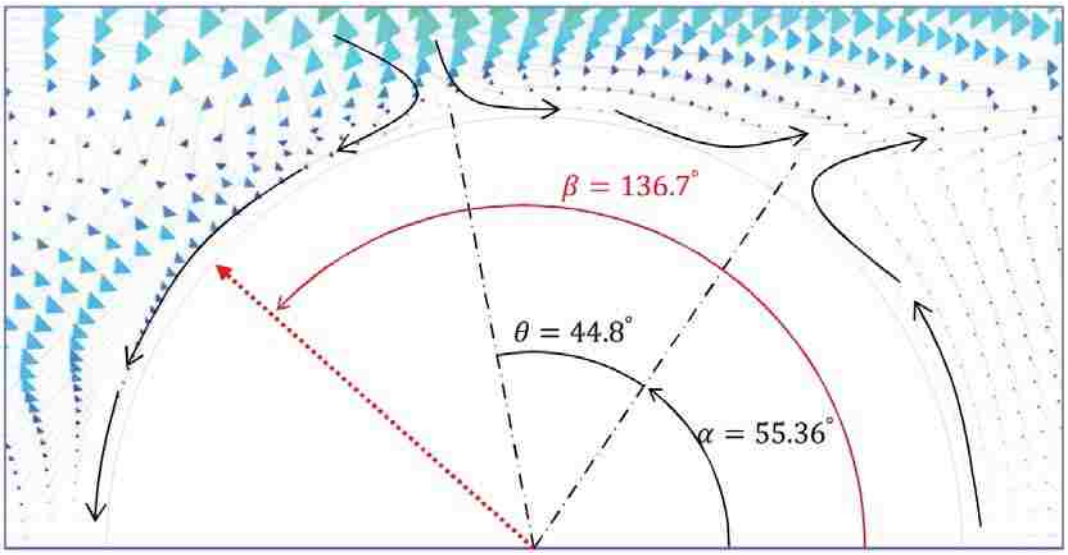

FIGURE C.12: Flow near the surface of second cylinder at Re = 260, $\theta = 44.8°$ and $\beta = 136.7°$.

no viscous force acts on the cylinder surface, in fact, this Reynolds number is a critical point for the viscous force. Beyond Re of 150, by increasing Re both pressure and viscous drag force increase in the upstream direction. As a case in point, velocity vectors in near vicinity of cylinder surface are illustrated at Reynolds number of 260 in figure C.12. It is observed that at this Reynolds number θ decreases to 44.8°. Moreover, in this case the shear stress finds its maximum at $\beta = 136.7° \pm 5.9°$ which is located out of the θ domain. Thus the downstream pointing viscous drag force component is very small, as such the net viscous drag force acts toward upstream.

Figure C.4(c) depicts the drag coefficients of the third cylinder. It is observed that while Reynolds number varies from 20 to 300 both pressure and viscous drag coefficients continuously decrease while remaining positive. It is found that before reaching the Re of 88, viscous effects dominate the pressure effects; however, at higher Reynolds numbers the opposite is true.

C.5.2 Strouhal Number–Flow Pattern

Figure C.13 illustrates the time evolution of the lift coefficient for Re of 100, 101, 105 and 110 to expose the transition from steady to unsteady regime. At Re · 100 the lift coefficient diagram experiences some fluctuations initially, however, they finally converge to zero (see figure C.13(a)). The frequency of these fluctuations is equal to the frequency of sideward movement of the downstream wake; also their amplitude is directly related to the width of zone in which the wake moves from side to side. Accordingly, at Re≤100 once lift coefficient diagram converges to zero, the flow pattern becomes steady, i.e., no wake movement, no vortex shedding. This steady flow is portrayed via vorticity contours in Figure C.14 at Re ranging from 20 to 80. All contours in this figure are due to the time t = 110 s and are depicted at the same vorticity levels. As it is seen, by increasing the Re downstream wake length increases. Once Re goes beyond 100 the lift coefficient never converges and starts to oscillate around zero, amplitude of these oscillations

increases with Re. Figure C.13(b) exhibits lift coefficient versus time for Re of 101. It is observed that the initial amplitude of oscillations decreases with time, however, the oscillations never vanishes and eventually stays constant but at a very small value. By increasing Re, the eventual amplitude of lift coefficient oscillations increases (see figures C.13(c) and C.13(d). Amplitude of lift coefficient oscillations is directly related to the width of the zone in which downstream wake fluctuates. Figure C.15 illustrates the effect of Re on the flow pattern during transition from steady to unsteady wake. At Re of 100 wake region is steady and no movement occurs, however, at Re = 101, downstream wake fluctuates in a very narrow zone. By increasing the Re, these fluctuations occur within a wider zone, and finally at Re around 105, vortex shedding starts, however, the frequency of vortex shedding is very small. This frequency increases with Re. Figure C.16 depicts flow pattern for Re ranging from 120 to 300. All snapshots are taken at t = 110 s and vorticity levels are set at the same values for all cases. To investigate the frequency of vortex shedding in each of these cases, the periodic behavior of surface averaged lift coefficient must be considered. Figures C.17 to C.19 illustrate the surface averaged lift coefficient versus time at Re = 120, 200 and 300 respectively. Moreover, these figures show time evolution of flow pattern in one complete period of time. According to these figures, frequency of lift coefficient oscillations and vortex shedding frequency is the same for all three cylinders at each specific Re, however, there is a constant phase difference between these oscillations, i.e., they are not maximum simultaneously. In other words, the three cylinders do not shed vortices at the same time. By increasing the Re from 120 to 300 the frequency of vortex shedding increases from 0.42 to 1.1 Hz. Consequently, the dimensionless frequency (Strouhal number)

$$St = \frac{f.D}{U} \tag{C.4}$$

increases as well. Here D and U are cylinder diameter and incoming flow velocity respectively. Once Re increases from 120 to 300, Strouhal number increases from 0.155 to 0.161. It should be considered that because of the incoming flow velocity in the denominator, the Strouhal number is less sensible to Re compared to frequency. Frequency and Strouhal number are portrayed versus Re in figure **??**. It is observed that in this range of Re there is an almost linear relation between them.

C.6 Conclusion

Current simulation reveals details about the relation between flow behaviour near the surface of three tandem cylinders and trend of drag coefficient components at low Re numbers. Also flow pattern in downstream of tandem unit of cylinders is correlated to lift coefficients oscillations and is illustrated via vorticity contours. The major findings which should be noted in the practical applications of flow over a three tandem cylinders in micro engineering are summarized.

- It was found that the time averaged lift force remains zero for all the cylinders over the range of studied conditions; only pressure and viscous drag forces were observed.
- Both pressure and viscous drag forces decreased with increasing Re for all three cylinders.

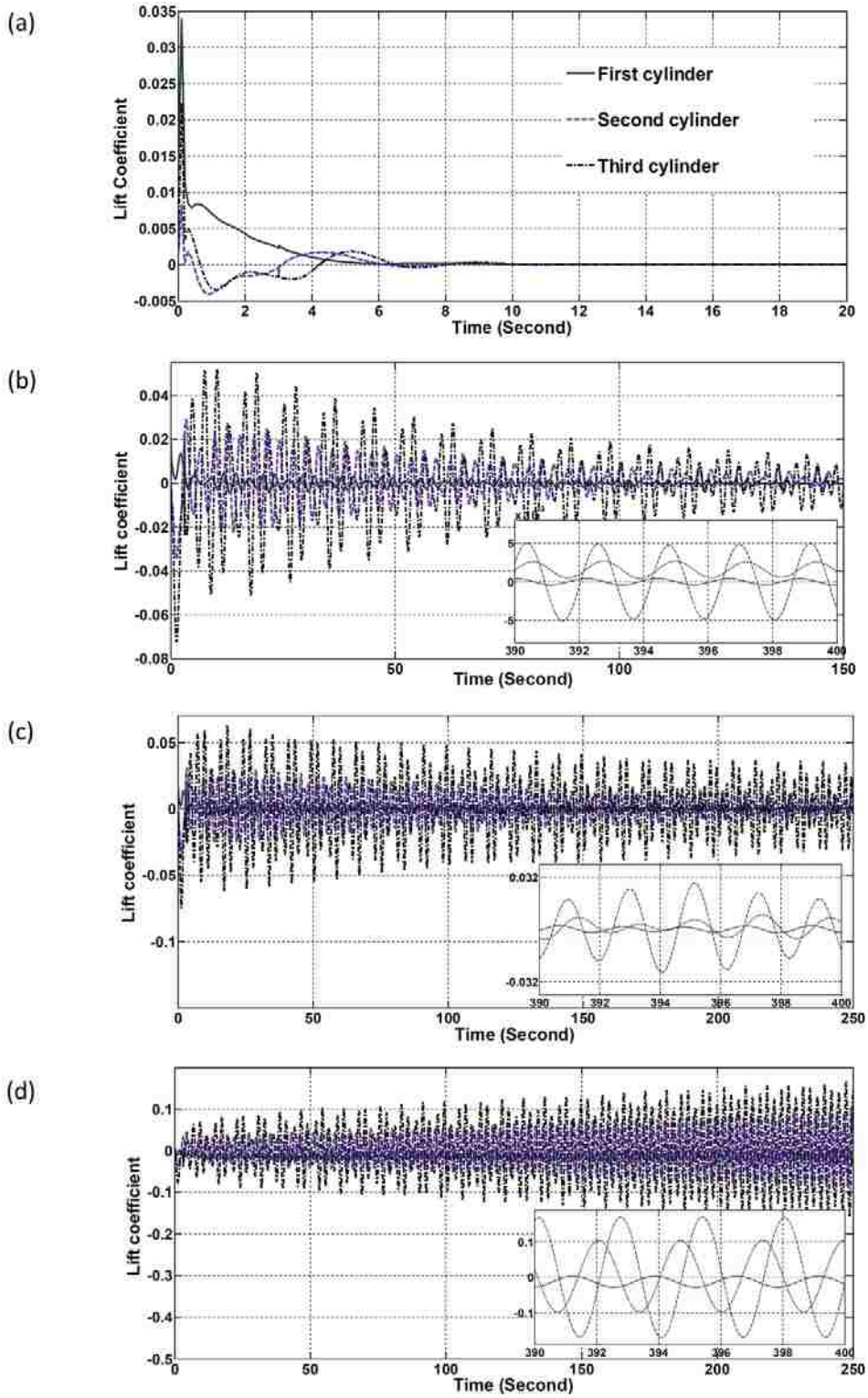

FIGURE C.13: Time convergence history of lift coefficient; (a) Re=100, (b) Re=101, (c) Re=105, (d) Re=110.

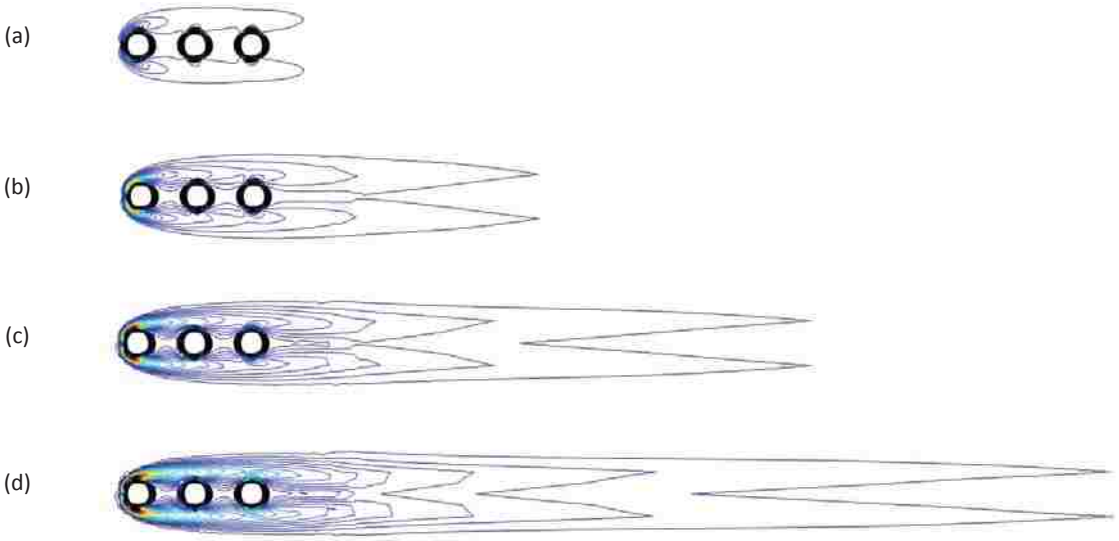

FIGURE C.14: Steady flow at Re≤100, t = 110s and vorticity level from 1.5 to 50 1/s; (a) Re=20, (b) Re=40, (c) Re=60, (d) Re=80.

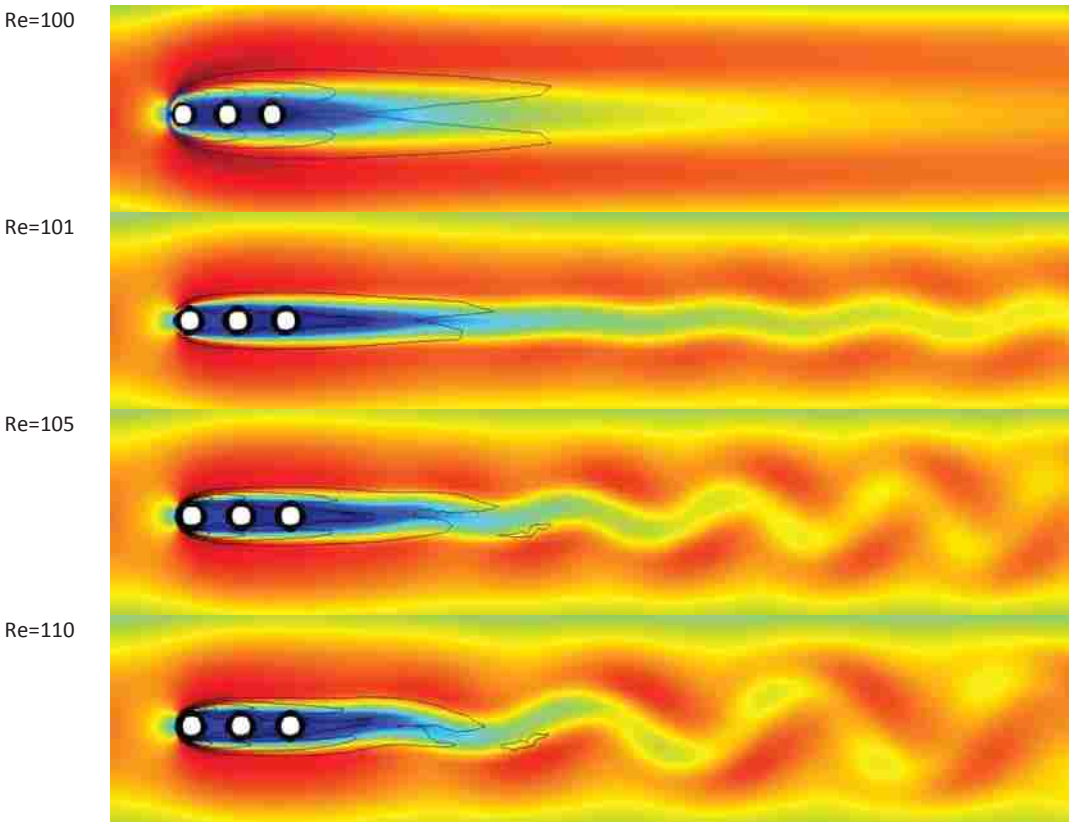

FIGURE C.15: Transition from steady to unsteady flow pattern. Contours are colored by velocity field, black lines are vorticity lines. Contours are prepared at the same moment (t = 110 s) and with the same levels (2 to 60 1/s) for all four cases.

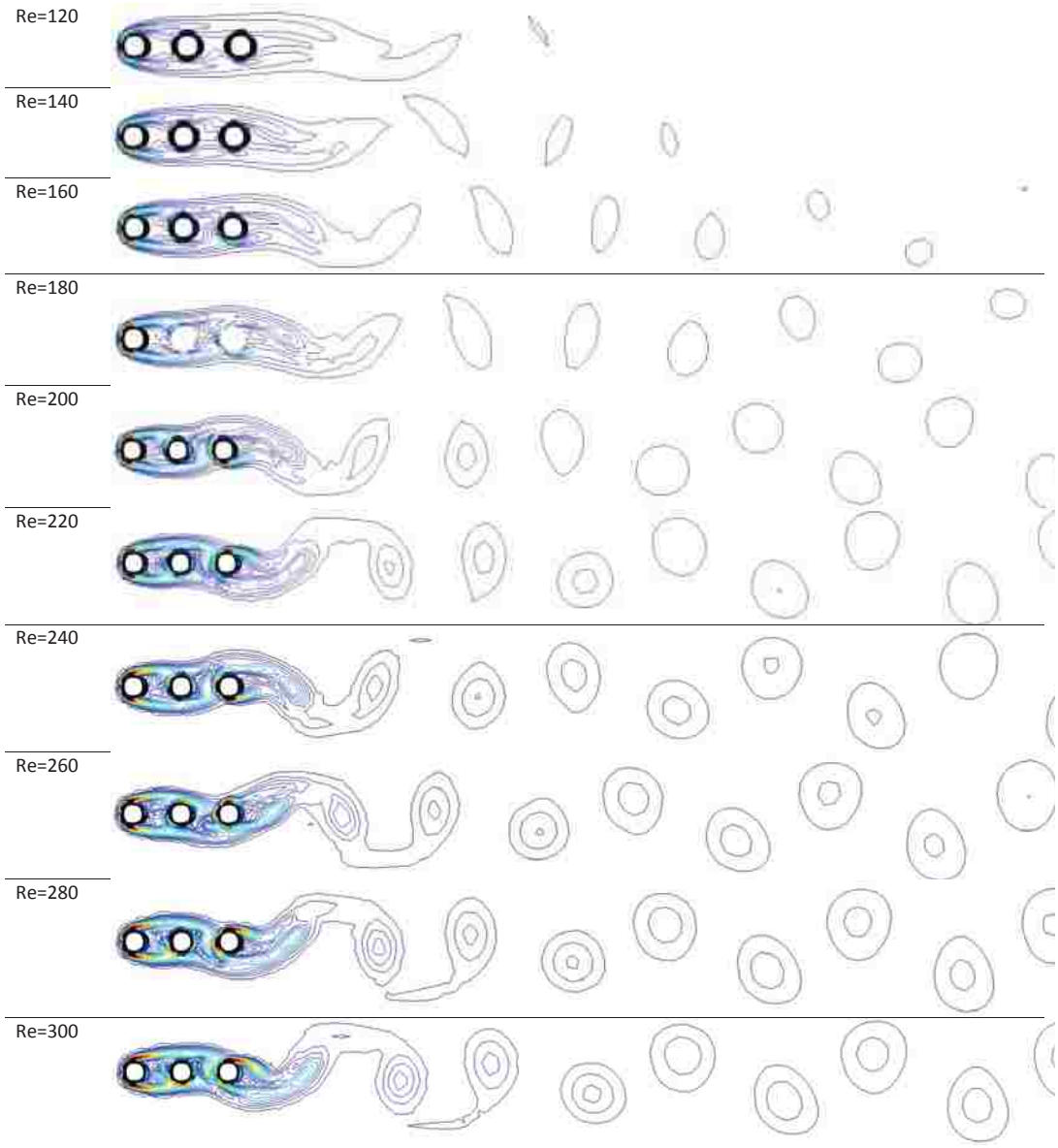

FIGURE C.16: Vorticity lines at Re ranging from 120 to 300 at t = 110 s. For all cases vorticity level is the same, incresing from 2 to 60 1/s in 3 1/s step.

- For the first cylinder, the pressure component of the total drag coefficient was always higher than the viscous one. Both remain positive over the range of conditions investigated.
- The drag coefficient of the second cylinder can be divided in four categories:

$$20 \leq Re \leq 42 : \begin{cases} C_p > 0 & pressure\,coefficient \\ C_f > 0 & viscous\,dissipation \\ C_D > 0 & total\,drag\,coefficient \end{cases}$$

$$42 \leq Re \leq 63 : \begin{cases} C_p < 0 & pressure\, coef\, ficient \\ C_f > 0 & viscous\, dissipation \\ C_D > 0 & total\, drag\, coef\, ficient \end{cases}$$

$$63 \leq Re \leq 150 : \begin{cases} C_p < 0 & pressure\, coef\, ficient \\ C_f > 0 & viscous\, dissipation \\ C_D < 0 & total\, drag\, coef\, ficient \end{cases}$$

$$150 \leq Re \leq 300 : \begin{cases} C_p < 0 & pressure\, coef\, ficient \\ C_f < 0 & viscous\, dissipation \\ C_D < 0 & total\, drag\, coef\, ficient \end{cases}$$

- For the third cylinder, for Re ¡ 88 the viscous component of the total drag coefficient was greater than the pressure component. Like the first cylinder, both pressure and viscous coefficients are always positive.
- For Re≥101 the flow became unsteady and vortex shedding started at Re = 105. The corresponding Strouhal number of this unsteady flow increases with increasing Re.

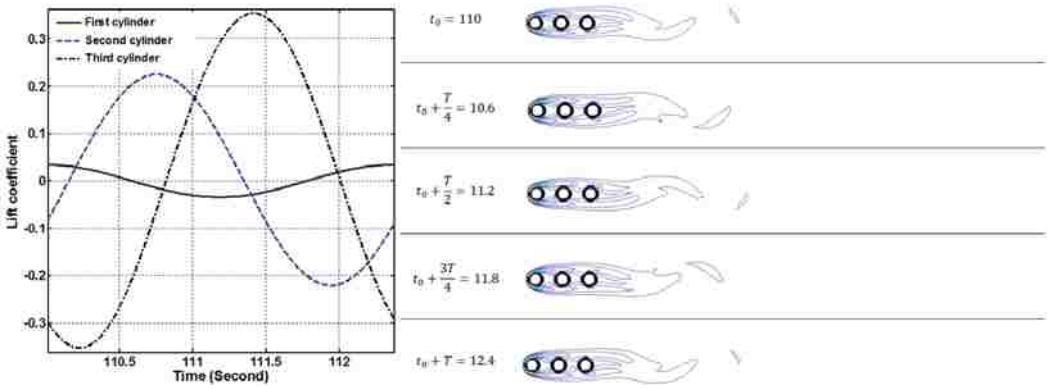

FIGURE C.17: Time evolution of flow pattern in one period of lift coefficient fluctuations coefficient at Re=120.

Acknowledgements

This work is made possible by Natural Sciences and Engineering Research Council of Canada. The lead author is most grateful to the Ontario Trillium Foundation for an Ontario Trillium Scholarship.

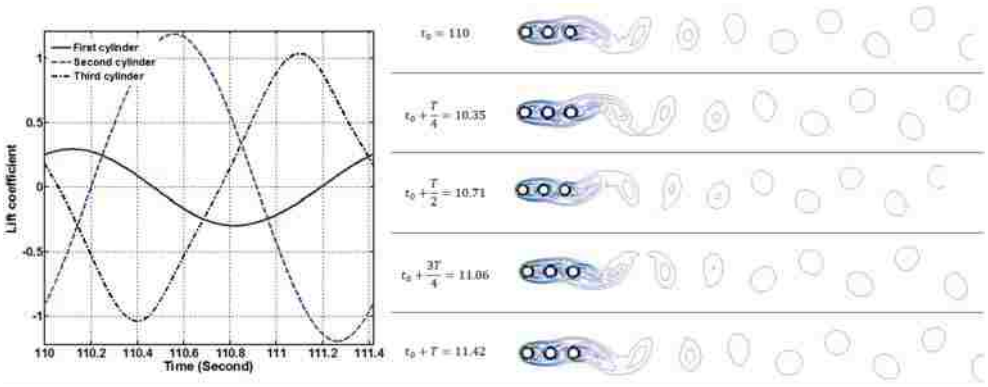

FIGURE C.18: Time evolution of flow pattern in one period of lift coefficient fluctuations coefficient at Re=200.

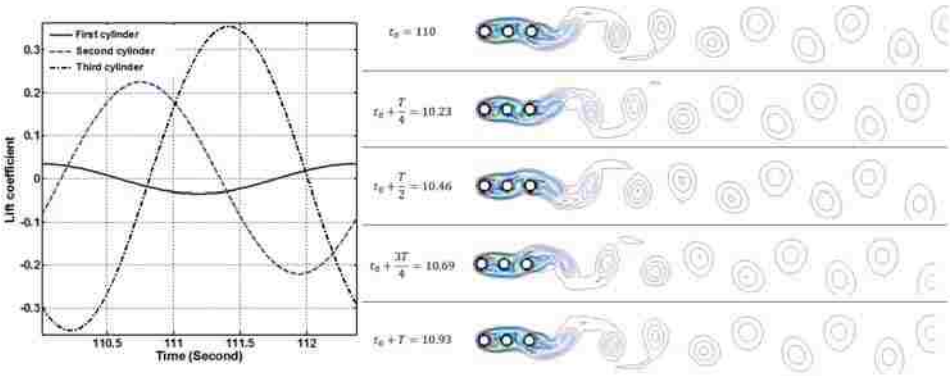

FIGURE C.19: Time evolution of flow pattern in one period of lift coefficient fluctuations coefficient at Re=300.

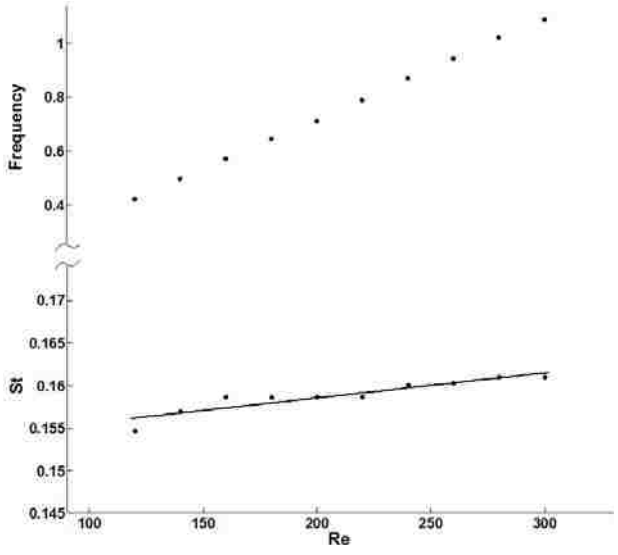

FIGURE C.20: Frequency of vortex shedding and the Strouhal number versus Re.

References

[1] Muralidhar, P., Ferrer, N., Daniello, R., and Rothstein, J. P., 2011. Influence of Slip on the Flow past Super Hydrophobic Circular Cylinders, Journal of Fluid Mechanics, 680, 459–476.

[2] Verma, A. and Mittal, S., 2011. A New Unstable Mode in the Wake of a Circular Cylinder, Physics of Fluids, 23, 121701(1–4).

[3] Vasconcelos, G. L., Moura, M. N., and Schakel, A. M. J., 2011. Vortex Motion around a Circular Cylinder, Physics of Fluids, 23, 123601(1–8).

[4] Rafiuddin Ahmed, M. and Talama, F., 2008. Flow Characteristics and Local Heat Transfer Rates for a Heated Circular Cylinder in a Cross Flow of Air, International Journal of Fluid Mechanics Research, 35, 76–93.

[5] Zuranski, J. A., Wojciechowski, J., and Kinash, R. I., 2002. Investigation of Strouhal Number of Circular Cylinders in Clusters, International Journal of Fluid Mechanics Research, 29, 216–223.

[6] Vakil, A. and Green, S. I., 2009. Drag and Lift Coefficients of Inclined Finite Circular Cylinders at Moderate Reynolds Numbers, Computers and Fluids, 38, 1771–1781.

[7] Lee, K. and Yang, K., 2009. Flow patterns past Two Circular Cylinders in Proximity, Computers and Fluids, 38, 778–788.

[8] Ding, H., Shu, C., Yeo, K. S., and Xu, D., 2007. Numerical Simulation of Flows around Two Circular Cylinders by Mesh-Free Least Square-Based Finite Difference Methods, International Journal of Numerical Methods for Heat and Fluid Flow, 53, 305–332.

[9] Sumner, D., Richards, M.D., and Akosile, O.O., 2008. Strouhal Number Data for Two Staggered Circular Cylinders, Journal of Wind Engineering and Industrial Aerodynamics, 96, 859–871.

[10] Wang, S. Y., Tian, F. B., Jia, L. B., Lu, X. Y., and Yin, X. Z., 2010. Secondary Vortex Street in the Wake of Two Tandem Circular Cylinders at Low Reynolds Number, Physical Review E, 81, 36305(1–9).

[11] Kumar, S., Laughlin, G., and Cantu, C., 2009. Near-Wake Structure behind Two Circular Cylinders in a Side-By-Side Configuration with Heat Release, Physical Review E, 80, 66307(1–11).

[12] Lam, K. and Cheung, C., 2010. Phenomena of Vortex Shedding and Flow Interference of Three Cylinders in Different Equilateral Arrangements, Physical Review E, 81, 36305(1–9).

[13] Sayers, A., 1990. Vortex Shedding from Groups of Three and Four Equispaced Cylinder Situated in a Cross Flow, Journal of Wind Engineering and Industrial Aerodynamics, 34, 213–221.

[14] Tatsuno, M., Amamoto, H., and Ishi, K., 1998. Effects of Interference among Three Equidistantly Arranged Cylinders in a Uniform Flow, Fluid Dynamics Research, 22, 297–315.

[15] Guillaume, D., LaRue, J., 1999. Investigation of the Flopping Regime with Two-, Three- and Four- Cylinder Arrays, Experiments in Fluids, 27, 145–156.

[16] Zhang, H. and Zhou, Y., 2001. Effect of Unequal Cylinder Spacing on Vortex Streets behind Three Side-By-Side Cylinders, Physics of Fluids, 13, 3675–3686.

[17] Wu, H.W., Perng, S.W., Huang, S. Y., and Jue, T.C., 2006. Transient Mixed Convective Heat Transfer Predictions around Three Heated Cylinders in a Horizontal Channel, International Journal of Numerical Methods for Heat and Fluid Flow, 16, 674–692.

[18] Harichandan, A. and Roy, A., 2010. Numerical Investigation of Low Reynolds Number Flow past Two and Three Circular Cylinders Using Unstructured Grid CFR Scheme, International Journal of Heat and Fluid Flow, 31, 154–171.

[19] Bao, Y., Zhou, D., and Huang, C., 2010. Numerical Simulation of Flow Over Three Circular Cylinders in Equilateral Arrangements at Low Reynolds Number by a Second-Order Characteristic-Based Split Finite Element Method, Computers and Fluids, 39, 882–899.

[20] Sharman, B., Lien, F. S., Davidson, L., and Norberg, C., 2005. Numerical Predictions of Low Reynolds Number Flows over Two Tandem Circular Cylinders, International Journal for Numerical Methods in Fluids, 47, 423–447.

VITA AUCTORIS

NAME:	Ahmadreza Vasel-Be-Hagh
PLACE OF BIRTH:	Iran, Mashhad
YEAR OF BIRTH:	1986
EDUCATION:	Malek Ashtar Highschool, Iran, Mashhad, 2004 **Ferdowsi University** of Iran, B.Sc., Iran, Mashhad, 2008 **Ferdowsi University** of Iran, M.Sc., Iran, Mashhad, 2011 **University of Windsor**, PhD, Canada, Windsor, ON, 2015